Fermilab FERMILAB-THESIS-1997-36

THE UNIVERSITY OF CHICAGO

SEARCHES FOR NEW PHYSICS IN DIPHOTON EVENTS IN $\bar{p}p$ COLLISIONS AT $\sqrt{s} = 1.8$ TEV

A DISSERTATION SUBMITTED TO
THE FACULTY OF THE DIVISION OF THE PHYSICAL SCIENCES
IN CANDIDACY FOR THE DEGREE OF
DOCTOR OF PHILOSOPHY

DEPARTMENT OF PHYSICS

BY
DAVID A. TOBACK

CHICAGO, ILLINOIS
DECEMBER, 1997

ACKNOWLEDGMENTS

No work in particle physics these days is ever the product of one person, and this is no exception. Hundreds of people and endless hours have been spent designing, building, testing, running, monitoring and repairing both the Fermilab Tevatron and the CDF detector. To name them all and their contributions here would be impossible, but without them this thesis never would have even begun.

This analysis is unusual and controversial in many respects. Not until very late was it clear how it would turn out. Without the support, expertise, and insight of the University of Chicago group, it would not have been possible.

First and foremost I would like to thank my advisor and mentor, Henry Frisch. This thesis exists because of his courage to pursue risky projects with zeal and resourcefulness. His trust, wisdom, creativity, and leadership have meant an enormous amount to me, and I am deeply thankful. It has been an absolute pleasure to work for such a first-rate individual. I hope he is proud of this, our work, and that one day I can do what he does and do it even a tenth as well.

I am also grateful to Mel Shochet for his consistent wisdom and down-to-earth sensibility. Such a clear-thinking and calming influence made

this difficult task much easier. His advice on the process and the future has been invaluable.

Special thanks go to the workhorses of the UC group: Peter Wilson, Ray Culbertson, Carla Grosso-Pilcher, Milciades Contreras and Alexis Amadon. I hope one day to be able to help graduate students the way you have been there for me. A big thanks to Marty Dipple for the brilliance and benign neglect which keep the computers running so well that people forget just how hard he works and how important he really is to everything that goes on at HEP. To my fellow graduate students: I am proud to be associated with you and grateful for your help, your encouragement, your time and your friendship. Thanks to David Saltzberg, Sacha Kopp and Jim Romano for introducing me to the wonderful world of CDF and all its idiosyncrasies. I am especially grateful to Jeff Berryhill, Marcus Hohlmann, and John Wahl, who spent the better part of four years in the trenches with me. Thanks for late nights at Jimmy's and the Weinkeller, softball games, the endless hours debugging code, stripping hundreds of data tapes, validating data sets, philosophizing about life, the future, analysis, basketball and football. If it hadn't been for you guys, I don't know if I ever would have made it. I could not have asked for a better set of friends to have as colleagues.

I would also like to thank the other physicists who have found their way into my life. I am indebted to them and their creativity and support. Thanks to Jon Rosner and Don York for getting me here and keeping me here. Thanks to David Stuart, Bob Blair, Fan Qun, Avi Yagil, Marjorie Shapiro, Steve Kuhlmann and Rob Harris, all of whom were an important part of this analysis. I would also like to thank Steve Mrenna, Chris Kolda and Gordy Kane for their immense assistance with many of the theoretical issues.

Thanks to the rest of my friends who made the few hours out of the

lab a life that was full and worth living. The Softball crew made each summer a pleasure. Thanks to Jordan Koss, Rob Wickham, Marcus Hohlmann, Justin Brooke, John Wahl, Mike Thayer, Jim Knight, Colin Bown, Breese Quinn and Joan Wolf for one championship and a couple of near misses. I would also like to thank Jenn Mason, Greg and Jenn Graham, Ted Quinn and Lucia Muñoz-Franco, Colin and Jen Bown, Breese and Suzanne Quinn, Jim and Judy Knight, Rob and Marianne Fleischman, Doug and Liz Walker, Mark Smith and Kristin Hammerbach, and Roberto and Heather Estrada for being there through the good times and the bad.

Finally, I would like to thank my family, Phyllis, Gary, Alison and Jonathan Toback, and Joan Wolf. They have always been there for me and words cannot begin to express my thanks to them. To Alison and Jonathan, thanks for being the best siblings a brother could ask for. To my parents, it has been, and continues to be, my great fortune to have such a special set of people whom I can call friends, mentors and cheerleaders. I don't know anyone who has parents like mine. I love you and thank you for helping me get to where I am today; it is very much your doing. And last, but certainly not least, to Joan, who makes my life complete and fills every day with love, joy, happiness and adventure: Bless you for coming into my life.

CONTENTS

ACKNOWLEDGMENTS iii

LIST OF ILLUSTRATIONS x

LIST OF TABLES xv

ABSTRACT xix

1 INTRODUCTION 1
- 1.1 Introduction 1
- 1.2 Overview 6
- 1.3 The CDF detector 6

2 Datasets and Photon Identification 11
- 2.1 Global Event Selection Variables 12
  - 2.1.1 Fiducial Volume For Photons 12
  - 2.1.2 Event Vertex Measurement 13
  - 2.1.3 Energy-Out-of-Time 13
- 2.2 Photon Identification 14
  - 2.2.1 Strip Chamber Shower Measurement 14
  - 2.2.2 Leakage into the Hadronic Calorimeters 15
  - 2.2.3 Electron Rejection 15
- 2.3 Photon Isolation 16
  - 2.3.1 Trigger Tower Isolation 16
  - 2.3.2 Cluster Isolation 16
  - 2.3.3 Track Isolation 17
  - 2.3.4 Extra Photon Removal 17
- 2.4 Diphoton Triggers 17
- 2.5 Final Offline Selection 18
- 2.6 Efficiency of the Selection Criteria 19

2.6.1 Vertex Selection Criteria 20
2.6.2 Energy-Out-of-Time Selection Criteria 20
2.6.3 Identification and Isolation Selection Criteria 21
2.7 Efficiencies of the Diphoton Triggers 22
2.7.1 Low-Threshold Diphoton Trigger 28
2.7.2 High-Threshold Trigger 28
2.8 Purity of the Diphoton Sample 29

3 Searches for Anomalous Events 33
3.1 Missing E_T 34
3.2 Jets 39
3.3 Electrons and Muons 42
3.4 Taus 49
3.5 b-Quarks 50
3.6 Additional Photons 57
3.7 Summary of the Searches 59

4 The $ee\gamma\gamma\not{E}_T$ Candidate event 61
4.1 The $Z^0 \to e^+e^-$ Control Sample 63
4.2 The Interaction Vertex 65
4.3 Timing Information 65
4.4 The Central Electron 68
4.5 The Central Photons 68
4.6 The Missing Transverse Energy 71
4.7 The Electron Candidate in the Plug Calorimeter 72
4.8 A Problem with the Electron Interpretation 72
4.8.1 VTX Tracking 74
4.8.2 SVX Tracking 76
4.9 Interpreting the Electromagnetic Cluster 83
4.9.1 Two Interactions 86
4.9.2 Anomalous Electron Detection 86
4.9.3 Photonic Interpretation 87
4.9.4 Hadronic τ decay 88
4.9.5 Jet Interpretation 92
4.9.6 Conclusion 92
4.10 A Study of the Kinematics of the Event 94
4.11 Conclusions 95

5 Estimating the Number of $ee\gamma\gamma\not{E}_T$ Events from Standard Model Sources **99**
5.1 Introduction 99
5.2 Standard Model $WW\gamma\gamma$ production 101
5.3 Standard Model $t\bar{t}$ Production 102
5.4 Setting up to Estimate the Number of Fake Events 104
5.4.1 The Main Part of the Event 105
5.4.2 Rates for Finding the Additional Objects 105
5.5 Estimating the Number of Expected Fake Events 110
5.5.1 Events with a Fake Object or Objects 110
5.5.2 Overlapping Events, Including Cosmic Rays 112
5.6 Total Standard Model Rates 114
5.6.1 The Total Standard Model Rate Including Processes Where the Plug Cluster is due to an Electron 116
5.6.2 The Total Standard Model Rate Excluding Processes Where the Plug Cluster is due to an Electron 116

6 Setting Limits with the $\gamma\gamma + X$ Analysis **119**
6.1 Anomalous $WW\gamma\gamma$ Production 119
6.2 Supersymmetric Models 121
6.2.1 Light Gravitino Scenarios 121
6.2.2 The $N_2 \to \gamma N_1$ Model 125
6.3 Acceptances and Limits Setting 129
6.4 Results 133
6.5 Conclusions 134

7 Conclusion **145**

A The $\mu^+\mu^-\gamma\gamma jj$ Candidate Event **149**
A.1 Event Kinematics 150
A.2 The Interaction Vertex 152
A.3 The Muon Candidates 155
A.4 The Central Photon Candidate 160
A.5 The Plug Photon Candidate 160
A.6 The Jets 161
A.7 The Missing E_T 162
A.8 Estimating the Number of $\mu^+\mu^-\gamma\gamma jj$ Events from Standard Model Sources 164
A.9 Comparing the Event to the $ee\gamma\gamma\not{E}_T$ Candidate Event 167
A.10 Physics Interpretation 167

A.11 Conclusions 169

B Comments on the Diphoton Purity Estimate 171

C Detailed Event Displays 173

D Comments on the Calculation of the Jet Fake Rates 182
D.1 The $\Delta\phi$ Distribution for Fake Electrons 183

E Comments on the Plug Electromagnetic Shower 190

F Comments on the Calculation of the χ^2 variables in the Plug Strip Chambers 199

G Comments on the SVX Stub Finding Algorithms 207
G.1 SVX Only Information for the $ee\gamma\gamma\not{E}_{\mathrm{T}}$ Candidate Event . . . 208

H Comments on the Electron Interpretation of the Cluster 217

I The Datasets Used in Chapter 5 220
I.1 Z^0/γ^* and W-Type Processes 220
I.2 Plug Electron Dataset 221
I.3 Diphoton Dataset 222
I.4 Photon + $\not{E}_{\mathrm{T}}$ Dataset 222

J Theory Results of the Minimal Gauge-Mediated Model 223

K Optimization of the Selection Thresholds for $\mathrm{E}_{\mathrm{T}}^{\gamma}$ and $\not{E}_{\mathrm{T}}$ 228

L A Check on the Limits Using Different E_{T} Thresholds 233

M Comments on Other Models and Limits from Other Experiments 241
M.1 Other Models 241
M.2 DØ and LEP Results 242

REFERENCES 244

LIST OF ILLUSTRATIONS

1.1 The Feynman diagram for $\tilde{e}$ pair production and decay in the $N_2 \to \gamma N_1$ scenario of Kane *et al.* 4
1.2 The Feynman diagram for $\tilde{e}$ pair production and decay in the light gravitino scenario 5
1.3 A schematic drawing of the CDF detector 8

2.1 The efficiency of the photon identification and isolation selection criteria as measured from the data 24
2.2 The efficiency of the photon identification and isolation selection criteria as predicted by the detector simulation 25
2.3 The ratio of efficiencies of the photon identification and isolation selection criteria as measured from the data and the detector simulation 26
2.4 The distribution of the variable σ_{CES} in the data and in the detector simulation 27
2.5 The low-threshold diphoton trigger efficiencies 30
2.6 The high-threshold diphoton trigger efficiencies 31

3.1 The resolution on one component of the $\not{E}_{\mathrm{T}}$ ($\not{E}_{\mathrm{T}}^{x}$) as determined from a sample of $Z^0 \to e^+e^-$ events 36
3.2 The $\Sigma \mathrm{E}_{\mathrm{T}}$ distribution for diphoton and $Z^0 \to e^+e^-$ events . . 37
3.3 A comparison of the $\not{E}_{\mathrm{T}}$ resolution for $Z^0 \to e^+e^-$ and diphoton events. 38
3.4 The $\not{E}_{\mathrm{T}}$ spectrum for diphoton events with $\mathrm{E}_{\mathrm{T}}^{\gamma} > 12$ GeV . . . 40
3.5 The $\not{E}_{\mathrm{T}}$ spectrum for diphoton events with $\mathrm{E}_{\mathrm{T}}^{\gamma} > 25$ GeV . . . 41
3.6 The number of jets, $\mathrm{N}_{\mathrm{Jet}}$, produced in association with dijets and $Z^0 \to e^+e^-$ decays 43
3.7 The number of jets, $\mathrm{N}_{\mathrm{Jet}}$, produced in association with diphoton pairs with $\mathrm{E}_{\mathrm{T}}^{\gamma} > 12$ GeV 44

3.8 The number of jets, N_{Jet}, produced in association with diphoton pairs with $E_T^\gamma > 25$ GeV 45
3.9 The E_T spectrum of τ candidates produced in association with diphoton pairs 52
3.10 The E_T spectrum for jets produced in association with diphoton pairs with $E_T^\gamma > 12$ GeV. 53
3.11 The E_T spectrum for jets produced in association with diphoton pairs with $E_T^\gamma > 25$ GeV 54
3.12 The E_T spectrum of b-tags produced in association with diphoton pairs 56
3.13 The E_T spectrum of additional photons produced in association with diphoton pairs 58

4.1 An event display for the $ee\gamma\gamma\not\!\!E_T$ candidate event 62
4.2 The transverse energy of electrons in the central and plug calorimeters in $Z^0 \to e^+e^-$ events. 64
4.3 The instantaneous luminosity and the number of primary vertices, as measured in $Z^0 \to e^+e^-$ events, during the course of the run. 66
4.4 The arrival times of electrons and photons at the face of the central hadronic calorimeter from $Z^0 \to e^+e^-$ events and from a sample of photons from cosmic rays 69
4.5 The values of the identification variables for electrons in the plug calorimeter from a sample of $Z^0 \to e^+e^-$ events 73
4.6 The expected trajectory for the cluster in the plug calorimeter as it passes through the SVX, VTX and CTC tracking chambers in the $ee\gamma\gamma\not\!\!E_T$ candidate event 75
4.7 The VTX occupancy as measured in the $ee\gamma\gamma\not\!\!E_T$ candidate event 77
4.8 The $\Delta\phi$ between the measured electron position from the strip chambers and the ϕ from the SVX tracker 79
4.9 The positions of the SVX clusters with 0.23 rad $< \phi <$ 0.33 rad 82
4.10 The measured impact parameter from the SVX tracker for electrons from $Z^0 \to e^+e^-$ events 84
4.11 The $\Delta\phi$ between the measured photon position and the stub found by the SVX tracker for a sample of central photons . . . 89
4.12 The VTX occupancy of photons with $E_T > 20$ GeV in the diphoton sample 90
4.13 A Monte Carlo simulation of one-prong hadronic decays of a τ interacting with the plug calorimeter 93

4.14 The invariant mass of the cluster in the plug calorimeter and the electron in the central calorimeter plotted vs. the $\not\!\!E_T$ as the energy of the cluster in the plug is varied 96

5.1 The invariant mass of the e^+e^- pair in Standard Model $WW\gamma\gamma \to ee\gamma\gamma\not\!\!E_T$ events 103

6.1 Masses of the gauginos vs. M_2 in the Minimal Gauge-Mediated Model 126
6.2 The dominant sparticle production cross sections vs. M_2 in the Minimal Gauge-Mediated Model 127
6.3 The distributions in E_T of the photons and $\not\!\!E_T$ in the Minimal Gauge-Mediated Model with $M_2 = 150$ GeV, $\tan\beta = 10$ and Sgn(μ)= 1 128
6.4 The distributions in E_T of the photons and $\not\!\!E_T$ for N_2N_2 production in the $N_2 \to \gamma N_1$ model 130
6.5 The acceptances for various points in the $\tan\beta$ vs. M2 plane in the Minimal Gauge-Mediated Model 137
6.6 The number of expected events for various points in the $\tan\beta$ vs. M_2 plane in the Minimal Gauge-Mediated Model 138
6.7 The acceptances and number of expected events for various points plotted vs. the N_1 mass in the Minimal Gauge-Mediated Model 139
6.8 The contour plot of the excluded region of the Minimal Gauge-Mediated Model in the $\tan\beta$ vs. M_2 plane 140
6.9 The contour plot of the excluded region of the Minimal Gauge-Mediated Model in the $\tan\beta$ vs. C_1 mass plane 141
6.10 The 95% C.L. cross section upper limit from the data vs. the N_1 mass in the Minimal Gauge-Mediated Model 142
6.11 The 95% C.L. cross section upper limit from the data vs. the C_1 mass in the Minimal Gauge-Mediated Model 143

A.1 The event display for the $\mu^+\mu^-\gamma\gamma jj$ candidate event 151
A.2 The invariant mass of pairs of muons passing the tight identification and isolation selection criteria, each with $P_T^\mu > 30$ GeV. 153
A.3 The number of tracks in the central tracking chamber as a function of track z position in the $\mu^+\mu^-\gamma\gamma jj$ candidate event . . . 156
A.4 The P_T weighted ϕ distribution of tracks associated with the two vertices in the $\mu^+\mu^-\gamma\gamma jj$ candidate event 157
A.5 The Sum P_T of tracks associated with other vertices in $\mu^+\mu^-$ events 158

A.6 The dijet invariant mass for jets produced in association with $\mu^+\mu^-$ pairs 163

C.1 The event display for the $ee\gamma\gamma\not{E}_T$ candidate event 174
C.2 The LEGO plot for the $ee\gamma\gamma\not{E}_T$ candidate event with the vertical scale in energy 175
C.3 The event display for the $\gamma\gamma + \not{E}_T$ candidate event 176
C.4 The event display for the $\gamma\gamma + e^{\text{central}}$ candidate event 177
C.5 The event display for the $\gamma\gamma + \mu\mu$ candidate event 178
C.6 The event display for the $\gamma\gamma + \tau$ candidate event 179
C.7 The event display for the first $\gamma\gamma + b$-jet candidate event . . . 180
C.8 The event display for the second $\gamma\gamma + b$-jet candidate event . . 181

D.1 The central photon fake rate as a function of E_T 185
D.2 The central electron fake rates as a function of E_T 186
D.3 The plug electron candidate fake rates as a function of E_T . . 187
D.4 The plug photon fake rates as a function of E_T 188
D.5 The $\Delta\phi$ distribution between the cluster centroid and an associated SVX stub for fake plug electron candidates 189

E.1 The event display for the cluster in the PEM in the $ee\gamma\gamma\not{E}_T$ candidate event 191
E.2 The energy deposited in each layer of the calorimeter for the electromagnetic cluster in the plug in the $ee\gamma\gamma\not{E}_T$ candidate event 193
E.3 The distribution of a χ^2 test between measured and expected pulse heights in the strip chambers in the plug calorimeter for electrons in the $Z^0 \to e^+e^-$ control sample 195
E.4 The energies, as measured by individual strips in the strip chambers, in the ϕ direction for the cluster in the plug calorimeter in the $ee\gamma\gamma\not{E}_T$ candidate event 196
E.5 The energies, as measured by individual strips in the strip chambers, in the η direction for the cluster in the plug calorimeter in the $ee\gamma\gamma\not{E}_T$ candidate event 197
E.6 A comparison of the energy deposition of the cluster in the plug using all 34 layers in the calorimeter and using just the strip chambers 198

F.1 Electron shower widths as measured in the plug strip chamber from the $Z^0 \to e^+e^-$ sample. 202

F.2 The width of electron showers, as measured in the strip chambers, as a function of energy of the electron 203
F.3 The width of electron showers, as measured in the strip chambers, as a function of η of the electron 204
F.4 The residual width of electron showers after energy and η dependences have been subtracted off 205
F.5 The normalized electron shower shape in the ϕ and η directions as measured in the plug strip chambers 206

G.1 The $\Delta\phi$ between the measured electron position from the strip chambers (CES and PES respectively) and the ϕ from the SVX tracker 209
G.2 The $\Delta\phi$ between the measured electron position and the ϕ from the SVX tracker after the fiducial requirement 210
G.3 The χ^2 distribution of SVX stubs found by the SVX tracker for electrons 211
G.4 The minimum charge deposited in any of the four SVX silicon layers corrected for path length for electrons 212
G.5 The $\Delta\phi$ between the measured electron position and the ϕ from the SVX tracker after all requirements 213
G.6 The resolution of the SVX track parameters for the $ee\gamma\gamma\not{E}_{\mathrm{T}}$ candidate event when no calorimeter information is used . . . 215
G.7 The correlation between SVX track parameters in the $ee\gamma\gamma\not{E}_{\mathrm{T}}$ candidate event when no calorimeter information is used . . . 216

K.1 The expected $\not{E}_{\mathrm{T}}$ distribution for Standard Model diphoton events with different photon E_{T} thresholds 230

L.1 The acceptances for various points in the $\tan\beta$ vs. M_2 plane using the $\mathrm{E}_{\mathrm{T}}^{\gamma} > 25$ GeV and $\not{E}_{\mathrm{T}} > 25$ GeV thresholds for the Minimal Gauge-Mediated Model 236
L.2 The number of expected events for various points in the $\tan\beta$ vs. M_2 plane using the $\mathrm{E}_{\mathrm{T}}^{\gamma} > 25$ GeV and $\not{E}_{\mathrm{T}} > 25$ GeV thresholds for the Minimal Gauge-Mediated Model 237
L.3 The number of expected events and acceptances for various points plotted vs. the N_1 mass using the $\mathrm{E}_{\mathrm{T}}^{\gamma} > 25$ GeV and $\not{E}_{\mathrm{T}} > 25$ GeV thresholds in the Minimal Gauge-Mediated Model 238
L.4 A contour plot of the excluded region of the Minimal Gauge-Mediated Model in the $\tan\beta$ vs. M_2 plane using the $\mathrm{E}_{\mathrm{T}}^{\gamma} > 25$ GeV and $\not{E}_{\mathrm{T}} > 25$ GeV thresholds. 239

LIST OF TABLES

2.1 The selection criteria used to identify $\gamma\gamma$ candidate events . . 19
2.2 The selection criteria used to identify isolated electrons in the central calorimeter 20
2.3 The efficiencies of the photon selection criteria 23
2.4 The selection criteria used to select a sample of e^+e^- events for use in evaluating the low-threshold trigger efficiency 28

3.1 The 4-vectors of the $\gamma\gamma + \not{E}_{\mathrm{T}}$ candidate event 39
3.2 The selection criteria used to identify isolated muons 47
3.3 The 4-vectors of the $\gamma\gamma + \mu\mu$ candidate event 48
3.4 The 4-vectors of the $\gamma\gamma + e$ candidate event 48
3.5 The identification and isolation selection criteria used to select hadronic decays of the τ 51
3.6 The 4-vectors of the $\gamma\gamma + \tau$ candidate event 55
3.7 The 4-vectors of the first $\gamma\gamma + b$ candidate event 55
3.8 The 4-vectors of the second $\gamma\gamma + b$ candidate event 57
3.9 The number of observed and expected $\gamma\gamma$ events with additional objects in 85 pb^{-1} 59

4.1 The requirements used to select the $Z^0 \to e^+e^-$ control sample 63
4.2 The vertices in the $ee\gamma\gamma\not{E}_{\mathrm{T}}$ candidate event 67
4.3 The measured values of the variables used to identify the central electron in the $ee\gamma\gamma\not{E}_{\mathrm{T}}$ candidate event 68
4.4 The measured values of the variables used to identify the central photons in the $ee\gamma\gamma\not{E}_{\mathrm{T}}$ candidate event 70
4.5 The measured values of the variables used to compare the cluster in the plug calorimeter in the $ee\gamma\gamma\not{E}_{\mathrm{T}}$ candidate event to electrons 74
4.6 The SVX stub-finding requirements for electrons 78

4.7 A list of all good SVX clusters with 0.23 rad $< \phi <$0.33 rad in the $ee\gamma\gamma\not{E}_{\rm T}$ candidate event 80
4.8 A list of all the bad strips in the SVX in the region 0.23 rad $< \phi <$ 0.33 rad. 81
4.9 The VTX and SVX results assuming the plug cluster came from a different vertex in the event 86
4.10 Other SVX stubs in the $ee\gamma\gamma\not{E}_{\rm T}$ candidate event found using the SVX tracker 91
4.11 The 4-vectors of the electron and photon candidates and the missing transverse energy in the $ee\gamma\gamma\not{E}_{\rm T}$ candidate event . . . 94
4.12 The kinematics of various combinations of the clusters in the $ee\gamma\gamma\not{E}_{\rm T}$ candidate event 97
4.13 The transverse mass for the measured $\not{E}_{\rm T}$ and various combinations of the electron and photon candidates within the $ee\gamma\gamma\not{E}_{\rm T}$ candidate event 98

5.1 The number of observed events for the various parts of the $ee\gamma\gamma\not{E}_{\rm T}$ signature 106
5.2 The estimated rates for finding fake objects (electrons, photons or $\not{E}_{\rm T}$) in an event from various processes 107
5.3 An estimate of the number of events passing the $ee\gamma\gamma\not{E}_{\rm T}$ selection criteria from events with fake electrons, photons or $\not{E}_{\rm T}$ . . 111
5.4 The number of events with the $ee\gamma\gamma\not{E}_{\rm T}$ signature due to two overlapping events 115

6.1 Standard Model $WW\gamma\gamma$ predictions for diphoton events with $E_{\rm T}^{\gamma} > 25$ GeV 121
6.2 The parameters used to simulate the $N_2 \to \gamma N_1$ scenario . . . 131
6.3 The corrections used to take into account differences between the true detector response and the detector simulation 132
6.4 The number of expected events, acceptances and the 95% C.L. cross section upper limits for the Minimal Gauge-Mediated Model with $M_2 < 150$ GeV 135
6.5 The number of expected events, acceptances and the 95% C.L. cross section upper limits for the Minimal Gauge-Mediated Model with $M_2 > 150$ GeV 136
6.6 The number of expected events, acceptances and 95% C.L. cross section upper limits for the $N_2 \to \gamma N_1$ model 144

A.1 The 4-vectors of $\mu^+\mu^-\gamma\gamma jj$ candidate event 150

A.2 The mass and P_T for sub-systems of the $\mu^+\mu^-\gamma\gamma jj$ candidate event 154
A.3 Summary of the muon identification and isolation variables in the $\mu^+\mu^-\gamma\gamma jj$ candidate event 159
A.4 Summary of the central photon variables in the $\mu^+\mu^-\gamma\gamma jj$ candidate event 160
A.5 Summary of the plug photon variables in the $\mu^+\mu^-\gamma\gamma jj$ candidate event 161
A.6 The jets in the $\mu^+\mu^-\gamma\gamma jj$ candidate event 162
A.7 The missing transverse energy in the $\mu^+\mu^-\gamma\gamma jj$ candidate event 164
A.8 The number of fake $\mu^+\mu^-\gamma\gamma jj$ events expected from Standard Model sources 167
A.9 The invariant masses of combinations of the leptons and photons in the $ee\gamma\gamma\not{E}_T$ and $\mu^+\mu^-\gamma\gamma jj$ candidate events 168

D.1 The rates at which jets pass the electron and photon selection criteria 183

I.1 The number of events in the $\gamma + \not{E}_T$ sample as additional selection criteria are added 222

J.1 The gaugino masses for various points in parameter space in the Minimal Gauge-Mediated Model with $M_2 < 150$ GeV 224
J.2 The gaugino masses for various points in parameter space in the Minimal Gauge-Mediated Model for $M_2 > 150$ GeV 225
J.3 The dominant production cross sections for various points in parameter space in the Minimal Gauge-Mediated Model for $M_2 < 150$ GeV 226
J.4 The dominant production cross sections for various points in parameter space in the Minimal Gauge-Mediated Model for $M_2 > 150$ GeV 227

K.1 The number of $\gamma\gamma + \not{E}_T$ candidate events expected from backgrounds for various combinations of the E_T^γ and $\not{E}_T$ thresholds 229
K.2 Results from the procedure used to select the optimal E_T^γ and $\not{E}_T$ selection criteria for the Minimal Gauge-Mediated Model with $M_2 < 150$ GeV 231
K.3 Results from the procedure used to select the optimal E_T^γ and $\not{E}_T$ selection criteria for the Minimal Gauge-Mediated Model with $M_2 > 150$ GeV 232

L.1 The number of expected events, acceptances and the 95% C.L. cross section upper limits from the Minimal Gauge-Mediated Model for $M_2 < 150$ GeV, but using $E_T^\gamma > 25$ GeV and $\not{E}_T > 35$ GeV 234
L.2 The number of expected events, acceptances and the 95% C.L. cross section upper limits from the Minimal Gauge-Mediated Model for $M_2 > 150$ GeV, but using $E_T^\gamma > 25$ GeV and $\not{E}_T > 35$ GeV 235
L.3 A comparison of the results from the $N_2 \to \gamma N_1$ model for the two different $\not{E}_T$ and photon E_T thresholds for all production processes 240
L.4 A comparison of the results from the $N_2 \to \gamma N_1$ model for the two different $\not{E}_T$ and photon E_T thresholds for $N_2 N_2$ production 240

M.1 The magnitude of μ for various points in M_2 vs. $\tan\beta$ parameter space for the Minimal Gauge-Mediated Model 243

ABSTRACT

We have searched for anomalous production of missing E_T ($\not\!\!E_T$), jets, leptons (e, μ, τ), b-quarks, or additional photons in events containing two isolated, central ($|\eta| < 1.0$) photons with $E_T > 12$ GeV. The results are consistent with Standard Model expectations, with the possible exception of one event that has in addition to the two photons a central electron, a high-E_T electromagnetic cluster, and large $\not\!\!E_T$. We set limits using two specific SUSY scenarios for production of diphoton events with $\not\!\!E_T$.

Chapter 1

INTRODUCTION

I think we're on the road to coming up with answers that I don't think any of us in total feel we have answers to.

- Kim Anderson, mayor of Naples, Florida

1.1 Introduction

The current understanding of fundamental particles and their interactions via the strong, electromagnetic and weak forces has come to be known as the Standard Model of particle physics [1]. However, there are many reasons to believe that physics beyond the Standard Model is likely [2, 3]. Since it is not obvious what form this new theory might take, there have been many searches for new particles, with null or inconclusive results [4]. During one such search, the Run 1 data taking period of the Fermilab Tevatron with $p\bar{p}$ collisions at $\sqrt{s} = 1.8$ TeV, an '$ee\gamma\gamma\not{E}_{\mathrm{T}}$' candidate event was recorded by the CDF detector [5, 6, 7]. This event has two high energy photons, a high energy electron, an electromagnetic cluster which passes the standard electron

selection criteria [8] and a large energy imbalance ($\not{E}_{\rm T}$). There is no obvious Standard Model interpretation of this event [9].

While the event was pointed out as being very unusual at an early stage [6, 10], there was no ongoing search for such events [11]. Without a good theoretical hypothesis to guide a search, an attempt to understand the event in terms of known Standard Model particles led to the speculation that the electrons and $\not{E}_{\rm T}$ come from $WW \to e\nu e\nu$ production [12]. Thus, the event would be $WW\gamma\gamma \to ee\gamma\gamma\not{E}_{\rm T}$, either as a rare fluctuation from Standard Model predictions [13] or some anomalous production.

The anomalous $WW\gamma\gamma$ production hypothesis can be tested quantitatively [12]. By assuming that the one event was produced at its mean cross section [14] and using the branching ratios of the W, the mean number of events in the other decay channels, or 'cousins' [15], can be predicted. For example, using the branching ratio of $W \to q_i\bar{q}_j \to jj$ and $W \to e\nu$ the mean number of $WW \to \gamma\gamma jjjj$ events can be predicted using

$$N_{Expected\ \gamma\gamma jjjj} = N_{Observed\ \gamma\gamma ee+\not{E}_{\rm T}}(\frac{Br(W \to jj)}{Br(W \to e\nu)})^2. \tag{1.1}$$

Using these simple arguments, and correcting for detection efficiencies, tens of events with the $\gamma\gamma jjjj$ signature are predicted to exist in the data and could be searched for. However, since it was not obvious that new particles were not involved, the search was generalized (without the same quantitative predictive power) to look for other events *like* the candidate in the $\gamma\gamma + X$ channel [12]. As in the event, each photon was required to have high-$\rm E_T$ ($\rm E_T > 25$ GeV); however instead of $ee\not{E}_{\rm T}$, X was allowed to be a high-$\rm E_T$ lepton (e, μ, τ, ν), quark (light quark jet, b-tagged jet, or $t \to Wb$) or boson (g, W, Z^0 or γ). No $\gamma\gamma jjjj$ events were observed with ≈ 30 expected from $WW\gamma\gamma$. Similarly, no leptonic or semileptonic decays of the WW pair were observed. The event is

thus very unlikely to be from any type of $WW\gamma\gamma$ production and consequently, the $\not{E}_{\rm T}$ was unlikely to be from a Standard Model neutrino from $W \to e\nu$ with the W either on-shell or off-shell [16]. The missing $\rm E_T$ could thus be from some new particle other than the left-handed neutrino. The lightest Supersymmetric particle [17] is a natural candidate [12].

While Supersymmetric models [17] predict new particles which would leave $\not{E}_{\rm T}$ in the detector, at the time there was no active interest in models with photonic final states [18]. After seeing the event and the preliminary results, it was immediately pointed out [19] that in the early 1980's there were predictions of Supersymmetric pair-production and decay of selectrons (see Figure 1.1) with each selectron decaying via $\tilde{e} \to eN_2 \to e\gamma N_1$ [20, 21]. Thus, this event could be an example of Supersymmetric particle production, and confirmation of the accompanying channels (*e.g.* $\tilde{\mu}\tilde{\mu}$, $\tilde{\tau}\tilde{\tau}$ etc.) could be observed in the form of $\mu\mu\gamma\gamma\not{E}_{\rm T}$ and $\tau\tau\gamma\gamma\not{E}_{\rm T}$ events. Again no such events with two central photons were observed [12], however the $\gamma\gamma jjjj$ signal was no longer required and the results were much less restrictive.

Soon after, a large number of theoretical papers discussing the event in the context of Supersymmetric, and other, scenarios appeared [22, 23, 24, 25, 26]. Of particular interest are Supersymmetric theories involving the decay $N_2 \to \gamma N_1$ [20, 23, 27] and theories with light gravitinos [22, 28, 29] which had been postulated in the 1970's [30]. The latter models can explain the event via the pair production and decay of selectrons via $\tilde{e} \to eN_1 \to e\gamma\tilde{G}$, or charginos via $C^{\pm} \to e\nu N_1 \to e\nu\gamma\tilde{G}$ (see Figure 1.2). Photonic final states are now commonly discussed as a standard method of searching for Supersymmetric signals [31].

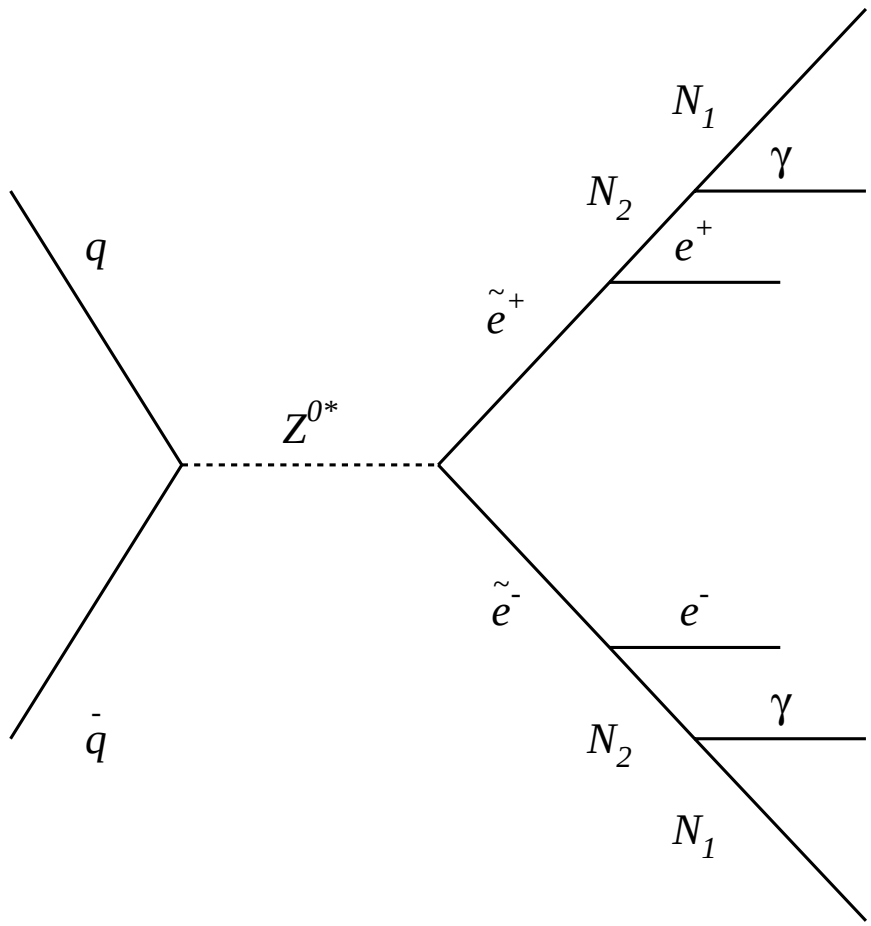

Figure 1.1: The Feynman diagram for $\tilde{e}$ pair production and decay in the $N_2 \rightarrow \gamma N_1$ scenario of Kane *et al.* Both selectrons decay via $\tilde{e} \rightarrow eN_2$ where N_2 is the next-to-lightest neutralino which in turn decays in turn decays via $N_2 \rightarrow \gamma N_1$.

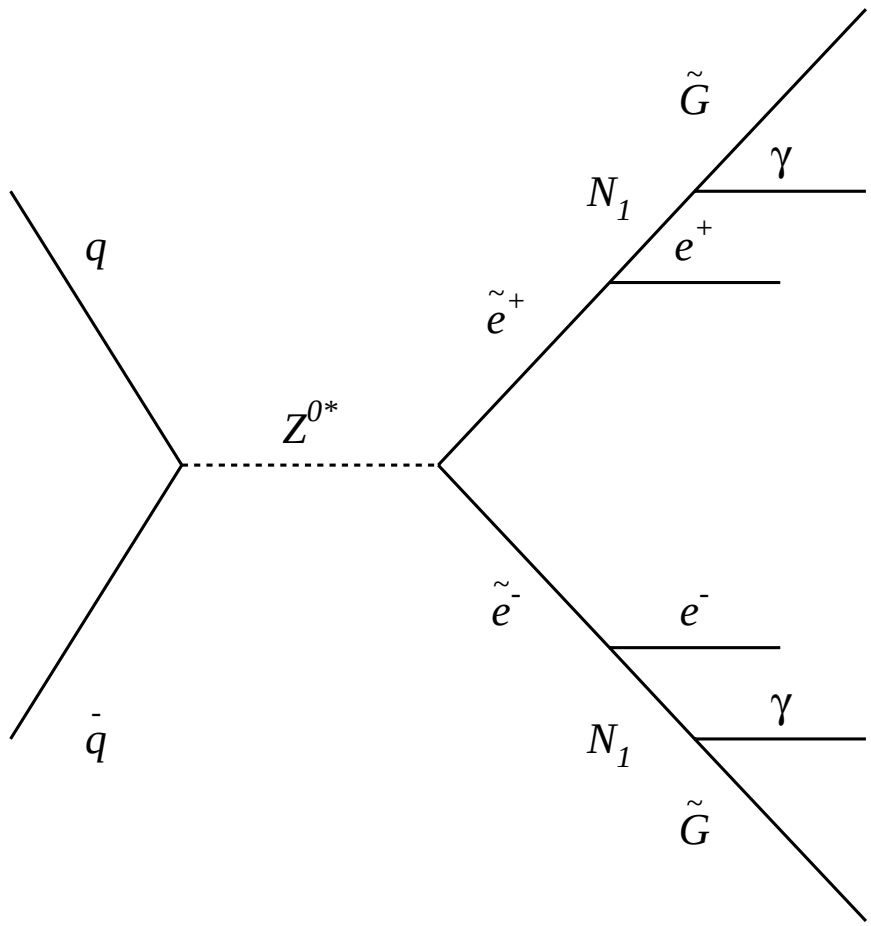

Figure 1.2: The Feynman diagram for $\tilde{e}$ pair production and decay in the light gravitino scenario. Both selectrons decay via $\tilde{e} \rightarrow eN_1$ where N_1 is the lightest neutralino which in turn decays via $N_1 \rightarrow \gamma\tilde{G}$.

1.2 Overview

This paper describes a full systematic search for other anomalous $\gamma\gamma$ events by examining events with two isolated, central ($|\eta| < 1.0$) photons with $E_T > 12$ GeV which contain missing E_T ($\not{E}_T$), jets, leptons (e, μ, τ), b-quarks, or additional photons. The search is based on 85 pb^{-1} of data from $\bar{p}p$ collisions at $\sqrt{s} = 1.8$ TeV collected with the CDF detector [32].

The remainder of this Chapter is devoted to a description of the detector. Chapter 2 discusses the diphoton event selection, the efficiencies of the selection criteria, and the purity of the sample. Chapter 3 discusses a search for anomalous events in the sample. Chapter 4 discusses a study of the $ee\gamma\gamma\not{E}_T$ candidate event, in particular the electron candidate at large η. Chapter 5 discusses the possible Standard Model sources for the $ee\gamma\gamma\not{E}_T$ signature and estimates the number of events expected from each. Chapter 6 discusses in more detail the possible interpretations of this event and places limits on some of the new models which have risen to explain it. Chapter 7 contains the conclusions. The appendices contain much of the technical detail used to derive many of the results, as well as additional information which might be of interest to the reader.

1.3 The CDF detector

The CDF detector is an azimuthally and forward-backward symmetric magnetic detector designed to study $\bar{p}p$ collisions at the Tevatron. A schematic drawing of the major detector components is shown in Figure 1.3. A more detailed description can be found in [32]; recent detector upgrades are described in [33, 34]. The magnetic spectrometer consists of tracking devices

inside a 3-m diameter, 5-m long superconducting solenoidal magnet which operates at 1.4 T. A four-layer silicon microstrip vertex detector (SVX) [33] makes measurements between the radii of 2.8 cm and 7.9 cm [35], and is used to identify b hadron decays. A set of vertex time projection chambers (VTX) surrounding the SVX provides measurements in the r-z plane up to a radius of 22 cm, and is used to find the z position of the $\bar{p}p$ interaction ($z_{\rm vertex}$). The 3.5-m long central tracking chamber (CTC), which provides up to 84 measurements between the radii of 31.0 cm and 132.5 cm, is used to measure the momentum of charged particles with momentum resolution $\sigma_p/p < 0.001p$ (p in GeV/c). The calorimeter, constructed of projective electromagnetic and hadronic towers, is divided into a central barrel which surrounds the solenoid coil ($|\eta| < 1.0$), 'end-plugs' formed of the pole-pieces of the magnet ($1.1 < |\eta| < 2.4$), and forward/backward modules ($2.4 < |\eta| < 4.2$). Wire chambers with cathode strip readout give 2-dimensional profiles of electromagnetic showers in the central and plug regions (CES and PES systems, respectively). A system of drift chambers (CPR) outside the solenoid and in front of the electromagnetic calorimeters uses the 1-radiation-length thick magnet coil as a 'preradiator', allowing photon/π^0 discrimination on a statistical basis by measuring the conversion probability[36]. Muons are identified with the central muon chambers, situated outside the calorimeters in the region $|\eta| < 1.1$.

The CDF detector is (in general) a well understood measuring instrument and there exists standard identification selection criteria for electrons, muons, taus, b-quarks, jets and $\not\!\!E_{\rm T}$ which were developed for, among other things, the top quark discovery and studies of its properties. Descriptions for each can be found in Refs. [37, 38, 39, 40, 41]. The fiducial region of the detector for measuring tracks from electrons and muons with the full power of the

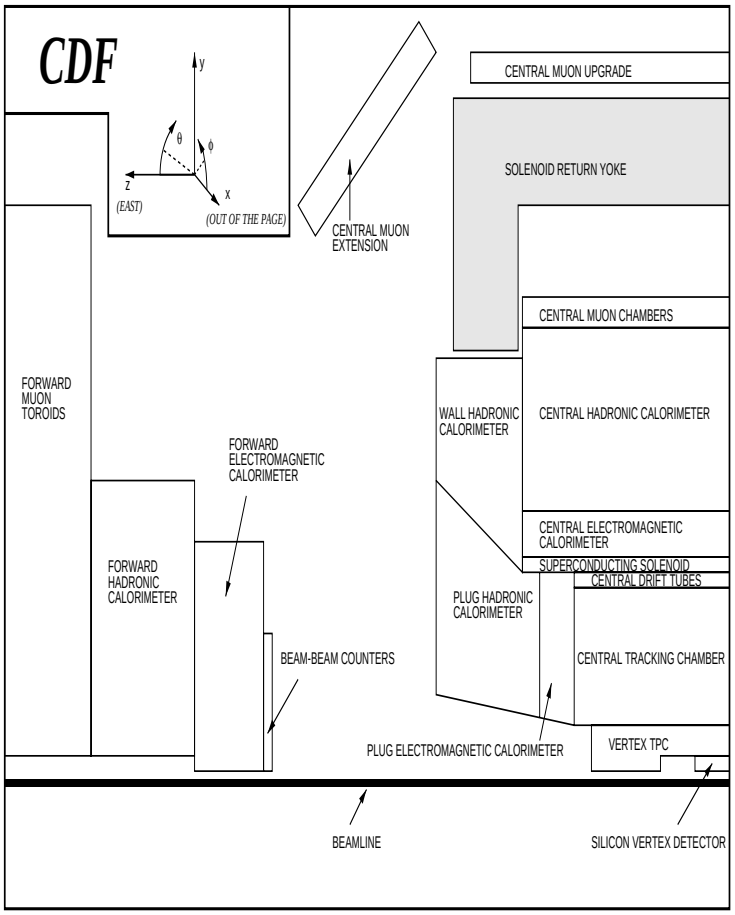

Figure 1.3: A schematic drawing of the CDF detector. One-quarter of the detector is shown.

central tracking chamber is roughly $|\eta| < 1.0$. Within $|\eta| < 1.0$, for electrons, there is a 18.7% geometric loss due to regions which are uninstrumented or do not give a good energy measurement [40]. The energy resolution on the electron is

$$(\frac{\delta E}{E})^2 = (\frac{(13.5 \pm 0.7)\%\ \mathrm{GeV}^{1/2}}{\sqrt{\mathrm{E_T}}})^2 + \kappa^2 \tag{1.2}$$

where κ is measured to be $1.0 \pm 1.0\%$ [37]. For muons, approximately 84% of the solid angle for $|\eta| < 0.6$ is covered. In the region $0.6 < |\eta| < 1.0$ the coverage is about 67%. The momentum resolution for muons is measured [37] to be

$$(\frac{\delta \mathrm{P_T}}{\mathrm{P_T}^2})^2 = 0.000\ 810 \pm 0.000\ 085(\mathrm{stat}) \pm 0.000\ 010(\mathrm{syst})\ (\mathrm{GeV}/c)^{-1}. \tag{1.3}$$

Hadronic decays of the tau lepton are identified in the region $|\eta| < 1.2$ [40]. In this search, jets are accepted in the region $|\eta| < 2.0$. However, jets can be found in the region $|\eta| < 4.2$. A reasonable parameterization for the energy resolution is given by $\Delta \mathrm{E_T^{jet}}/\mathrm{E_T^{jet}} = 80\%/\sqrt{\mathrm{E_T[GeV]}} \oplus 4\%$ for jets with $\mathrm{E_T} < 125$ GeV and $0.2 < |\eta| < 0.8$, and $(15 \pm 2)\%$, independent of $\mathrm{E_T}$ for $0.95 < |\eta| < 1.25$ [40]. For events with an interaction with $|z_{\mathrm{vertex}}| < 30$ cm, b-jets can be identified using displaced vertices in the SVX [41].

Photon identification and efficiency are described in more detail in Chapter 2. The $\not{E}_\mathrm{T}$ calculation used in this search has been customized for this analysis and is described in Chapter 3.

Chapter 2

Datasets and Photon Identification

Before beginning, prepare carefully.

- Cicero

Photons are identified using the central region of the CDF detector, $|\eta| < 1.0$, which contains calorimeters and tracking chambers. Since the interaction of a high energy photon with the detector is similar to that of an electron, many of the same techniques for identifying electrons are used to identify photons [36, 38]. The calorimeters are used to distinguish between photons produced as part of the $\bar{p}p$ collision and those which are produced in the decay of hadrons, such as $\pi^0 \rightarrow \gamma\gamma$. The tracking chambers are used to provide additional rejection against jets of hadrons as well as against electrons which are the other primary background.

Diphoton candidate events are selected using three criteria: global event selection, photon identification and photon isolation. The full set of

selection criteria are listed in Table 2.1. The following sections discuss the variables used to select events as well as the requirements on each.

2.1 Global Event Selection Variables

To insure that events are well measured and help reduce cosmic ray backgrounds, photons are required to be in the fiducial region of the detector, have a well measured primary vertex and have no significant energy measured out-of-time with the collision.

2.1.1 Fiducial Volume For Photons

In the central barrel region of the detector, covering the angular region $-1.1 < \eta < 1.1$, the electromagnetic (CEM) calorimeter is made of shower counters arranged in a projective tower geometry. Each tower is composed of absorber sheets interspersed with scintillator. The towers are constructed in 48 wedges, each consisting of 10 towers in η by one tower in ϕ. Proportional chambers are embedded near shower maximum, 6 radiation lengths within the electromagnetic calorimeters. These chambers, called the central electron strip (CES) chambers have wires in the $r-\phi$ view and cathode strips in the z view. For more details on the CEM see Refs. [32, 38].

Of the central region defined by $|\eta| < 1.1$, approximately 80% in $\eta - \phi$ space is in the fiducial volume for photons. The position of a photon candidate is determined using the CES shower position and is required to lie within 21 cm of the tower center ($|X_{\rm wire}| < 21.0$ cm) in the $r - \phi$ view so that the shower is fully contained in the active region. For low-E_T photons the fiducial region is reduced to $|X_{\rm wire}| < 17.5$ cm for reasons which are explained in

Section 2.4. The region $|\eta| < 0.05$, where the two halves of the detector meet, are excluded. The region $0.77 < \eta < 1.0, 75^\circ < \phi < 90^\circ$ is uninstrumented because it is the penetration for the cryogenic connections to the solenoidal magnet. In addition, the region $1.0 < |\eta| < 1.1$ is excluded because of the smaller depth of the electromagnetic calorimeter in the region. Within the angular region $0.05 < |\eta| < 1.0$ and $0 < \phi < 2\pi$ the fiducial coverage is roughly 87% for high-E_T photons and 73% for low-E_T photons. The energy resolution for this region of the CEM is measured to be [37]

$$(\frac{\delta E}{E})^2 = (\frac{(13.5 \pm 0.7)\%\ \mathrm{GeV}^{1/2}}{\sqrt{\mathrm{E_T}}})^2 + \kappa^2 \tag{2.1}$$

where κ is measured to be $1.0 \pm 1.0\%$.

2.1.2 Event Vertex Measurement

The position in z of the primary event vertex, z_{vertex}, is measured by the vertex tracking chamber (VTX) [42]. The z position of the interactions were distributed around the nominal interaction in an approximately Gaussian distribution with $\sigma \approx 30$ cm. A requirement of $|z_{\mathrm{vertex}}| < 60$ cm is used to maintain the projective geometry of the detector.

2.1.3 Energy-Out-of-Time

Every tower in the central hadronic calorimeter has timing information associated with the energy deposited [32]. To reduce cosmic ray interaction backgrounds which might occur during the event, all energy deposited at time t must occur within a window around the nominal collision time, t_0, to be considered 'in time' with the collision. The window is defined by

$$-20 \text{ nsec} < t - t_0 < 35 \text{ nsec}. \tag{2.2}$$

The event is rejected if any tower has more than 1 GeV deposited outside the timing window.

2.2 Photon Identification

Photon candidates are identified as electromagnetic clusters of energy deposited in the central electromagnetic calorimeter [43]. Each cluster is required to be consistent with being produced from a single prompt photon shower. To reject against backgrounds from electrons and hadronic jets, each candidate is required to pass a series of identification selection criteria. Electrons, which have shower characteristics very similar to those of photons, can be easily removed by identifying the associated track. Hadronic jets, which can contain photons from neutral meson decays, can be removed since they typically contain multiple particles which can be identified by the calorimeter and/or tracking chamber.

2.2.1 Strip Chamber Shower Measurement

To observe the longitudinal development of a shower, strip chambers (CES) are embedded 6 radiation lengths into the central electromagnetic calorimeter. Since a shower from a photon is generally initiated much earlier in the calorimeter than for a hadron, a shower shape measurement is used for photon identification. A χ^2 test separately compares the energy deposited in the z view and in the $r-\phi$ view to that expected from test beam data [38, 44]. The average of the two measurements, χ^2_{CES}, is required to be below 10. In addition, the shower development for each candidate is required to be within 2

standard deviations, $\sigma_{\rm CES}$, with that expected from the measured CEM energy and vertex position [45]. The distribution, in $\sigma_{\rm CES}$, is shown in Figure 2.4.

2.2.2 Leakage into the Hadronic Calorimeters

The ratio Had/EM of the energy in the hadronic towers of the photon cluster (Had) to the energy in the electromagnetic towers in the photon cluster (EM) is used to reject hadronic backgrounds [38]. The electromagnetic calorimeters nearly contain electromagnetic showers, while hadron showers in general deposit energy in both the hadronic and electromagnetic compartments. Each photon, for events with both photons with E_T^γ>22 GeV, is required to have Had/EM $< 0.055 + 0.00045 \times E^\gamma$. This parameterization is derived from test beam data, and is measured to be better than 99% efficient [44].

2.2.3 Electron Rejection

Within the 1.4 T axial magnetic field of the solenoidal magnet is the central tracking chamber (CTC), a large drift chamber with 84 layers of sense wires organized into 9 superlayers. Four of the superlayers are tilted at $\pm 3^\circ$ with respect to the z axis so as to provide stereo position measurement of charged particle tracks. Electrons, which will shower similarly to photons in the calorimeter, can be rejected by the presence of a high momentum track pointing at a photon candidate. Each photon candidate is required to have no charged track pointing at it. However, to reduce the inefficiency due to unrelated particles, a single track is allowed to point at the cluster if the track has a measured $P_T \leq 1$ GeV.

2.3 Photon Isolation

Photons from the radiative decays of heavy new particles are, in general, expected to be "isolated." That is, they are not expected to be produced in association with other nearby particles. A number of different isolation variables are used as a topology requirement and help further reduce hadronic jet backgrounds.

2.3.1 Trigger Tower Isolation

For low energy photons, the energy in a 3x3 trigger tower array [46] around the primary tower (in both Hadronic and Electromagnetic calorimeters, but not including the primary electromagnetic tower) is summed and is referred to as E_{3x3}^{Iso}. A requirement, both at the trigger level (see Section 2.4) and offline, of E_{3x3}^{Iso}<4 GeV is imposed on each photon if either photon candidate has E_T^{γ}<22 GeV. For high energy photons, the leakage of the shower into the hadronic compartments makes this requirement inefficient, and it is removed if both photons have $E_T^{\gamma} > 22$ GeV.

2.3.2 Cluster Isolation

The cluster isolation, Iso^{Cal}, is similar to the trigger tower isolation, but is more efficient for higher energy photons since it scales with the photon energy. The Iso^{Cal} variable is defined as

$$Iso^{Cal} = \frac{E_T^{cone} - E_T^{cluster}}{E_T^{cluster}},$$

where E_T^{cone} is the sum of the electromagnetic and hadronic transverse energies in all of the towers (including the photon cluster) in a cone of

$R = \sqrt{(\Delta\eta)^2 + (\Delta\phi)^2} = 0.4$ centered around the photon cluster, and $E_T^{cluster}$ is the electromagnetic transverse energy in the photon cluster [38]. Each photon, for events with both photons with E_T^{γ}>22 GeV, is required to have Iso^{Cal} <0.1.

2.3.3 Track Isolation

While there may be no track pointing directly at the cluster, tracks near the cluster may indicate that the cluster is due to a jet. The track isolation is defined as the scalar sum of the transverse momenta of all tracks in a cone of radius R=0.4 in $\eta - \phi$ space centered on the photon. Each photon, for events with both photons with E_T^{γ}>22 GeV, is required to have the sum be less than 5.0 GeV.

2.3.4 Extra Photon Removal

To remove photons from $\pi^0 \rightarrow \gamma\gamma$ production, photon candidates which have a second electromagnetic cluster, as measured by either the strip or wire chambers, are rejected. To maintain a constant efficiency for all photon energies [47] separate requirements for low energy and high energy photon candidates are made:

$$E^{cluster}_{2nd\ strip\ or\ wire} \leq -0.00945 + 0.144 \times E_T^{\gamma} \quad (E_T^{\gamma} < 17.88\ \text{GeV})$$
$$E^{cluster}_{2nd\ strip\ or\ wire} \leq 2.39 + 0.01 \times E_T^{\gamma} \quad (E_T^{\gamma} > 17.88\ \text{GeV}).$$

2.4 Diphoton Triggers

The initial data sample for the search consists of events with two photon candidates selected by the three-level trigger [48]. At Level 1, (L1), events are required to have two electromagnetic calorimeter trigger towers [46] which measure more than 4 GeV. At Level 2 (L2), two triggers, one optimized

for good background rejection at low E_T and the other for high efficiency at high E_T, are 'OR'd [49]. The low-threshold diphoton trigger requires two electromagnetic clusters with $E_T > 10$ GeV and less than 4 GeV in a 3-by-3 array of trigger towers around the cluster (E_{3x3}^{Iso}); the high-threshold (16 GeV) trigger has no isolation requirement. Corresponding Level 3 (L3) triggers require cluster energies calculated with the offline photon algorithm [36] to be above the 10 and 16 GeV thresholds respectively. The low-threshold trigger also requires the clusters be in the restricted fiducial region of the calorimeter ($|X_{\rm wire}| < 17.5$) to ensure a good cluster measurement in the strip chambers.

Each L3 trigger requires one of a set of L2 triggers to have passed. The low-threshold trigger ($E_T > 10$ GeV) requires either the L2 low-threshold trigger or a dielectron trigger [50] which requires two electromagnetic clusters with $E_T > 6$ GeV, and corresponding tracks with $P_T > 4.7$ GeV. The high-threshold trigger requires either the L2 high-threshold trigger (16 GeV), a single electromagnetic cluster trigger which requires 50 GeV of energy [51], or a single jet trigger which requires a cluster above 100 GeV [51].

2.5 Final Offline Selection

The final set of offline selection criteria are listed in Table 2.1. The two different sets of selection criteria correspond to the two trigger paths and allow the efficiencies to be well measured. The low-threshold criteria require both photons to have $E_T^\gamma > 12$ GeV (where the 10 GeV trigger becomes $> 98\%$ efficient) while the high-threshold criteria are used if both photons have $E_T^\gamma > 22$ GeV (where the 16 GeV trigger becomes $> 98\%$ efficient). The final data set consists of 2239 events.

Global Event Cuts	
$\lvert z_{\rm Vertex}\rvert < 60.0$ cm E_T out-of-time = 0 GeV	
Photon Identification and Isolation Cuts	
Central ($\lvert\eta\rvert < 1.0$) $\leq$1 3D tracks pointing at the cluster, $P_T < 1$ GeV $\chi^2_{\rm CES} < 10.0$ $\lvert\sigma_{\rm CES}\rvert < 2.0$ $E^{\rm cluster}_{\rm 2nd\ strip\ or\ wire} \leq -0.00945 + 0.144 \times E^{\gamma}_T$ ($E^{\gamma}_T < 17.88$ GeV) $E^{\rm cluster}_{\rm 2nd\ strip\ or\ wire} \leq 2.39 + 0.01 \times E^{\gamma}_T$ ($E^{\gamma}_T > 17.88$ GeV)	
12 GeV $< E^{\gamma 2}_T <$ 22 GeV	$E^{\gamma 2}_T \geq$ 22 GeV
Tight Fiducial $E^{\rm Iso}_{3x3} \leq$ 4 GeV	Loose Fiducial Had/EM $< 0.055 + 0.00045$E. $\rm Iso^{Cal} < 0.10$ P_T of tracks in a cone of $0.4 < 5.0$ GeV

Table 2.1: The selection criteria used to identify diphoton candidate events.

2.6 Efficiency of the Selection Criteria

Since electron and photon showers are nearly identical, the efficiencies of the selection criteria listed in Table 2.1 are measured using electrons. Two samples of electrons from $Z^0 \rightarrow e^+e^-$ events are used: one from the data [52] and one generated using the PYTHIA Monte Carlo generator [53] and a detector simulation [54]. Each sample is composed of events with one electron candidate in the fiducial region which passes tight identification and isolation criteria (see Table 2.2), a second candidate in the fiducial region with $E_T > 20$ GeV, a matching track with $P_T > 13$ GeV and an invariant pair mass, $M_{e^+e^-}$, within 10 GeV of the Z^0 mass. These requirements, as shown in Ref. [38], produce a fairly pure and unbiased sample of electrons. The efficiency for each requirement is calculated in the following sections; differences between data and Monte Carlo are quantified as corrections, C, to the data.

Requirement
$E_T > 20$ GeV
$E/p < 1.8$
Had/EM < 0.05
Lshr < 0.2
$\chi^2_{\rm strip} < 10$
$\lvert\Delta x\rvert$(track-shower) < 1.5 cm
$\lvert\Delta z\rvert$(track-shower) < 3.0 cm
$\lvert\Delta z\rvert$(vertex-track) < 5.0 cm
$E_T^{\rm Iso}/\ E_T < 0.10$

Table 2.2: The selection criteria used to identify isolated electrons in the central calorimeter. These are the same requirements as used in the top-quark discovery and are described in Ref. [39].

2.6.1 Vertex Selection Criteria

The efficiency of the vertex selection criterion is measured using a subset of the $Z^0 \to e^+e^-$ sample selected by requiring both electron candidates to pass the selection criteria in Table 2.2, but without the $|z_{\rm vertex}| < 60$ cm requirement [39]. There are 1557 events in the sample, 1448 of which have a vertex with $|z_{\rm vertex}| < 60$ cm for an efficiency of $\epsilon^{\rm Data}_{\rm z\ vertex} = (93.0 \pm 0.6_{stat})\%$. Similarly, in the Monte Carlo there are 1303 events in the sample, 1256 of which have a vertex with $|z_{\rm vertex}| < 60$ cm for an efficiency of $\epsilon^{\rm MC}_{\rm z\ vertex} = (96.4 \pm 0.5_{stat})\%$ and $C_{\rm z\ vertex} = \frac{\epsilon_{\rm Data}}{\epsilon_{\rm MC}} = 0.965 \pm 0.008_{stat}$.

2.6.2 Energy-Out-of-Time Selection Criteria

The efficiency of the Energy-Out-of-Time (ETOUT) selection criteria is measured using the same $Z^0 \to e^+e^-$ sample as above but with the additional vertex requirement of $|z_{\rm vertex}| < 60$ cm. There are 1448 events in this sample, 1412 of which have ETOUT=0. Since this value is not simulated in the Monte

Carlo detector simulations the efficiency and correction are taken to be

$$C_{\mathrm{ETOUT}} = \epsilon_{\mathrm{ETOUT}} = (97.5 \pm 0.4_{stat})\%. \tag{2.3}$$

2.6.3 Identification and Isolation Selection Criteria

The efficiency of the identification and isolation selection criteria are estimated to be equal to the fraction of the Z^0 'second' electrons which pass the identification and isolation selection criteria. For every event in the $Z^0 \rightarrow e^+e^-$ sample one of the electrons is randomly selected and compared to the selection requirements. From the sample of events which pass, the number of *other* (second) electrons passing the requirements is used to calculate the efficiency, ϵ_{raw}.

The results are shown in Table 2.3 and Figures 2.1, 2.2 and 2.3 which give the efficiencies and ratio of efficiencies as selection criteria are added and as a function of $\mathrm{E}_{\mathrm{T}}^{\gamma}$. Figure 2.3 shows that while the detector simulation is optimistic, the ratio of efficiencies is fairly flat as a function of E_{T}.

The σ_{CES} distribution is different for electrons and photons and is not well modeled in the detector simulation. The efficiency is estimated using a sample of central electromagnetic clusters with Had/Em < 0.05, $\mathrm{E}_{\mathrm{T}}^{\gamma} > 12$ GeV, no associated track and $\chi^2_{\mathrm{CES}} < 4$. The distribution for data and Monte Carlo is shown in Figure 2.4. While the mean is offset by $\sim$0.6 in the Monte Carlo, the width is the same as in the data. In the data there are 4369 events, 4349 of which have $|\sigma_{\mathrm{CES}}| < 2$; the efficiency is taken to be $\epsilon_{\sigma_{\mathrm{CES}}} = (99.5 \pm 0.1_{\mathrm{stat}})\%$. The σ_{CES} is requirement is not used in Monte Carlo simulations, so no correction is made.

A second sample of events with $\mathrm{M}_{\mathrm{e^+e^-}} > 30$ GeV allows the study of lower $\mathrm{E}_{\mathrm{T}}^{\gamma}$ photons. Unfortunately, while this sample accepts lower E_{T} electrons,

it has a higher background fraction. Since the efficiencies for backgrounds are different from those for real electrons, a slightly biassed efficiency measurement occurs. This difference is included as part of the systematic error. The results are shown in Figures 2.1, 2.2 and 2.3.

Since the efficiencies are not flat as a function of E_T^γ, an additional systematic uncertainty is estimated as half the range of efficiencies (5%). This is added in quadrature with the statistical uncertainties. The total photon identification (ID) and isolation (Iso) efficiency is $\epsilon_{(\text{ID and Iso})} = \epsilon_{\text{raw}} \times \epsilon_{\sigma_{\text{CES}}}$ and is measured to be $\epsilon^{\text{Low Threshold}}_{(\text{ID and Iso})} = (68 \pm 3)\%$ and $\epsilon^{\text{High Threshold}}_{(\text{ID and Iso})} = (84 \pm 4)\%$. The correction for the diphoton pair, $C_{(\text{Id and Iso})}$, to be used in Chapter 6, is determined using:

$$C_{(\text{Id and Iso})} = \left(\frac{\epsilon^{\text{Data}}_{(\text{ID and Iso})}}{\epsilon^{\text{MC}}_{(\text{ID and Iso})}}\right)^2. \tag{2.4}$$

The measured values are $C_{(\text{Id and Iso})} = 0.69 \pm 0.07$ and 0.84 ± 0.08 for the low-threshold and high-threshold selection criteria, respectively [55].

2.7 Efficiencies of the Diphoton Triggers

The diphoton triggers are unusual in CDF in that the L2 and L3 $E_T^{\gamma 2}$ thresholds are identical *and* they require the corresponding L2 trigger. Since the L2 clustering algorithm measures energies slightly differently from those in L3 [43], the L2 and L3 triggers become fully efficient at different values of $E_T^{\gamma 2}$. Conveniently, when the L2 trigger is fully efficient, the L3 trigger is already fully efficient.

High E_T^γ threshold requirements					
Requirement	Events (Data)	Eff. (%)	Events (MC)	Eff. (%)	Corr.
Sample	1661	—	1341	—	—
Track requirement	1589	95.7	1333	99.4	0.962
$\chi^2_{\rm CES} < 10$	1463	88.1	1278	95.3	0.924
2nd cluster	1441	86.8	1251	93.3	0.930
Had/Em	1420	85.5	1247	93.0	0.919
$\rm Iso^{Cal}$	1408	84.8	1231	91.8	0.923
Track Iso	1403	84.5	1227	91.5	0.923
Correction (Per Leg) = 0.92 ± 0.01					
Low E_T^γ threshold requirements					
Requirement	Events (Data)	Eff. (%)	Events (MC)	Eff. (%)	Corr.
Sample	1192	—	948	—	—
Track Requirement	1135	95.2	942	99.4	0.958
$\chi^2_{\rm CES} < 10$	1046	87.8	905	95.5	0.919
2nd cluster	1030	86.4	881	92.9	0.930
$E^{\rm Iso}_{3\rm x3}$	819	68.7	780	82.3	0.835
Correction (Per Leg) = 0.84 ± 0.02					

Table 2.3: The efficiencies of the selection criteria as each criterion is added. All uncertainties are statistical only. The final column, Corr., is the ratio of the efficiencies as measured in the data and as measured using the Monte Carlo simulation. These values are used in Chapter 6 as corrections to results from the Monte Carlo simulations.

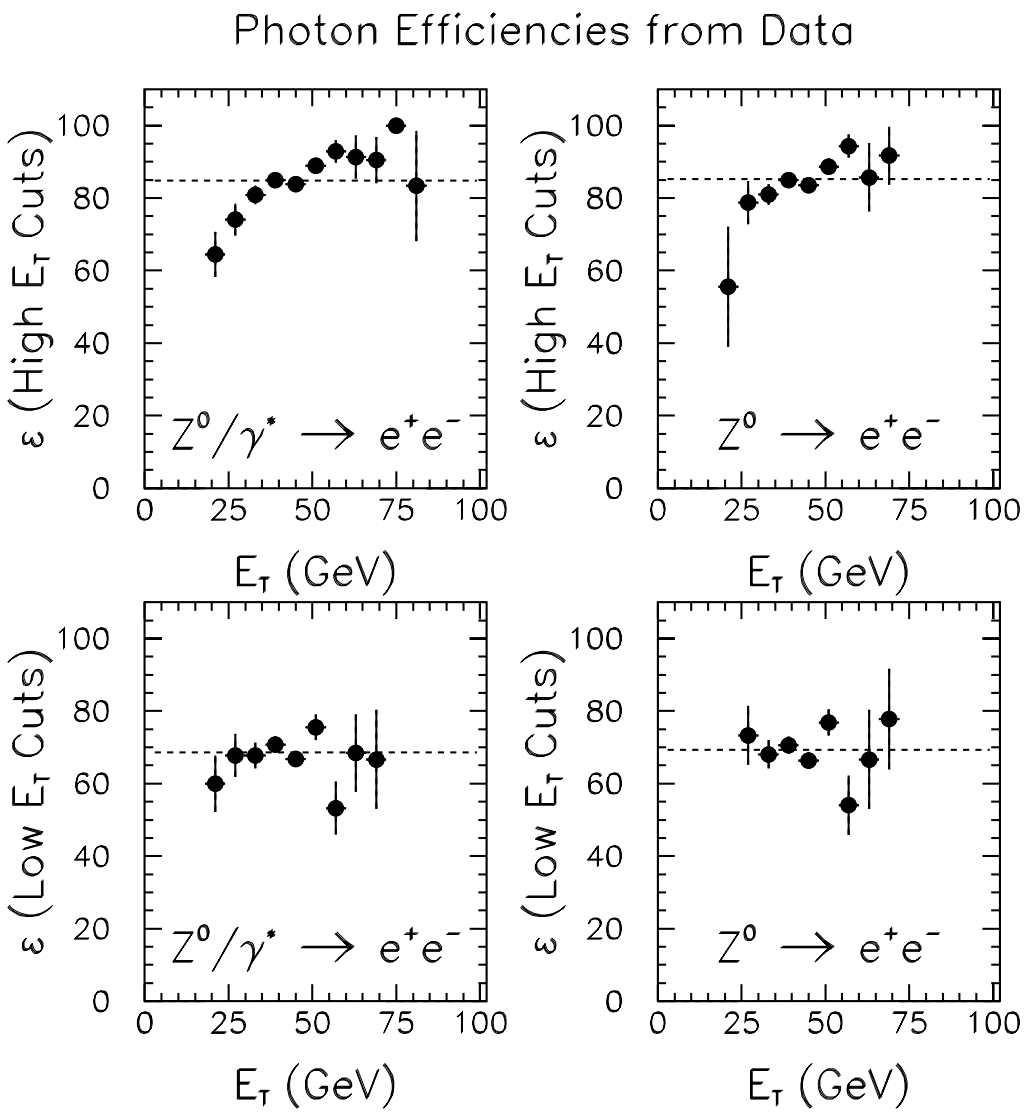

Figure 2.1: The efficiency of the photon identification and isolation selection criteria as a function of E_T as measured from a sample of e^+e^- events in the data. The left hand plots show the results for events with $M_{e^+e^-} > 30$ GeV, the right hand plots for 81 GeV $< M_{e^+e^-} <$ 101 GeV. The upper plots show the results for the high E_T^γ threshold selections, the lower plots for the lower E_T^γ threshold selections. The dashed line is the average efficiency.

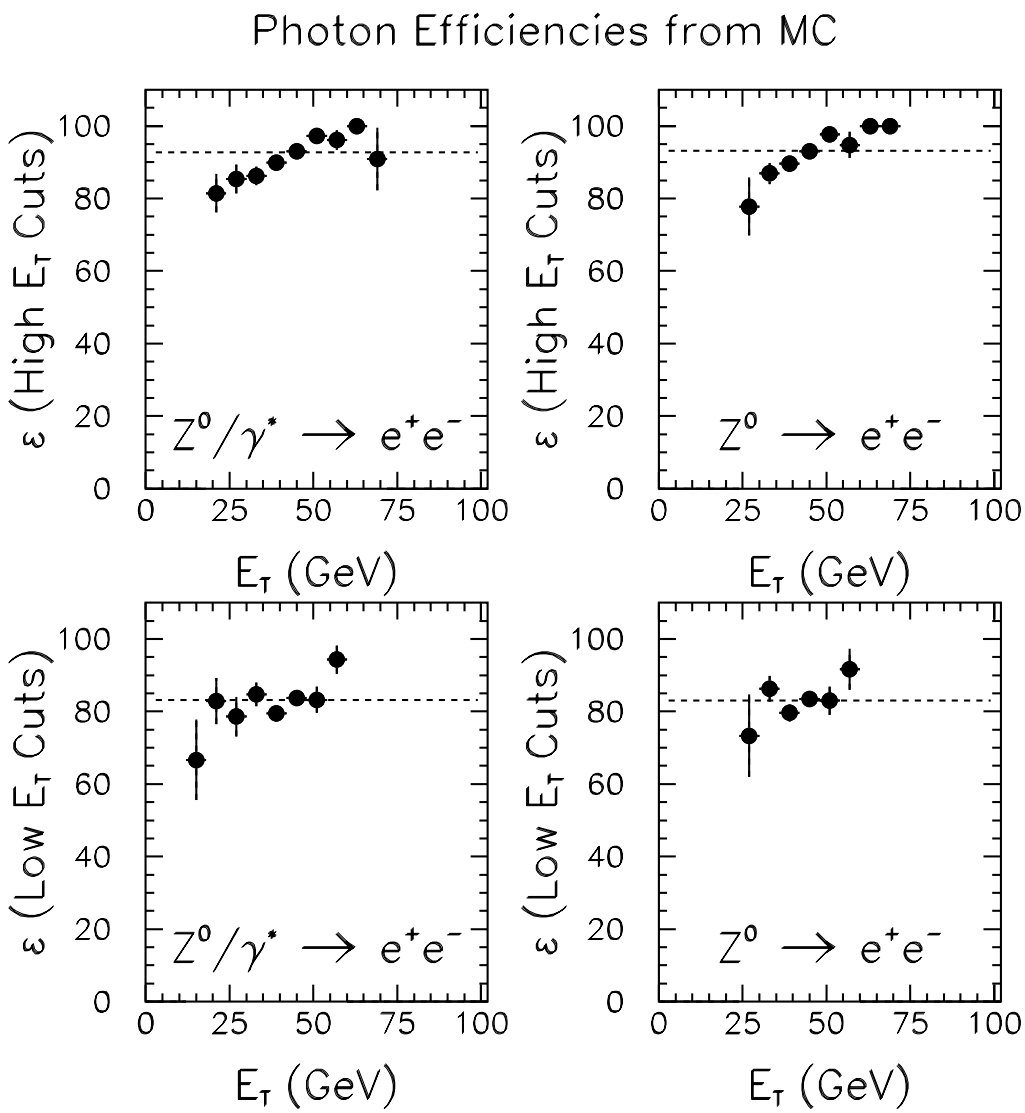

Figure 2.2: The efficiency of the photon identification and isolation selection criteria as a function of E_T as predicted using a sample of e^+e^- events from a detector simulation. The left hand plots show the results for events with $M_{e^+e^-} > 30$ GeV, the right hand plots for 81 GeV $< M_{e^+e^-} <$ 101 GeV. The upper plots show the results for the high E_T^γ threshold selection criteria, the lower plots for the lower E_T^γ threshold selection criteria. The dashed line is the average efficiency.

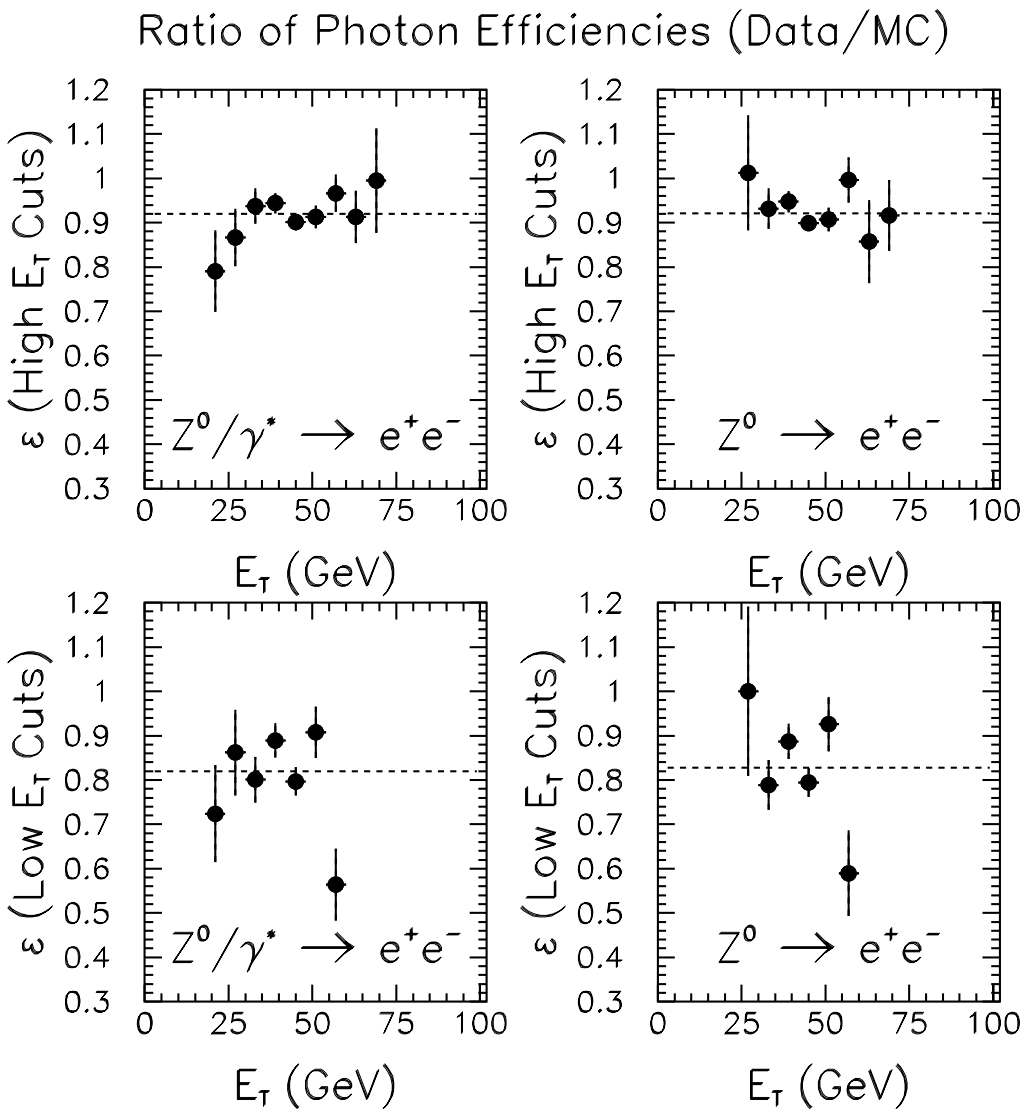

Figure 2.3: The ratio of efficiencies of the photon identification and isolation selection criteria as measured from the data and the detector simulation. The ratio is estimated as a function of E_T. The left hand plots show the results for events with $M_{e^+e^-} > 30$ GeV, the right hand plots for 81 GeV $< M_{e^+e^-} <$ 101 GeV. The upper plots show the results for the high E_T^γ threshold selection criteria, the lower plots for the lower E_T^γ threshold selection criteria. The dashed line is the average correction factor.

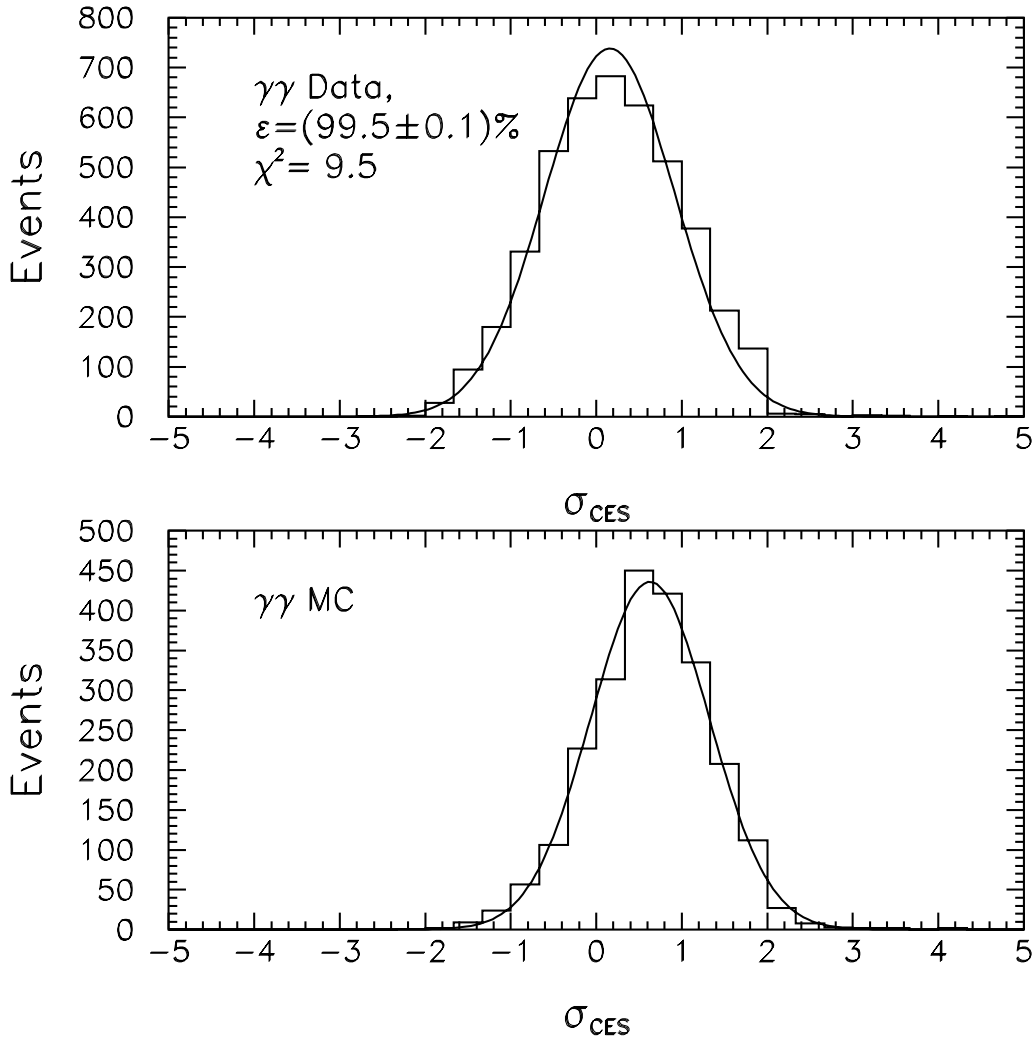

Figure 2.4: The distribution of $\sigma_{\rm CES}$ in the data and in the detector simulation. The variable $\sigma_{\rm CES}$ is a comparison between the shower development and that expected from the measured CEM energy and vertex position. Each photon is required to have $|\sigma_{\rm CES}| < 2.0$. Since the simulation does not model the mean of this distribution well, the requirement is not part of the Monte Carlo offline selection. The efficiency is $\epsilon_{\sigma_{\rm CES}} = (99.5 \pm 0.1)\%$, where the uncertainty is statistical only.

2.7.1 Low-Threshold Diphoton Trigger

The efficiencies of the low-threshold diphoton triggers are measured using a sample of low-E_T e^+e^- events. Each event is required to pass the L2 dielectron trigger, the L3 low-threshold diphoton trigger and the selection criteria listed in Table 2.4. There are 1570 events in the sample. Figure 2.5a shows the efficiency of the L2 low-threshold trigger as a function of the isolation energy in a 3-by-3 array of trigger towers around the cluster, E^{Iso}_{3x3}. Since the $E^{Iso}_{3x3} < 4$ GeV requirement is part of the offline selection, the efficiency is determined using a subset of events which have $E^{Iso}_{3x3} < 4$ GeV. Figure 2.5b shows the trigger efficiency as a function of E^{γ}_{T}; the efficiency is flat as a function of E^{γ}_{T} above 12 GeV. Above 12 GeV there are 444 events; 425 pass the trigger requirement for an efficiency of $\epsilon^{\text{Low Threshold}}_{\text{Trigger}} = (96 \pm 1_{stat})\%$.

e^+e^- Sample Selection Criteria
Two central electromagnetic clusters with $E_T > 8$ GeV
Pass the L2 dielectron trigger
Low E^{γ}_{T} threshold fiducial requirement
$\lvert z_{\text{vertex}} \rvert < 60$ cm
$\chi^2_{\text{CES}} < 10$
$0.5 < E/P < 1.5$

Table 2.4: The selection criteria used to select a sample of e^+e^- events for use in evaluating the low-threshold trigger efficiency. The selection criteria used here are described in detail in Ref. [38].

2.7.2 High-Threshold Trigger

To measure the efficiency of the high-threshold triggers a set of 2131 diphoton candidate events which pass the selection criteria in Table 2.1 and also pass the low-threshold triggers are used. The trigger efficiencies for the L2 trigger and the L2-L3 high-threshold trigger path are shown in Figure 2.6.

The efficiency is flat as a function of E_T^γ above 22 GeV; the L3 trigger is fully efficient by the time the L2 trigger is fully efficient. Above 22 GeV there are 121 events; 121 pass the trigger requirement for an efficiency of $\epsilon_{\text{Trigger}}^{\text{High Threshold}} = 100\%$.

2.8 Purity of the Diphoton Sample

Since the purity of the sample is of less importance than the efficiency for searches for anomalous events, the selection criteria have been chosen to have high efficiency. However, even after requiring each photon to pass all of the selection criteria, there are still a substantial number of background events in the sample. The backgrounds are primarily due to hadronic jets which contain pions, kaons or etas each of which can decay to multiple photons.

To estimate the photon backgrounds, each photon candidate is compared to the single photon hypothesis and the $\pi^0 \rightarrow \gamma\gamma$ hypothesis. For candidates with $E_T < 35$ GeV, the strip chamber system can distinguish the difference between a single γ and $\pi^0 \rightarrow \gamma\gamma$. For higher energies, $E_T > 35$ GeV, the two photons cannot be resolved in the CES. Instead the central preradiator system (CPR) is used to measure the conversion probability in the magnet coil.

In both cases, it is not possible to separate real (prompt) photons and backgrounds on an event-by-event basis. However, standard techniques allow the extraction of purity information on a statistical basis in large samples [36, 56]. Using these techniques on both candidates, and taking into account possible correlations, the average purity is estimated to be $(15 \pm 4)\%$.

Note again that the purity of the sample is of less importance than the efficiency for searches for rare events. While this result indicates that most

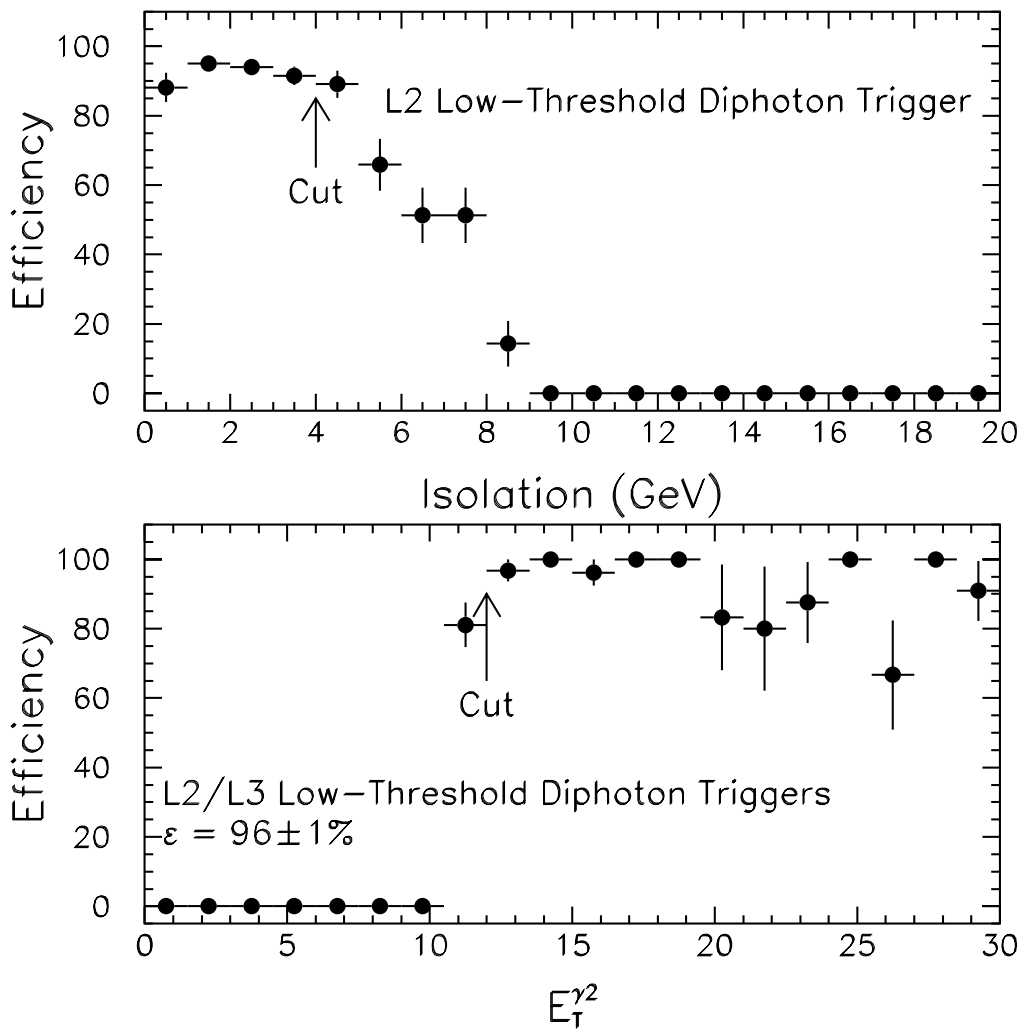

Figure 2.5: The top plot shows the efficiency of the L2 low-threshold trigger as a function of the E_{3x3}^{Iso} selection. The lower plot shows the efficiency of the L2/L3 low-threshold trigger path as a function of E_T^{γ}. The trigger is fully efficient for $E_T^{\gamma} > 12$ GeV and has an efficiency of $(96 \pm 1_{stat})\%$.

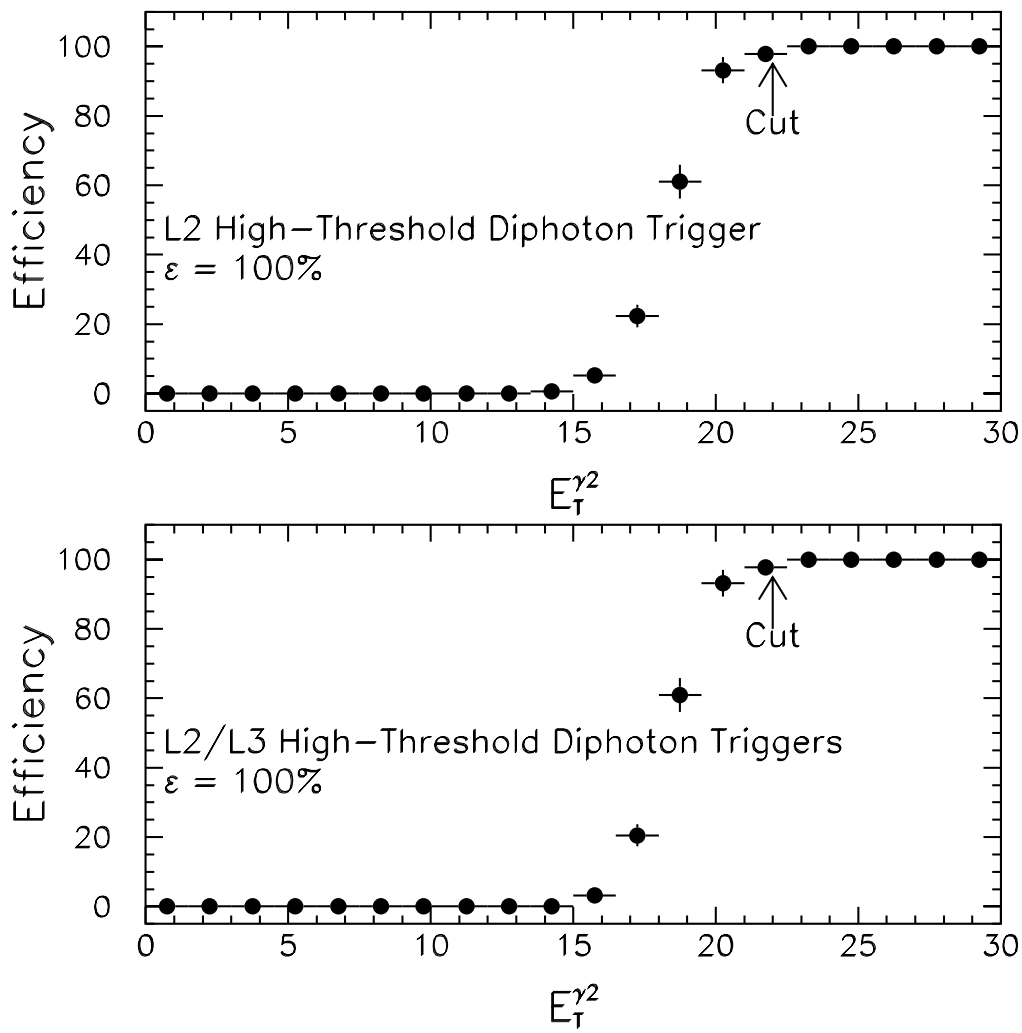

Figure 2.6: The efficiency of the L2 high-threshold and the L2/L3 high-threshold triggers as a function of E_T^{γ}. The trigger is fully efficient for $E_T^{\gamma} > 22$ GeV and has an efficiency of 100%.

of the events in the sample are not from prompt diphoton production, it does not affect either the results of the $\gamma\gamma + X$ search or the limit setting procedure except as a dilution.

Chapter 3

Searches for Anomalous Events

No scientific activity teeters more precariously on the precipice between bravery and foolishness than a search for unobserved objects justified only by their necessity in theory.

- Steven Jay Gould

In many models involving physics beyond the Standard Model, cascade decays of heavy new particles generate $\gamma\gamma$ signatures with associated quarks, leptons and/or gauge bosons. However, there are Standard Model processes which produce or fake these final states at measurable rates. Anomalous events, those which do not appear to be from Standard Model sources, are searched for using two values of the photon E_T thresholds: $E_T = 12$ GeV and $E_T = 25$ GeV. The E_T=12 GeV threshold has better acceptance for low-Q^2 decays to photons, but has more background. The $E_T = 25$ GeV threshold accepts many fewer Standard Model events and so has better discrimination for high-Q^2 decays. Each of the 2239 events in the diphoton sample, is searched for the presence of $\not\!\!E_T$, jets, electrons, muons, taus, b-quarks, or additional photons.

3.1 Missing E_T

The standard method for inferring the presence of particles that do not interact in the calorimeter, such as neutrinos, is measuring the missing transverse energy ($\not{E}_T$) [37]. The $\not{E}_T$ is defined as the negative of the vector sum of the transverse energy in all calorimeter towers with $|\eta| < 3.6$. The $\not{E}_T$ is corrected for the measured detector response to jets and takes into account cracks between detector components and nonlinear calorimeter response [39, 57, 58]. In addition, the $\not{E}_T$ is corrected for the presence of muons, which do not deposit their total energy in the calorimeter [39]. The energies of photons (and any electrons in the event) are subjected to small corrections ($\sim 1\%$) derived from an *in situ* calibration of the calorimeter [59].

While these corrections improve the $\not{E}_T$ resolution on average, some events still have a substantially mismeasured $\not{E}_T$. Many of these events can be removed by rejecting events which have a jet with uncorrected $E_T > 10$ GeV pointing within $10°$ in azimuth of the $\not{E}_T$. Since this requirement introduces an unnecessary inefficiency, and a possible bias, for searching for leptons, bosons, or jets, it is only imposed when searching for the presence of $\not{E}_T$ and in making all $\not{E}_T$ plots. The requirement only removes 48 of the 2239 events in the sample.

The $\not{E}_T$ resolution is measured using $Z^0 \to e^+e^-$ events [60]. A sample is selected as having two electrons, each passing the requirements of Table 2.2, and M_{ee} within 10 GeV of the mass of the Z^0. The resolution is plotted in Figure 3.1 as a function of $\Sigma E_T^{\text{Corrected}}$ where $\Sigma E_T^{\text{Corrected}} = \Sigma E_T - E_T^{e_1} - E_T^{e_2}$. In the region $\Sigma E_T^{\text{Corrected}} < 150$ GeV the distribution is well-parameterized by

$$\sigma(\not{E}_T^x) = (2.66 \pm 0.34 \ \text{GeV}) + (0.043 \pm 0.007) \times \Sigma E_T^{\text{Corrected}}. \tag{3.1}$$

The $\Sigma E_T^{\text{Corrected}}$ distributions for $Z^0 \to e^+e^-$ and diphoton events are shown

in Figure 3.2. As a check, in Figure 3.3 the resolution from e^+e^- events is compared to that from the diphoton sample. The results from the two samples are consistent with each other within statistics.

Standard Model diphoton events have no intrinsic $\not{E}_T$; thus the expected $\not{E}_T$ distribution can be predicted from the resolution alone. This has the advantage that the estimate is determined entirely by the data. For every event the expected $\not{E}_T$ distribution can be calculated using a Monte Carlo method which smears the X and Y components of the true $\not{E}_T$ (assumed to be zero) by the resolution (estimated from $\Sigma E_T^{Corrected}$). Repeating the procedure 200 times per event yields the expected $\not{E}_T$ distribution for that event. Summing over all events gives the distribution for the entire sample. The systematic uncertainty on the distribution is found by repeating the entire procedure 1000 times but varying the resolution within its uncertainty.

The data are shown along with the expectations from the resolution simulation in Figures 3.4 and 3.5. With the exception of one event on the tail on the distribution, the '$ee\gamma\gamma\not{E}_T$' candidate event [7] ($\not{E}_T = 55 \pm 7$ GeV), the data agree well with the expectations. For a photon E_T threshold of 12 GeV only the one event with $\not{E}_T > 35$ GeV is observed, with a expectation of 0.5 ± 0.1 events. For a photon threshold E_T of 25 GeV, two events are observed with $\not{E}_T > 25$ GeV, with 0.5 ± 0.1 events expected. The $ee\gamma\gamma\not{E}_T$ candidate event will be discussed in more detail in Chapter 4. The other event has both photons above 25 GeV and $\not{E}_T = 34$ GeV. However, on close inspection, it appears to be due to two mis-measurements. The event contains an energetic jet which points directly at the region between the plug and forward calorimeters and near the $\not{E}_T$ in ϕ. However, one of the photons is at the edge of the fiducial region and may be undermeasured [61], causing

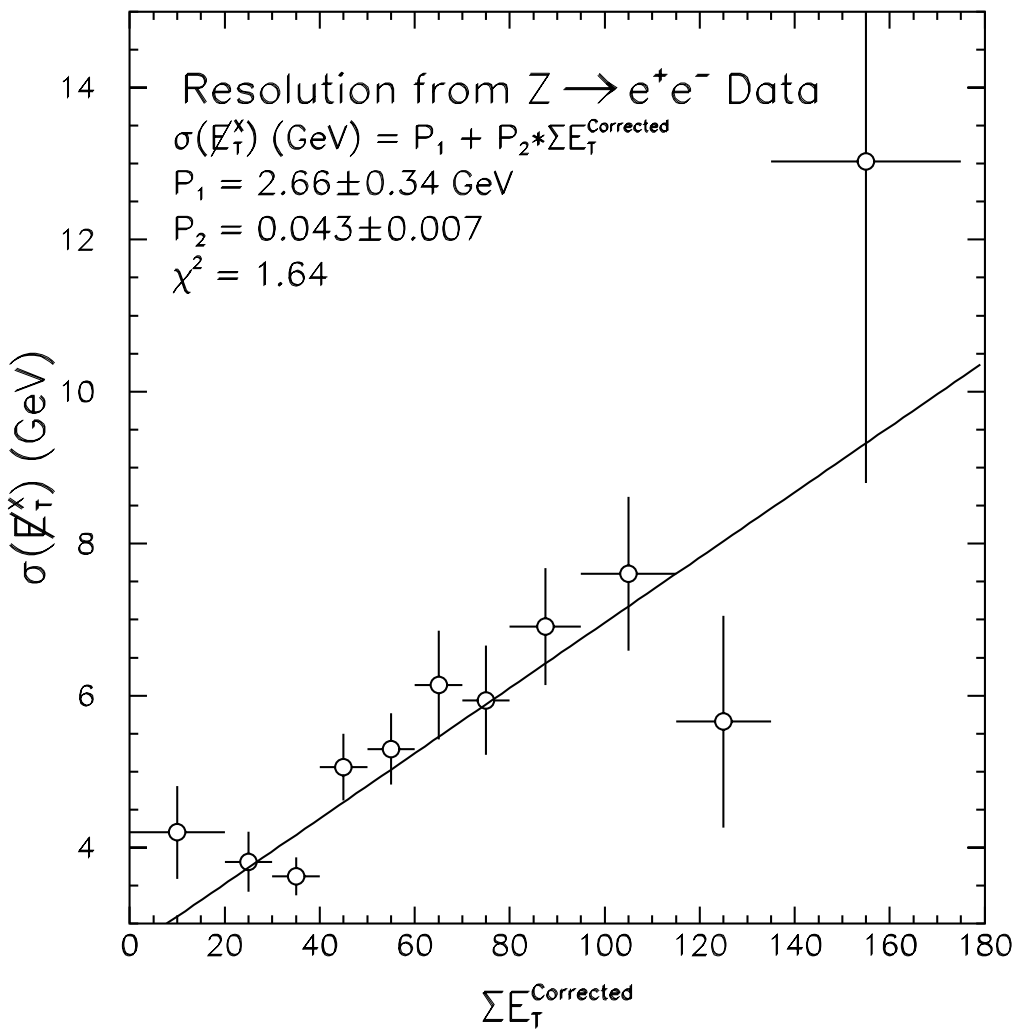

Figure 3.1: The resolution on one component of the $\not{E}_{\rm T}$ ($\not{E}^x_{\rm T}$) as determined from a sample of $Z^0 \rightarrow e^+e^-$ events. The resolution is well-parameterized by $\sigma(\not{E}^x_{\rm T}) = (2.66 \pm 0.34$ GeV$) + (0.043 \pm 0.007) \times \Sigma {\rm E}_{\rm T}^{\rm Corrected}$ for $\Sigma {\rm E}_{\rm T}^{\rm Corrected} < 150$ GeV.

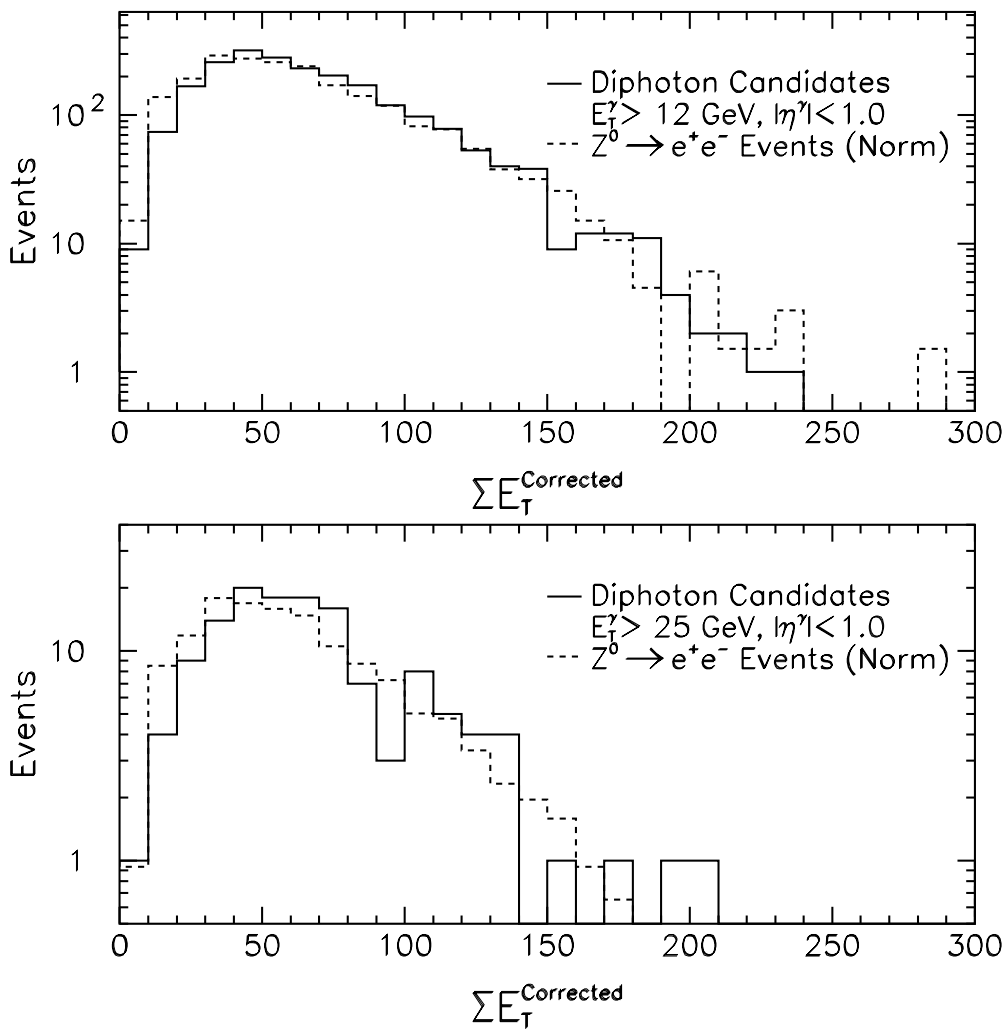

Figure 3.2: The total corrected transverse energy in the event, $\Sigma E_T^{Corrected}$, for diphoton and $Z^0 \rightarrow e^+e^-$ events. The variable $\Sigma E_T^{Corrected}$ is defined as $\Sigma E_T^{Corrected} = \Sigma E_T - E_T^{e_1} - E_T^{e_2}$.

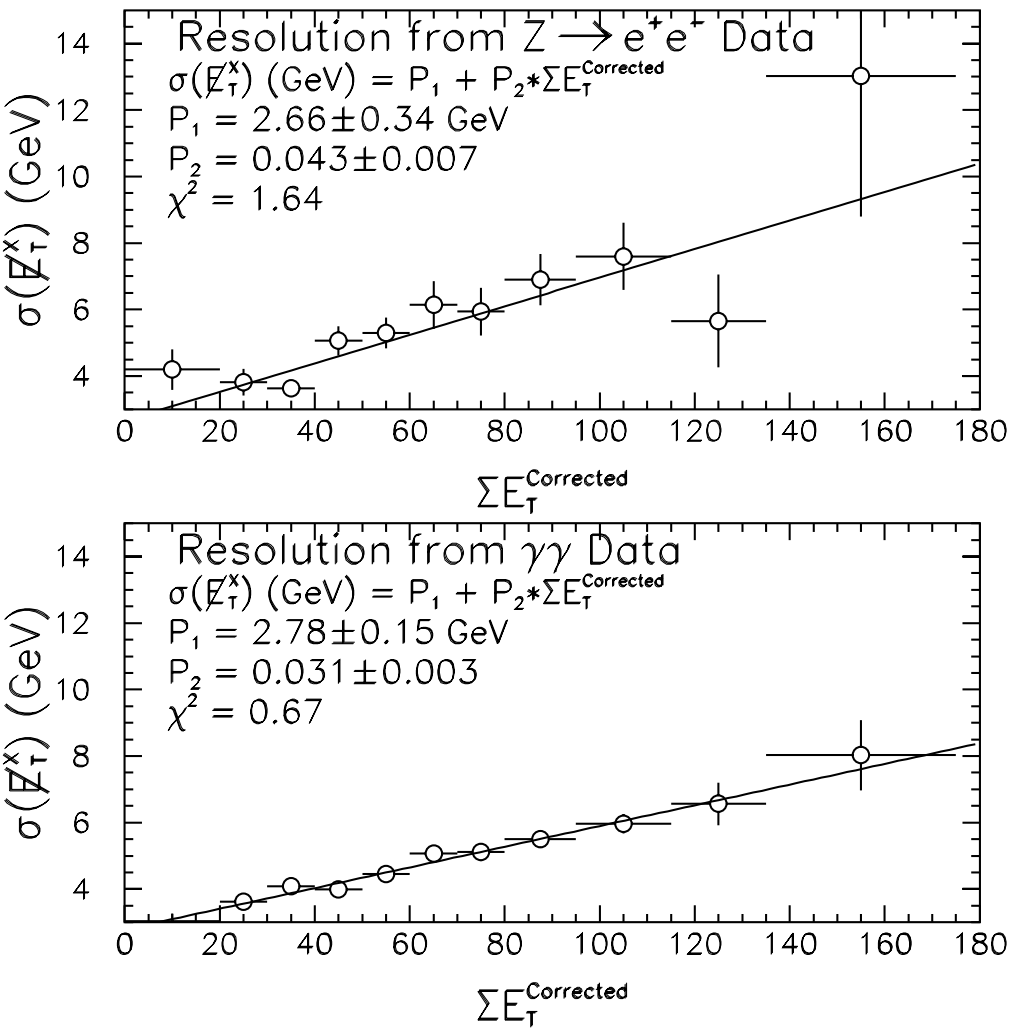

Figure 3.3: A comparison of the $\not\!\!E_{\rm T}$ resolution for $Z^0 \to e^+e^-$ and diphoton events. The resolutions, as measured using both samples, are consistent with each other within statistics.

the ϕ position of the $\not\!\!E_T$ to be just far enough away from the jet to pass the $\Delta\phi_{\not\!\!E_T-\mathrm{jet}} > 10^\circ$ requirement. The 4-vectors of the event are given in Table 3.1.

Run 67397, Event 47088					
	P_x (GeV/c)	P_y (GeV/c)	P_z (GeV/c)	E (GeV)	E_T (GeV)
γ_1	-85.8	1.6	63.4	106.7	85.8
γ_2	30.8	-15.9	6.4	35.3	34.7
j_1	40.1	18.8	237	242	44.4
$\not\!\!E_T$	33.6	-5.5	–	–	34.1

Table 3.1: The 4-vectors of the $\gamma\gamma + \not\!\!E_T$ candidate event. Note that this event may be due to mis-measurement. The $\Delta\phi$ between the jet and the $\not\!\!E_T$ is 34°, the jet points at the region between the plug and forward calorimeters and the second photon, γ_2, is at the edge of the fiducial region of the central calorimeter and may be undermeasured [61].

3.2 Jets

To search for anomalous production of quarks and gluons, the number of jets, N_{Jet}, is counted in a manner identical to that used in the top-quark discovery [39, 62]. Each jet is required to have uncorrected $E_T > 10$ GeV and $|\eta| < 2.0$. The distributions in the number of jets are shown in Figures 3.7 and 3.8 for photon E_T thresholds of 12 GeV and 25 GeV respectively.

While there are cross section predictions for $\gamma\gamma$, $\gamma\gamma + 1$ jet and $\gamma\gamma +$ 2 jet production [63], there is currently no theoretical prediction for higher jet multiplicities. However, it has been known for some time that the ratio between n-jet and $(n-1)$-jet cross sections for W and Z^0 production can be approximated by a constant [64], i.e,

$$R_n = \frac{\sigma(V \ + \ n\,\mathrm{jets})}{\sigma(V \ + \ (n-1)\,\mathrm{jets})} \tag{3.2}$$

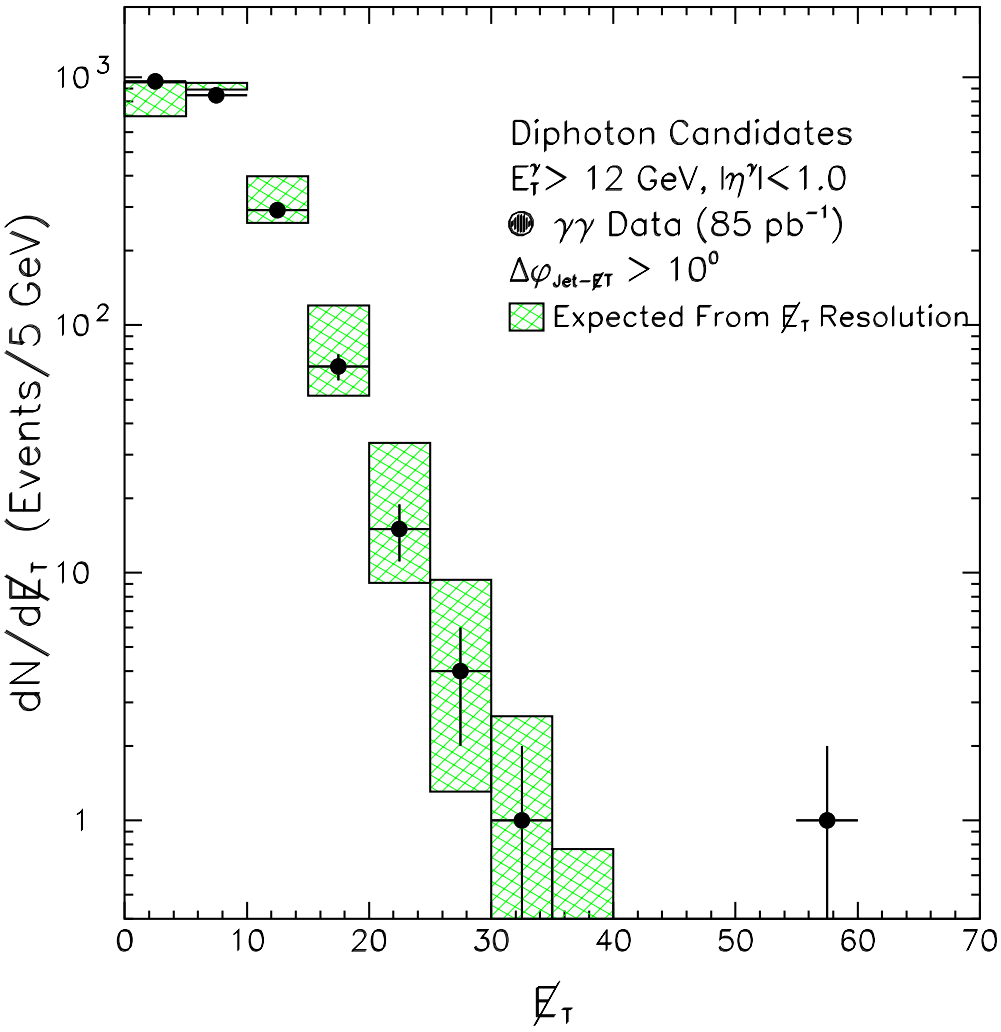

Figure 3.4: The $\not{E}_T$ spectrum for diphoton events with $E_T^\gamma > 12$ GeV in the data. The boxes indicate the range of the values of the $\not{E}_T$ distribution predicted from detector resolution. The one event on the tail is the $ee\gamma\gamma\not{E}_T$ candidate event, described in detail in Chapter 4.

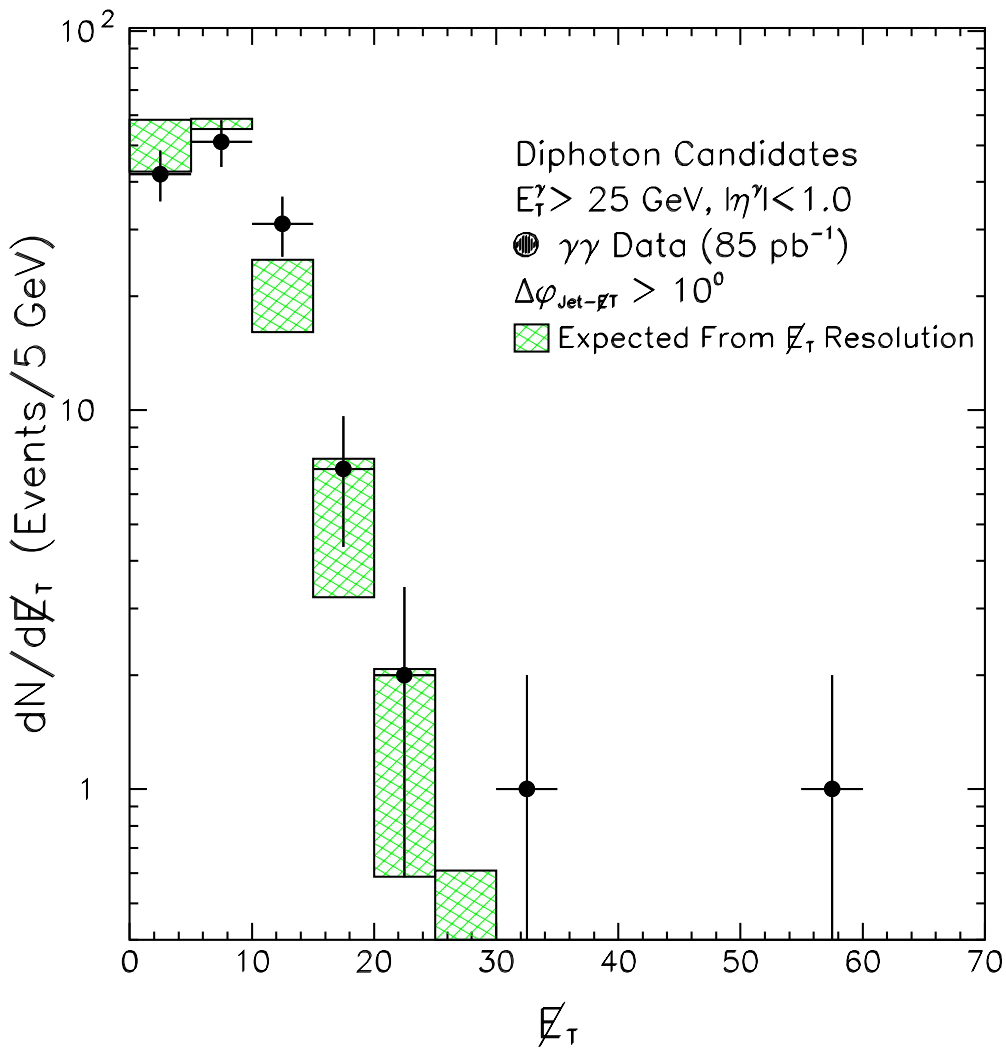

Figure 3.5: The $\not{E}_T$ spectrum for diphoton events with $E_T^\gamma > 25$ GeV in the data. The boxes indicate the range of the values of the $\not{E}_T$ distribution predicted from detector resolution. The one event on the tail is the $ee\gamma\gamma\not{E}_T$ candidate event, described in detail in Chapter 4.

where V is either a W or a Z^0. This has been confirmed within resolution in the CDF data [65] and is expected to hold for most processes since additional jets are typically due to initial state and final state radiation. As a check, the N_{Jet} distributions in $Z^0 \rightarrow e^+e^-$ events and dijet events ($e.g,\ \bar{p}p \rightarrow q\bar{q} \rightarrow jj$, or $\bar{p}p \rightarrow gg \rightarrow jj$) have been studied. The $Z^0 \rightarrow e^+e^-$ sample is the same as in the previous section; the dijet sample is selected by requiring two jets with uncorrected $E_T > 10$ GeV and $|\eta| < 2.0$. For the dijet data sample, N_{Jet} is defined to be the total number of jets in the event minus the two jets which were used to select the sample. The N_{Jet} distributions for both samples are shown in Figure 3.6 and, as expected, are well described by using an exponential, $\exp^{\beta-(\alpha \times N_{Jet})}$. The slope, α, of the N_{Jet} distribution for the dijet sample is measured to be $\alpha = 1.54 \pm 0.01_{stat}$. The slope of the N_{Jet} distribution for the $Z^0 \rightarrow e^+e^-$ sample is measured to be $\alpha = 1.71 \pm 0.04_{stat}$.

To look for anomalous N_{Jet} production in the $\gamma\gamma$ data, an exponential fit for small values of N_{Jet} is used to extrapolate to the large N_{Jet} region [66]. The slope for diphoton events with $E_T^\gamma > 12$ GeV and $N_{Jet} \leq 3$ is measured to be $\alpha = 1.82 \pm 0.06_{stat}$. The parameterization predicts 1.6 ± 0.4 events with 4 or more jets; 2 events are observed. For diphoton events with $E_T^\gamma > 25$ GeV and $N_{Jet} \leq 2$, the slope is measured to be $\alpha = 1.6 \pm 0.2_{stat}$. The parameterization predicts 1.7 ± 1.5 events with 3 or more jets; 0 events are observed.

3.3 Electrons and Muons

Electrons and muons produced in association with photon pairs are required to be isolated, have $E_T > 25$ GeV, and be in the central part of the detector ($|\eta| < 1.0$). They are identified with the same identification and isolation selection requirements (see Tables 2.2 and 3.2) used in the top-quark

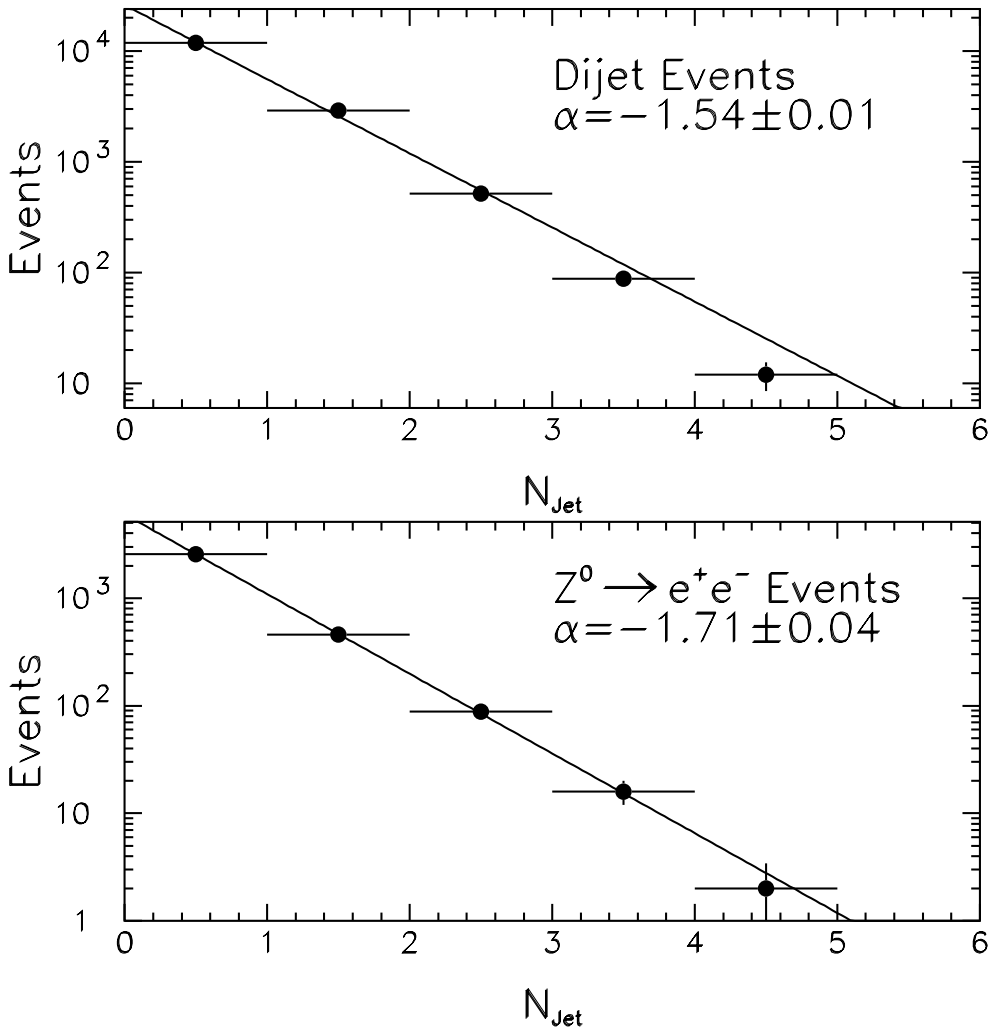

Figure 3.6: The number of jets, N_{Jet}, produced in association with dijets and $Z^0 \rightarrow e^+e^-$ decays. For the dijet data sample, N_{Jet} is defined to be the total number of jets in the event minus the two jets which were used to select the sample. The slope of the exponential fit, α, is indicated on each plot.

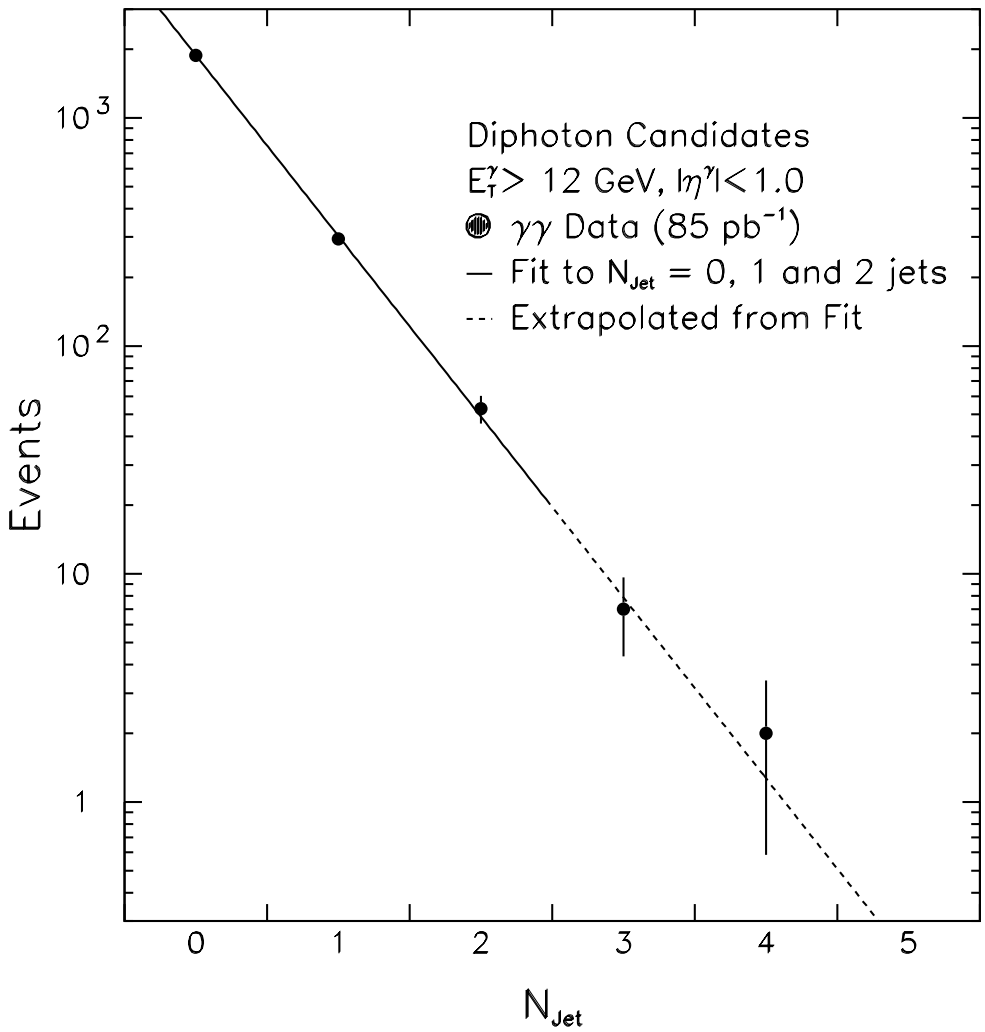

Figure 3.7: The number of jets, N_{Jet}, produced in association with diphoton pairs with $E_T^\gamma > 12$ GeV. The line is an exponential fit to the data with $N_{Jet} \leq 3$, and is extrapolated to $N_{Jet} \geq 4$.

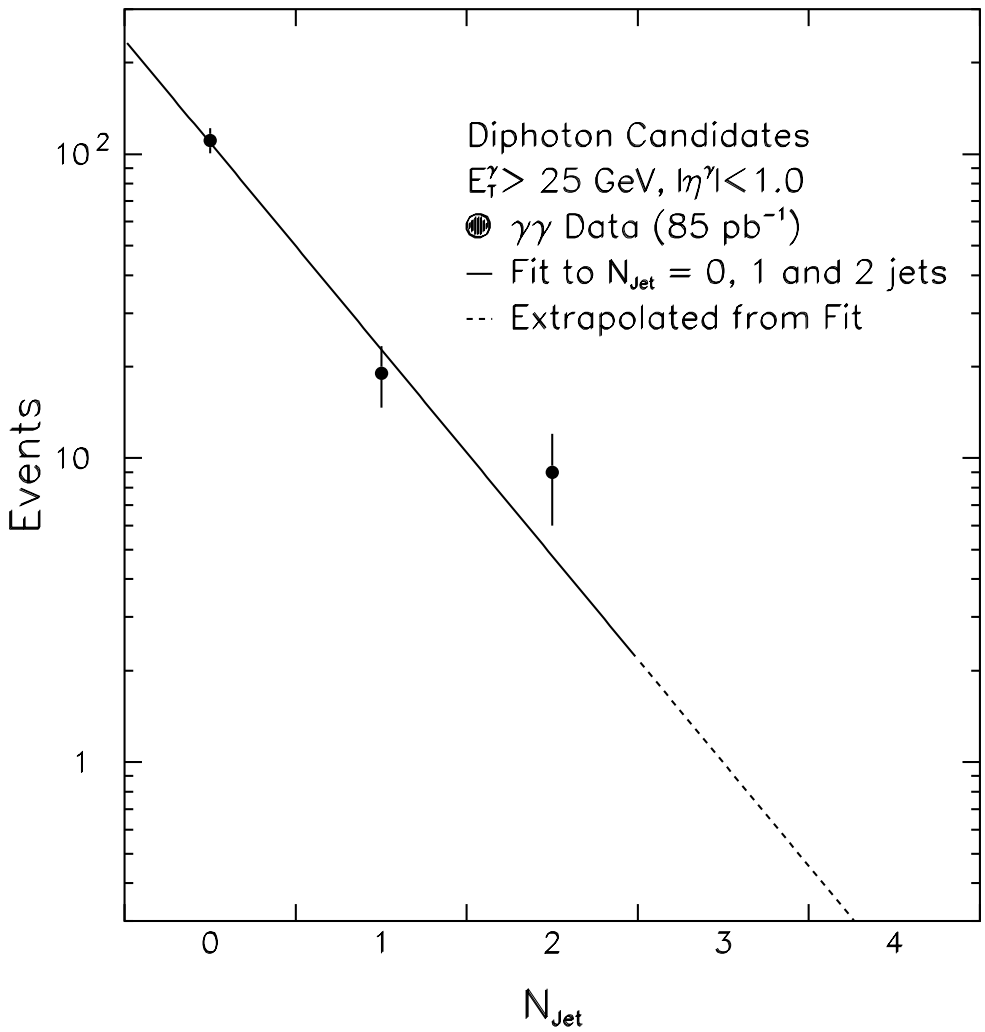

Figure 3.8: The number of jets, N_{Jet}, produced in association with diphoton pairs with $E_T^\gamma > 25$ GeV. The line is an exponential fit to the data with $N_{Jet} \leq 2$, and is extrapolated to $N_{Jet} \geq 3$.

discovery [39]. A total of 3 events with a central electron or muon are found in the data. The first event has two muons and two photons. Unfortunately, this event is not terribly unusual, as shown below, and is kinematically very different from the $ee\gamma\gamma\not{E}_{\rm T}$ candidate event (see Table 3.3). Furthermore it is consistent with a double-radiative Z^0 decay, $\bar{p}p \rightarrow Z^0 \rightarrow \mu^+\mu^-\gamma\gamma$, since the 4-body invariant mass is $m_{\mu^+\mu^-\gamma\gamma} = 92 \pm 1$ GeV/c^2. The second event (see Table 3.4) has a single electron. There is some indication that this event is also due to the decay of a Z^0 boson. While there is no track in the central tracking chamber pointing at either photon, the SVX indicates that there may have been a charged particle pointing at one of the photons, γ_2 in Table 3.4 [67]. This indicates that this could be $Z^0 \rightarrow e^+e^-\gamma$ where one of the electrons emitted a photon (via Bremstrahlung) in which the photon carried away most of the energy and the electron was lost in the calorimeter. Another possible explanation is that the track of one of the electron was not found in the central tracking chamber. Furthermore, the invariant mass of the two photons and the electron is $m_{e^+\gamma\gamma} = 91 \pm 2$ GeV/c^2. The third event is the '$ee\gamma\gamma\not{E}_{\rm T}$' candidate event and will be discussed further in Chapter 4.

The dominant sources of $e\gamma\gamma$ and $\mu\gamma\gamma$ production are Standard Model $W\gamma$ and $Z^0\gamma$. The production and decay of $W\gamma \rightarrow \ell\nu\gamma$ and $Z^0\gamma \rightarrow \ell^+\ell^-\gamma$ production, where ℓ is an electron, muon or tau, are simulated using the PYTHIA [53] Monte Carlo and a detector simulation [54]. Additional final state photons are added automatically by PYTHIA through additional initial or final state radiation. The Monte Carlo predicts $\sigma_{Z^0\gamma} = 6.7$ pb. In a sample of 15,000 $Z^0\gamma$ simulated events 1 event passes the $\ell\gamma\gamma$ cuts (the event has 2 muons passing the selection criteria in Table 3.2). For $W\gamma$ the Monte Carlo estimates $\sigma_{W\gamma}$=37 pb. No events passing the cuts are found in 10,000 simulated events. The number of events with the $\ell\gamma\gamma$ signature from the Monte

Requirement
$P_T > 20$ GeV/c
$\|d_0\| < 0.3$ cm
$\|\Delta x_{CMU}\| < 2$ cm
$\|\Delta x_{CMP}\| < 5$ cm
$\|\Delta x_{CMX}\| < 5$ cm
$\|\Delta z(\text{vertex-track})\| < 5.0$ cm
$N_{ASL} \geq 3$
$N_{SSL} \geq 2$
$N_{ASL}+N_{SSL} \geq 6$
$E_{EM} < 2$ GeV
$E_{Had} < 6$ GeV
$E_{EM}+E_{Had} > 0.1$ GeV
$E_T^{Iso}/ P_T < 0.10$
$\Sigma P_T^{Iso}/ P_T < 0.10$

Table 3.2: The selection criteria used to identify isolated muons. These are the same requirements as used in the top-quark discovery are described in detail in Ref. [39, 68].

Carlo is thus predicted to be

$$\begin{aligned} N_{\text{exp}} &= L \cdot \sigma \cdot A \\ &= (85 \text{ pb}^{-1}) \cdot (6.7 \text{ pb}) \cdot (\frac{1}{15,000}) = 0.04 \pm 0.04_{stat}. \end{aligned} \tag{3.3}$$

Another source of $e\gamma\gamma$ events, but which is not correctly simulated with the Monte Carlo, is $Z^0\gamma \rightarrow e^+e^-\gamma$ where one of the electrons is identified as a photon. This can occur if the electron emits a photon via Bremstrahlung (the photon carries away most of the energy and the electron is lost in the detector) or the track of the electron is not found by the central tracking chamber. The rate at which electrons are 'identified' as a photon is determined from a sample of $Z^0 \rightarrow e^+e^-$ events from the data. The sample is selected by requiring the presence of a central electron passing the requirements in

Run 69571, Event 769815					
	P_x (GeV/c)	P_y (GeV/c)	P_z (GeV/c)	E (GeV)	E_T (GeV)
γ_1	12.4	5.3	-1.4	13.5	13.4
γ_2	-16.0	-5.3	-3.2	17.1	16.8
μ_1	28.2	9.5	-33.4	44.7	29.7
μ_2	-26.5	-4.9	-14.9	30.8	27.0
$\not{E}_T$	7.1	-0.3	–	–	7.1

Table 3.3: The 4-vectors of the $\gamma\gamma + \mu\mu$ candidate event. This event is consistent with a double-radiative Z^0 decay, $\bar{p}p \rightarrow Z^0 \rightarrow \mu^+\mu^-\gamma\gamma$ ($m_{\mu^+\mu^-\gamma\gamma} = 92 \pm 1$ GeV/c^2).

Run 63541, Event 304680					
	P_x (GeV/c)	P_y (GeV/c)	P_z (GeV/c)	E (GeV)	E_T (GeV)
γ_1	-13.7	-19.9	-28.8	37.6	24.2
γ_2	-9.8	-13.1	-10.1	19.2	16.3
e_1	19.7	35.0	5.0	40.4	40.1
$\not{E}_T$	-4.3	0.4	–	–	4.4

Table 3.4: The 4-vectors of the $\gamma\gamma + e$ candidate event. The invariant mass of the two photons and the electron indicates that this may be a Z^0 ($m_{e^+\gamma\gamma} = 91 \pm 2$ GeV/c^2) where one of the electrons was identified as a photon or the electron emitted all its energy in a photon via Bremstrahlung.

Table 2.2, a second electromagnetic cluster which passes all the photon cuts *except* the track requirement, and a pair invariant mass within 15 GeV of the Z^0 mass. There are 1853 events in the sample, 35 after requiring the second electromagnetic cluster to have no tracks pointing at it. By assuming the 1853 events are a pure sample of $Z^0 \rightarrow e^+e^-$ events and the 35 events are examples of events where the electron was identified as a photon, the 'fake' rate is estimated to be $(1.9 \pm 0.3_{stat})\%$ per electron.

To turn this fake rate into the number of expected $e\gamma\gamma$ events, a sample of $ee\gamma$ events is selected and used in conjunction with the fake rate.

The sample is selected by requiring a central electron, a photon passing the cuts in Table 2.1 and a third electromagnetic cluster selected using all the electron selection criteria with the exception of the track requirement. This sample, presumably $ee\gamma$, consists of 12 events. Multiplying by the fake rate yields a expectation of $0.2 \pm 0.1_{stat}$ events in the data. Summing this source with the $W\gamma$ and $Z^0\gamma$ Monte Carlo predictions gives an expectation of $(0.04 \pm 0.04_{stat})$ + $(0.2 \pm 0.1_{stat}) = 0.3 \pm 0.1_{stat}$ $\ell\gamma\gamma$ events in the data. Similarly, for the photon threshold of $\mathrm{E}_{\mathrm{T}}^{\gamma} > 25$ GeV the methods predict a total of 0.1 ± 0.1 events, dominated by events in which electrons fake photons; only one event, the $ee\gamma\gamma\not{E}_{\mathrm{T}}$ candidate event, is observed in the data.

The number of $\ell\ell\gamma\gamma$ events in the data is dominated by $Z\gamma$ production. In the Monte Carlo simulation one event has two leptons and two photons, and using Equation 3.3 a total of $0.04 \pm 0.04_{stat}$ events with $\ell\ell\gamma\gamma$ are expected in the data. While the $ee\gamma\gamma\not{E}_{\mathrm{T}}$ event remains unexplained, the $\mu\mu\gamma\gamma$ event appears to be an upward fluctuation of the rate of $Z^0\gamma$, and is not terribly unusual.

3.4 Taus

Hadronic decays of the τ lepton are identified with the selection criteria used in the measurement of $t\bar{t}$ production and decay into $e\tau$ and $\mu\tau$ final states [40]. Table 3.5 contains a list of the τ identification requirements. One $\tau\gamma\gamma$ candidate is observed in the data with $\mathrm{E}_{\mathrm{T}}^{\gamma} > 12$ GeV; none with $\mathrm{E}_{\mathrm{T}}^{\gamma} > 25$ GeV. Hadronic jets from light quarks or gluons, produced in association with diphoton pairs, can fake hadronic τ decays. The number of events passing the $\tau\gamma\gamma$ selection criteria in the data, where the τ is due to a jet passing the τ identification requirements, is estimated using the methods of Ref. [40].

The method assigns a fake probability to each jet in the full $\gamma\gamma$ sample which is τ-taggable ($E_T > 25$ GeV and $|\eta| < 1.2$). The total event rate is found by summing over all jets. The E_T spectrum of jets which could fake a τ with $E_T >$ 25 GeV and $|\eta| < 1.2$ is shown in Figures 3.10a and 3.11a. Figure 3.9 shows the E_T spectrum for τ leptons measured in the data as well as for backgrounds from fake τ's. A total of 0.2 ± 0.1 events where a jet fakes a τ are expected in the data for $E_T^\gamma > 12$ GeV, and 0.03 ± 0.03 events for $E_T^\gamma > 25$ GeV, both consistent with observation. The number of events with the $\tau\gamma\gamma$ signature from $W\gamma$ and $Z^0\gamma$ production are estimated by the Monte Carlo to be tiny in comparison.

The most likely interpretation is that the 'τ' is from a jet which fakes the τ signature. The kinematics of the event, see Table 3.6, indicate that the τ is not likely to be due to the decay of a vector boson via $W \to \tau\nu$ or $Z \to \tau\tau$. The $W \to \tau\nu$ hypothesis is unlikely as $\not{E}_T = 14.5$ GeV, which would be low, even for a $W \to \tau\nu, \tau \to \nu X$ decay chain. Furthermore, the $\not{E}_T$ in the event is likely to be spurious as there is a jet which is only 5.5° away, in ϕ from the $\not{E}_T$. The invariant mass of the $\tau\gamma\gamma$ system is 69.3 GeV and does not indicate that this is the decay of a Z^0.

3.5 b-Quarks

Jets from b-quarks are identified using the b-tagging jet algorithm (SECVTX) developed for the top-quark discovery [39, 41]. Two $b\gamma\gamma$ candidate events are observed in the data with $E_T^\gamma > 12$ GeV; none with $E_T^\gamma > 25$ GeV. Quarks and gluons produced in association with diphoton pairs are real and fake sources of b-jets. The number of $b\gamma\gamma$ events from these sources is estimated using the same methods as developed for the top-quark discovery [39, 41, 69].

Preliminary Requirements
At least one calorimeter seed tower with $\mathrm{E_T} > 4$ GeV ≤ 6 towers with $\mathrm{E_T} > 1$ GeV in a cluster (cone 0.4) Seed track with $\mathrm{P_T} > 4.5$ GeV within 0.4 of cluster center No additional cut on total cluster $\mathrm{E_T}$
Identification and Isolation Cuts
Track multiplicity in 10° cone: use 1-prongs and 3-prongs only E/p cut: $0.5 < \frac{\mathrm{E_T}}{\mathrm{P_T}^{trk+\pi^0}} < 2.0$ (1-prongs) $0.5 < \frac{\mathrm{E_T}}{\mathrm{P_T}^{trk+\pi^0}} < 1.5$ (3-prongs) Sliding RMS cluster width cut: $\sigma_{cl} < 0.11 - 0.025 \times \mathrm{E_T}/100$ (1-prongs) $\sigma_{cl} < 0.13 - 0.034 \times \mathrm{E_T}/100$ (3-prongs) Mass cut: $m_{trk+\pi^0} < 1.8$ GeV # of π^0's: $\#\pi^0 < 3$ Isolation: $I_{trk} < 1$ GeV/c Electron removal: Reject 1-prongs with $E/p < 4, \mathrm{EMFrac} > 0.9$ or clusters with EMFrac > 0.95 as electrons Muon removal: Reject clusters with $\mathrm{E_T} < 8$ GeV, $0.05 < E_{EM} < 2$ GeV, $0.5 < E_{Had} < 5$ GeV or with a muon stub with $\lvert\phi_\tau - \phi_{stub}\rvert < 15^o$ as muons

Table 3.5: The identification and isolation selection criteria used to select hadronic decays of the τ. These are the same criteria used in the measurement of top decays into $e\tau$ and $\mu\tau$ final states, described in more detail in Ref. [40].

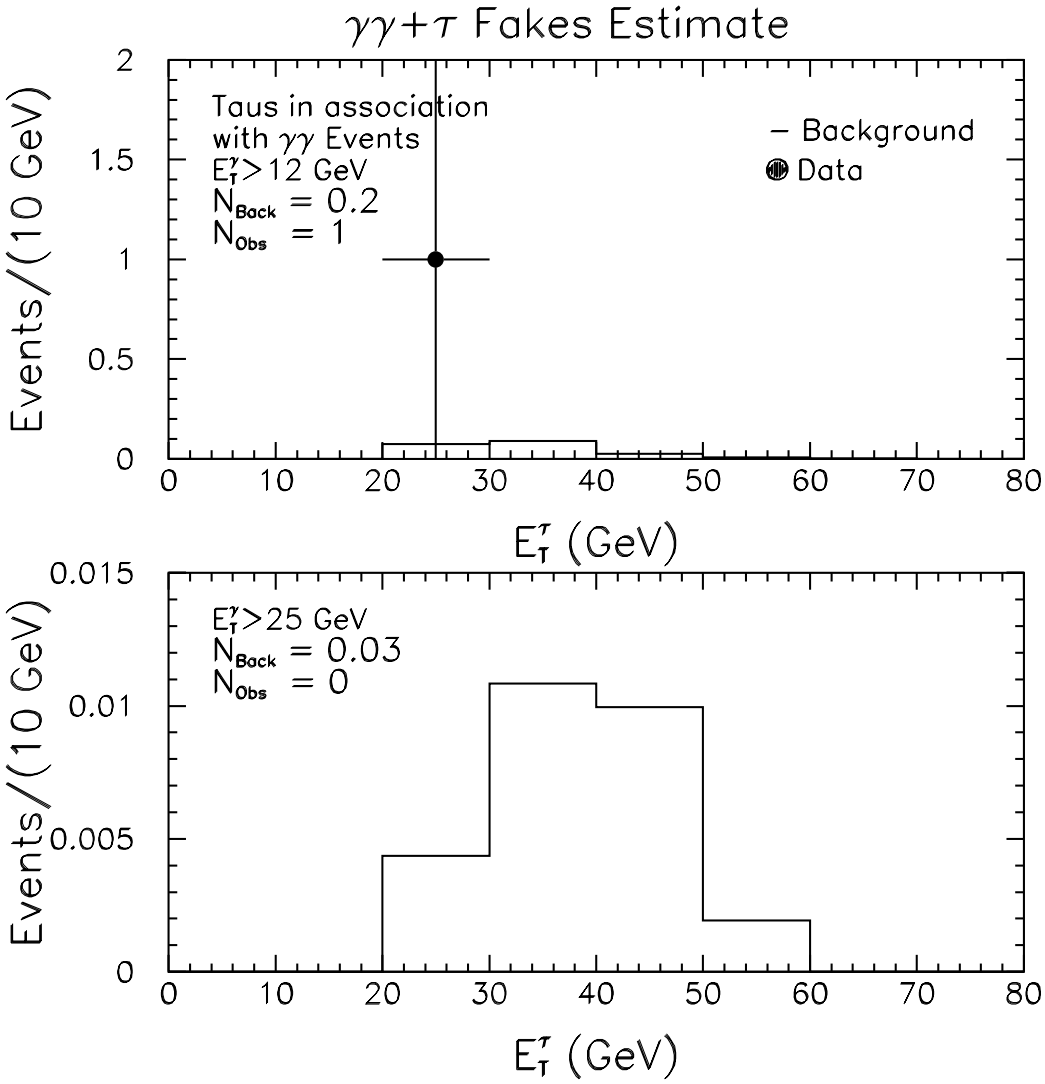

Figure 3.9: The E_T spectrum of τ candidates produced in association with diphoton pairs. Only the hadronic decays of the τ are included. The upper plot is for diphoton events in which both photons have $E_T^\gamma > 12$ GeV. There are no events with a τ candidate in the data for $E_T^\gamma > 25$ GeV, as shown in the lower plot. The point represents the one event in the data; the histogram is the expectation from fake τ's.

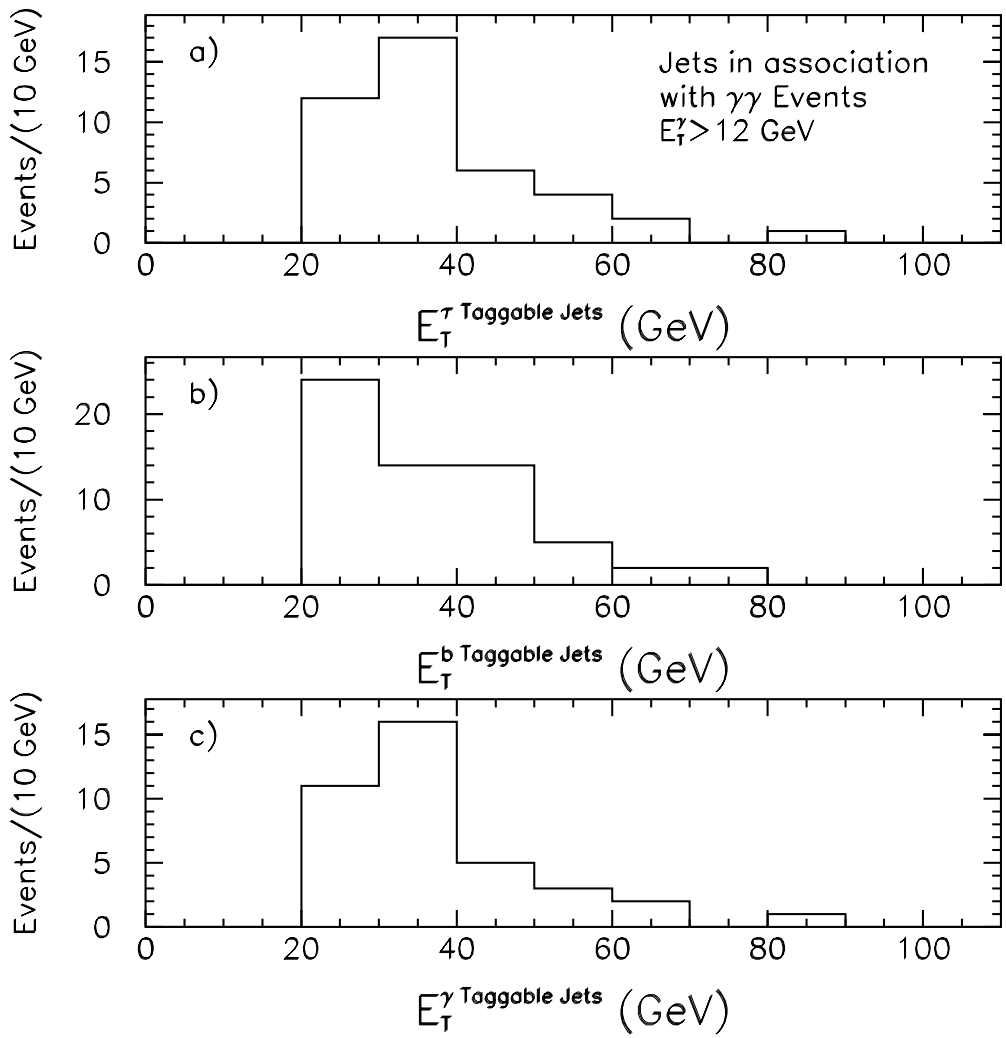

Figure 3.10: The E_T spectrum for jets produced in association with diphoton pairs with $E_T^\gamma > 12$ GeV. These plots are used to estimate the number of $\gamma\gamma$ events with extra τ's, b-jets or photons. The top plot shows the E_T spectrum for jets used to estimate the τ fake rate. Each jet in the plot must be τ-taggable ($E_T > 25$ GeV and $|\eta| < 1.2$). The middle plot shows the jets which are b-taggable ($E_T > 25$ GeV and SVX-'taggable' [41]). The lower plot shows the γ-taggable jets ($E_T > 25$ GeV and $|\eta| < 1.0$).

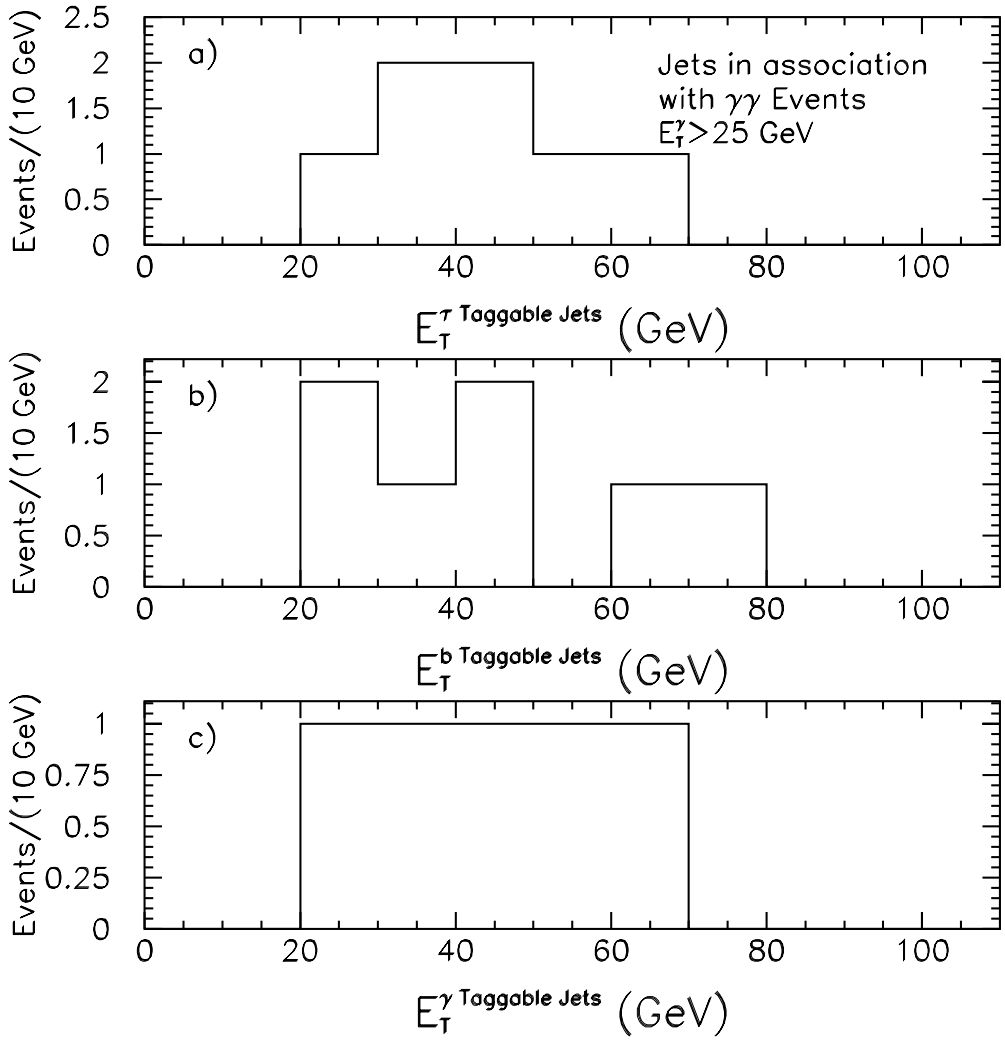

Figure 3.11: The E_T spectrum for jets produced in association with diphoton pairs with $E_T^\gamma > 25$ GeV. These plots are used to estimate the number of $\gamma\gamma$ events with extra τ's, b-jets or photons. The top plot shows the E_T spectrum for jets used to estimate the τ fake rate. Each jet in the plot must be τ-taggable ($E_T > 25$ GeV and $|\eta| < 1.2$). The middle plot shows the jets which are b-taggable ($E_T > 25$ GeV and SVX-'taggable' [41]). The lower plot shows the γ-taggable jets ($E_T > 25$ GeV and $|\eta| < 1.0$).

Run 66392, Event 23895					
	P_x (GeV/c)	P_y (GeV/c)	P_z (GeV/c)	E (GeV)	E_T (GeV)
γ_1	3.6	23.3	3.9	23.9	23.6
γ_2	-11.5	15.4	5.6	20.0	19.2
τ	14.6	-20.7	26.3	36.6	25.4
j_1	-13.5	-9.2	11.3	20.2	16.6
j_2	19.1	6.4	33.5	39.4	20.3
$\not{E}_T$	-12.7	-7.0	–	–	14.5

Table 3.6: The 4-vectors of the $\gamma\gamma + \tau$ candidate event. Note that the while the $\not{E}_T$ in the event is 14.5 GeV, the first jet, j_1, is only 5.5° in ϕ away from the $\not{E}_T$.

Again the method assigns a probability to each jet in the full $\gamma\gamma$ sample which is SVX-taggable [41] and the total event rate is found by summing over all jets. The E_T spectrum of jets which could fake a b-tag with $E_T > 25$ GeV are shown in Figures 3.10b and 3.11b. Figure 3.12 shows the E_T spectrum of the b-tagged jets and the expectations from the background prediction. A total of 1.3 ± 0.7 $b\gamma\gamma$ events are expected to be in the sample due to real and fake sources of $\gamma\gamma + b$ for $E_T^\gamma > 12$ GeV; 0.1 ± 0.1 for $E_T^\gamma > 25$ GeV. The 4-vectors of the objects in the two $b\gamma\gamma$ events are given in Tables 3.7 and 3.8.

Run 63033, Event 337739					
	P_x (GeV/c)	P_y (GeV/c)	P_z (GeV/c)	E (GeV)	E_T (GeV)
γ_1	-21.6	-8.2	-16.7	28.5	23.1
γ_2	-14.3	-22.1	-12.8	29.3	26.4
b-jet	44.8	40.8	37.6	71.8	61.0
j_2	4.9	13.0	12.4	18.6	13.9
$\not{E}_T$	-4.0	-4.5	–	–	6.1

Table 3.7: The 4-vectors of the first $\gamma\gamma + b$ candidate event.

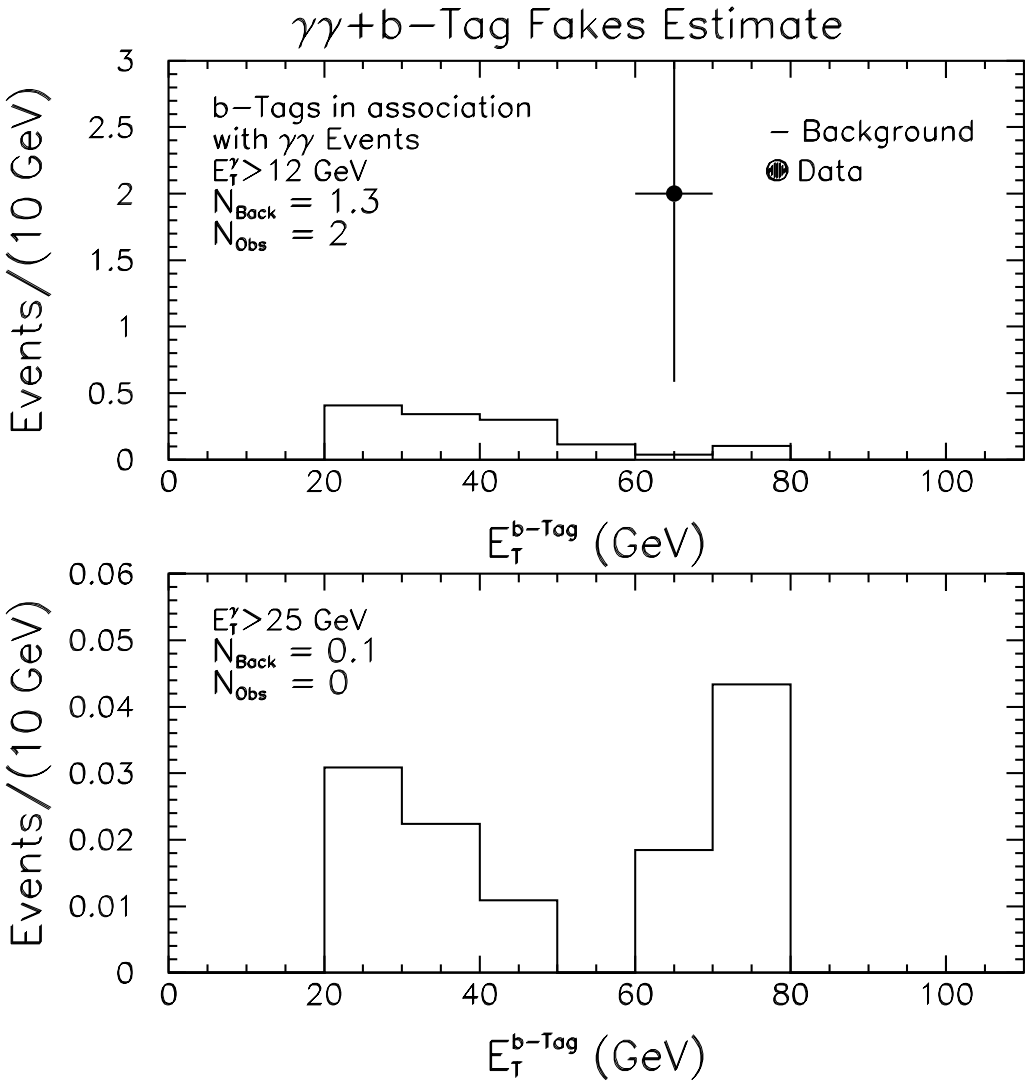

Figure 3.12: The E_T spectrum of b-tags produced in association with diphoton pairs. The upper plot is for diphoton events in which both photons have $E_T^\gamma > 12$ GeV. The lower plot is for diphoton events in which both photons have $E_T^\gamma > 25$ GeV. The point represents the data; the histogram is the expectation from real and fake sources of b-tags.

Run 64811, Event 62109					
	P_x (GeV/c)	P_y (GeV/c)	P_z (GeV/c)	E (GeV)	E_T (GeV)
γ_1	-7.1	20.2	-11.1	24.1	21.4
γ_2	-23.6	9.5	-10.8	27.6	25.4
b-jet	37.6	48.6	-4.1	62.2	62.0
j_2	4.1	-67.5	17.5	70.4	68.1
j_3	-8.8	-5.6	-16.6	19.6	10.4
$\not{E}_T$	-0.9	-12.8	–	–	12.9

Table 3.8: The 4-vectors of the second $\gamma\gamma + b$ candidate event. Note that while the $\not{E}_T$ in the event is 12.9 GeV, the second jet, j_2, is only 7.4° in ϕ away from the $\not{E}_T$.

3.6 Additional Photons

To search for events with additional photons with $E_T > 25$ GeV, events are required to have three photons which pass the selection criteria in Table 2.1. One photon must have $E_T > 25$ GeV and pass the high-threshold requirements, any two other photons in the event must both pass the same selection criteria (low-threshold or high-threshold) [70]. No events are observed with more than two photons. To estimate the rate at which jets fake the photon signature, a method similar to that in the τ analysis is used [40, 71]. The E_T spectra of jets which could fake a γ (E_T >25 GeV, $|\eta| < 1.0$) is shown in Figures 3.10c and 3.11c. The average rate at which jets fake the photon signature is approximately 1.3×10^{-3}/jet and is essentially flat as a function of E_T for $E_T > 25$ GeV. A total of 0.1 ± 0.1 events are estimated to be in the sample due to $\gamma\gamma$ + fake γ for $E_T^\gamma > 12$ GeV; 0.01 ± 0.01 for $E_T^\gamma > 25$ GeV. The E_T spectrum for photon background sources in which jets fake additional photons is shown in Figure 3.13.

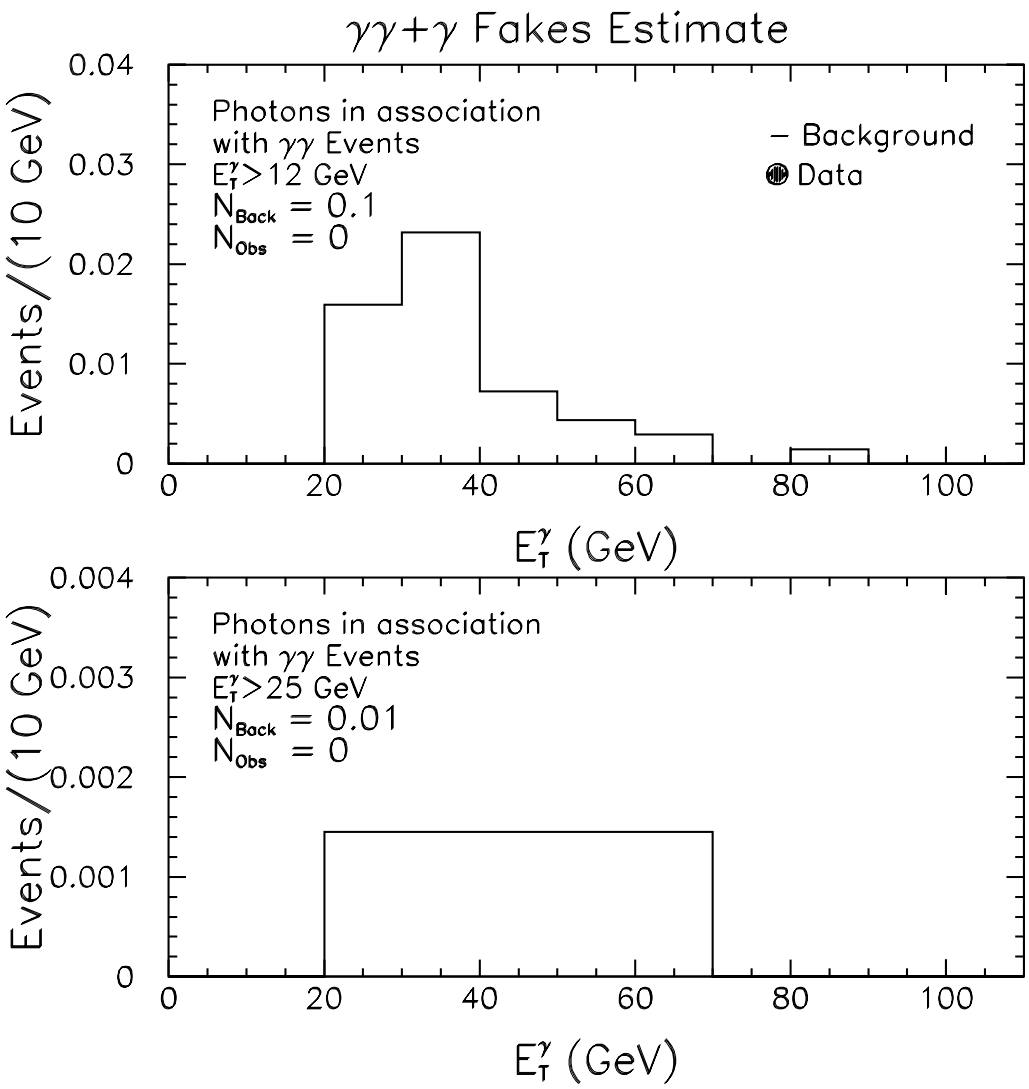

Figure 3.13: The E_T spectrum of additional photons produced in association with diphoton pairs. There are no events in the data with an additional photon. The upper and lower plots shown the expectation from fake γ's for thresholds of $E_T^\gamma > 12$ GeV and $E_T^\gamma > 25$ GeV respectively.

3.7 Summary of the Searches

Table 3.9 summarizes the observed and expected numbers of events with $\not\!\!E_T$, N_{Jets}, additional leptons, b-tags and photons. With the one possible exception of the $ee\gamma\gamma\not\!\!E_T$ candidate, the data appear to be well predicted by the background expectations. The $ee\gamma\gamma\not\!\!E_T$ candidate event is discussed in the next Chapter.

$E_T^\gamma > 12$ GeV Threshold			
Object	Obs.	Exp.	Ref.
$\not\!\!E_T > 35$ GeV	1	0.5 ± 0.1	–
$N_{Jet} \geq 4$, $E_T^{Jet} > 10$ GeV, $\lvert\eta^{Jet}\rvert < 2.0$	2	1.6 ± 0.4	–
Central e or μ, $E_T^{e \text{ or } \mu} > 25$ GeV	3	0.3 ± 0.1	[39]
Central τ, $E_T^\tau > 25$ GeV	1	0.2 ± 0.1	[40]
b-tag, $E_T^b > 25$ GeV	2	1.3 ± 0.7	[39]
Central γ, $E_T^{\gamma 3} > 25$ GeV	0	0.1 ± 0.1	–
$E_T^\gamma > 25$ GeV Threshold			
Object	Obs.	Exp.	Ref.
$\not\!\!E_T > 25$ GeV	2	0.5 ± 0.1	–
$N_{Jet} \geq 3$, $E_T^{Jet} > 10$ GeV, $\lvert\eta^{Jet}\rvert < 2.0$	0	1.7 ± 1.5	–
Central e or μ, $E_T^{e \text{ or } \mu} > 25$ GeV	1	0.1 ± 0.1	[39]
Central τ, $E_T^\tau > 25$ GeV	0	0.03 ± 0.03	[40]
b-tag, $E_T^b > 25$ GeV	0	0.1 ± 0.1	[39]
Central γ, $E_T^{\gamma 3} > 25$ GeV	0	0.01 ± 0.01	–

Table 3.9: The number of observed and expected $\gamma\gamma$ events with additional objects in 85 pb^{-1}. Note that the $ee\gamma\gamma\not\!\!E_T$ candidate event appears in multiple categories.

Chapter 4

The $ee\gamma\gamma\not{E}_T$ Candidate event

"Faith" is a fine invention
When Gentlemen can see -
but microscopes are prudent
In an Emergency.

- Emily Dickenson, 1860

The '$ee\gamma\gamma\not{E}_T$' candidate event, shown in Figure 4.1, consists of two high-E_T photons, a central electron, an electromagnetic cluster in the plug calorimeter with E_T= 63 GeV which passes the electron selection criteria used for Z^0 identification [38], and the largest $\not{E}_T$ ($\not{E}_T$ = 55 $\pm$ 7 GeV) in the diphoton sample. While the event does not have any obvious Standard Model interpretation and could be the first observation of new physics, it could also be due to one or more detection pathologies [72]. A detailed study of the event consequently is important.

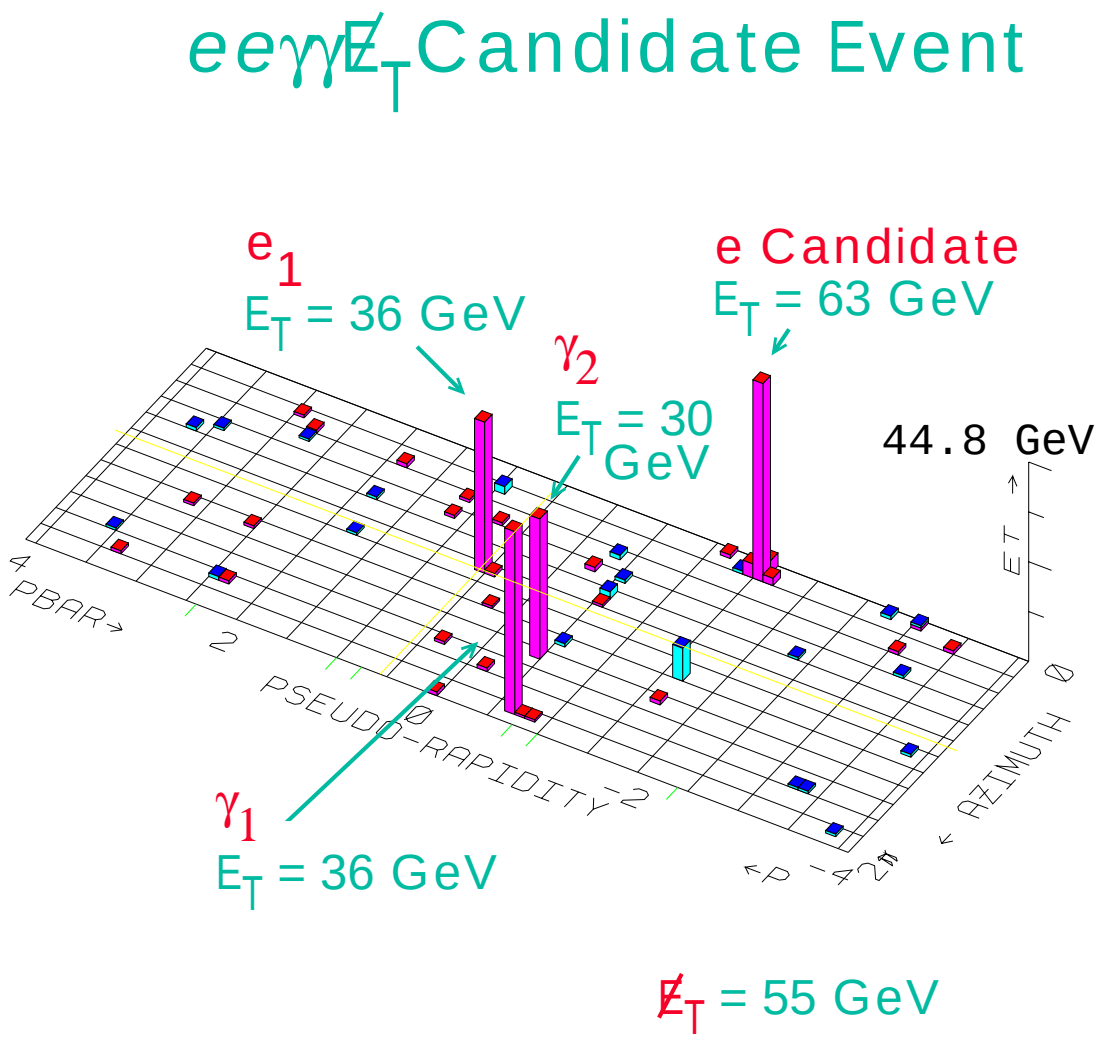

Figure 4.1: An event display for the $ee\gamma\gamma\not{E}_T$ candidate event.

4.1 The $Z^0 \rightarrow e^+e^-$ Control Sample

The characteristics of the $ee\gamma\gamma\not{E}_{\mathrm{T}}$ candidate event are studied using a control sample of 1009 well-measured $Z^0 \rightarrow e^+e^-$ events. Each event in the sample is required to have one electron in the central part of the detector, one electron in the plug calorimeter, and a pair invariant mass within 15 GeV of the Z^0 mass (91 GeV). The requirements are listed in Table 4.1. The distributions in $\mathrm{E_T}$ for the electrons in the sample are shown in Figure 4.2.

Good Run $\lvert z_{\mathrm{vertex}} \rvert < 60$ cm No energy out-of-time with the event
An isolated electron in the central region with $\mathrm{E_T}$ >25 GeV
Plug Electron with: $\mathrm{E_T} > 25$ GeV Fiducial Had/Em<0.05 VTX Occupancy > 0.5 $\chi^2_{\mathrm{3x3}} < 3.0$ $\chi^2_{\mathrm{Depth}} < 15.0$ PES active region $(\chi^2_{\eta\,\mathrm{Strips}} > 0, \chi^2_{\phi\,\mathrm{Strips}} > 0)$ $\mathrm{E_T^{Iso}/E_T} < 0.1$
$76 < \mathrm{M_{e^+e^-}} < 106$ GeV

Table 4.1: The requirements used to select the $Z^0 \rightarrow e^+e^-$ control sample with one electron in the central calorimeter and one electron in the plug calorimeter. The requirements used to select isolated electrons in the central calorimeter are given in Table 2.2 and are the same as those used to identify electrons in the top-quark discovery [39]. The requirements used to select electrons in the plug calorimeter are the same as those used to identify $Z^0 \rightarrow e^+e^-$ decays in the measurement of the ratio $R = \frac{\sigma \cdot Br(\bar{p}p \rightarrow W \rightarrow e\nu)}{\sigma \cdot Br(\bar{p}p \rightarrow Z^0 \rightarrow ee)}$ [38].

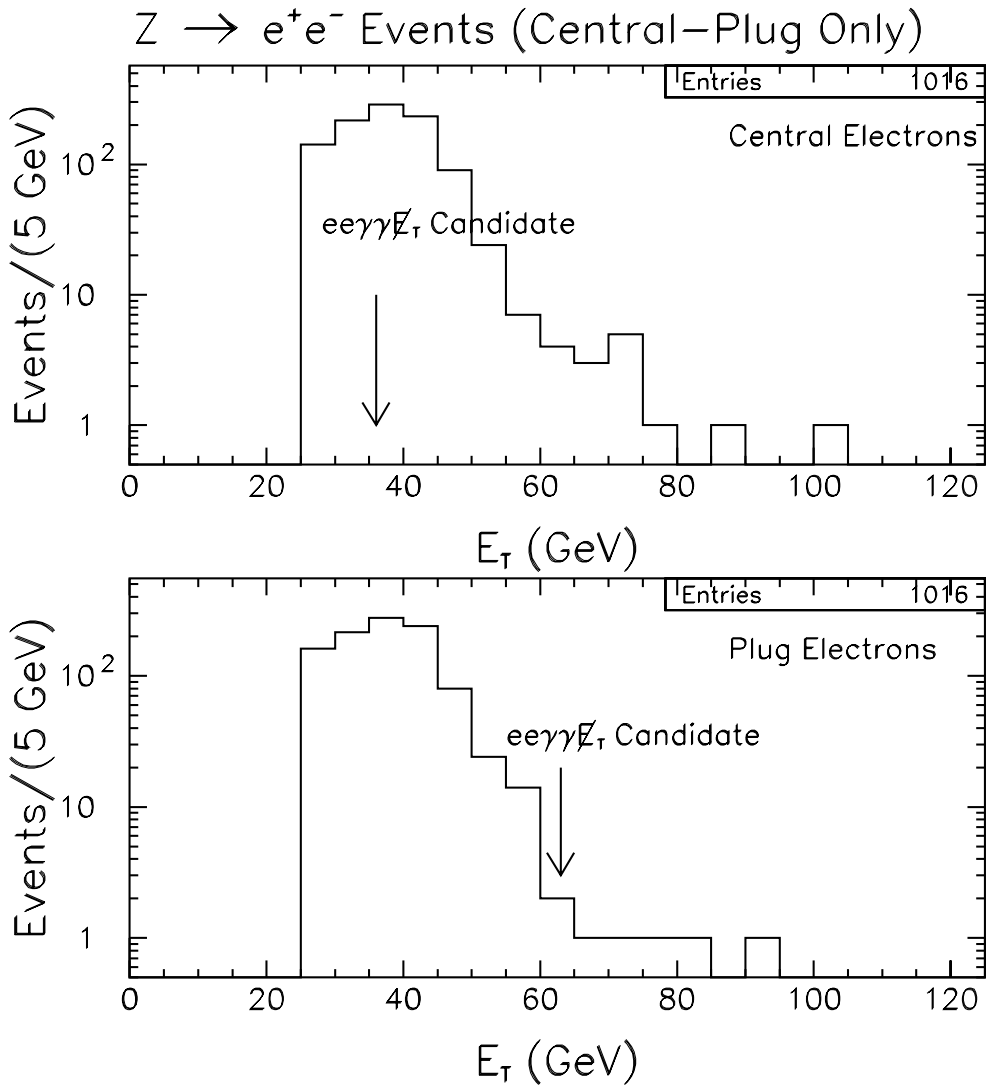

Figure 4.2: The transverse energy of electrons in the central and plug calorimeters in $Z^0 \to e^+e^-$ events. The arrows indicate the measured values of the E_T for the electron candidates in the $ee\gamma\gamma\not{E}_T$ candidate event.

4.2 The Interaction Vertex

The primary vertex [73], determined using the track from the central electron, is situated at $z = 20.4$ cm. The scalar sum of the transverse momentum of the 14 tracks associated with the vertex is 40.6 GeV and includes 31.8 GeV due to the electron in the central calorimeter. Note that since there is no track associated with a photon and the calorimeter has no pointing capabilities, the z position of the vertex for the photons cannot be determined. Similarly, since there is no CTC track for the cluster in the plug calorimeter [74], its vertex cannot be determined.

There are three other vertices in the event which are typical of soft $\bar{p}p$ collisions [75, 76] and are described in Table 4.2. The instantaneous luminosity, $\mathcal{L}$, during this particular part of the run was measured to be $\mathcal{L} = 1.43 \times 10^{31}/\text{cm}^2 \cdot \text{sec}$; at this luminosity there should be, on average, 2.5 primary vertices. Figure 4.3 shows the instantaneous luminosity and number of primary vertices as measured in $Z^0 \rightarrow e^+e^-$ events during the course of the run. There is no indication that the electron candidates, photon candidates or the missing transverse energy are due to anything other than the single $\bar{p}p$ collision which occurred at $z = 20.4$ cm.

4.3 Timing Information

Every tower in the central hadronic calorimeter has timing information associated with any energy deposited. All energy deposited at time t must occur within a window around the nominal collision time, t_0, to be considered 'in time' with the collision. The window is defined by

$$-20 \text{ nsec} < t - t_0 < 35 \text{ nsec}. \tag{4.1}$$

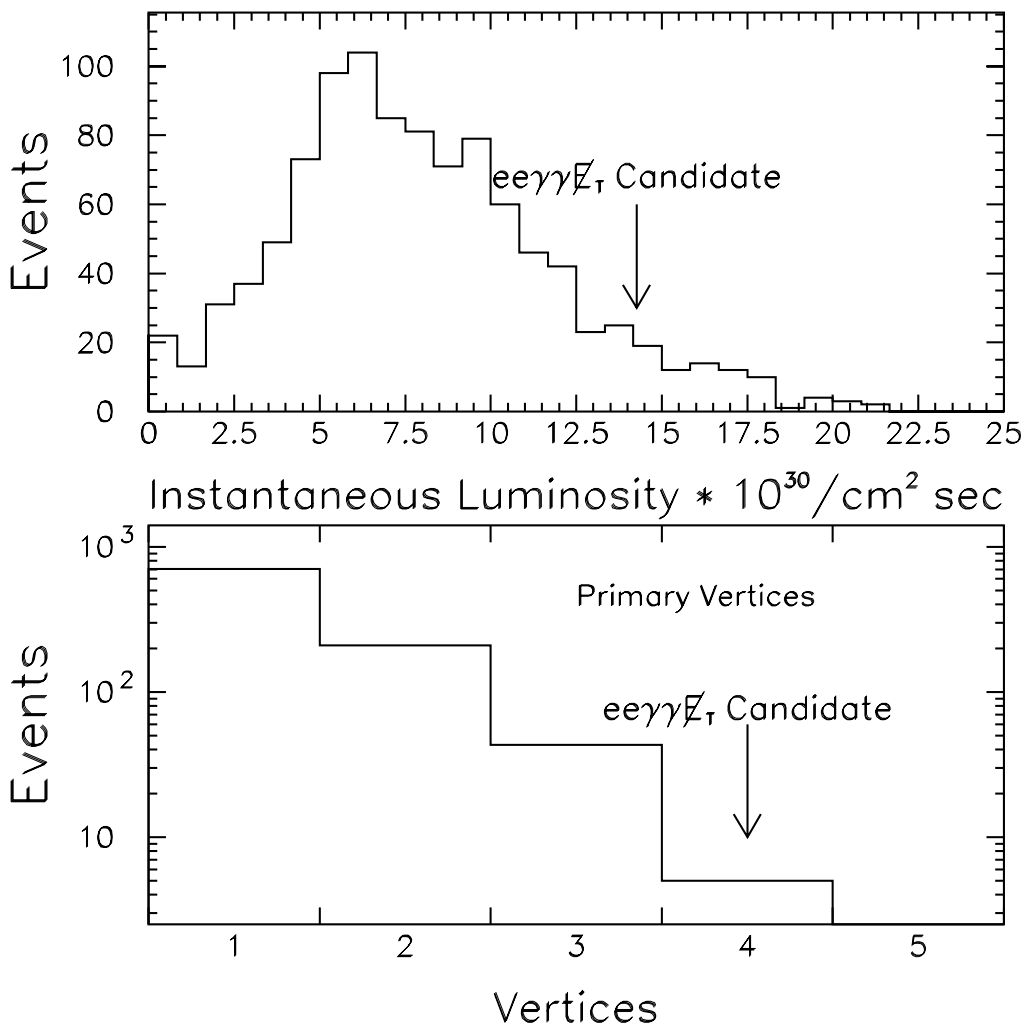

Figure 4.3: The instantaneous luminosity and the number of primary vertices, as measured in $Z^0 \to e^+e^-$ events, during the course of the run. The arrows indicate the values measured in the $ee\gamma\gamma\not{E}_{\mathrm{T}}$ candidate event.

z_{vertex}	ΣP_T of tracks associated with the vertex
20.4 cm	40.6 GeV
-8.9 cm	1.3 GeV
-38.9 cm	5.0 GeV
-33.7 cm	5.4 GeV

Table 4.2: The vertices in the $ee\gamma\gamma\not{E}_T$ candidate event. ΣP_T is the scalar sum of the transverse momentum of tracks associated with the vertex. The primary vertex at 20.4 cm has $\Sigma P_T = 40.6$ GeV which includes the P_T of the central electron. The other vertices are typical of soft $\bar{p}p$ collisions [75, 76]. Note that the last two vertices are not completely independent as they share tracks with a total of 2.03 GeV of ΣP_T.

and is centered at 7.5 nsec, the typical time-of-flight for relativistic particles to travel from the interaction point at the center of the detector to the face of the calorimeter. Any tower with energy deposited outside the timing window might indicate the presence of a cosmic ray interaction in the event. No tower in the $ee\gamma\gamma\not{E}_T$ candidate event has more than 1 GeV of energy deposited outside the timing window.

Timing information for clusters in the central electromagnetic calorimeter can be found if the shower also deposits energy in the hadronic calorimeters [77]. Figure 4.4 shows the timing for central electrons from the $Z^0 \rightarrow e^+e^-$ control sample as well as for a sample of photons from cosmic rays [78]. The electron arrival time distribution is centered at approximately 7 nsec, as expected, and has a time resolution of ≈ 4 nsec. In contrast, cosmic rays have an arrival rate which is flat in time and extends to large times (see Figure 4.4b). In the $ee\gamma\gamma\not{E}_T$ candidate event only the central electron and one of the photons (γ_1 in Table 4.11) have associated timing information [77]. The arrival times of the clusters are measured to be 15 nsec and 18 nsec after the nominal collision time respectively, well within expectations, and consistent

with each other. There is no indication that any of the energy deposited in the event is due to a cosmic ray interaction in the detector.

4.4 The Central Electron

The electron in the central calorimeter passes all the standard electron identification and isolation requirements used in top-quark studies[39]. The measured values of the identification variables as well as the selection criteria are given in Table 4.3.

Requirement	Value
$E_T > 25$ GeV	$E_T = 36.4$ GeV
$E/P < 1.8$	$E/P = 1.15$
$Had/EM < 0.05$	$Had/EM = 0.026$
$Lshr < 0.2$	$Lshr = -0.007$
$\chi^2_{strip} < 10.0$	$\chi^2_{strip} = 2.13$
$\lvert\Delta x_{track-shower}\rvert < 1.5$ cm	$\Delta x = 0.02$ cm
$\lvert\Delta z_{track-shower}\rvert < 3.0$ cm	$\Delta z = -0.50$ cm
$\lvert\Delta z_{vertex-track}\rvert < 5.0$ cm	$\Delta z = 1.31$ cm
$\lvert z_{vertex}\rvert < 60.0$ cm	$z_{vertex} = 20.4$ cm
Fiducial	Yes
$E_T^{Iso}/E_T < 0.1$	$E_T^{Iso}/E_T = 0.02$

Table 4.3: The measured values of the variables used to identify the central electron in the $ee\gamma\gamma\not{E}_T$ candidate event. The selection criteria are those used to identify electrons in the top-quark analyses. For a full description of these variables see Refs.[38, 39].

4.5 The Central Photons

Both photon candidates in the event pass all the selection requirements in Table 2.1. The values of the variables used in the selection, as well as the selection criteria, are shown in Table 4.4. While it is true that the

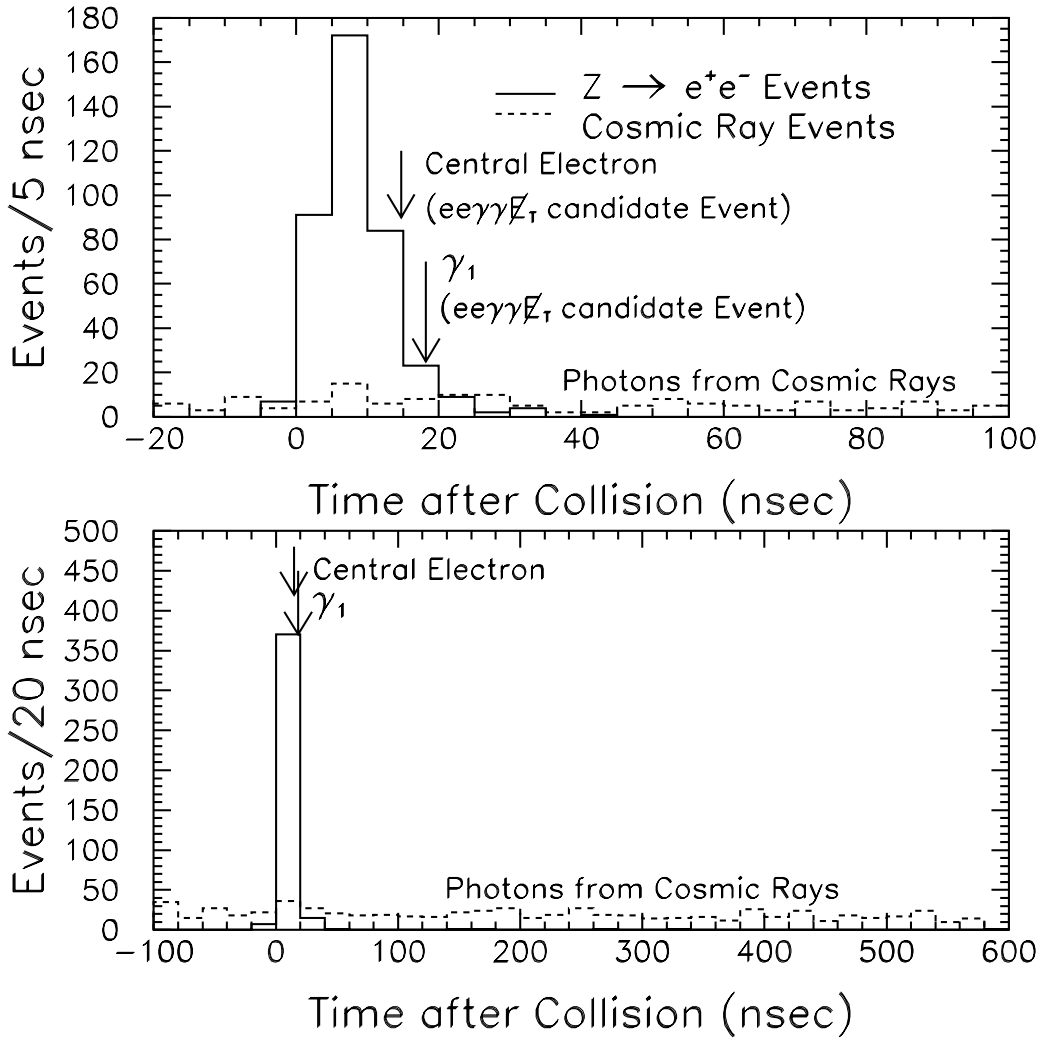

Figure 4.4: The arrival times of electrons and photons at the face of the central hadronic calorimeter from $Z^0 \rightarrow e^+e^-$ events and from a sample of photons from cosmic rays. In the $ee\gamma\gamma\not{E}_{\rm T}$ candidate event only the central electron and one of the photons (γ_1 in Table 4.11) have associated timing information and are indicated by the arrows. There is no indication that any of the energy deposited in the event is due to a cosmic ray interaction in the detector.

purity of the sample is low ($(15 \pm 4)\%$), it is not possible to determine if these photons are directly produced or are from a $\pi^0 \rightarrow \gamma\gamma$ decay except on a statistical basis. The fact that the showers pass the selection criteria (in particular the $\chi^2_{\rm CES}$ and $\sigma_{\rm CES}$ requirements) implies that the showers are consistent with coming from the interaction region.

Photon 1	
Requirements	Value
$E_T > 22$ GeV	$E_T = 36$ GeV
$\leq$1 3D tracks, $P_T < 1$ GeV	# 3D Tracks = 0
$\chi^2_{\rm CES} < 10$	$\chi^2_{\rm CES} = 1.9$
$\lvert\sigma_{\rm CES}\rvert < 2.0$	$\sigma_{\rm CES}$ = -0.29
$E^{\rm cluster}_{\rm 2nd\ strip\ or\ wire} \leq 2.39 + 0.01 \times E^{\gamma}_T = 2.92$ GeV	$E_{\rm 2nd\ Strip} = 0.0$
	$E_{\rm 2nd\ Wire} = 1.4$ GeV
Fiducial [79]	Yes
Had/EM $< 0.055 + 0.00045E = 0.079$	Had/EM $= 0.012$
$E^{\rm Iso}_T/E_T < 0.10$	$E^{\rm Iso}_T/E_T = 0.050$
$\Sigma P_T(\Delta R = 0.4) < 5.0$	$\Sigma P_T(\Delta R = 0.4) = 0.39$
Photon 2	
Requirements	Value
$E_T > 22$ GeV	$E_T = 32$ GeV
$\leq$1 3D tracks, $P_T < 1$ GeV	# 3D Tracks = 0
$\chi^2_{\rm CES} < 10$	$\chi^2_{\rm CES} = 3.9$
$\lvert\sigma_{\rm CES}\rvert < 2.0$	$\sigma_{\rm CES}$ = -1.6
$E^{\rm cluster}_{\rm 2nd\ strip\ or\ wire} \leq 2.39 + 0.01 \times E^{\gamma}_T = 2.76$ GeV	$E_{\rm 2nd\ Strip} = 0.0$
	$E_{\rm 2nd\ Wire} = 1.2$ GeV
Fiducial [79]	Yes
Had/EM $< 0.055 + 0.00045E = 0.072$	Had/EM $= 0.012$
$E^{\rm Iso}_T/E_T < 0.10$	$E^{\rm Iso}_T/E_T = 0.015$
$\Sigma P_T(\Delta R = 0.4) < 5.0$	$\Sigma P_T(\Delta R = 0.4) = 1.7$

Table 4.4: The measured values of the variables used to identify the central photons in the $ee\gamma\gamma\not{E}_T$ candidate event.

4.6 The Missing Transverse Energy

The missing transverse energy in the $ee\gamma\gamma\not{E}_T$ candidate event is measured to be 55 GeV. The uncertainty on this measurement is determined using the resolution parameterization of Section 3.1. The scalar sum of the transverse energy deposited in the calorimeters, ΣE_T, is measured to be $\Sigma E_T = 267.7$ GeV. The majority of the transverse energy ($\approx$ 60%) is deposited in clusters in the electromagnetic calorimeters where the energy resolution is good [80]. The rest of the energy in the calorimeter is unclustered. To use the $\not{E}_T$ resolution method of Chapter 3, the ΣE_T is corrected by subtracting off all the electromagnetic clusters:

$$\begin{aligned} \Sigma E_T^{\text{Corrected}} &= \Sigma E_T^{\text{Measured}} - E_T^{\text{Central e}} - E_T^{\text{Plug Cluster}} - E_T^{\gamma_1} - E_T^{\gamma_2} \qquad (4.2) \\ &= 267.7 \text{ GeV} - 36.3 \text{ GeV} - 63.3 \text{ GeV} - 36.2 \text{ GeV} - 32.3 \text{ GeV} \\ &= 99.6 \text{ GeV} \end{aligned}$$

Using Equation 3.1 yields

$$\begin{aligned} \sigma(\not{E}_T) &= 2.66 \text{ GeV} + (0.043 \times \Sigma E_T^{\text{Corrected}}) \qquad (4.3) \\ &= 2.66 \text{ GeV} + (0.043 \times 99.6 \text{ GeV}) \\ &= 6.9 \text{ GeV} \end{aligned}$$

for a final result of $\not{E}_T = 55 \pm 7$ GeV. There are no jets in the event and all the clusters appear to be well measured. There is no indication that the $\not{E}_T$ is the result of a measurement pathology or due to a cosmic ray interaction.

Because the momenta of the four clusters (the two photons and the two electron candidates) are measured by the electromagnetic calorimeters, the resolution on each is a few per cent. The total P_T of the 4-cluster system is 48 $\pm$ 2 GeV, opposite to the $\not{E}_T$ and in good agreement with the measured

magnitude. This is a further indication that the imbalance is not caused by spurious energy elsewhere in the detector.

4.7 The Electron Candidate in the Plug Calorimeter

The cluster in the plug calorimeter passes all the standard electron identification and isolation selection criteria used for $Z^0 \rightarrow e^+e^-$ identification [38]. In addition it passes all the requirements used to identify electrons in the region of the plug calorimeter used in the top-quark discovery [39, 81]. Table 4.5 and Figure 4.5 show a comparison of the values of the measured variables for the cluster to those of electrons from the $Z^0 \rightarrow e^+e^-$ control sample. The fact that the shower passes the selection criteria (in particular the $\chi^2_{3\text{x}3} = 1.3$ and $\chi^2_{\text{Depth}} = 0.43$ requirements) implies that the shower is consistent with being from a single, isolated electron emanating from the interaction point. However, a closer inspection reveals a possible discrepancy with the electron hypothesis.

4.8 A Problem with the Electron Interpretation

The tracking information along the trajectory between the primary vertex at $z = 20.4$ cm and the cluster in the calorimeter indicates that the cluster is not due to an electron [82]. Figure 4.6 shows the expected path of the particle as it passes through the SVX, VTX and CTC tracking chambers. The standard electron identification selection criteria only use the information from the CTC and VTX detectors. However, in this particular event there is

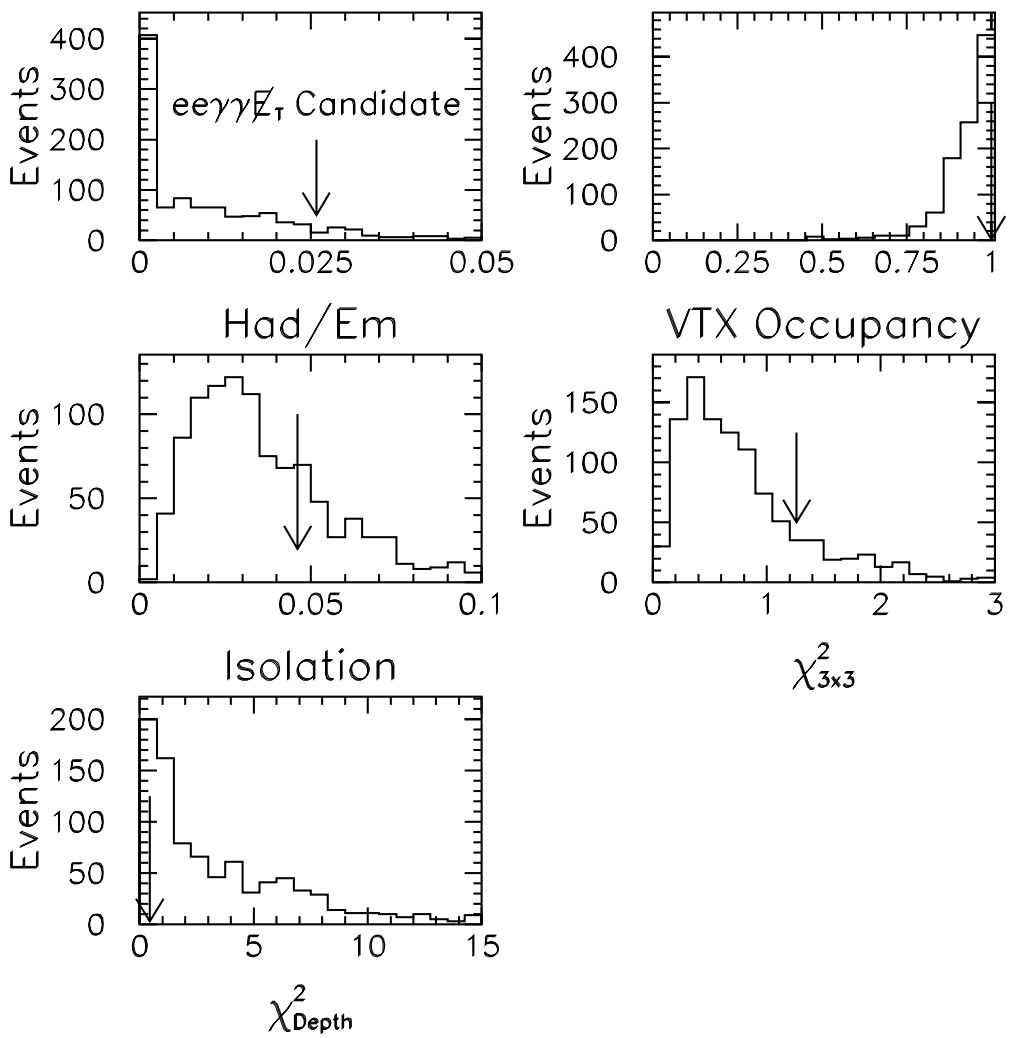

Figure 4.5: The values of the identification variables for electrons in the plug calorimeter from a sample of $Z^0 \rightarrow e^+e^-$ events. The arrows represent the measurement for the cluster in the $ee\gamma\gamma\not{E}_T$ candidate event.

Requirement	Value
$E_T > 25$ GeV	$E_T = 63$ GeV
$\chi^2_{3x3} < 3.0$	$\chi^2_{3x3} = 1.3$
Had/EM < 0.05	Had/EM$= 0.03$
$E_T^{Iso}/E_T < 0.1$	$E_T^{Iso}/E_T = 0.05$
VTX occupancy $> 50\%$	VTX occupancy $= 1.0$
Fiducial	Yes
Additional Selection Criteria used in the top-quark Analysis	
$\chi^2_{Depth} < 15.0$	$\chi^2_{Depth} = 0.43$
3D Track through 3 CTC axial superlayers	# Track $= 0$

Table 4.5: The measured values of the variables used to compare the cluster in the plug calorimeter in the $ee\gamma\gamma\not{E}_T$ candidate event to electrons. The requirements are those used to identify electrons from $Z^0 \rightarrow e^+e^-$ events in the plug calorimeter and are described in Ref. [38]. The additional selection criteria are those used to identify electrons in the top-quark analysis [39].

no expectation of finding a track in the central tracking chamber because the trajectory only passes through the innermost layers [74].

4.8.1 VTX Tracking

The VTX is a system of eight octagonal time projection modules surrounding the beam pipe and mounted end-to-end along the beam direction. For every event detailed $r - z$ tracking, with some ϕ resolution, provides a measurement of the vertex position as well as additional tracking information for individual charged particles. The standard electron identification requirements uses a VTX occupancy measurement which is defined to be the ratio of the number of layers in the VTX in which the electron deposits charge divided by the number of layers in the VTX expected to be traversed by the electron, given the electron's trajectory. For more information on the VTX and electron identification see Refs. [32, 38].

The expected particle trajectory, from the vertex at $z = 20.4$ cm to

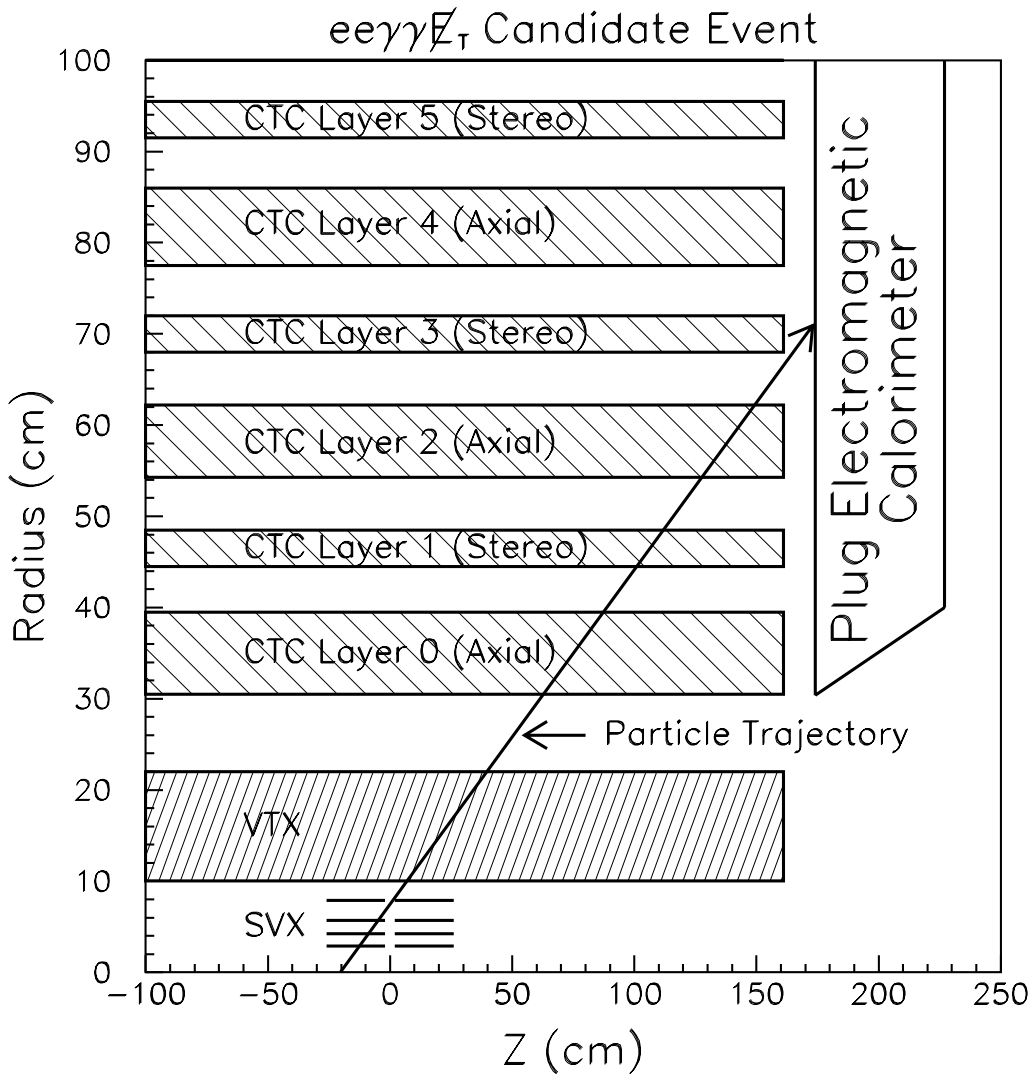

Figure 4.6: The expected trajectory for the cluster in the plug calorimeter as it passes through the SVX, VTX and CTC tracking chambers in the $ee\gamma\gamma\not{E}_{\mathrm{T}}$ candidate event.

the cluster position at $\phi \approx 0.3$ rad, $\eta \approx -1.7$, passes through the fiducial part of the VTX. A total of 7 hits are recorded with 7 hits expected [83] for an occupancy of 100%. Figure 4.7 shows the VTX occupancy as a function of η for ϕ = 0.3 rad, and as a function of ϕ for η = -1.72. There appears to be a charged particle trajectory at the η and ϕ of the cluster. The VTX does not provide a precision measurement of the trajectory and cannot distinguish between single and multiple particles heading in the direction of the cluster in the plug calorimeter. The information is completely consistent with the interpretation of the cluster as an electron.

4.8.2 SVX Tracking

The standard electron identification selection criteria do not use the SVX because the detector is not instrumented outside of the region $|z| < 30$ cm. However, for interactions which occur within $|z| < 30$ cm, the SVX can often be used to provide precision tracking for electrons [84, 85, 86]. The SVX is a single-sided silicon microstrip detector made from 300μm thick silicon wafers. Three wafers are bonded together to form a 25.5 cm long 'ladder' with the strips running lengthwise to provide $r - \phi$ coordinate measurements. Four layers of ladders (numbered 0-3) are placed at radii of 2.86 cm, 4.26 cm, 5.69 cm, and 7.87 cm and arranged in a projective wedge that subtends 30° in ϕ. Twelve wedges form a "barrel"; Two barrels are placed end-to-end along the beam direction to cover the region 1 cm $< |z| <$ 28 cm. The SVX tracking results are described using three different terms: hit, cluster and stub. When a charged particle traverses the SVX it typically deposits energy in 2 or 3 strips per layer. If enough energy is deposited in a strip it is referred to as a 'hit.' A 'cluster' finding algorithm joins the adjacent hits on the layer and determines

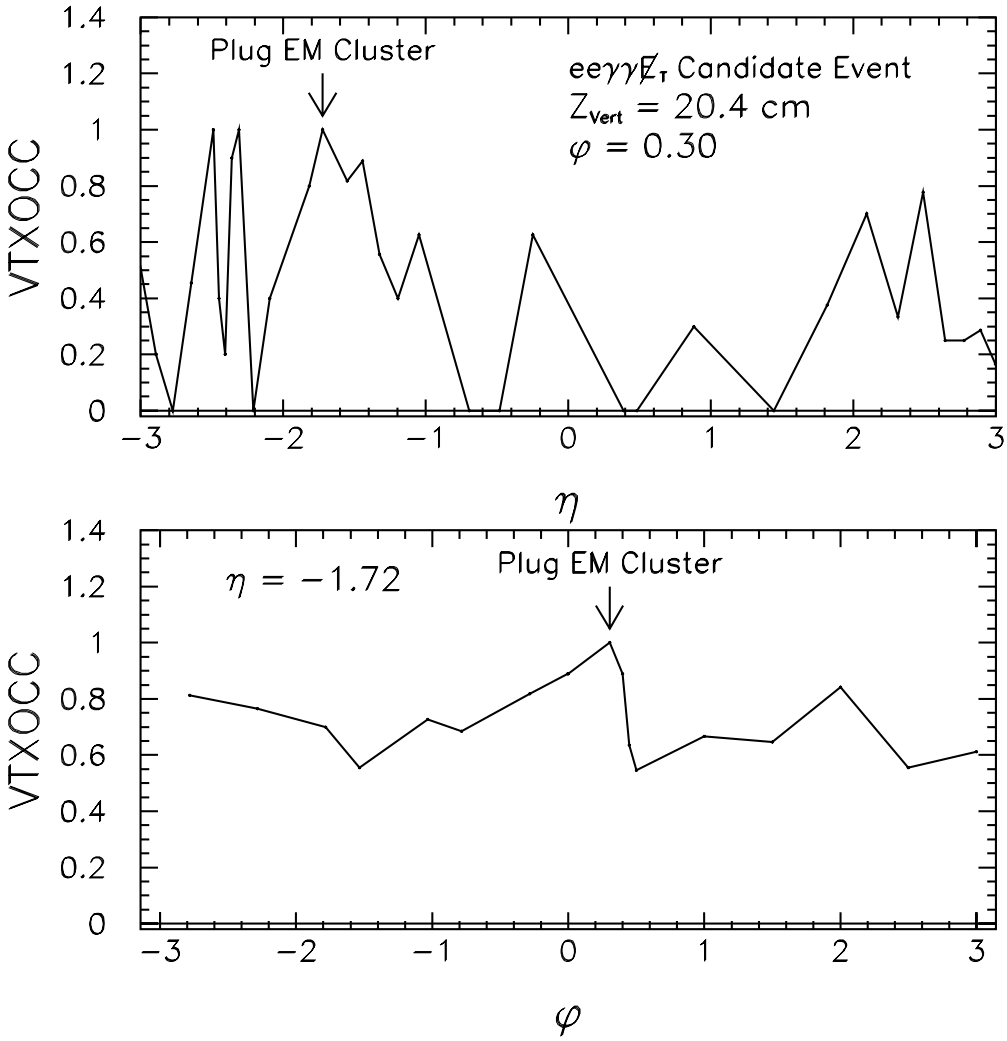

Figure 4.7: The VTX occupancy as measured in the $ee\gamma\gamma\not{E}_{\mathrm{T}}$ candidate event. The trajectory is assumed to come from the vertex at z=20.4 cm.

a mean position with a typical resolution in ϕ of 5-15 mrad as shown in Table 4.7. Joining 3 or more clusters on different layers produces a 'stub' with a typical resolution of 1.5 mrad. For more details on the SVX as well as the stub-finding algorithms see Refs. [33, 34, 84, 85, 86].

The SVX stub-finding algorithm searches for SVX clusters in the region of $\approx \pm 100$ mrad around the ϕ of the electron candidate [86]. Any stub found is required to pass the requirements in Table 4.6 to insure that is well-measured [87, 88]. Figure 4.8 shows the $\Delta\phi$ between the measured ϕ position in the strip chambers (CES and PES respectively) and from the SVX stub for electrons from the $Z^0 \rightarrow e^+e^-$ control sample. Two peaks, corresponding to the bending of positively and negatively charged electrons in the magnetic field, are clearly visible. Any event with large $\Delta\phi$ would be from mismeasured or fake stubs [89].

Cut Description	Requirement
SVX Fiducial	Trajectory must pass through ≥ 3 layers of the SVX $1\text{ cm} < \lvert z^{\text{Layer}}_{\text{Trajectory}} \rvert < 26\text{ cm}$ ≥ 3 layers with clusters
Well Measured	$\chi^2_{\text{SVX}} < 2.0$
Correct η	$80 < Q^{\text{Central}}_{\text{Min}} < 200$ $100 < Q^{\text{Plug}}_{\text{Min}} < 200$

Table 4.6: The SVX stub-finding requirements for electrons. Any stub found by the SVX tracker must pass through the fiducial part of the SVX, be well-measured and be consistent with being from an electron in the central or plug calorimeter. For more detail on the requirements see Ref. [87, 88].

In the $ee\gamma\gamma\not{E}_{\text{T}}$ candidate event, the SVX tracker finds stubs for all four electromagnetic clusters [90]. However, only the central electron and the electromagnetic cluster in the plug have stubs that pass the requirements of Table 4.6. For the electron in the central calorimeter, the $\Delta\phi$ measurement is

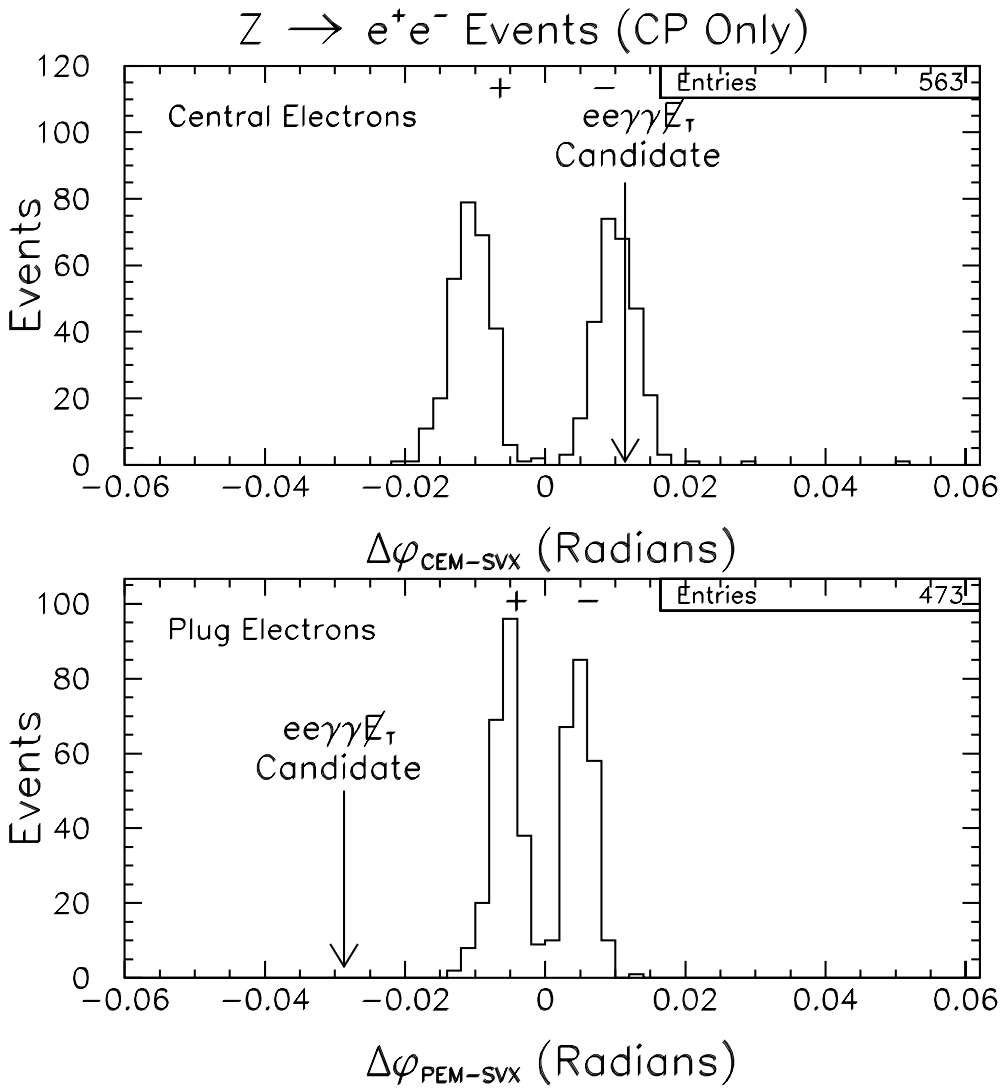

Figure 4.8: The $\Delta\phi$ between the measured electron position from the strip chambers (CES and PES) and the ϕ from the SVX tracker for electrons in the $Z^0 \rightarrow e^+e^-$ control sample. The two peaks correspond to the bending of positively and negatively charged electrons in the magnetic field.

consistent with the negative charge determination from the track in the central tracking chamber as shown in Figure 4.8.

Barrel	Layer	Length	Radii (cm)	ϕ (radians)
$z > 0$	1	3	4.3962	0.313±0.008
$z > 0$	3	5	7.9866	0.249±0.063
$z > 0$	3	6	7.9880	0.258±0.076
$z < 0$	0	2	2.8679	**0.269±0.003**
$z < 0$	0	3	2.8672	0.319±0.005
$z < 0$	1	3	4.2803	**0.267±0.008**
$z < 0$	2	3	5.7165	**0.267±0.011**
$z < 0$	3	3	7.8823	0.306±0.015

Table 4.7: A list of all good SVX clusters with 0.23 rad$< \phi <$ 0.33 rad in the $ee\gamma\gamma\not{E}_{\mathrm{T}}$ candidate event. 'Length' is the number of SVX hits in the cluster. The clusters found by the SVX stub-finding algorithm for the cluster in the plug are in boldface.

The stub found by the SVX tracker for the cluster in the plug is problematic. The $\Delta\phi$ between an SVX stub and the measured position in the PES, due to bending in the magnetic field, is expected to be -2.6 mrad for a 63 GeV positron. The position, in ϕ, of the electromagnetic cluster as measured by the strip chambers in the plug calorimeter (PES) is $\phi_{\mathrm{PES}} = 0.2940$ rad. There are no SVX clusters in the region 0.29 rad $< \phi <$ 0.30 rad in either SVX barrel as seen in Figure 4.9 and Table 4.7. However, the algorithm does pick up a three-cluster stub near the expected path which is in the barrel with $z < 0$ (as would be expected for the trajectory [91]). The stub appears to be well measured, $\chi^2_{\mathrm{SVX}} = 0.54$ and $Q_{\mathrm{Min}} = 145$, but has $\phi_{\mathrm{SVX}} = 0.2654$ rad for $\Delta\phi = -29$ mrad which would be very unusual for an electron; again see Figure 4.8.

The non-observation of an SVX stub with the correct $\Delta\phi$ is very unusual for an electron [92]. While a malfunction in the PES would be an appealing explanation [82], there is no indication of a ϕ mismeasurement in the calorimeter. Table 4.8 lists all the bad strips in the SVX in the region

0.23 rad $< \phi <$ 0.33 rad. Note that the trajectory passes very near (or at) a dead strip in barrel 1 (z <0), layer 0, and could cause the loss of a cluster. Also note that for layer 1, the trajectory passes near a gap between silicon crystals at z = 9.6 cm. These could possibly account for two of the three missing clusters. The SVX cluster finding efficiency is $\approx$ 95% due almost entirely to dead strips and gaps between crystals. With that efficiency, the average probability to miss all three clusters is 1.4×10^{-4}; however if the true trajectory passes through the two bad regions, the probability of also losing the third cluster is only less than about 1% [93].

Barrel	Layer	ϕ	Strip Width
$z < 0$	2	0.2373	0.0010
$z < 0$	3	0.2410	0.0007
$z > 0$	0	0.2606	0.0021
$z > 0$	0	0.2962	0.0021
$z > 0$	3	0.3225	0.0007
$z > 0$	3	0.3246	0.0007
$z > 0$	3	0.3232	0.0007
$z > 0$	3	0.3239	0.0007

Table 4.8: A list of all the bad strips in the SVX in the region 0.23 rad $< \phi <$ 0.33 rad. The strip width is the angle, in radians, subtended by the physical strip width.

Another quantity of interest is the impact parameter of the stub with respect to the position of the collision. Prompt electrons should have an impact parameter which is consistent with zero within resolution. The distribution in the impact parameter of stubs associated with central and plug electrons from $Z^0 \rightarrow e^+e^-$ events is shown in Figure 4.10 along with the results for the electron candidates in the $ee\gamma\gamma\not{E}_{\mathrm{T}}$ candidate event. While the stub associated with the central electron has a small impact parameter (46 $\pm$45) μm, the stub at $\phi = 0.265$ rad has a large value, 90$\pm$45 μm, which is on the tail of the

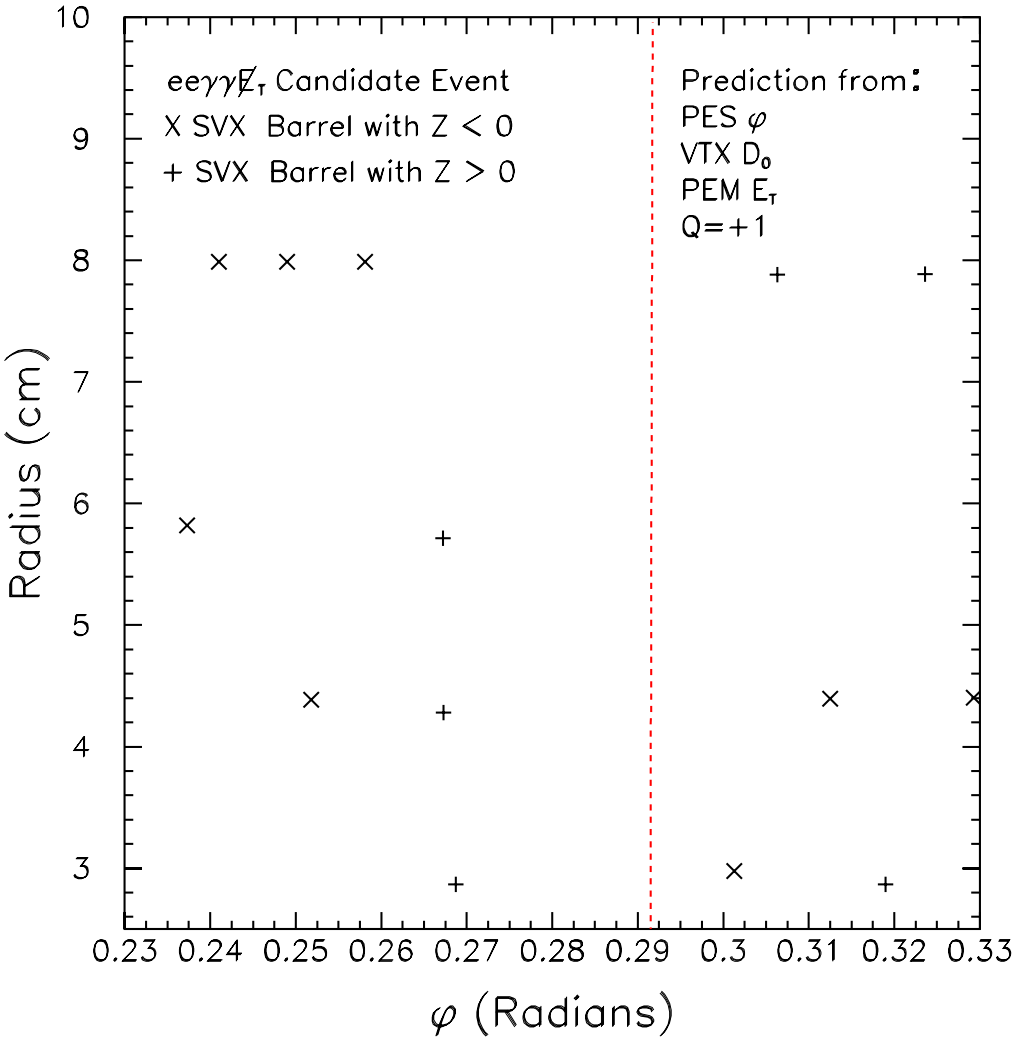

Figure 4.9: The positions of the SVX clusters with 0.23 rad $< \phi <$ 0.33 rad. The dashed line is the expected trajectory from the primary vertex to the cluster in the plug calorimeter using the measured cluster position and E_T.

distribution but not inconsistent with the prompt hypothesis. Note that the impact parameter measurement is highly dependent on whether or not the ϕ position and energy information from the calorimeter is used [94]; if the stub is unrelated to the cluster, removing the calorimeter information from the tracking algorithm can change the mean value of the impact parameter, as well as its uncertainty, by an order of magnitude [95].

The tracking information is confusing and would be highly unusual for an electron (no others like it are found in the sample of 1009 well-measured plug electrons). Since there is no associated track in the central tracking chamber, it is not obvious that the stub has anything to do with the cluster in the calorimeter. Since there are no other large energy clusters in the $\eta - \phi$ region suggested by the stub, either this is an SVX or PES failure, or the stub is due to a low $\mathrm{P_T}$ charged particle which is not seen in the calorimeter. Based on the $|\Delta\phi|$ distribution of the $Z^0 \rightarrow e^+e^-$ events, the probability that this observation is due to an electron is estimated to be less than 0.3% at 95% C.L.

4.9 Interpreting the Electromagnetic Cluster

To summarize, the relevant experimental facts about the electromagnetic cluster in the plug calorimeter in the $ee\gamma\gamma\not{E}_{\mathrm{T}}$ candidate event are:

1. The cluster easily passes all the standard electron identification selection criteria.

2. There are no SVX clusters in the region 0.29 rad $< \phi <$ 0.30 rad and 3 are expected. There is a bad SVX strip in layer 0 and a gap in the coverage in layer 1 which may lie along the trajectory and cause clusters to be lost. There is a high quality SVX stub which is near the expected

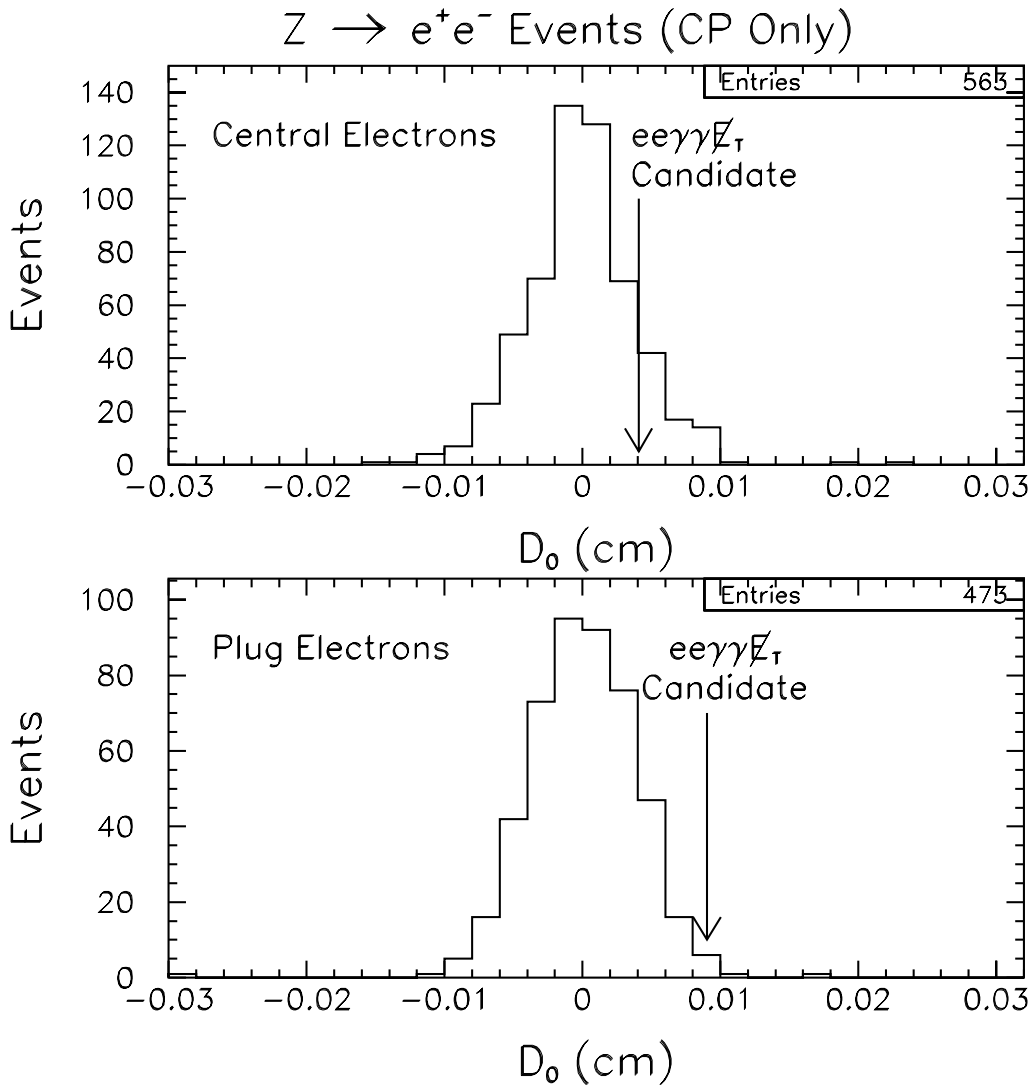

Figure 4.10: The measured impact parameter from the SVX tracker for electrons from $Z^0 \to e^+e^-$ events. The central electron in the $ee\gamma\gamma\not{E}_T$ candidate event has an impact parameter of $46\pm45\mu$m. The nearest SVX stub to the ϕ of the cluster in the plug electromagnetic calorimeter has an impact parameter of $90\pm45\mu$m. Both are consistent with zero within resolution.

trajectory, but is not necessarily correlated with the plug cluster. The stub is well measured [88] and appears to be due to a charged particle traveling at an η consistent with the cluster. However, the probability for an electron to have $|\Delta\phi| > 0.03$ rad between the stub and the cluster is estimated to be less than 0.3% at 95% C.L.

3. Assuming the energy and position of the plug cluster are due to the particle which made this stub, the best fit impact parameter of the SVX stub is $90 \pm 45 \mu$m. While this is not inconsistent with the prompt electron hypothesis (a 2σ deviation), the result is highly dependent on the calorimeter information [95]. If the calorimeter information is removed from the SVX track finding algorithm, the impact parameter information becomes inconclusive.

4. The VTX occupancy indicates that there is at least one charged particle traveling in the direction of the PEM cluster (this could be the track associated with the SVX stub).

The above list indicates that while many of the measurements of the cluster are consistent with an electron emanating from the primary interaction, some are inconsistent. One possibility is that the stub or cluster come from separate $\bar{p}p$ interactions. Another possibility is that the cluster is due to an unusual interaction of the electron with the detector. A third possibility is that the cluster is due to a different type of particle such as a photon with a nearby particle from underlying event, a hadronic τ decay, or a hadronic jet which faked the electron signature. These possibilities are discussed in the next Sections.

4.9.1 Two Interactions

One possibility is that the cluster or the SVX stub comes from a different $\bar{p}p$ interaction. As a check, the VTX and SVX results are investigated using the other vertices in the event; the results are summarized in Table 4.9. The trajectory from a vertex to the plug passes through the SVX fiducial region for only one other vertex; there are no stubs associated with it. The VTX occupancy along the trajectories from the other vertices do not indicate a better choice. There is no indication that the stub or cluster is from a different vertex [76].

Vertex (cm)	SVX Clusters (Exp/Obs)	D_0 (μm)	VTX Occ (Exp/Obs)
20.4	3/3	90±45	7/7
-8.9	3/0	-	9/3
-38.9	0/-	-	10/7
-33.7	0/-	-	10/4

Table 4.9: The VTX and SVX results assuming the cluster in the plug comes from a different vertex in the event. Due to the cluster position in the plug calorimeter, only vertices with -13 cm $< z_{\rm vert} <$ 38 cm could give three or more clusters in the SVX.

4.9.2 Anomalous Electron Detection

Since all evidence, with the exception of the SVX information, is consistent with the single isolated electron hypothesis it is instructive to consider reasons that a large mismatch might exist for real electron candidates [96]. For example, the electron could have emitted an energetic photon, via Bremstrahlung, while traversing the detector, or the electron could have had an elastic scattering with a nucleus. If the photon emission or collision occurs after the electron leaves the SVX, then there should be at least two final state

particles and the SVX stub should, by conservation of momentum, point to the energy-weighted mean of the energy deposition in the calorimeter (within the expected resolution and bending due to the magnetic field). No evidence for a second cluster is seen in the calorimeter [82]. If the photon emission occurs before the electron reaches the SVX, then the initial direction of the electron must have been directly toward the center of the electromagnetic cluster (again by conservation of momentum). In this case the SVX stub is due to the electron going off with low momentum, and the electromagnetic cluster is due to the photon. However, the impact parameter would be roughly 5 times that observed [96]. A final scenario is that the photon emission or collision occurs in the SVX. If this were the case, there should be a deviation, or kink, along the trajectory defined by the SVX hits and the primary vertex. No such occurance is seen.

4.9.3 Photonic Interpretation

Since electrons and photons will interact with the calorimeter in similar ways, the cluster could be a photon with a nearby, but unrelated, charged particle. Figure 4.7 shows that while the occupancy in the VTX has a local maximum at $\phi = 0.3$ rad, it is above 0.5 for all values of ϕ. Thus, even if the SVX stub is due to an unrelated, low-momentum charged particle that causes the local maximum in the VTX, the cluster would, by a side band estimate, still not pass any reasonable photon VTX occupancy requirement. To estimate the probability that the SVX tracker might find a stub unrelated to the cluster in the plug, the SVX stub-finding algorithm is used. Instead of using the ϕ position of the cluster, the ϕ is varied between 0 and 2π in increments of 0.01 rad. Table 4.10 lists all SVX stubs found using this procedure that pass

the selection criteria in Table 4.6. A total of 8.4% of ϕ space has a good stub of which 1.8% is due to the stub at $\phi = 0.265$ rad. It is not improbable to find an unrelated stub or high VTX occupancy in this event.

Another way to estimate the probability for a photon to have an SVX stub and high VTX occupancy is to use the central photon sample from Chapter 2 but with the additional requirement of $E_T^\gamma > 20$ GeV. There are 268 events in the sample for a total of 536 photons. Figures 4.11 and 4.12 show the $\Delta\phi$ and VTX occupancy distributions for the photons in the sample. A total of 277 photons pass through the fiducial region of the SVX, 16 have an SVX stub which pass the requirements in Table 4.6, and 6 have $|\Delta\phi| > 0.03$ rad ($\approx 2\%$). A total of 58 of the 536 photons have a VTX occupancy of greater than 50% ($\approx$ 10%). The bottom part of Figure 4.12 shows that most of the photons with a stub have very low VTX occupancy. No event with $|\Delta\phi|$ >0.03 rad has a VTX occupancy greater than 0.5 indicating that there is no correlation (at low statistics) between large VTX occupancy and large $|\Delta\phi|$ [97]. While the cluster could be due to a photon with a soft track nearby, it is an unusual example as estimated by the diphoton sample, and the hypothesis cannot be proved or excluded.

4.9.4 Hadronic τ decay

The cluster could be due to the hadronic (1-prong) decay of a τ lepton. For example, the decay $\tau \rightarrow \pi^+\pi^0\nu_\tau$ produces a π^+ which could generate the SVX stub and VTX occupancy, and a π^0 which decays via $\pi^0 \rightarrow \gamma\gamma$ and could generate a calorimeter cluster that is largely electromagnetic energy and that passes the remaining electron identification selection criteria. However, as shown below, most hadronic τ decays will not shower predominantly in

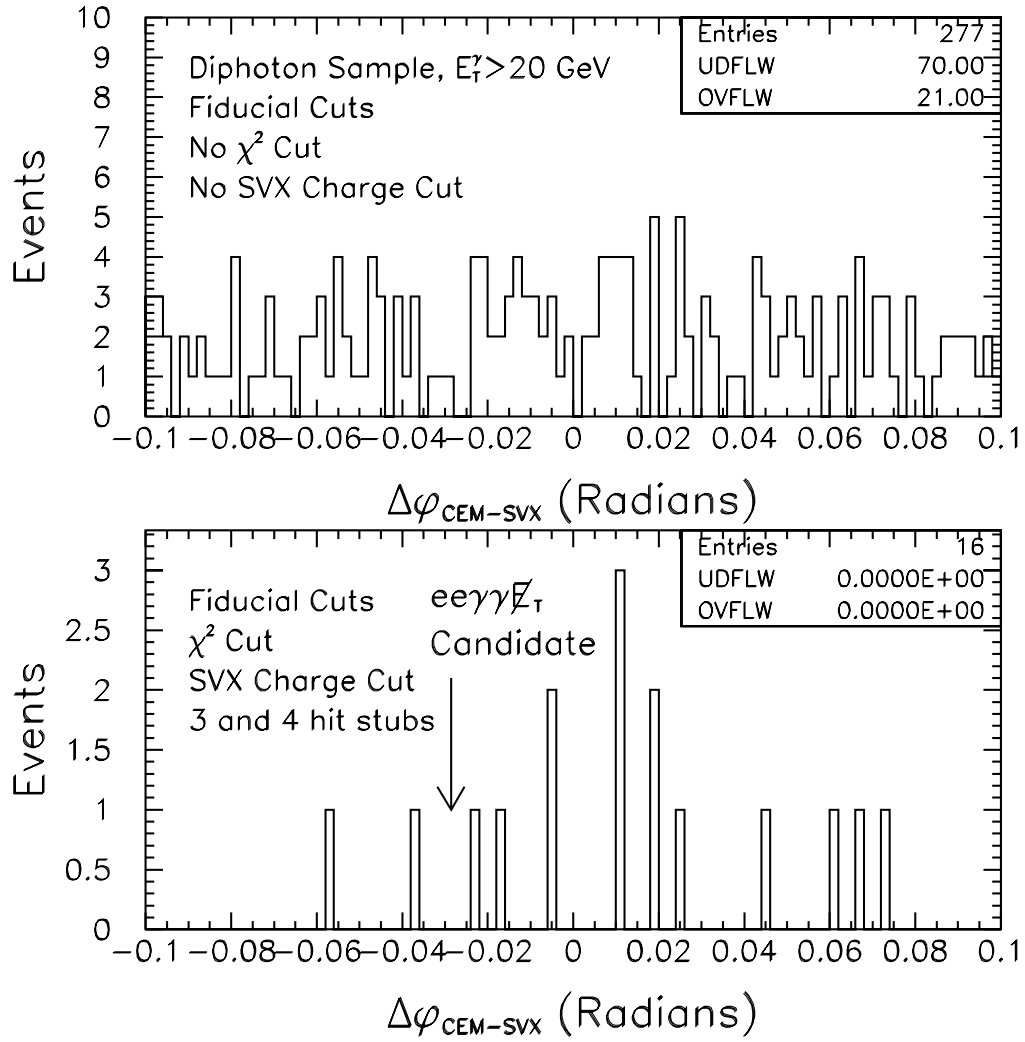

Figure 4.11: The $\Delta\phi$ between the measured photon position and the stub found by the SVX tracker for a sample of central photons. A total of 277 photons in the sample pass through the fiducial region of the SVX, 16 of which have a stub found by the SVX tracker that passes the requirements in Table 4.6. Only 6 photons have a stub with $|\Delta\phi|$ >0.03 rad.

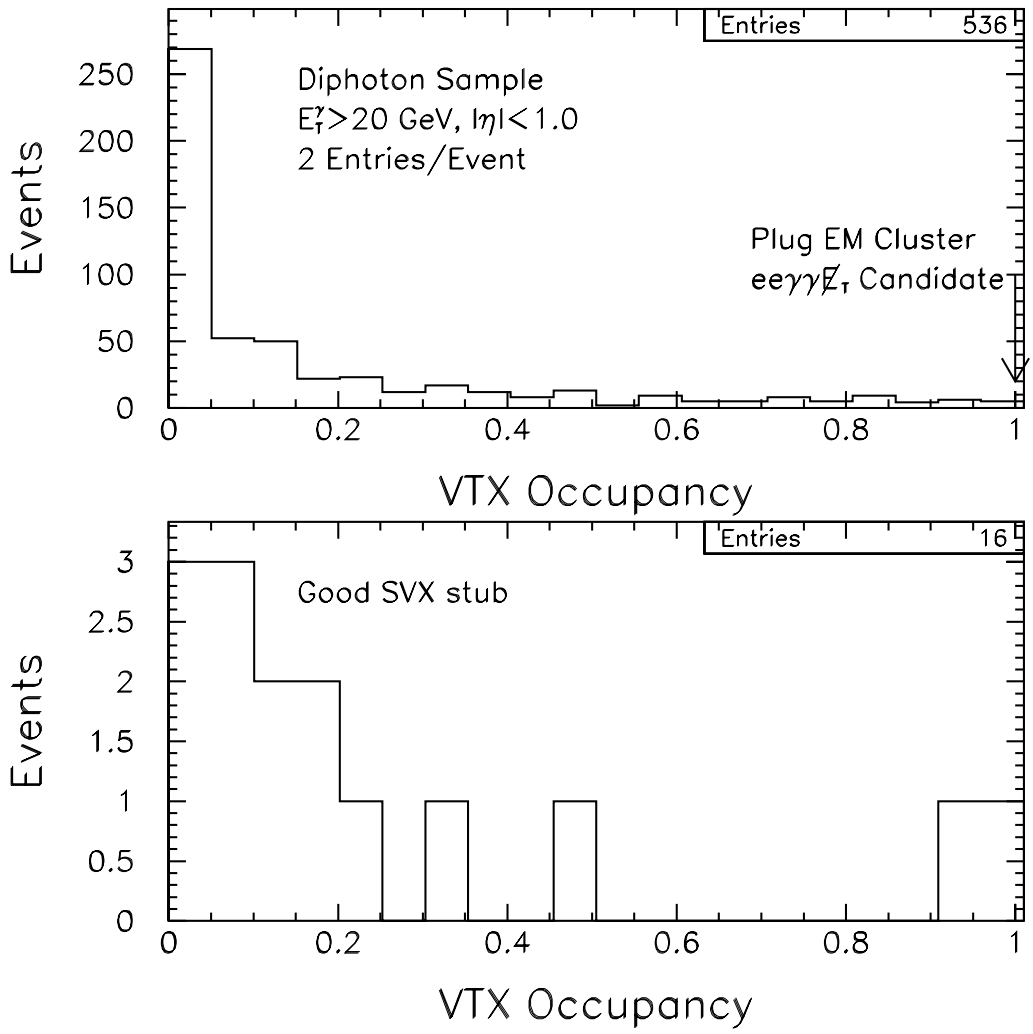

Figure 4.12: The VTX occupancy of photons with $E_T > 20$ GeV in the diphoton sample. Note that 58 of the 536 photons have a VTX occupancy of greater than 50%. The lower plot shows the VTX occupancy for photons which have an associated stub found by the SVX tracker.

ϕ_{Stub}	$\lvert\Delta\phi\rvert$
0.2654	0.11
0.4695	0.14
1.990	0.16
2.682	0.05
3.469	0.07
	$\Sigma\Delta\phi = 0.53$
	$\frac{\Sigma\Delta\phi}{2\pi} = 8.4\%$

Table 4.10: Other SVX stubs in the $ee\gamma\gamma\not\!\!E_{\text{T}}$ candidate event found using the SVX stub-finding algorithm. To find stubs, the η of the cluster was used, but the ϕ was allowed to vary between 0 and 2π in increments of 0.01 rad. All stubs are required to pass the requirements in Table 4.6. The $|\Delta\phi|$ is a measure of the region in which the stub is found by the SVX tracker and passes the selection criteria.

the electromagnetic calorimeter. The cluster in the event deposits roughly 180 GeV in the electromagnetic calorimeter and only 5 GeV in the hadronic calorimeter. The probability that a τ might fake the electron signature, but not be from the $\tau \rightarrow e\nu\nu\nu$ decay chain, is estimated using a Monte Carlo to simulate a sample of τ's with a one-prong decay (excluding the electron and muon decays) interacting with the plug calorimeter [54, 98]. Unfortunately, the standard CDF detector simulation does not correctly model the VTX occupancy or the χ^2 variables in the calorimeter or strip chambers in the plug, each of which provide rejection against the hadronic decays. To avoid an underestimate of the probability, the simulated cluster is not required to pass these requirements. The top part of Figure 4.13 shows the electromagnetic fraction of the energy of clusters produced by the τ. The rate at which τ events pass the Had/EM and calorimeter isolation selection criteria (corrected for the 50% one-prong branching fraction [4]) is plotted in the bottom of Figure 4.13 as a function of the ratio of reconstructed cluster energy to the original τ energy.

For most of phase space the fake rate is flat, typically around 3%; however at the end points it rises to almost 10%.

While the cluster in the PEM could be due to the hadronic decay of a τ, and there is no evidence to the contrary, this would be an unusual example as estimated by the Monte Carlo. Furthermore, it would significantly change the interpretation and kinematics of the event [99]. Ignoring additional tracking information from the SVX and VTX, as well as potential rejection power from the calorimeter, the probability of a τ to pass the electron selection criteria is conservatively estimated to be less than a few percent per τ.

4.9.5 Jet Interpretation

A jet associated with the event, either as part of the partonic process or from initial or final state radiation, could fluctuate to pass all the electron selection criteria. The rate at which a jet passes the electron selection criteria is estimated using a method similar to that in the τ analysis in Chapter 3 [40, 71, 100]. The fake-rate per jet is consistent with being a constant for jets with $E_T > 25$ GeV with a probability of approximately 2.2×10^{-3}/jet. Thus, although the cluster could be due a jet which fluctuated to pass the electron selection criteria it would be an unusual example.

4.9.6 Conclusion

Although the cluster passes all of the standard electron selection criteria, the tracking information provides evidence that the cluster is not due to an electron. The cluster could be interpreted as a photon, the hadronic decay of a tau lepton, or simply as a jet. While all three scenarios are reasonable *a priori*, and are consistent with the facts, each is unlikely in that this would

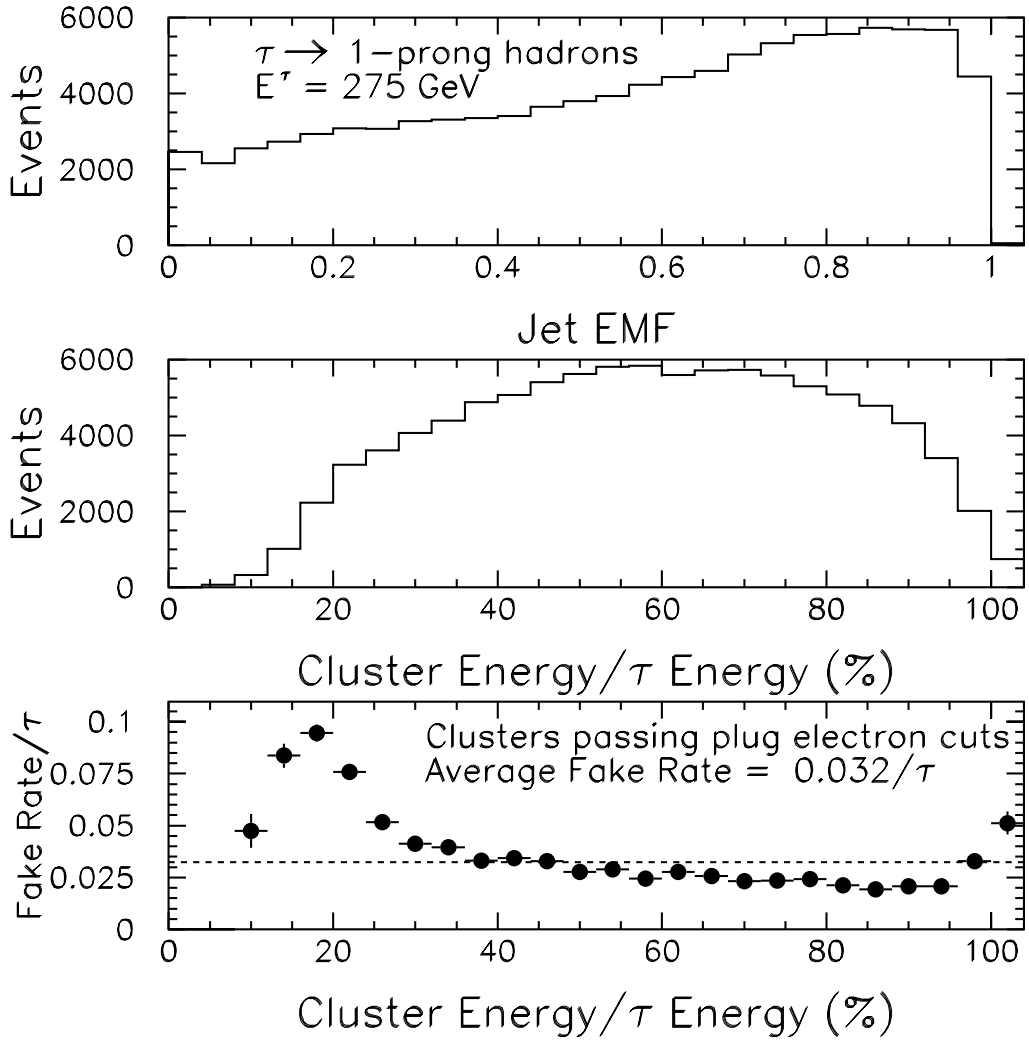

Figure 4.13: A Monte Carlo simulation of one-prong hadronic decays of a τ interacting with the plug calorimeter. The electromagnetic fraction (EMF) of the energy deposited in the electromagnetic and hadronic calorimeters is shown in the top plot. The measured cluster energy as a fraction of the true energy of the τ is shown in the middle plot. The rate at which τ events pass the Had/EM and isolation selection criteria (corrected for the 50% one-prong branching fraction) as a function of ratio of reconstructed cluster energy to original τ energy is shown in the bottom plot.

be an unusual example of any of them. There simply is not enough information to establish the origin of the cluster.

4.10 A Study of the Kinematics of the Event

A study of the kinematics of the $ee\gamma\gamma\not{E}_T$ candidate event is potentially useful in helping understanding its origin. The energies and momenta are given in Table 4.11. There are no additional jets with $E_T^{Corrected} > 10$ GeV. Figure 4.14 shows the $\not{E}_T$ of the system if the energy of the cluster in the plug calorimeter were mismeasured. For simplicity, the cluster is denoted as e, and in the plot, M_{ee} is plotted vs. $\not{E}_T$ for different correction factors, C, such that $E_{used} = C \times E_m$easured. The $\not{E}_T$ cannot be reduced below 25 GeV for any value of C. While the value of the $\not{E}_T$ is at a local minimum for $M_{ee} \approx M_{Z^0}$, where $\not{E}_{T_{min}} = 26.6$ GeV, it would mean that a particle (or particles) with 51 GeV ($\sigma = 2$ GeV) of electromagnetic energy was mismeasured as having 183 GeV of energy.

Run 68739, Event 257646					
	P_x (GeV/c)	P_y (GeV/c)	P_z (GeV/c)	E (GeV)	E_T (GeV)
γ_1	32.1(9)	-16.8(5)	-35(1)	50(1)	36(1)
γ_2	-12.9(4)	-29.6(9)	-22.5(7)	39(1)	32.3(9)
e^-	-34(1)	11.5(3)	21.7(6)	42(1)	36(1)
Plug EM Cluster	60(2)	19.0(5)	-172(5)	183(5)	63(2)
$\not{E}_T$	-54(7)	13(7)	—	—	55(7)

Table 4.11: The 4-vectors of the electron and photon candidates and the missing transverse energy in the $ee\gamma\gamma\not{E}_T$ candidate event. The parentheses represent the uncertainty in the last digit and are as determined in Chapters 2 and 3 [32, 80]. There are no additional jets with $E_T^{Corrected} > 10$ GeV.

Table 4.12 lists the masses and transverse momentum for various

combinations of the clusters in the event. One of the most interesting combinations is the $e_{\rm central}\gamma_2$ combination which has an invariant mass of 91.7 GeV/c^2 and a $\rm P_T$ of 4.1 GeV. While this could be a Z^0 where one electron faked the photon signature (there is no track or SVX stub pointing at the photon) this would be unusual, as estimated in Section 3.3. Table 4.13 lists the calculated transverse masses for various combination of the clusters and the $\not\!\!E_{\rm T}$. While the $e_{\rm central}\not\!\!E_{\rm T}$ combination is inconsistent with the decay of a W via $W \rightarrow e\nu$ (it has $\rm M_T = 4.3$ GeV/c^2) the $e_{\rm central}\gamma_1\not\!\!E_{\rm T}$ combination could be the radiative decay of a W via $W \rightarrow e\nu\gamma$ ($\rm M_T = 70.4$ GeV/c^2).

While part of the event may be due to leptonic or radiative decays of W and/or Z^0 bosons, the interpretation of the event is not obvious. Furthermore, the kinematics do not suggest any obvious indication that the event is due to two overlapping events.

4.11 Conclusions

After a detailed study of the $ee\gamma\gamma\not\!\!E_{\rm T}$ candidate event, the conclusion appears to be that it originates from a single $\bar{p}p$ collision and consists of a high quality isolated electron, two isolated photons in the central calorimeter, significant $\not\!\!E_{\rm T}$, and an electromagnetic cluster in the plug calorimeter with a problematic interpretation. While the cluster passes all of the standard electron selection criteria, further investigation reveals its interpretation is not obvious. The tracking chambers indicate that there is clearly a charged particle (or particles) traveling in the direction of the cluster but not directly at it, indicating that the cluster might not due to an electron. The cluster could be interpreted as a photon, the hadronic decay of a tau lepton, or simply as a jet. While all of three scenarios are reasonable *a priori*, and are consistent

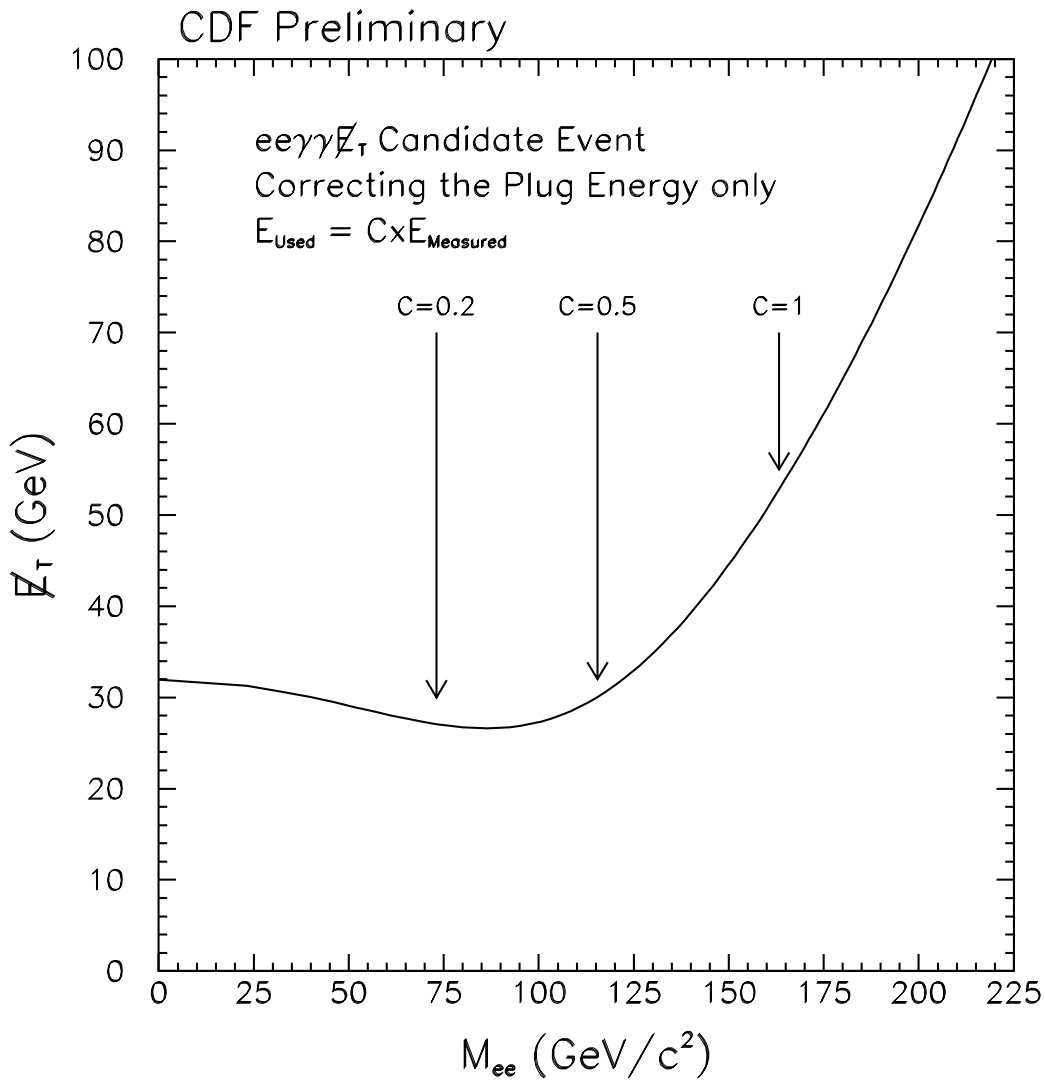

Figure 4.14: The invariant mass of the cluster in the plug calorimeter, here denoted as an e, and the electron in the central calorimeter (M_{ee}) plotted vs. the $\not\!\!E_T$ as the energy of the cluster in the plug is varied. Note that the minimum value of the $\not\!\!E_T$ is 26.6 GeV and occurs when M_{ee} is close to the Z^0 mass ($M_{ee} = 86$ GeV). However, this requires a correction factor of C = 0.28. The mass of the ee pair is equal to the mass of the Z^0 when the correction factor is C = 0.31, and results in $\not\!\!E_T = 26.7$ GeV.

Objects	M^{System} (Gev/c^2)	P_T^{System} (Gev)	$\not{E}_T$ (GeV)	$\phi_{(\not{E}_T)}$ (degrees)	H_T (Gev/c^2)
$e_{plug}e_{central}\gamma_1\gamma_2$	232.4	48.1	52.8	167.2	221.2
$e_{plug}\gamma_1\gamma_2$	121.8	84.4	89.0	164.9	221.1
$e_{central}\gamma_1\gamma_2$	121.4	38.2	32.0	73.8	137.0
$e_{plug}e_{central}\gamma_1$	200.4	13.1	20.0	194.9	152.0
$e_{plug}e_{central}\gamma_2$	195.6	59.7	66.9	195.6	202.8
$e_{plug}e_{central}$	163.3	40.0	47.5	227.3	147.1
$\gamma_1\gamma_2$	47.3	50.4	49.3	121.2	118.1
$e_{plug}\gamma_1$	97.0	48.7	54.1	173.3	149.8
$e_{plug}\gamma_2$	56.5	92.6	99.1	183.8	198.7
$e_{central}\gamma_1$	64.1	50.7	43.4	18.6	112.1
$e_{central}\gamma_2$	91.7	5.8	4.1	166.6	76.8

Table 4.12: The kinematics of various combinations of the clusters in the $ee\gamma\gamma\not{E}_T$ candidate event. The combination of clusters is referred to as a system. Column 4 ($\not{E}_T$) is the transverse imbalance of that particular sub-system and takes into account the underlying event. The H_T is the transverse mass of the system along with its imbalance. The cluster in the plug is simply referred to as e_{Plug} for simplicity. The lowest $\not{E}_T$ attainable by simply removing one electron or photon candidate from the event is 20.0 GeV, which occurs by removing γ_2. By removing both the central photon and the cluster in the plug the $\not{E}_T$ becomes 4.1 GeV.

with the facts, each is unlikely in that this would be an unusual example of any of them. There simply is not enough information to establish the origin of the cluster. The unambiguous interpretation of the $ee\gamma\gamma\not{E}_T$ candidate event remains a mystery.

Objects	M_T (Gev/c^2)
$e_{plug}e_{central}\gamma_1\gamma_2\not{E}_T$	221.1
$e_{plug}\gamma_1\gamma_2\not{E}_T$	182.0
$e_{central}\gamma_1\gamma_2\not{E}_T$	141.2
$e_{plug}e_{central}\gamma_1\not{E}_T$	180.4
$e_{plug}e_{central}\gamma_2\not{E}_T$	187.0
$e_{plug}e_{central}\not{E}_T$	144.2
$\gamma_1\gamma_2\not{E}_T$	111.9
$e_{plug}\gamma_1\not{E}_T$	148.5
$e_{plug}\gamma_2\not{E}_T$	146.2
$e_{central}\gamma_1\not{E}_T$	70.4
$e_{central}\gamma_2\not{E}_T$	113.2
$e_{plug}\not{E}_T$	111.6
$e_{central}\not{E}_T$	4.3
$\gamma_1\not{E}_T$	52.8
$\gamma_2\not{E}_T$	86.9

Table 4.13: The transverse mass for the measured $\not{E}_T$ and various combinations of the electron and photon candidates within the $ee\gamma\gamma\not{E}_T$ candidate event. The cluster in the plug calorimeter, for simplicity, is labeled e_{Plug}. The transverse mass of the $e_{central}\not{E}_T$ and the '$e_{plug}\not{E}_T$' candidate pairs are 4.3 GeV/c^2 and 111.6 GeV/c^2 respectively and are thus unlikely to be from the decay $W \rightarrow e\nu$. However, the $e_{central}\gamma_1\not{E}_T$ combination could be due to the radiative decay of a W via $W \rightarrow e\nu\gamma$ (M_T = 70.4 GeV/c^2).

Chapter 5

Estimating the Number of $ee\gamma\gamma\not{E}_{\mathrm{T}}$ Events from Standard Model Sources

There are more things in heaven and earth, Horatio,
Than are dreamt of in your philosophy.

- William Shakespeare, Hamlet

The '$ee\gamma\gamma\not{E}_{\mathrm{T}}$' candidate event is obviously unusual. While a detailed study of the event does not indicate the source of the event, it is useful to make a quantitative estimate of the rate at which various Standard Model processes might produce or fake such a signature.

5.1 Introduction

The estimation of the probability of a single event has measure zero. It is more instructive to define an event topology and estimate the number

of events which pass that set of selection requirements from Standard Model sources. In an attempt to make the requirements similar to the standard *a priori* criteria used in CDF W and Z^0 analyses, the event topology is defined by the following list of requirements;

- One isolated electron in the central calorimeter with $E_T > 25$ GeV
- A second isolated electromagnetic cluster, in the central or plug calorimeters, which passes the electron identification requirements with $E_T > 25$ GeV.
- Two isolated central photons, $E_T > 25$ GeV
- $\not{E}_T > 25$ GeV
- An electron-electron invariant mass above the mass of the Z^0: we use 110 GeV.

A subtlety in the topology requirement is that the cluster in the plug calorimeter is possibly not an electron. To take this into account, the possible Standard Model sources are divided into two classes- those in which the cluster in the plug is caused by an electron, and those in which it is not. In both cases, electron candidates are required to pass the standard identification and isolation requirements described in the previous Chapter [39, 101, 102]. Both photons are required to pass the high-threshold requirements in Table 2.1. The primary sources are Standard Model $WW\gamma\gamma$ and $t\bar{t}$ production, events in which jets fake electrons and/or photons, cosmic ray interactions, and overlapping events.

5.2 Standard Model $WW\gamma\gamma$ production

The Standard Model process that is most likely to produce the signature directly (assuming the cluster in the plug calorimeter is due to an electron) is $WW\gamma\gamma$ production via the decay:

$$p\bar{p} \rightarrow W^+W^-\gamma\gamma \rightarrow (e^+\nu)(e^-\bar{\nu})\gamma\gamma \tag{5.1}$$

with each ν leaving the detector and causing $\not{E}_{\mathrm{T}}$. To estimate the rate the MADGRAPH Monte Carlo [103, 104] is used to simulate the process in lowest order. The cross-section, $\sigma_{WW\gamma\gamma}$, is estimated to be $\sigma_{WW\gamma\gamma} = 0.15 \pm 0.05$ fb for two photons with $\mathrm{E_T} > 10$ GeV, and $|\eta| < 4.0$. The PYTHIA/JETSET [53, 54] Monte Carlo is used to model the fragmentation, underlying event structure, and detector response. A total of 150,000 events with both W's decaying via $W \rightarrow e\nu$ are simulated.

A total of 1503 of the events simulated pass all the selection criteria (except the invariant mass requirement). This corresponds to an expected rate in 85 pb^{-1} of 1.6×10^{-6} events. The invariant mass spectra of the electron pair are shown in Figure 5.1. Of the 1503 events, 738 events have an invariant mass greater than 110 GeV. The rate at which $WW\gamma\gamma$ events produce the $ee\gamma\gamma\not{E}_{\mathrm{T}}$ signature is estimated as:

$$\begin{aligned} N^{High\ mass}_{WW\gamma\gamma\rightarrow ee\gamma\gamma\not{E}_{\mathrm{T}}} &= L \cdot \sigma_{WW\gamma\gamma} \cdot Br(W^+W^- \rightarrow e^+e^-\nu\bar{\nu}) \cdot A \\ &= 85\ \mathrm{pb}^{-1} \cdot (0.15 \times 10^{-3}\ \mathrm{pb}) \cdot \frac{1}{81} \cdot \frac{738}{150,000} \\ &= 7.7 \times 10^{-7}\ \mathrm{events} \end{aligned} \tag{5.2}$$

where A is the acceptance, defined to be the number of events in the sample passing all the requirements divided by the number of events simulated, and the branching ratio $Br(W^+W^- \rightarrow e^+e^-\nu\bar{\nu}) \approx \frac{1}{9} \times \frac{1}{9} = \frac{1}{81}$.

Taking into account the uncertainty on the cross section, the luminosity (85±6.8 pb^{-1}), and differences between detection efficiencies in the data and in the detector simulation, a total of $(8 \pm 4) \times 10^{-7}$ events is taken as the best estimate for $WW\gamma\gamma$ producing two electrons, two photons and $\not\!\!E_{\mathrm{T}}$ in the observed topology [105].

5.3 Standard Model $t\bar{t}$ Production

Another source, in which both electrons are real, is Standard Model $t\bar{t}$ production and decay. Both t-quarks decay via $t \to Wb$, both W's decay via $W \to e\nu$, and the photons are produced from radiation from internal fermion lines or are from jets which fake the photon signature. A sample of 22000 $t\bar{t}$ events with $t \to Wb$ and $W \to e\nu$ is simulated using the PYTHIA Monte Carlo and a detector simulation [53, 54]. In the sample, a total of 1335 events pass the two electron requirements with $\mathrm{M}_{\mathrm{e^+e^-}} > 110$ GeV and $\not\!\!E_{\mathrm{T}} > 25$ GeV, one of which has an additional central photon. The rate of finding an extra photon in $e^+e^-\not\!\!E_{\mathrm{T}}$ events is thus estimated to be:

$$\begin{aligned} P_{\text{Extra Photon}} &\approx \frac{N_{e^+e^-\gamma\not\!\!E_{\mathrm{T}}}^{\mathrm{M}_{\mathrm{e^+e^-}}>110\ \mathrm{GeV}}}{N_{e^+e^-\not\!\!E_{\mathrm{T}}}^{\mathrm{M}_{\mathrm{e^+e^-}}>110\ \mathrm{GeV}}} \\ &= \frac{1}{1335} = 7.5 \times 10^{-4}. \end{aligned} \tag{5.3}$$

As a check with better statistics, the $\mathrm{M}_{\mathrm{e^+e^-}} > 110$ GeV requirement is removed leading to

$$\begin{aligned} P_{\text{Extra Photon}} &\approx \frac{N_{e^+e^-\gamma\not\!\!E_{\mathrm{T}}}}{N_{e^+e^-\not\!\!E_{\mathrm{T}}}} \\ &= \frac{4}{3653} = 1.1 \times 10^{-3}. \end{aligned} \tag{5.4}$$

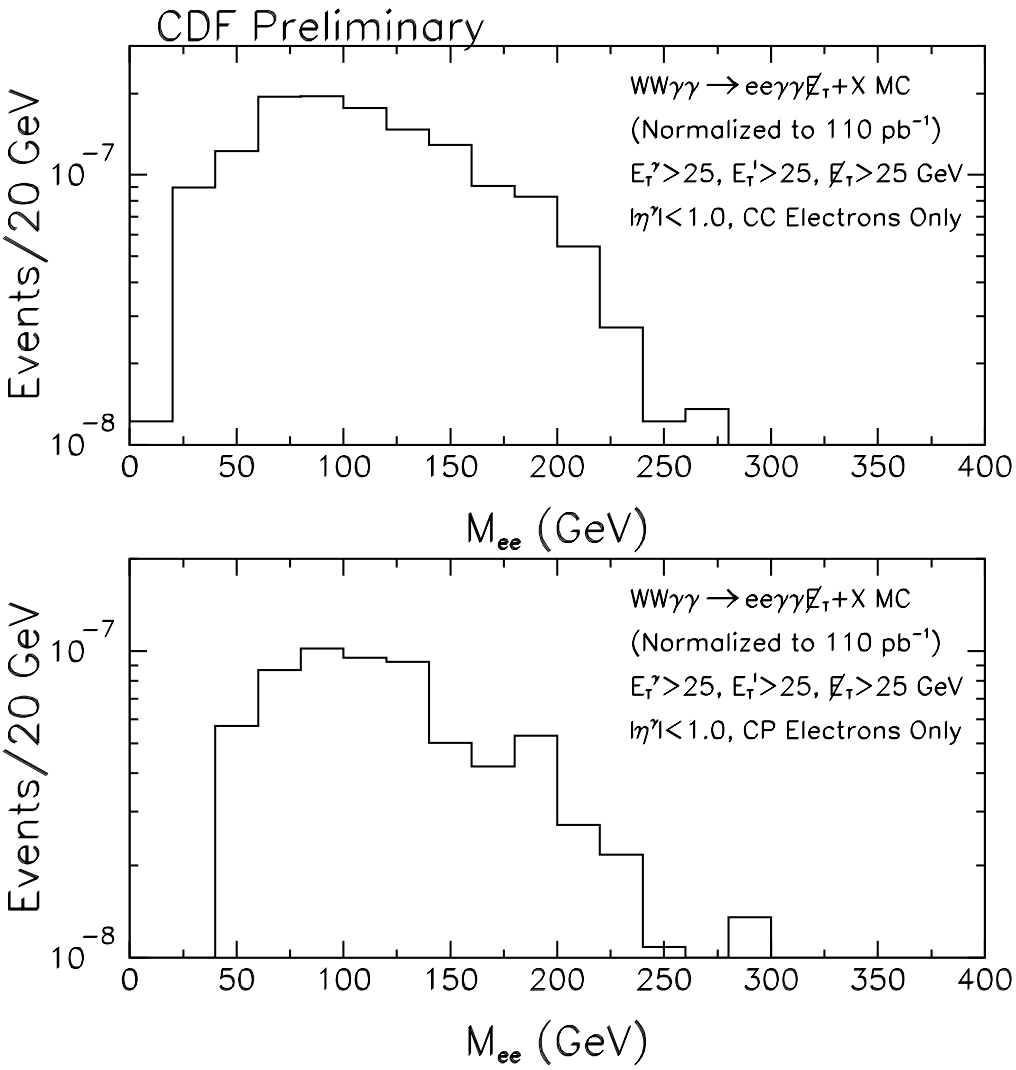

Figure 5.1: The invariant mass of the e^+e^- pair in Standard Model $WW\gamma\gamma \rightarrow ee\gamma\gamma\not{E}_T$ events. The simulation corresponds to 8.1×10^{10} pb^{-1} of data and predicts that 1.6×10^{-6} events of $ee\gamma\gamma\not{E}_T$ should be observed, with 7.7×10^{-7} events with $M_{e^+e^-} > 110$ GeV. Events with both electrons in the central calorimeter are referred to as CC while events with one electron in the central and one in the plug are referred to as CP.

Thus, the acceptance is estimated to be

$$A_{t\bar{t}\to e^+e^-\gamma\gamma\not{E}_T} = \frac{N_{e^+e^-\gamma\not{E}_T}^{M_{e^+e^-}>110\ \mathrm{GeV}}}{N_{\mathrm{Sample}}} \times P_{\mathrm{Extra\ Photon}} \tag{5.5}$$
$$= \frac{1}{22000} \times (1.1 \times 10^{-3}) = 5.0 \times 10^{-8}$$

where, to be conservative, the larger of the two values for the extra photon rate is used. The number of $t\bar{t}$ events which produce the $ee\gamma\gamma\not{E}_T$ signature is thus estimated by:

$$\mathrm{N_{Exp}} = L \cdot \sigma_{t\bar{t}} \cdot Br(W^+W^- \to e^+e^-\nu\bar{\nu}) \cdot A_{t\bar{t}\to e^+e^-\gamma\gamma\not{E}_T} \tag{5.6}$$
$$= (85\ \mathrm{pb}^{-1}) \cdot (5\mathrm{pb}) \cdot \frac{1}{81} \cdot (5.0 \times 10^{-8}) = 2.6 \times 10^{-7}\ \mathrm{Events.}$$

Taking into account the uncertainty on the $t\bar{t}$ cross section, the luminosity, differences between detection efficiencies in the data and in the detector simulation, the extra photon rates and statistical uncertainties in the sample, the rate is estimated to be $(3 \pm 3) \times 10^{-7}$ events. This estimate, while conservative, is still roughly a factor of 2 below the estimate from Standard Model $WW\gamma\gamma$ production.

5.4 Setting up to Estimate the Number of Fake Events

Other processes which contribute to the Standard Model production rate of $ee\gamma\gamma\not{E}_T$ events include events with jets that fake either photons or electrons, two Standard Model overlapping events, or additional objects from cosmic rays interacting or radiating in the detector. To estimate the number of events from these sources, the rate at which a *part* of the event occurs is multiplied by the probability that the rest of constituent parts of the event

occur in a random event. For example, to estimate the rate at which $WWjj$ production fakes the event signature, the rate at which $W^+W^- \rightarrow e^+\nu e^-\bar{\nu}$ events occur and pass the $ee\not{E}_T$ requirements is multiplied by the probability that two jets are produced in association with the WW and both fake the photon requirements.

5.4.1 The Main Part of the Event

The number of observed events in various channels which constitute a part of the $ee\gamma\gamma\not{E}_T$ signature are listed in Table 5.1. The datasets used to measure or estimate these numbers are described in Appendix I and are selected using the standard electron, photon and $\not{E}_T$ identification requirements described in Chapters 2 and 3. The rates at which jets fake the photon and electron selection criteria are estimated using a method similar to that in Chapter 3 [40, 71]. The results are given in the Table 5.1 and are essentially flat as a function of E_T for $E_T > 25$ GeV.

5.4.2 Rates for Finding the Additional Objects

The second part of the estimate requires a determination of the probability of finding an extra object or objects, such as real or fake photons, in the event. The results for fake $\not{E}_T$, real and fake photons, and fake electrons are summarized in Table 5.2.

Missing Energy Fake Rate

The $\not{E}_T$ fake rate is defined to be the average rate in highly electromagnetic events in which there is no expected $\not{E}_T$, and yet more than 25 GeV of $\not{E}_T$ is observed. This rate is estimated to be equal to the number of $Z^0 \rightarrow e^+e^-$ events with $\not{E}_T > 25$ GeV, divided by the total number of $Z^0 \rightarrow e^+e^-$ can-

Type of Event	Observed Number of events
W-Type Events	
$e_{\mathrm{central}}\not\!\!E_{\mathrm{T}}$	58000
$e_{\mathrm{central}}\not\!\!E_{\mathrm{T}} + \gamma$	4
$e_{\mathrm{central}}\not\!\!E_{\mathrm{T}}$ + Central Jet	1383 Events, 1513 jets
$e_{\mathrm{central}}\not\!\!E_{\mathrm{T}}$ + Plug Jet	597 Events, 620 jets
$e_{\mathrm{plug}}\not\!\!E_{\mathrm{T}}$	40000
$e_{\mathrm{plug}}\not\!\!E_{\mathrm{T}} + \gamma$	4
Photon-Type Events	
$e_{\mathrm{central}}\gamma$	49
$e_{\mathrm{plug}}\gamma$	22
$e_{\mathrm{central}}\gamma\gamma$	0
$e_{\mathrm{plug}}\gamma\gamma$	0
$\gamma\gamma$	218
$\gamma\gamma + \not\!\!E_{\mathrm{T}}$ Events	3
Cosmic-Type Events	
$\gamma + \not\!\!E_{\mathrm{T}}$	3181
Z^0/γ^*-Type Events(CC/CP)	
ee	1660/1771
$ee\not\!\!E_{\mathrm{T}}$	12/7
$ee\gamma$	0/2
$Z^0 \rightarrow e^+e^-$	1470/1613
$Z^0 \rightarrow e^+e^- + \not\!\!E_{\mathrm{T}}$	9/3
$Z^0 \rightarrow e^+e^- + \gamma$	0/1
$\mathrm{M_{ee}} > 110$ GeV	40/40
$\mathrm{M_{ee}} > 110$ GeV $+ \not\!\!E_{\mathrm{T}}$	1/3
$\mathrm{M_{ee}} > 110$ GeV $+ \gamma$	0/1
Other numbers	
Bunch Crossings	3×10^{12}
Central electron fake rate	$< 7.4 \times 10^{-5}$/ jet (95% C.L.)
Central photon fake rate	1.3×10^{-3}/ jet
Plug electron fake rate	2.2×10^{-3}/ jet

Table 5.1: The number of observed events for the various parts of the $ee\gamma\gamma\not\!\!E_{\mathrm{T}}$ signature, used to calculate fake and overlap rates. Note that $Z^0 \rightarrow e^+e^-$ events require 81 GeV $< \mathrm{M_{e^+e^-}} <$ 101 GeV and that the one surviving event in the $\mathrm{M_{ee}} > 110$ GeV $+ \gamma$ category is the $ee\gamma\gamma\not\!\!E_{\mathrm{T}}$ event.

Type of Rate	Rate/Event
Rate for finding additional fake $\not\!\!E_T$ $R_{\not\!\!E_T} \approx \frac{\text{ee}\not\!\!E_T\text{ Events}}{\text{ee Events}}$ $= \frac{9+3}{1470+1613}$ $= 3.9 \times 10^{-3}$	3.9×10^{-3}
Rate for finding an additional central photon $R_{\gamma\text{ Candidate}} \approx R_\gamma^{\text{fake}} + R_\gamma^{\text{radiation}}$ $\approx P_{\text{Extra Jet}} \times P_\gamma^{\text{fake}} + \frac{\text{ee}\gamma\text{ Events}}{\text{ee Events}}$ $= \frac{1513}{58000} \times (1.3 \times 10^{-3}) + \frac{0+2}{1660+1771}$ $= 3.4 \times 10^{-5} + 5.8 \times 10^{-4}$ $= 6.2 \times 10^{-4}$	6.2×10^{-4}
Rate for finding an additional plug electron candidate $R^{\text{fake}}_{\text{Plug Cluster}} \approx P_{\text{Extra Jet}} \times P^{\text{fake}}_{\text{Plug } e}$ $= \frac{620}{58000} \times (2.2 \times 10^{-3})$ $= 2.3 \times 10^{-5}$	2.3×10^{-5}
Rate for finding an additional central electron (95% C.L.) $R^{95\%\text{ C.L.}}_{\text{Central e}} \approx P_{\text{Extra Jet}} \times P^{\text{fake}}_{\text{Central e}}$ $= \frac{1513}{58000} \times (7.4 \times 10^{-5})$ $= 1.9 \times 10^{-6}$	$<1.9 \times 10^{-6}$ (95% C.L.)

Table 5.2: The estimated rates for finding fake objects (electrons, photons or $\not\!\!E_T$) in an event from various processes. Note that the rate for finding an additional central photon is probably an overestimate by a factor of two because both methods include contributions from real photons as well as fakes.

didates [60, 106]. Summing the number of events with both electrons in the central calorimeter (CC) and the number of events with one central electron and one electron in the plug (CP) yields a total of $1470 + 1613 = 3083$ events, $9 + 3 = 12$ of which have $\not\!\!E_T > 25$. The $\not\!\!E_T$ fake rate is thus (conservatively) estimated to be:

$$\begin{aligned} R_{\not\!\!E_T} &\approx \frac{\text{ee}\not\!\!E_T\text{ Events}}{\text{ee Events}} \\ &= \frac{9+3}{1470+1613} = 3.9 \times 10^{-3}. \end{aligned} \tag{5.7}$$

Additional Photon Rate

The probability that there will be an additional high-E_T photon in a given event is estimated to be the sum of two processes [107]: physics processes (initial or final state radiation) and fake processes (a jet faking the photon signature). The fraction of events with an additional γ from physics processes is estimated to be equal to the fraction $\frac{\mathrm{W}\gamma\ \mathrm{Events}}{\mathrm{W\ Events}}$. Events with a W are selected as having a tight central electron and $\not\!\!E_T > 25$ GeV. From Table 5.1:

$$\begin{aligned} R_\gamma^{\mathrm{Radiation}} &\approx \frac{\mathrm{W}\gamma\ \mathrm{Events}}{\mathrm{W\ Events}} \\ &= \frac{e\gamma\not\!\!E_T\ \mathrm{Events}}{e\not\!\!E_T\ \mathrm{Events}} = \frac{4}{58000} = 6.9 \times 10^{-5}. \end{aligned} \tag{5.8}$$

Similarly, the probability is estimated to be equal to the probability of observing an extra photon in $Z^0/\gamma^* \rightarrow ee$ events:

$$\begin{aligned} R_\gamma^{\mathrm{Radiation}} &\approx \frac{\mathrm{e^+e^-}\gamma\ \mathrm{Events}}{\mathrm{e^+e^-\ Events}} \\ &= \frac{0+2}{1660+1771} = 5.8 \times 10^{-4}. \end{aligned} \tag{5.9}$$

To be conservative, the larger of the two results is used, $R_\gamma^{\mathrm{Radiation}} = 5.8 \times 10^{-4}$, even though the $ee\gamma\gamma\not\!\!E_T$ candidate event is part of the sample of $e^+e^-\gamma$ events.

The fraction of events with an additional photon from a jet in the central calorimeter which fakes the photon signature is estimated to be the product of two probabilities: the probability that an event will have an extra central jet with $E_T > 25$ GeV, and the probability that a jet will fake a photon. The probability that an event will have an extra central jet from physics processes is estimated to be equal to the fraction $\frac{\mathrm{Additional\ Central\ Jets\ in\ W\ events}}{\mathrm{Total\ number\ of\ W\ events}}$. Again W events are selected by requiring a tight central electron and $\not\!\!E_T > 25$ GeV. Additional jets are required to have $E_T > 25$ GeV and $|\eta| < 1.0$. Putting this

together with the photon fake rate (from Table 5.1) gives:

$$\begin{aligned} R_{\gamma}^{\text{fake}} &\approx P_{\text{Extra Jet}} \times P_{\gamma}^{\text{fake}} \\ &= \frac{1513}{58000} \times (1.3 \times 10^{-3}) = 3.4 \times 10^{-5}. \end{aligned} \tag{5.10}$$

Summing the two results gives a total rate for an additional central photon:

$$\begin{aligned} R_{\gamma\ \text{Candidate}} &= R_{\gamma}^{\text{fake}} + R_{\gamma}^{\text{Radiation}} \\ &= (3.4 \times 10^{-5}) + (5.8 \times 10^{-4}) = 6.2 \times 10^{-4}. \end{aligned} \tag{5.11}$$

Additional Plug 'Electron' Rate

The probability of finding an additional electron candidate in the plug calorimeter in an event is dominated by the rate at which jets fake the electron signature. Using similar methods with $W \rightarrow e\nu$ events, and requiring the jets to be in the region $1.2 < |\eta| < 2.2$ yields:

$$\begin{aligned} R_{\text{Plug electron}}^{\text{fake}} &= P_{\text{Plug Jet}} \times P_{\text{Jet fakes an electron}} \\ &= \frac{620}{58000} \times (2.2 \times 10^{-3}) = 2.3 \times 10^{-5}. \end{aligned} \tag{5.12}$$

Additional Central Electron Rate

The fraction of events with an additional central electron from a jet fake is estimated in a similar manner using $W \rightarrow e\nu$ events and requiring jets to have $|\eta| < 1.0$. Since the electron fake rate is a 95% C.L. upper limit, a limit on the fake rate is determined via:

$$\begin{aligned} R_{\text{Central electron}}^{\text{fake 95\% C.L. upper limit}} &= P_{\text{Central Jet}} \times P_{\text{Jet fakes an electron}} \\ &\leq \frac{1513}{58000} \times (7.4 \times 10^{-5}) = 1.9 \times 10^{-6}. \end{aligned} \tag{5.13}$$

5.5 Estimating the Number of Expected Fake Events

Events can fake the $ee\gamma\gamma\not{E}_{\mathrm{T}}$ signature in two main ways: events in which there is one or more fake objects (electrons or photons), and events in which there are two collisions which occur at the same time each producing part of the event (overlapping events).

As a check, the number of real $ee\gamma\gamma\not{E}_{\mathrm{T}}$ events is predicted and compared to the $WW\gamma\gamma$ Monte Carlo estimate. The event rate is estimated to be equal to the number of ee events with with $\mathrm{M_{ee}} > 110$ GeV and $\not{E}_{\mathrm{T}} > 25$ GeV in the data, multiplied by the rate at which two additional central photons are produced in association with the event. Taking the 4 $ee\not{E}_{\mathrm{T}}$ events with $\mathrm{M_{ee}} > 110$ GeV from Table 5.1, and two factors of 5.8×10^{-4} for real photon production yields:

$$\begin{aligned} N_{ee\gamma\gamma\not{E}_{\mathrm{T}}} &\approx N_{ee\not{E}_{\mathrm{T}}}^{\mathrm{M_{ee}}>110\ \mathrm{GeV}} \times R_{\gamma}^{\mathrm{Radiation}} \times R_{\gamma}^{\mathrm{Radiation}} \\ &= 4 \times (5.8 \times 10^{-4}) \times (5.8 \times 10^{-4}) = (1 \pm 1) \times 10^{-6} \text{ Events.} \end{aligned} \tag{5.14}$$

This compares well with the $(8 \pm 4) \times 10^{-7}$ events expected from the $WW\gamma\gamma$ Monte Carlo estimate [108].

5.5.1 Events with a Fake Object or Objects

The number of expected events where part of the event is 'real' and part of the event is 'faked' is summarized in Table 5.3. The Real Process rates are estimated using Table 5.1, and the Fake Process rates are given in Table 5.2. Contributions from events with fake central electrons have not been included as the expected rate is negligible compared to the other sources. A total of 2.6×10^{-7} events are expected in the data due to fake sources.

Real Process	Fake Process 1	Fake Process 2	Fake Process 3	Events in 85 pb^{-1}
$e^+e^-\gamma\not{E}_{\mathrm{T}}$ 2.3×10^{-3}	$\gamma^{\text{Fake from Jet}}$ $\times\ 3.4\times10^{-5}$	— —	— —	$= 7.8\times10^{-8}$
$e^+e^-\gamma\gamma$ 2.7×10^{-5}	$\not{E}_{\mathrm{T}}^{\text{Fake}}$ $\times\ 3.9\times10^{-3}$	— —	— —	$= 1.1\times10^{-7}$
$e_{\mathrm{Central}}\gamma\gamma\not{E}_{\mathrm{T}}$ 2.3×10^{-3}	$e_{\mathrm{Plug}}^{\text{Fake from Jet}}$ $\times\ 2.3\times10^{-5}$	— —	— —	$= 5.4\times10^{-8}$
$ee\not{E}_{\mathrm{T}}$ 4	$\gamma^{\text{Fake from Jet}}$ $\times\ 3.4\times10^{-5}$	$\gamma^{\text{Fake from Jet}}$ $\times\ 3.4\times10^{-5}$	— —	$= 4.5\times10^{-9}$
$e_{\mathrm{Central}}\gamma\not{E}_{\mathrm{T}}$ 4	$\gamma^{\text{Fake from Jet}}$ $\times\ 3.4\times10^{-5}$	$e_{\mathrm{Plug}}^{\text{Fake from Jet}}$ $\times\ 2.3\times10^{-5}$	— —	$= 3.1\times10^{-9}$
$ee\gamma$ 4.7×10^{-2}	$\gamma^{\text{Fake from Jet}}$ $\times\ 3.4\times10^{-5}$	$\not{E}_{\mathrm{T}}^{\text{Fake}}$ $\times\ 3.9\times10^{-3}$	— —	$= 6.1\times10^{-9}$
$e_{\mathrm{central}}\gamma\gamma$ 2.9×10^{-2}	$e_{\mathrm{Plug}}^{\text{Fake from Jet}}$ $\times\ 2.3\times10^{-5}$	$\not{E}_{\mathrm{T}}^{\text{Fake}}$ $\times\ 3.9\times10^{-3}$	— —	$= 2.6\times10^{-9}$
$e_{\mathrm{Central}}\gamma$ 49	$\gamma^{\text{Fake from Jet}}$ $\times\ 3.4\times10^{-5}$	$e_{\mathrm{Plug}}^{\text{Fake from Jet}}$ $\times\ 2.3\times10^{-5}$	$\not{E}_{\mathrm{T}}^{\text{Fake}}$ $\times\ 3.9\times10^{-3}$	$= 1.5\times10^{-10}$
$e_{\mathrm{Central}}\not{E}_{\mathrm{T}}$ 58000	$\gamma^{\text{Fake from Jet}}$ $\times\ 3.4\times10^{-5}$	$\gamma^{\text{Fake from Jet}}$ $\times\ 3.4\times10^{-5}$	$e_{\mathrm{Plug}}^{\text{Fake from Jet}}$ $\times\ 2.3\times10^{-5}$	$= 1.5\times10^{-9}$
ee 80	$\gamma^{\text{Fake from Jet}}$ $\times\ 3.4\times10^{-5}$	$\gamma^{\text{Fake from Jet}}$ $\times\ 3.4\times10^{-5}$	$\not{E}_{\mathrm{T}}^{\text{Fake}}$ $\times\ 3.9\times10^{-3}$	$= 3.5\times10^{-10}$
Sum				$\approx 2.6\times10^{-7}$

Table 5.3: An estimate of the number of events passing the $ee\gamma\gamma\not{E}_{\mathrm{T}}$ selection criteria from events with fake electrons, photons or $\not{E}_{\mathrm{T}}$. Individual rates are estimated as being equal to the number of observed events (the Real Process) multiplied by the rate at which additional objects from fakes (Fake Process) are observed in the event. The real process rate is taken or estimated from Table 5.1 and the fake process rates are taken from Table 5.2.

The 'real process' rates (Column 1) in Table 5.3 are derived from Table 5.1 as follows:

- $e^+e^-\gamma\not{E}_T$: The 4 events from the data with $M_{ee} > 110$ GeV and $\not{E}_T > 25$ GeV, multiplied by a factor of 5.8×10^{-4} for a real additional central photon.

- $e^+e^-\gamma\gamma$: The 80 events in the data with $M_{ee} > 110$ GeV, multiplied by two factors of 5.8×10^{-4} for real additional central photons.

- $e_{\rm Central}\gamma\gamma\not{E}_T$: The 4 $e_{\rm central}\not{E}_T + \gamma$ events, multiplied by a factor of 5.8×10^{-4} for a real additional central photon.

- $e^+e^-\not{E}_T$: The 4 events from the data with $M_{ee} > 110$ GeV and $\not{E}_T > 25$ GeV. Note that this is consistent with the 5 events of the WW analysis (which include 1.2 events background) [109].

- $e_{\rm Central}\gamma\not{E}_T$: The 4 $e_{\rm Central}\gamma\not{E}_T$ events.

- $ee\gamma$: The 80 ee events in the data with $M_{ee} > 110$ GeV, multiplied by a factor of 5.8×10^{-4} for a real additional central photon.

- $e_{\rm Central}\gamma\gamma$: The 49 $e_{\rm Central}\gamma$ events, multiplied by a factor of 5.8×10^{-4} for a real additional central photon.

- $e_{\rm Central}\gamma$: The 49 $e_{\rm Central}\gamma$ events.

5.5.2 Overlapping Events, Including Cosmic Rays

Events in which two collisions occur at the same time, each producing part of the event, can fake the $ee\gamma\gamma\not{E}_T$ signature. The rate of expected events from each source is estimated to be equal to the rate at which one part of the

event occurs, multiplied by the probability of the rest of the signature occurring in a second overlapping event. The total rate sums over all processes and includes contributions from cosmic rays which leave a photon in the detector as well as real physics contributions which might occur in an overlapping event.

The probability of getting a particular type of overlapping event is estimated to be equal to the number of events with that signature, divided by the total number of events studied by the detector during the course of the run [110]. Every event measured by the detector can contain multiple $\bar{p}p$ collisions from the same proton anti-proton 'bunch crossing' in the Fermilab Tevatron. The total number of bunch crossings, and thus the number of events studied by the CDF detector, is estimated to be

$$\begin{aligned} \text{Bunch Crossings} &= \frac{\text{Integrated Luminosity}}{\text{Avg. Luminosity} \times \text{Bunch Crossing Interval}} \\ &= \frac{85\ \text{pb}^{-1}}{(8 \times 10^{30}\ \text{cm}^2/\text{sec}) \times 3.5\mu\text{sec}} = 3 \times 10^{12} \end{aligned} \tag{5.15}$$

Note that this is different from the number of $\bar{p}p$ collisions which occurred during the run. The number of collisions is estimated using

$$\begin{aligned} \text{N}_{\text{collisions}} &= \sigma_{\bar{p}p} \times L \\ &= 51\ \text{mb} \times 85\ \text{pb}^{-1} = 4 \times 10^{12}. \end{aligned} \tag{5.16}$$

To be consistent (and conservative), only the number of bunch crossings is used since there are multiple collisions per crossing.

As an example, the probability for a specific event to contain an overlapping $\gamma + \not{E}_{\text{T}}$ event (due primarily to cosmic ray interactions) is estimated using the 3181 $\gamma + \not{E}_{\text{T}}$ events in the data and the 3×10^{12} bunch crossings via:

$$R_{\gamma+\not{E}_{\text{T}}} = \frac{3181}{3 \times 10^{12}} = 1.1 \times 10^{-9}. \tag{5.17}$$

The results for the dominant sources of overlap events are summarized in Table 5.4. To take into account the fact that there are 4 interactions in the $ee\gamma\gamma\not{E}_{\rm T}$ candidate event, the estimate is multiplied by 6 to reflect the 6 possible permutations of any two of the four interactions causing the signature. Summing all the sources, the total rate due to overlapping events is estimated to be $(8 \pm 8) \times 10^{-9}$ events.

The process 1 rates (Column 1) in Table 5.4 are derived as follows:

- $e_{\rm plug}\gamma\gamma$: The 22 $e_{\rm plug}\gamma$ events in the data, multiplied by the fake+real additional photon rate of 6.2×10^{-4}.
- $ee\gamma$: The 80 ee events in the data with $\rm M_{ee} > 110$ GeV, multiplied by the fake+real additional photon rate of 6.2×10^{-4}.
- $e\gamma\gamma$: The 49 $e\gamma$ events in the data, multiplied by the fake+real additional photon rate of 6.2×10^{-4}.
- $WW\gamma$: The 4 WW events in the data, multiplied by the fake+real additional photon rate of 6.2×10^{-4}.
- $W\gamma\gamma$: The 4 $e\gamma\not{E}_{\rm T}$ events in the data, multiplied by the fake+real additional photon rate of 6.2×10^{-4}.
- $e_{\rm Plug}\not{E}_{\rm T}$: The 40000 $e_{\rm plug}\not{E}_{\rm T}$ events in the data. Note that these events come from both W and cosmic ray production.

5.6 Total Standard Model Rates

The possible Standard Model sources are divided into two classes-those in which the second electromagnetic cluster passing the electron selection criteria is caused by an electron, and those in which it is not.

Process 1	Process 2	Calculation	Expected Events
$WW_{high\ mass}$	$\gamma\gamma$	$4 \times \frac{218}{3\times10^{12}}$	2.9×10^{-10}
$W\gamma$	$W\gamma$	$4 \times \frac{4}{3\times10^{12}}$	5.3×10^{-12}
$W\gamma\gamma \rightarrow e_{\rm plug}\gamma\gamma$	$W \rightarrow e_{\rm central}\not{E}_{\rm T}$	$1.4 \times 10^{-2} \times \frac{58000}{3\times10^{12}}$	2.6×10^{-10}
$ee\gamma$	$\gamma\not{E}_{\rm T}$	$4.9 \times 10^{-2} \times \frac{3181}{3\times10^{12}}$	5.2×10^{-11}
$W\gamma\gamma \rightarrow e_{\rm central}\gamma\gamma$	$e_{\rm Plug}\not{E}_{\rm T}$	$3.0 \times 10^{-2} \times \frac{40000}{3\times10^{12}}$	4.0×10^{-10}
$WW\gamma$	Cosmic $\rightarrow \gamma$	$2.5 \times 10^{-3} \times \frac{3181}{3\times10^{12}}$	2.6×10^{-12}
Sum			$\approx 1.4 \times 10^{-9}$
Sum$\times$ 6			$\approx 8 \times 10^{-9}$

Table 5.4: The number of events with the $ee\gamma\gamma\not{E}_{\rm T}$ signature due to two overlapping events. These include double interactions, two separate events occurring in the same bunch crossing, as well as an event with additional objects from a cosmic ray which interacted or radiated in the detector. The number of expected events is estimated to be equal to the rate of the 'real' part of the event (process 1) times the probability of observing a particular type of overlapping event (process 2). The probability is defined to be equal to the number of events with the signature divided by the number of bunch crossings in the data (3×10^{12}). To take into account the fact that 4 interactions are observed in this event the estimate is multiplied by 6.

5.6.1 The Total Standard Model Rate Including Processes Where the Plug Cluster is due to an Electron

The Standard Model estimate for the number of events with the $ee\gamma\gamma\not{E}_{\mathrm{T}}$ signature is dominated by real $WW\gamma\gamma$ production. A total of 1.6×10^{-6} $ee\gamma\gamma\not{E}_{\mathrm{T}}$ events are expected, 7.7×10^{-7} with an invariant mass above 110 GeV. Standard Model $t\bar{t}$ production contributes an additional 2.6×10^{-7} events. The total fake rate, split roughly equally between $ee\gamma\gamma$ + fake $\not{E}_{\mathrm{T}}$, $ee\gamma\not{E}_{\mathrm{T}}$ + fake photon and $e\gamma\gamma\not{E}_{\mathrm{T}}$ + fake plug electron, contributes a total of 2.6×10^{-7} events. Overlaps and cosmic rays are estimated to contribute a total of 8×10^{-9} events. The total (using the $WW\gamma\gamma$ production with invariant mass greater than 110 GeV) is 1.3×10^{-6} events. Including the uncertainties in the method, as well as on the numbers used, the total rate is estimated to be:

$$N_{\mathrm{Expected}}^{\mathrm{Standard\ Plug\ e\ Requirements}} = (1 \pm 1) \times 10^{-6} \text{ events.} \tag{5.18}$$

5.6.2 The Total Standard Model Rate Excluding Processes Where the Plug Cluster is due to an Electron

With the addition of the SVX data and a thorough scrutiny of the plug cluster, there are good indications that the cluster may not be due to an electron. Because this additional information excludes the dominant backgrounds, each of which produce two electrons, it lowers the Standard Model predicted rates. In particular it lowers substantially the expectation from $WW\gamma\gamma$ and $t\bar{t}$ production. The total, dominated by $e\gamma\gamma\not{E}_{\mathrm{T}}$ + fake plug elec-

tron, is 6.1×10^{-8}. Overlaps are again negligible. Including the uncertainties in the method, as well as on the numbers used, the total rate is estimated to be:

$$N_{\text{Expected}}^{\text{Plug Cluster not an e}} = (6 \pm 6) \times 10^{-8} \text{ events.} \tag{5.19}$$

Chapter 6

Setting Limits with the $\gamma\gamma + X$ Analysis

A little knowledge is a dangerous thing

- Alexander Pope

The absence of a satisfactory Standard Model explanation of the '$ee\gamma\gamma\not{E}_{\mathrm{T}}$' candidate event leaves open the possibility of new physics interpretations. A number of theories put forward to explain the event predict that other events from related decay modes should appear in the $\gamma\gamma + X$ searches. Since there is no evidence of these events in the central diphoton sample, quantitative limits can be set on such scenarios.

6.1 Anomalous $WW\gamma\gamma$ Production

It is improbable *a priori* that the $ee\gamma\gamma\not{E}_{\mathrm{T}}$ candidate event is from Standard Model $WW\gamma\gamma$ production, as shown in Chapter 5. However, the

event could be an example of anomalous $WW\gamma\gamma$ production [111]. This hypothesis can be tested quantitatively by assuming that the one event was produced at its mean cross section [14]. Using a Monte Carlo of Standard Model $WW\gamma\gamma$ [103, 104] the mean number of events in the other WW decay channels, dubbed 'cousins' [15], can be estimated. Two samples are simulated: $WW \rightarrow X$ where X are all decay channels of the WW pair, and $WW \rightarrow \ell_i\nu_i\ell_j\nu_j$ where ℓ is an electron, muons or tau. Each sample contains 100,000 events. Events which pass the high-$\mathrm{E_T}$ diphoton selection criteria ($\mathrm{E_T^\gamma} > 25$ GeV) are searched for multijet (3 or more jets as defined in Chapter 3) or dilepton (2 or more leptons in any combination as defined in Chapter 3) signatures. The results are shown in Table 6.1. Only 3 jets are required because the acceptance is almost cut in half by requiring a fourth jet, as shown in the Table. Also, to be conservative, the number of cousins in the $\gamma\gamma jjj$ channel is estimated using all leptonic decays (e, μ or τ) of the WW pair as normalization rather than just the ee channel.

The number of $\gamma\gamma + jjj$ events from anomalous $WW\gamma\gamma$ production is estimated using:

$$N_{\gamma\gamma jjj}^{\mathrm{Expected}} \approx N_{\gamma\gamma\ell_i\ell_j+\not{E}_\mathrm{T}}^{\mathrm{Observed}} \times \left(\frac{\mathrm{Rate}\ (WW\gamma\gamma \rightarrow \gamma\gamma jjj)}{\mathrm{Rate}\ (WW\gamma\gamma \rightarrow \gamma\gamma\ell_i\ell_j + \not{E}_\mathrm{T})}\right). \qquad (6.1)$$

The Monte Carlo estimates that in the diphoton sample with $\mathrm{E_T} > 25$ GeV, $WW\gamma\gamma$ production should produce events with 3 or more jets 31.3 times more often than events with two photons, two charged leptons and $\not{E}_\mathrm{T}$. With one $\gamma\gamma\ell\ell\not{E}_\mathrm{T}$ candidate event and no events with 3 or more jets in the data (see Table 3.9 and Figure 3.8) anomalous $WW\gamma\gamma$ is excluded as the source of this event at the 95% C.L.

$\gamma\gamma$ + Multijet Signatures				
Channel	Events			Data
	MC Sample $WW\gamma\gamma \rightarrow \gamma\gamma + X$	SM $WW\gamma\gamma$ (L=85 pb^{-1})	Anomalous $WW\gamma\gamma$	
$\geq$ 3 Jets	2130	2.7×10^{-4}	31.3	0
$\geq$ 4 Jets	1125	1.4×10^{-4}	16.5	0
$\gamma\gamma$ + Leptonic Signatures				
Channel	Events			Data
	MC Sample $WW\gamma\gamma \rightarrow l\bar{\nu}\bar{l}\nu\gamma\gamma$	SM $WW\gamma\gamma$ (L=85 pb^{-1})	Anomalous $WW\gamma\gamma$	
Dilepton + $\not\!\!E_T$	613	8.7×10^{-6}	1.0	1

Table 6.1: Standard Model $WW\gamma\gamma$ predictions for diphoton events with $E_T^\gamma > 25$ GeV. Standard Model $WW\gamma\gamma$ production has a cross section of 0.15 fb for two photons with $E_T > 10$ GeV, and $|\eta| < 4.0$. The anomalous $WW\gamma\gamma$ production cross section is normalized to the number of $ll\gamma\gamma\not\!\!E_T$ events. The Monte Carlo samples have 100,000 events simulated.

6.2 Supersymmetric Models

Several theories, have been proposed to explain the $ee\gamma\gamma\not\!\!E_T$ candidate event [10, 22, 23, 26, 27, 25, 29, 112]. The trademark of the Supersymmetric versions is the production of a lightest Supersymmetric particle (LSP). In every event, either by direct production or by cascade, the LSP leaves the detector and causes an energy imbalance [17]. For this reason, limits are set on two different Supersymmetric scenarios using the $\gamma\gamma + \not\!\!E_T$ analysis.

6.2.1 Light Gravitino Scenarios

In light gravitino scenarios [28, 29] the gravitino can have a mass on the order of 1 eV and for most of the parameter space the lightest neutralino, N_1, has a branching ratio of $\approx$100% into $\gamma\tilde{G}$. The lifetime of the N_1 depends on $M_{\tilde{G}}$; the decay occurs inside the detector for a gravitino mass less than approximately 1 KeV. The $\tilde{G}$ is very weakly interacting and escapes the de-

tector leaving an energy imbalance. These models can produce the $ee\gamma\gamma\not{E}_{\rm T}$ signature, for example, via:

$$C_1C_1 \to (\nu\tilde{e})(\nu\tilde{e}) \to \nu(eN_1)\nu(eN_1) \to e\nu(\gamma\tilde{G})e\nu(\gamma\tilde{G}) \to ee\gamma\gamma\not{E}_{\rm T} \qquad (6.2)$$

For concreteness, limits on light gravitino scenarios are set using the Minimal Gauge-Mediated Model (MGM) [29, 113]. As in supergravity models, the Supersymmetry breaking occurs in a hidden sector; unlike the Supergravity models in which $\Lambda_{\rm SUSY} \sim 10^{11}$ GeV, in the MGM models, $\Lambda_{\rm SUSY} \sim 10^{5-9}$ GeV. Thus in these models,

$$\begin{aligned} M_{\tilde{G}} &\simeq \frac{\Lambda^2_{\rm SUSY}}{M_{\rm Plank}} \qquad (6.3) \\ &\simeq \frac{(10^{5-9}\ {\rm GeV})^2}{10^{18}\ {\rm GeV}} \simeq 1\ {\rm eV} - 100\ {\rm KeV} \end{aligned}$$

making it the lightest Supersymmetric particle (LSP) by far. Because the coupling of the gravitino is very weak, it is not produced directly in $p\bar{p}$ collisions, but is rather the end product of all supersymmetric decay chains. In particular, the next-to-lightest SUSY particle (NLSP), which in the model considered will be the lightest neutralino, N_1, will decay dominantly via $N_1 \to \gamma + \tilde{G}$. The lifetime of N_1 depends on $M_{\tilde{G}}$; one finds that the decay occurs inside the detector for $M_{\tilde{G}} \lesssim 1$ KeV.

In gauge-mediated models, the SUSY breaking is then communicated to the observable sector [114] via gauge interactions, instead of by gravitational couplings as in supergravity. Gaugino masses arise through one-loop diagrams and are given by:

$$M_i(\Lambda) = \frac{\alpha_i(\Lambda)}{4\pi}\Lambda. \qquad (6.4)$$

where Λ is the effective SUSY-breaking scale communicated to the observable sector, with the condition that $\Lambda \leq \Lambda_{\rm SUSY}$. (For simplicity Equation 6.4 is

assumed to be true at the scale Λ. In some versions of the MGM, Equation 6.4 holds at scales far above Λ, but this would not change the results significantly.) Notice that this relation reproduces the normal gaugino mass unification of supergravity:

$$\frac{M_1}{\alpha_1} = \frac{M_2}{\alpha_2} = \frac{M_3}{\alpha_3}, \tag{6.5}$$

so at the weak scale, substituting the PDG values [4] $\alpha_3 = 0.120, \alpha_2 = \frac{1}{29.68}$ and $\alpha_1 = \frac{1}{58.98}$, leads to the result $M_1 : M_2 : M_3 \approx 1 : 2 : 7$.

The scalar masses arise through two-loop diagrams and are approximated by:

$$m^2(\Lambda) = 2\Lambda^2 \left\{ C_3 \left[\frac{\alpha_3(\Lambda)}{4\pi}\right]^2 + C_2 \left[\frac{\alpha_2(\Lambda)}{4\pi}\right]^2 + \frac{3}{5}\left(\frac{Y}{2}\right)^2 \left[\frac{\alpha_3(\Lambda)}{4\pi}\right]^2 \right\} \tag{6.6}$$

where Y is the hypercharge of the scalar and is defined via $Q = T_3 + \frac{Y}{2}$ where $T_3 = 0, \pm\frac{1}{2}$ is its weak isospin. The constants C_3 and C_2 are given by $C_3 = \frac{4}{3}$ for colored scalars and zero otherwise; $C_2 = \frac{3}{4}$ for SU(2) doublets and zero otherwise. Using

$$\begin{aligned}
(u_L, d_L): &\quad Y = +\frac{1}{3}, C_2 = \frac{3}{4}, C_3 = \frac{4}{3} \\
u_R^c: &\quad Y = -\frac{4}{3}, C_2 = 0, C_3 = \frac{4}{3} \\
d_R^c: &\quad Y = +\frac{2}{3}, C_2 = 0, C_3 = \frac{4}{3} \\
(\nu_L, e_L): &\quad Y = -1, C_2 = \frac{3}{4}, C_3 = 0 \\
e_R^c: &\quad Y = +2, C_2 = 0, C_3 = 0 \\
(H_u^+, H_u^0): &\quad Y = +1, C_2 = \frac{3}{4}, C_3 = 0 \\
(H_d^0, H_d^-): &\quad Y = -1, C_2 = \frac{3}{4}, C_3 = 0.
\end{aligned} \tag{6.7}$$

one finds mass ration of $\tilde{q} : \tilde{g} : \tilde{\ell}_L : \tilde{W} : \tilde{\ell}_R : \tilde{B} = 11.6 : 7.0 : 2.5 : 2 : 1.1 : 1$. These ratios receive significant corrections from the renormalization group

evolution between the Λ-scale and the weak scale. For the range of masses for under consideration, the (approximate) final masses occur in the ratios 9.3 : 6.4 : 2.6 : 2.0 : 1.9 : 1. There is some $\tan\beta$ and $\mathrm{Sgn}(\mu)$ dependence on this result, but it is weak, particularly as the overall mass scale increases. One of the advantages of the Minimal Gauge-Mediated Model is that all scalar and gaugino masses are given, to lowest order, only in terms of one unknown parameter, Λ, or alternatively any one mass, which is chosen to be M_2.

The process of gauge-mediation does not in itself explain the origin of the μ-term of the MSSM which couples the two Higgs doublets to one another, or the value of $\tan\beta$. However, if the spectrum of the model is required to include only those fields of the MSSM, then the Higgs potential can be minimized and the value of μ^2 can be determined in terms of the Z^0-mass and other scalar masses (given a choice of Λ). In particular,

$$\mu^2 = \frac{m_{H_d}^2 - m_{H_u}^2 \tan^2\beta}{\tan^2\beta - 1} - \frac{1}{2} m_{Z^0}^2. \tag{6.8}$$

The sign of μ, $\mathrm{Sgn}(\mu)$, and $\tan\beta$ are taken as input parameters. Finally note that in gauge-mediated models the trilinear soft term, often called the A-term, is very small and can be taken to be zero for all purposes.

The values of μ^2 derived from Eq. (6.8) are generally large compared to the gaugino masses, so that in the neutralino/chargino sector one finds $N_1 \simeq \tilde{B}$, $N_2 \simeq \tilde{W}_3$, and $C_1 \simeq \tilde{W}^{\pm}$. The production processes at the Tevatron are then dominated by $C_1 N_2$ and $C_1^+ C_1^-$ production throughout most of parameter space because of the large $W^{\pm}\tilde{W}^{\mp}\tilde{W}_3$, $Z\tilde{W}^+\tilde{W}^-$ and $\gamma\tilde{W}^+\tilde{W}^-$ couplings in the MSSM. Meanwhile the cross sections of $N_1 N_1$ and $C_1 N_1$ are small in these models due to the absence of $Z\tilde{B}\tilde{B}$, $\gamma\tilde{B}\tilde{B}$ and $W^{\pm}\tilde{W}^{\mp}\tilde{B}$ couplings. For moderate values of the gaugino masses (i.e, just above those excluded by LEP) the squark masses are so large as to have negligible cross section.

As an example, setting $\Lambda = 100$ TeV leads to

$$M_{C_1} \approx M_{\tilde{W}} \approx M_2 \approx \frac{(1/29.68)}{4\pi} \cdot (100 \text{ TeV}) = 268 \quad \text{GeV}. \tag{6.9}$$

To summarize, the Minimal Gauge-Mediated Model can be completely described by three parameters: the $SU(2)$ gaugino mass M_2, the ratio of the Higgs vacuum expectation values $\tan\beta$, and the sign (+ or -) of the Higgs mixing parameter Sgn(μ). For most of parameter space pair-production of sparticles (dominated by gaugino pair production) eventually leads to final states producing $\gamma\gamma + \not{E}_{\mathrm{T}}$.

Full calculations and simulations are done using the SPYTHIA Monte Carlo and a detector simulation [54, 115, 116, 117] for a total of 50 points in parameter space: $M_2 = 75$, 100, 125, 150 and 200 GeV, $\tan\beta = 1.1$, 2, 5, 10 and 25 and Sgn(μ)= ± 1. Figure 6.1 shows the gaugino masses vs. M_2. Figure 6.2 shows the dominant production cross sections, again vs. M_2. Figure 6.3 shows distributions in $\mathrm{E_T}$ of the photons and $\not{E}_{\mathrm{T}}$ (after simulation and the full diphoton and $\Delta\phi_{\not{E}_{\mathrm{T}}-\mathrm{jet}}$ requirements of Section 3.1) for $M_2 = 150$ GeV, $\tan\beta = 10$ and Sgn(μ)= 1.

6.2.2 The $N_2 \to \gamma N_1$ Model

The $N_2 \to \gamma N_1$ model of Kane *et al.* [20, 27, 118] is more typical of Supergravity scenarios [17] except that it only encompases a small amount of parameter space. The model predicts the N_2 to be pure photino, N_1 to be pure higgsino and the higgsino to be lighter than the photino. This is accomplished by setting $M_1 \approx M_2$, $\tan\beta \approx 1$ and $-M_1 \leq \mu \leq 0$. With these conditions the Supersymmetric breaking scale, Λ, and consequently the gravitino mass, are large. In this case, the N_1 is the LSP, or is at least long-lived enough to escape the detector. The dominant decay of the N_2 is through the one-loop

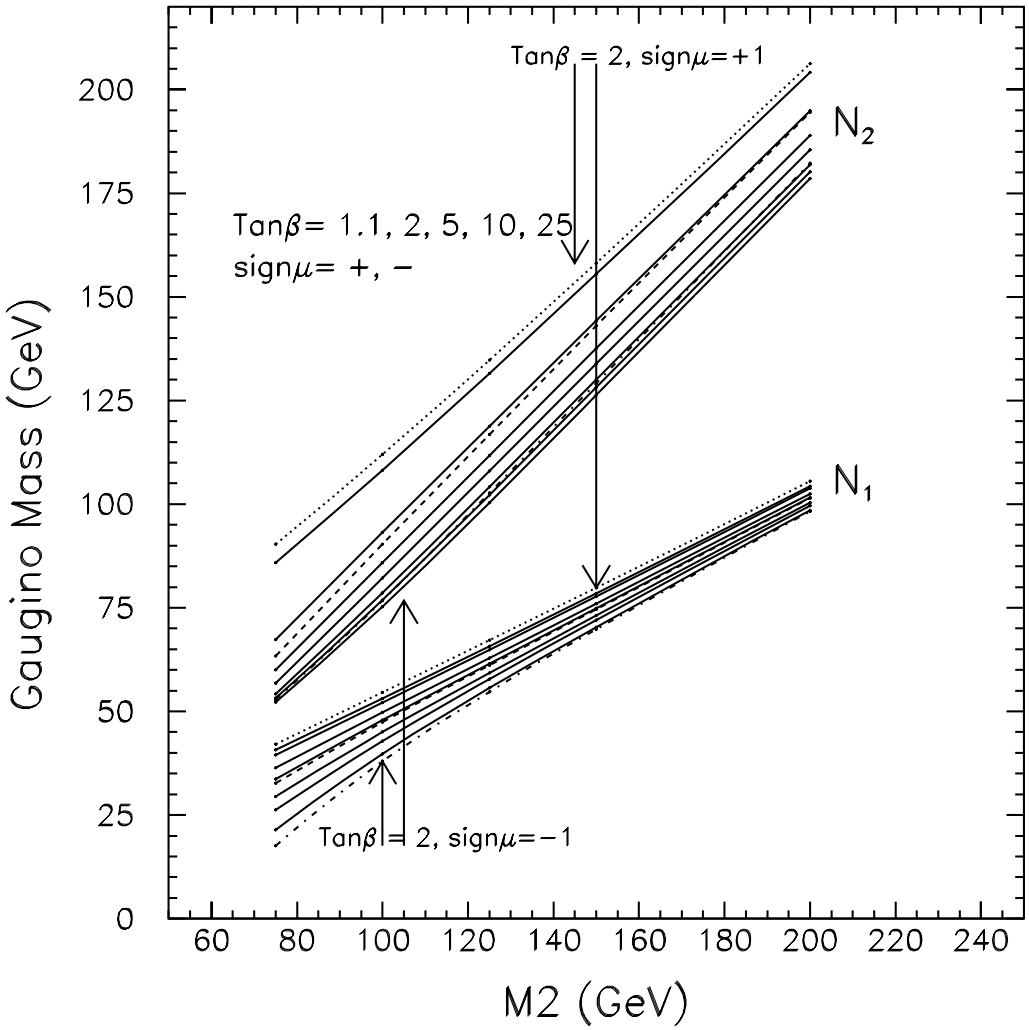

Figure 6.1: Masses of the gauginos vs. M_2 in the Minimal Gauge-Mediated Model. Each line corresponds to a different choice of $\tan\beta$ and $\mathrm{Sgn}(\mu)$.

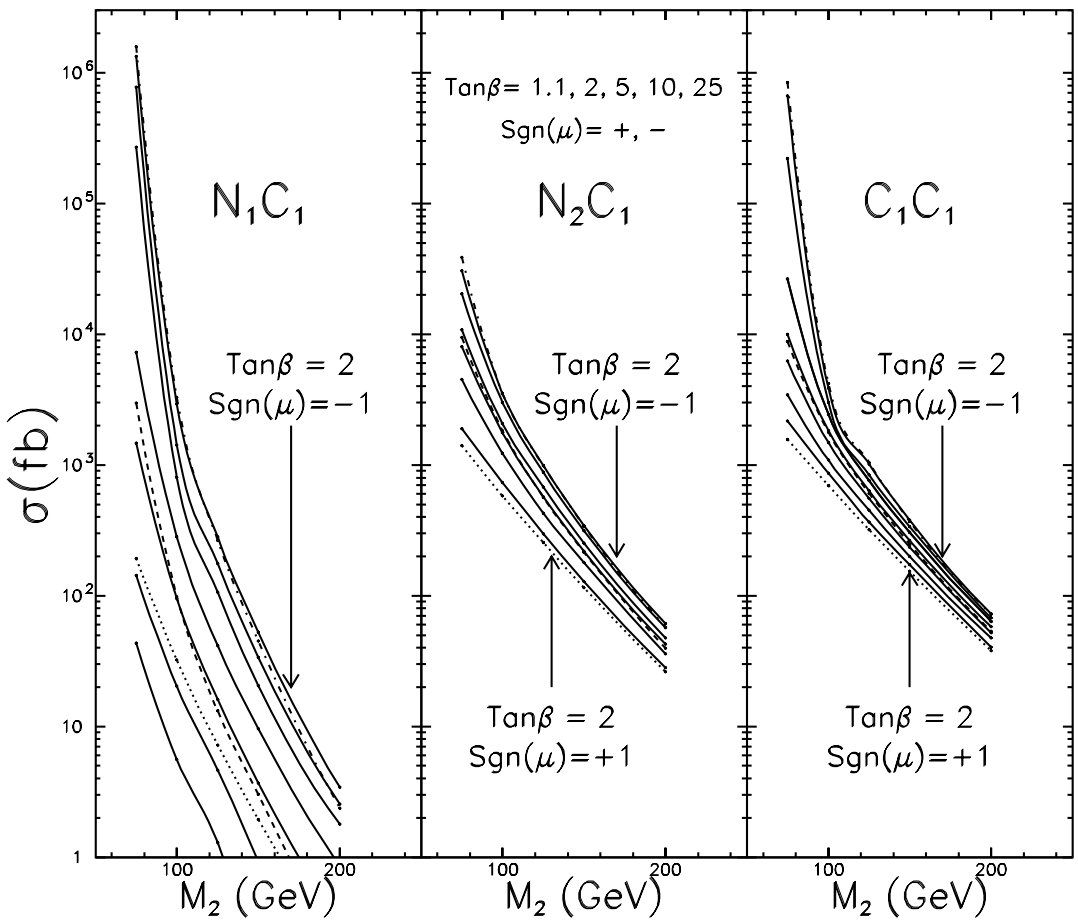

Figure 6.2: The dominant sparticle production cross sections vs. M_2 in the Minimal Gauge-Mediated Model. Each line corresponds to a different choice of $\tan\beta$ and $\mathrm{Sgn}(\mu)$.

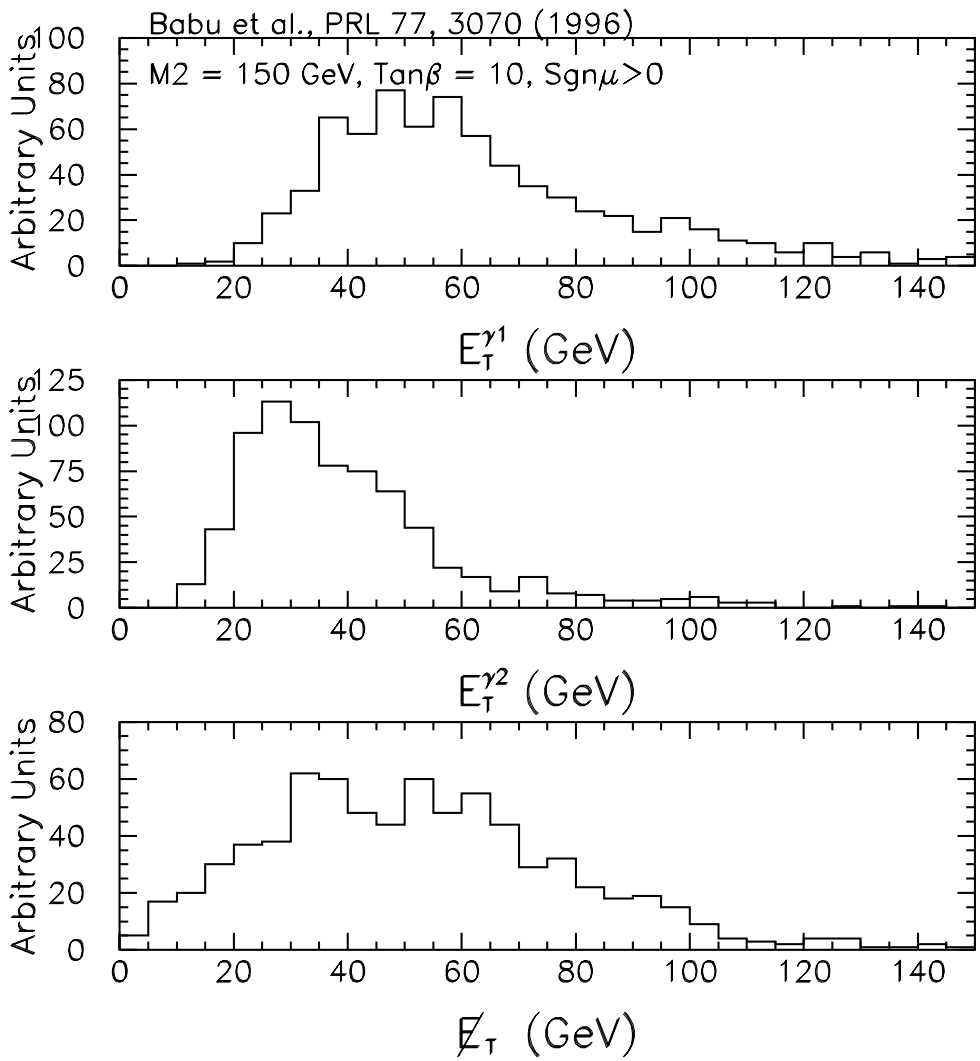

Figure 6.3: The distributions in E_T of the photons and $\not{E}_T$ in the Minimal Gauge-Mediated Model with $M_2 = 150$ GeV, $\tan\beta = 10$ and Sgn(μ)= 1. The sample is normalized to 5000 events generated, which correspond to an integrated luminosity of 7,163 pb^{-1}.

radiative decay and has $\mathrm{Br}(N_2 \to \gamma N_1) \approx 100\%$. The $ee\gamma\gamma\not{E}_{\mathrm{T}}$ signature can be produced, for example, via:

$$\tilde{e}_L\tilde{e}_L \to (eN_2)(eN_2) \to e(\gamma N_1)e(\gamma N_1) \to ee\gamma\gamma\not{E}_{\mathrm{T}}. \tag{6.10}$$

For concreteness, limits are set on a particular point in parameter space [119]. The parameters, listed in Table 6.2, are selected assuming that the $ee\gamma\gamma\not{E}_{\mathrm{T}}$ candidate event is in fact an $ee\gamma\gamma\not{E}_{\mathrm{T}}$ event, is due to the pair-production and decay of selectrons as in Equation 6.10, and is produced at a typical cross section (≈ 1 fb^{-1}). For these parameters, $\mathrm{M}_{N_1} = 36.6$ GeV, $\mathrm{M}_{N_2} = 64.6$ GeV and the total sparticle production cross section is 11.5 pb.

To provide a normalization point for future model-builders to estimate the detector efficiency, N_2N_2 production ($\sigma_{N_2N_2} \approx 2$ fb) is used to set cross section limits. The distributions in E_{T} of the photons and $\not{E}_{\mathrm{T}}$ (after simulation and the full diphoton and $\Delta\phi_{\not{E}_{\mathrm{T}}-\mathrm{jet}}$ requirements of Section 3.1) are shown in Figure 6.4.

6.3 Acceptances and Limits Setting

The acceptance for a given model is determined using the following equation:

$$Acc = \Sigma A^i_{\mathrm{MC}} \times C^i_{(\mathrm{ID\ and\ Iso})} \times C_{z_{\mathrm{vertex}}} \times C_{\mathrm{ETOUT}} \times C^i_{\mathrm{Trig}} \tag{6.11}$$

where the index, i, is for the two different regions (12 GeV $< \mathrm{E}_{\mathrm{T}}^{\gamma_2} <$22 GeV and $\mathrm{E}_{\mathrm{T}}^{\gamma_2} >$22 GeV) to take into account the different trigger requirements and photon selections, A^i_{MC} is the acceptance from the Monte Carlo using the full detector simulation for the different regions, $C^i_{(\mathrm{ID\ and\ Iso})}$ is the correction for differences between photon identification and isolation variables in the data

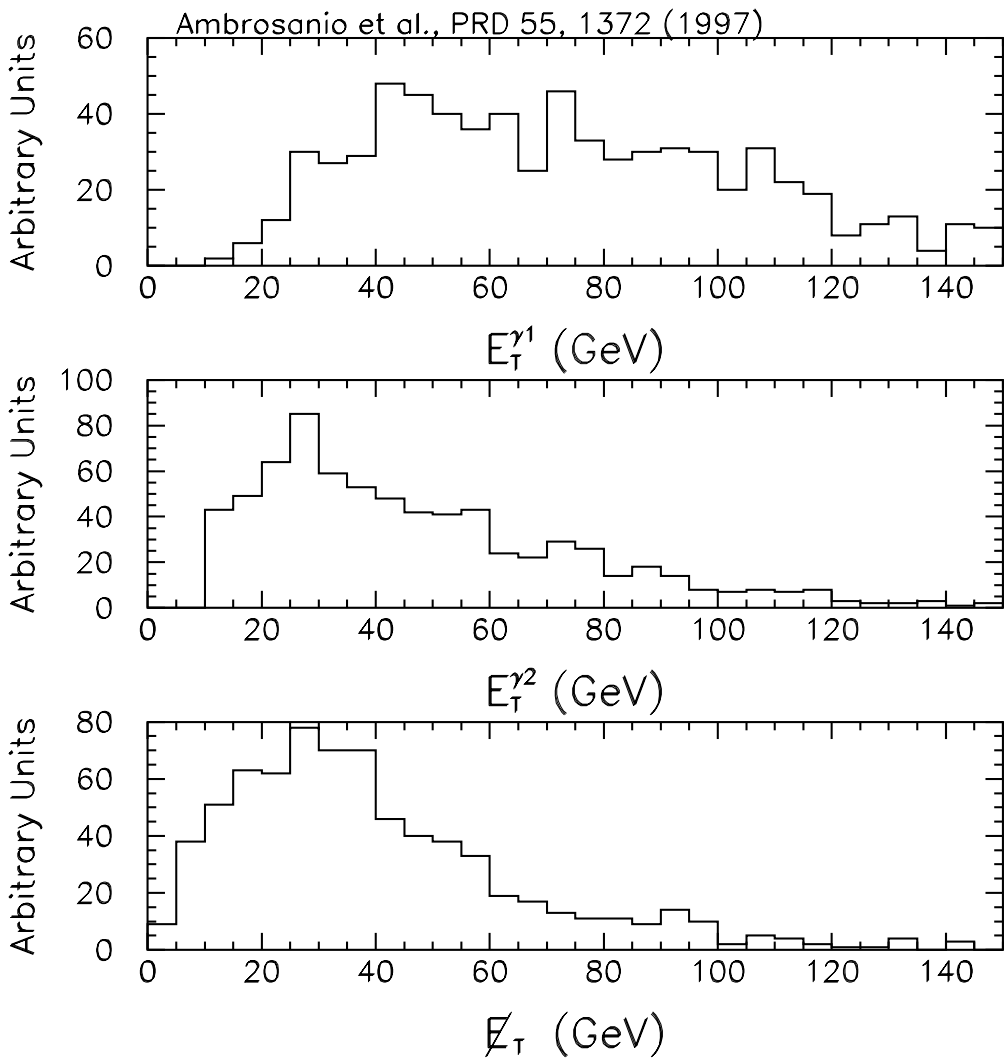

Figure 6.4: The distributions in E_T of the photons and $\not{E}_T$ for N_2N_2 production in the $N_2 \to \gamma N_1$ model with $M_{N_2} = 64.6$ GeV, and $M_{N_1} = 36.6$ GeV. The sample is normalized to 5000 events generated, which correspond to a luminosity of 2,272 fb^{-1}.

Parameter	Value
SFermions	
$M_{SQuarks}$	500.0 GeV
$M_{Left-Handed\,SLeptons}$	105.0 GeV
$M_{Right-Handed\,SLeptons}$	272.0 GeV
$M_{Left-Handed\,SNeutrinos}$	99.6 GeV
$M_{Right-Handed\,SNeutrinos}$	(don't exist)
Electroweak Sector	
$\tan\beta$	1.18
μ	-37.0 GeV
M_1	64.7 GeV
M_2	64.3 GeV
Gluino Mass	
$M_3 = M_{Gluino}$	225.0 GeV
Higgs Sector	
M_h	70.2 GeV
M_H	229 GeV
M_A	200 GeV
M_{H^+}	216 GeV
Chargino/Neutralino Masses	
M_{N_1}	36.6 GeV
M_{N_2}	64.6 GeV
M_{N_3}	90.5 GeV
M_{N_4}	118 GeV
M_{C_1}	79.6 GeV
M_{C_2}	110 GeV
N_2/N_1 Constraints	
$< N_1\|\tilde{H}_b >^2$	0.997
$< N_2\|\tilde{\gamma} >^2$	1.000
$Br(N_2 \to \gamma N_1)$	$\approx 100\%$

Table 6.2: The parameters used to simulate the $N_2 \to \gamma N_1$ scenario. These are taken from Ref.[27], Appendix B, Table 12.

and in the detector simulation, $C_{z_{\rm vertex}}$ is the correction for differences between the distributions of the interaction point, $z_{\rm vertex}$, in the data and that simulated in Monte Carlo, $C_{\rm ETOUT}$ is the efficiency of the energy-out-of-time requirement and $C^i_{\rm Trig}$ is the correction for the trigger efficiency.

After a full simulation of the model using the Monte Carlo and detector simulation [54, 115] the acceptance, $A_{\rm MC}$, is determined using

$$A_{\rm MC} = \frac{N_{\rm Passing\ all\ Selection\ Criteria}}{N_{\rm Simulated}} \tag{6.12}$$

where $N_{\rm Passing\ all\ Selection\ Criteria}$ is the number of events in the sample passing the selection criteria of Section 3.1 and $N_{\rm Simulated}$ is the number of simulated events. The remaining corrections (taken from Chapter 2) are summarized in Table 6.3.

Correction	12 GeV $< E_T^{\gamma 2} <$22 GeV Sample	$E_T^{\gamma 2} >$22 GeV Sample
ID and Iso	0.69 ± 0.07	0.84 ± 0.08
$\lvert z_{\rm vertex}\rvert < 60$ cm	0.965 ± 0.008	0.965 ± 0.008
ETOUT = 0	0.975 ± 0.004	0.975 ± 0.004
Trigger	0.96 ± 0.01	1.0
Total Correction	0.62 ± 0.06	0.79 ± 0.08

Table 6.3: The corrections used to take into account differences between the true detector response and the detector simulation. The identification and isolation requirement corrections are labeled as ID and Iso. The energy out-of-time requirement correction is labeled as ETOUT.

The 95% C.L. cross section upper limit, $\sigma^{95\% C.L.}$, is set by counting the number of events in the data (without a background subtraction) above the E_T^γ and $\not{E}_T$ thresholds. The cross section, σ is related to the number of observed events, N, by the relation:

$$\sigma = \frac{N}{L \cdot Acc} \tag{6.13}$$

where the luminosity, L = 85±6.8 pb^{-1}. The 95% C.L. upper limit on the cross section is defined such that 95% of the time (including systematic and

statistical uncertainties [120]) the number of 'observed' signal events in a series of pseudo-experiments is more than the number of observed events in the data. To find this cross section a Monte Carlo ensemble of 25,000 pseudo-experiments is used to simulate the number of 'expected' signal events for a cross section.

6.4 Results

A single set of requirements, $E_T^\gamma > 12$ GeV and $\not{E}_T > 35$ GeV, is chosen as it is estimated to exclude the maximal amount of parameter space for the light gravitino model [121]. The acceptances are typically between 1% and 10%, as shown in Figure 6.5 in the $\tan\beta$ vs. M_2 plane. Figure 6.6 shows the number of expected events in the same plane. The acceptance and number of expected events vs. the N_1 mass are shown in Figure 6.7.

Only one event in the diphoton data sample passes the requirements (the $ee\gamma\gamma\not{E}_T$ candidate event). The 95% C.L. upper limits are summarized in Tables 6.4 and 6.5. Figures 6.8 and 6.9 show the contour plot of the excluded region in the $\tan\beta$ vs. M_2 plane and $\tan\beta$ vs. C_1 mass plane, respectively. Figures 6.10 and 6.11 show the limits as a function of the N_1 and C_1 masses, respectively. The lines show the experimental limit and the theoretically predicted cross section for the lowest value of the N_1 or C_1 mass which is excluded. The N_1 is excluded for $M_{N_1} < 65$ GeV at 95% C.L. (this occurs at $\tan\beta = 5$, $\mu > 0$). The C_1 is excluded for $M_{C_1} < 120$ GeV at 95% C.L. (this occurs at $\tan\beta = 5$, $\mu < 0$) respectively.

The same selection criteria are used for the $N_2 \to \gamma N_1$ model with the results given in Table 6.6. The model is not excluded by the data as only 2.4 events from all sparticle production and decay are expected to pass the selection criteria. To provide a normalization point for those interested, the de-

tector efficiency and 95% C.L. upper limit for N_2N_2 production ($\sigma_{N_2N_2} \approx 2$ fb) is estimated. The acceptance is 5.4% with a 95% C.L. cross section upper limit of 1.1 pb. These results, along with the light gravitino results, are comparable [122] to those of LEP [123] and the DØ collaboration [124].

6.5 Conclusions

The diphoton data set is clearly a good place to search for new physics. The fact that there are no $\gamma\gamma+ \geq 3$ jets in the data excludes a model of anomalous $WW\gamma\gamma$ production as the source of the $ee\gamma\gamma\not{E}_{\mathrm{T}}$ candidate at 95% C.L. Similarly, the diphoton + $\not{E}_{\mathrm{T}}$ data show no evidence for new physics with the possible exception of the $ee\gamma\gamma\not{E}_{\mathrm{T}}$ candidate event. Although, we have some sensitivity to Supersymmetric models with photonic final states, there is a large amount of parameter space which remains unexplored. More data is required.

M_2 GeV	$\tan\beta$	$\frac{\lvert\mu\rvert}{\mu}$	M_{N_1} GeV	M_{C_1} GeV	$\sigma^{95\%C.L.}$ (pb)	σ^{Theory} (pb)	Acc (%)	Events (85 pb^{-1})
75	1.1	1	40.7	85.3	2.06	5.84	2.8(3)	14(1)
75	1.1	-1	32.7	61.5	5.83	25.64	1.0(2)	22(4)
75	2	1	42.1	90.1	2.13	4.44	2.7(3)	10(1)
75	2	-1	17.7	38.6	1851	2466	0.003(1)	7(2)
75	5	1	39.5	70.3	5.34	9.84	1.1(2)	9(2)
75	5	-1	21.5	40.0	1484	2046	0.005(2)	9(3)
75	10	1	36.4	61.0	12.41	19.12	0.5(1)	9(2)
75	10	-1	26.2	45.1	517	1033	0.013(3)	11(3)
75	25	1	33.7	55.6	11.48	38.02	0.6(1)	18(4)
75	25	-1	29.4	49.1	115.6	327.8	0.052(9)	15(3)
100	1.1	1	53.1	107.9	1.20	1.94	4.8(4)	7.9(7)
100	1.1	-1	47.4	89.5	1.68	4.16	3.4(3)	12(1)
100	2	1	54.6	111.7	1.16	1.57	4.9(4)	6.6(5)
100	2	-1	38.0	69.3	5.93	11.47	1.0(2)	10(2)
100	5	1	52.1	94.9	1.29	2.66	4.5(4)	10.1(9)
100	5	-1	39.7	68.4	5.80	11.28	1.0(2)	10(2)
100	10	1	49.7	86.5	1.87	3.73	3.1(3)	10(1)
100	10	-1	42.8	72.5	3.96	8.08	1.5(2)	10(1)
100	25	1	47.8	81.6	1.86	4.68	3.1(3)	12(1)
100	25	-1	45.0	75.9	2.14	6.40	2.7(3)	15(2)
125	1.1	1	65.7	131.4	0.77	0.77	7.4(5)	4.8(4)
125	1.1	-1	61.1	116.4	0.93	1.30	6.1(5)	6.8(5)
125	2	1	67.2	134.6	0.78	0.67	7.3(5)	4.2(3)
125	2	-1	54.7	98.4	1.48	2.40	3.9(4)	8.0(7)
125	5	1	64.8	119.9	0.96	0.99	5.9(5)	5.0(4)
125	5	-1	55.6	96.2	1.60	2.42	3.6(3)	7.4(7)
125	10	1	62.9	112.2	0.93	1.27	6.1(5)	6.6(5)
125	10	-1	57.8	99.5	1.21	2.04	4.7(4)	8.2(7)
125	25	1	61.5	107.7	0.91	1.51	6.3(5)	8.0(6)
125	25	-1	59.3	102.5	0.94	1.83	6.1(5)	9.4(7)

Table 6.4: The number of expected events, acceptances and the 95% C.L. cross section upper limits for the Minimal Gauge-Mediated Model with $M_2 < 150$ GeV. The parenthesis represent the uncertainty in the last digit. The acceptance, Acc, is as defined in Equation 6.11. The uncertainty on the number of expected events includes only the uncertainty in the acceptance.

M_2 GeV	$\tan\beta$	$\frac{\lvert\mu\rvert}{\mu}$	M_{N_1} GeV	M_{C_1} GeV	$\sigma^{95\%C.L.}$ (pb)	σ^{Theory} (pb)	Acc (%)	Events (85 pb^{-1})
150	1.1	1	78.4	155.4	0.60	0.34	9.4(6)	2.8(2)
150	1.1	-1	74.6	142.7	0.70	0.51	8.2(6)	3.6(3)
150	2	1	79.8	158.1	0.68	0.31	8.4(6)	2.2(2)
150	2	-1	69.8	126.5	0.83	0.80	6.9(5)	4.7(4)
150	5	1	77.7	144.9	0.72	0.42	7.9(6)	2.8(2)
150	5	-1	70.4	123.5	0.83	0.82	6.8(5)	4.8(4)
150	10	1	76.0	137.9	0.69	0.51	8.1(6)	3.5(3)
150	10	-1	72.0	126.3	0.79	0.74	7.3(5)	4.6(3)
150	25	1	74.8	133.6	0.73	0.59	7.9(6)	3.9(3)
150	25	-1	73.2	128.9	0.72	0.68	8.0(6)	4.6(3)
200	1.1	1	104.3	204.2	0.72	0.08	7.9(6)	0.53(4)
200	1.1	-1	101.4	194.4	0.68	0.10	8.3(6)	0.73(5)
200	2	1	105.5	206.2	0.69	0.07	8.3(6)	0.52(4)
200	2	-1	98.2	181.0	0.76	0.14	7.5(6)	0.90(7)
200	5	1	103.8	195.2	0.63	0.09	9.0(6)	0.71(5)
200	5	-1	98.5	177.0	0.58	0.15	9.9(7)	1.25(9)
200	10	1	102.5	189.0	0.55	0.11	10.4(7)	0.93(6)
200	10	-1	99.6	179.0	0.57	0.14	9.9(7)	1.16(8)
200	25	1	101.6	185.3	0.52	0.12	10.8(7)	1.10(7)
200	25	-1	100.4	181.2	0.56	0.13	10.1(7)	1.13(8)

Table 6.5: The number of expected events, acceptances and the 95% C.L. cross section upper limits for the Minimal Gauge-Mediated Model with $M_2 > 150$ GeV. The parenthesis represent the uncertainty in the last digit. The acceptance, Acc, is as defined in Equation 6.11. The uncertainty on the number of expected events includes only the uncertainty in the acceptance.

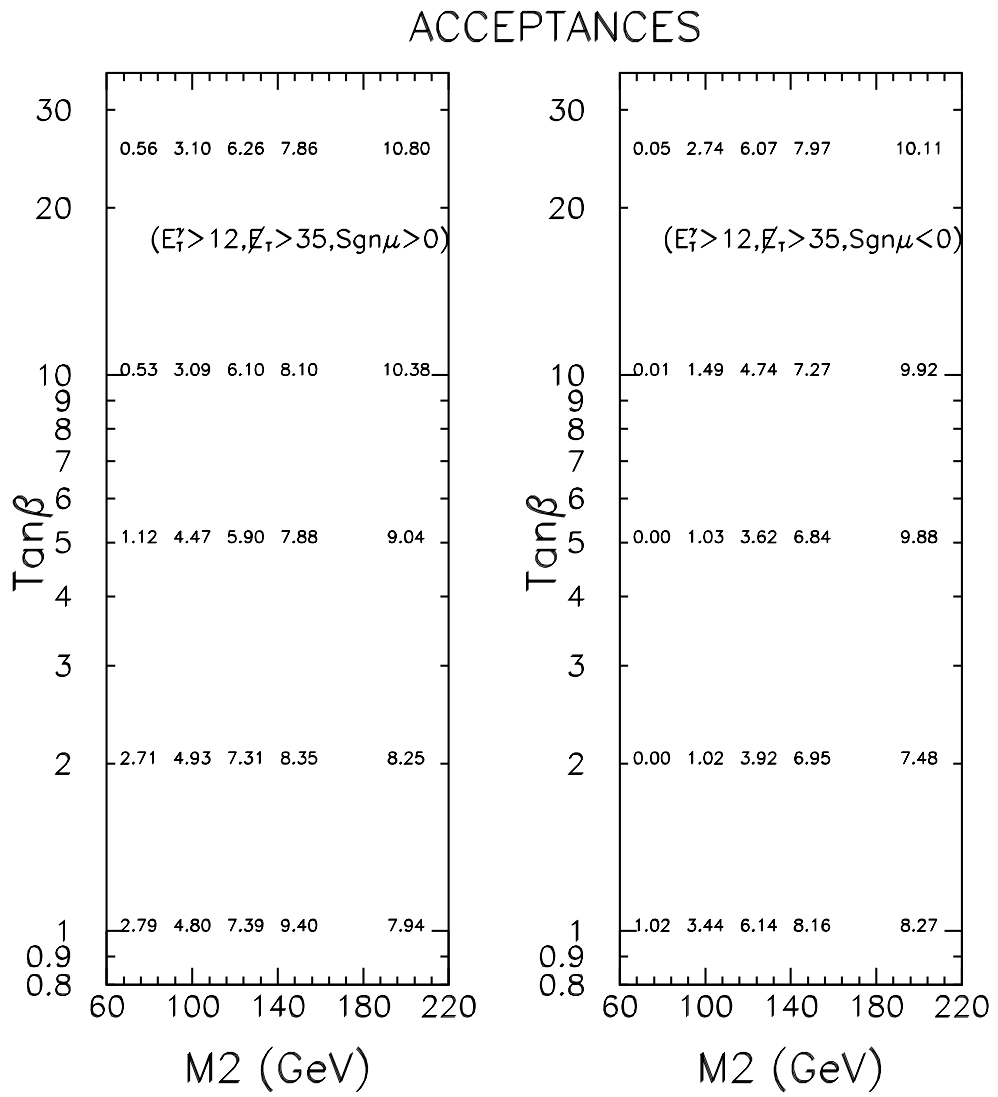

Figure 6.5: The acceptances for various points in the $\tan\beta$ vs. M_2 plane in the Minimal Gauge-Mediated Model. The left hand plot shows the acceptance for Sgn(μ)>0, the right hand for Sgn(μ)<0.

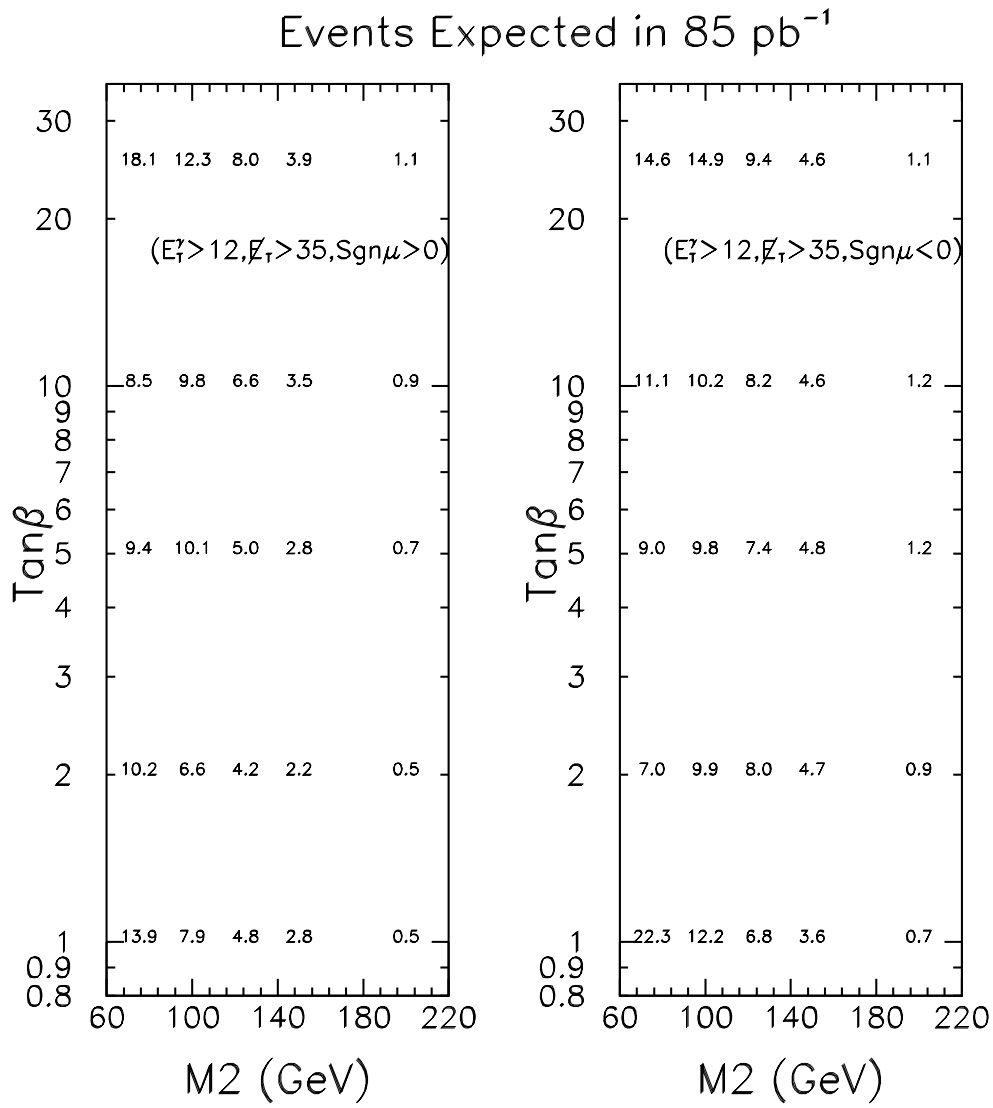

Figure 6.6: The number of expected events for various points in the $\tan\beta$ vs. M_2 plane in the Minimal Gauge-Mediated Model. The left hand plot shows the acceptance for Sgn(μ)> 0, the right hand for Sgn(μ)< 0.

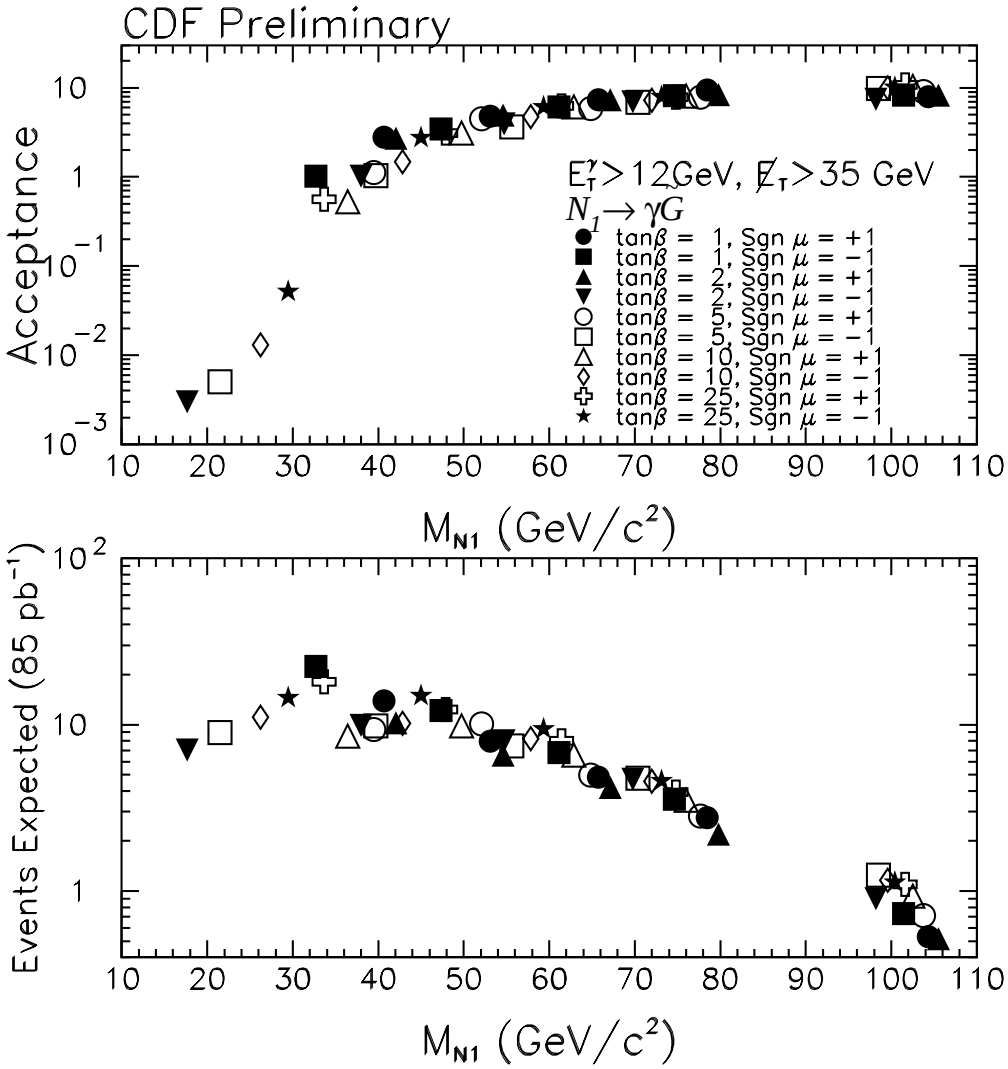

Figure 6.7: The acceptances (upper plot) and the number of expected events (lower plot) for various points plotted vs. the N_1 mass in the Minimal Gauge-Mediated Model.

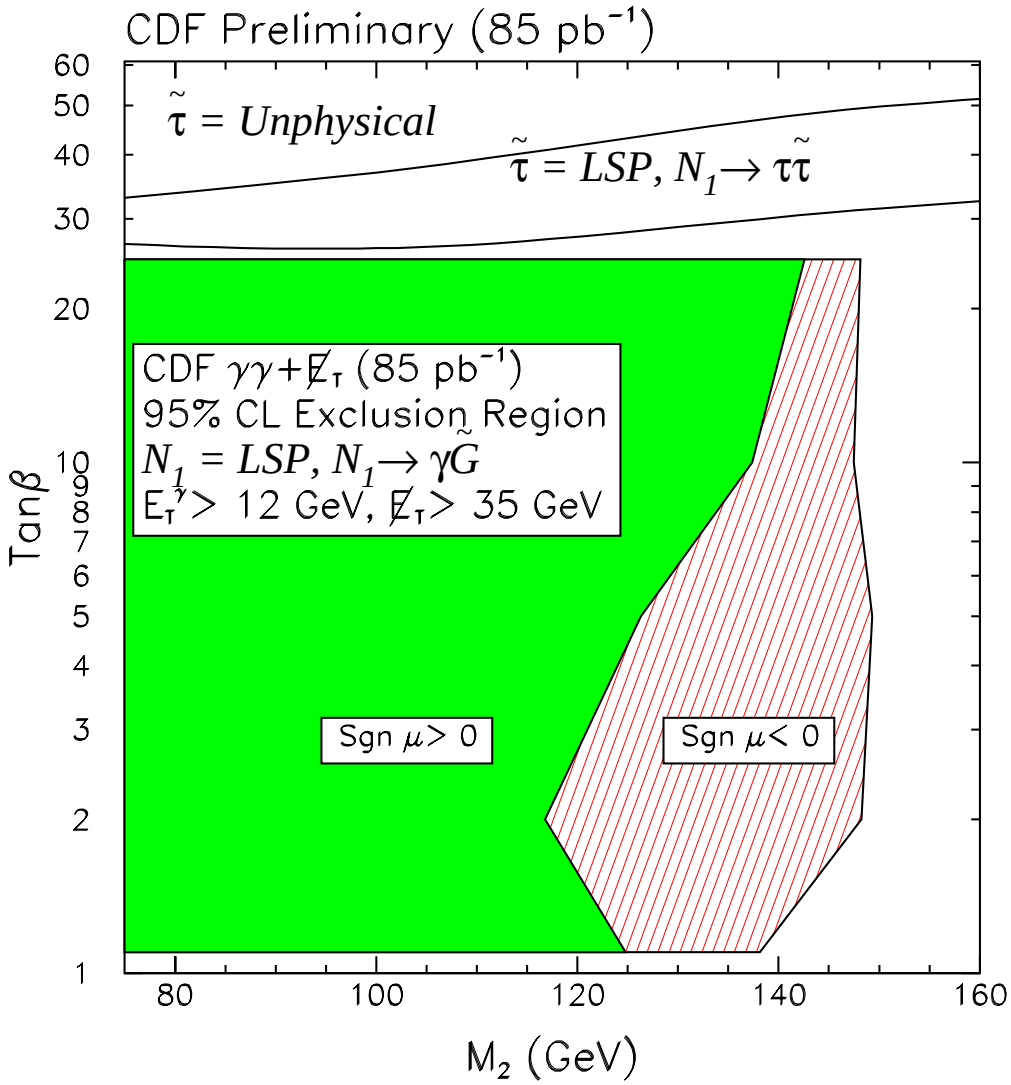

Figure 6.8: The contour plot of the excluded region of the Minimal Gauge-Mediated Model in the $\tan\beta$ vs. M_2 plane.

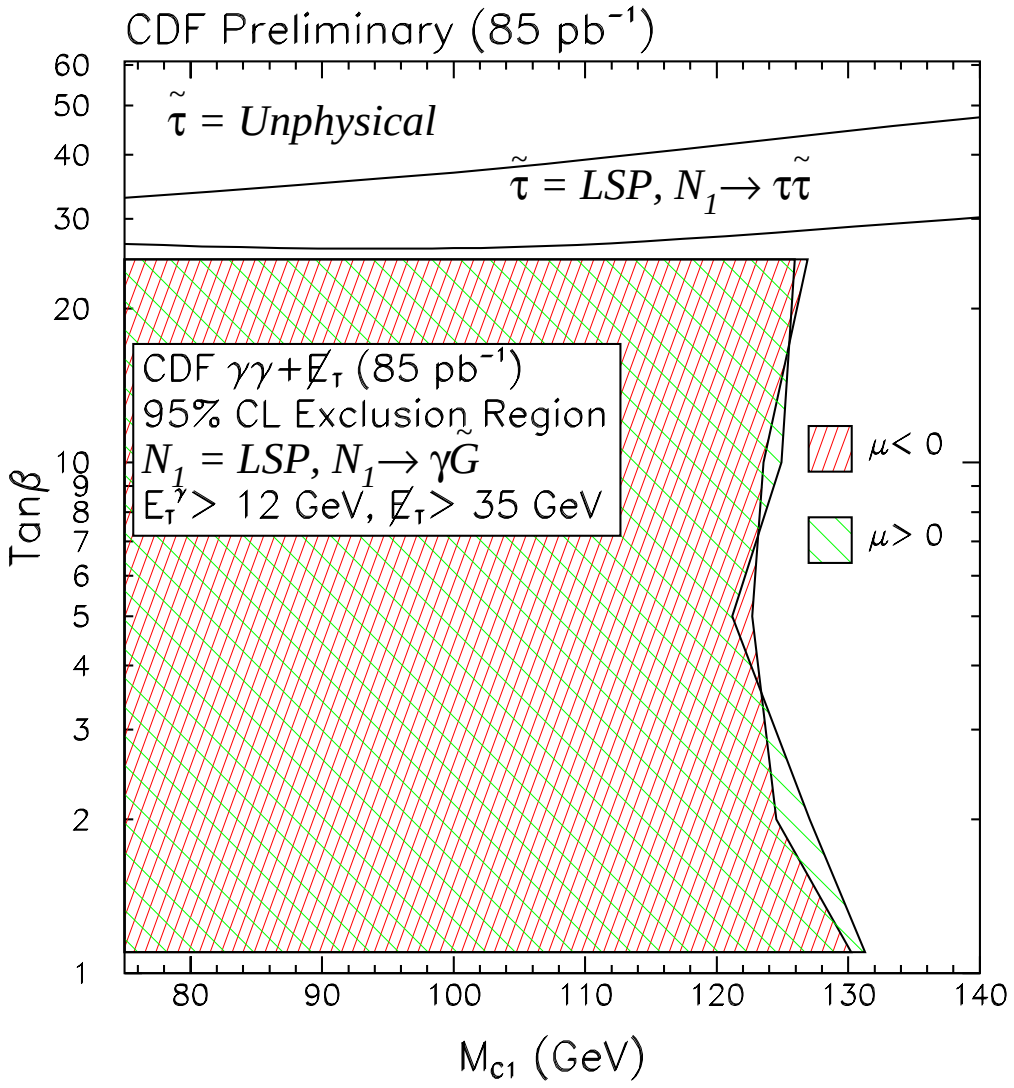

Figure 6.9: The contour plot of the excluded region of the Minimal Gauge-Mediated Model in the $\tan\beta$ vs. C_1 mass plane.

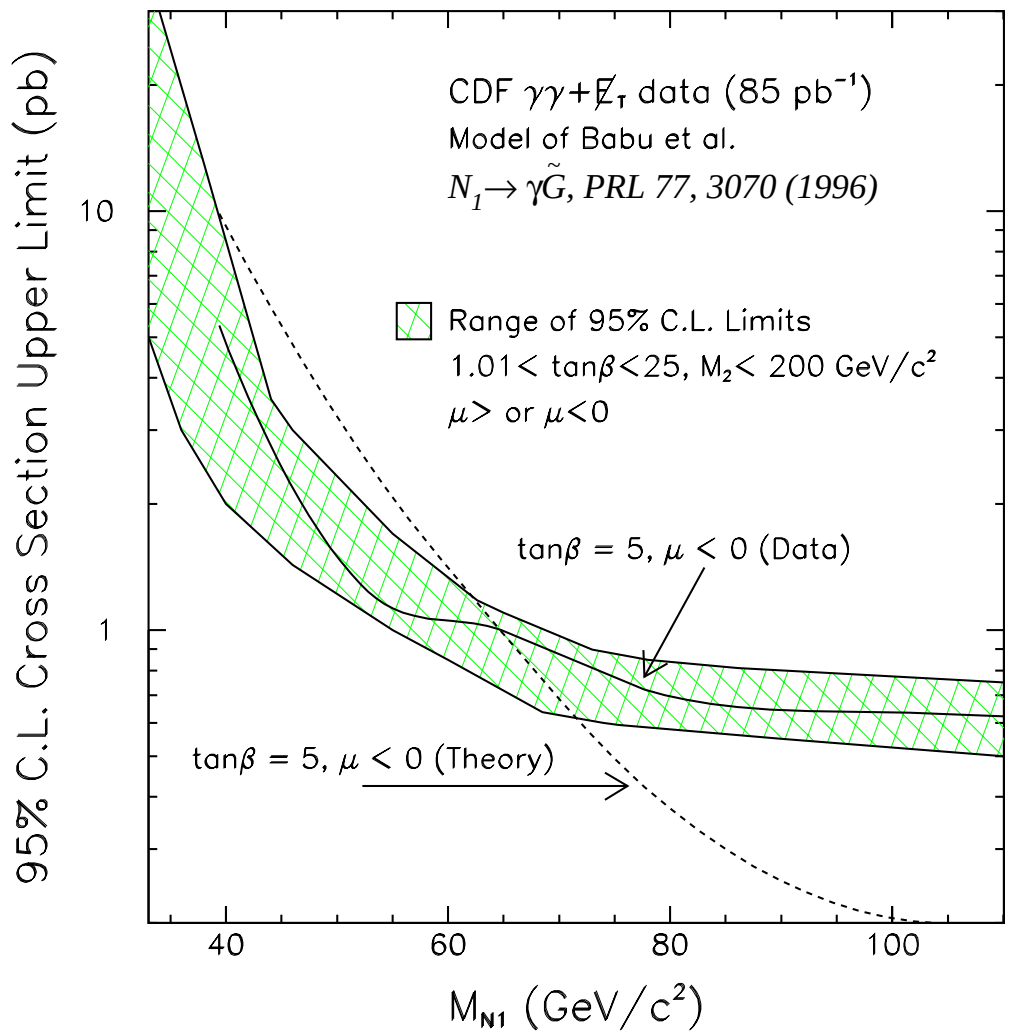

Figure 6.10: The 95% C.L. cross section upper limit from the data vs. the N_1 mass in the Minimal Gauge-Mediated Model. The shaded region shows the range of cross section limits as the parameters are varied within the ranges $1 < \tan\beta < 25, M_2 < 200$ GeV, and $\mu > 0$ or $\mu < 0$. The lines show the experimental limit (solid line) and the theoretically predicted cross section (dashed line) for the lowest value of M_{N_1} that is excluded ($\mathrm{M}_{N_1} < 65$ GeV at 95% C.L., for $\tan\beta = 5$, $\mu > 0$).

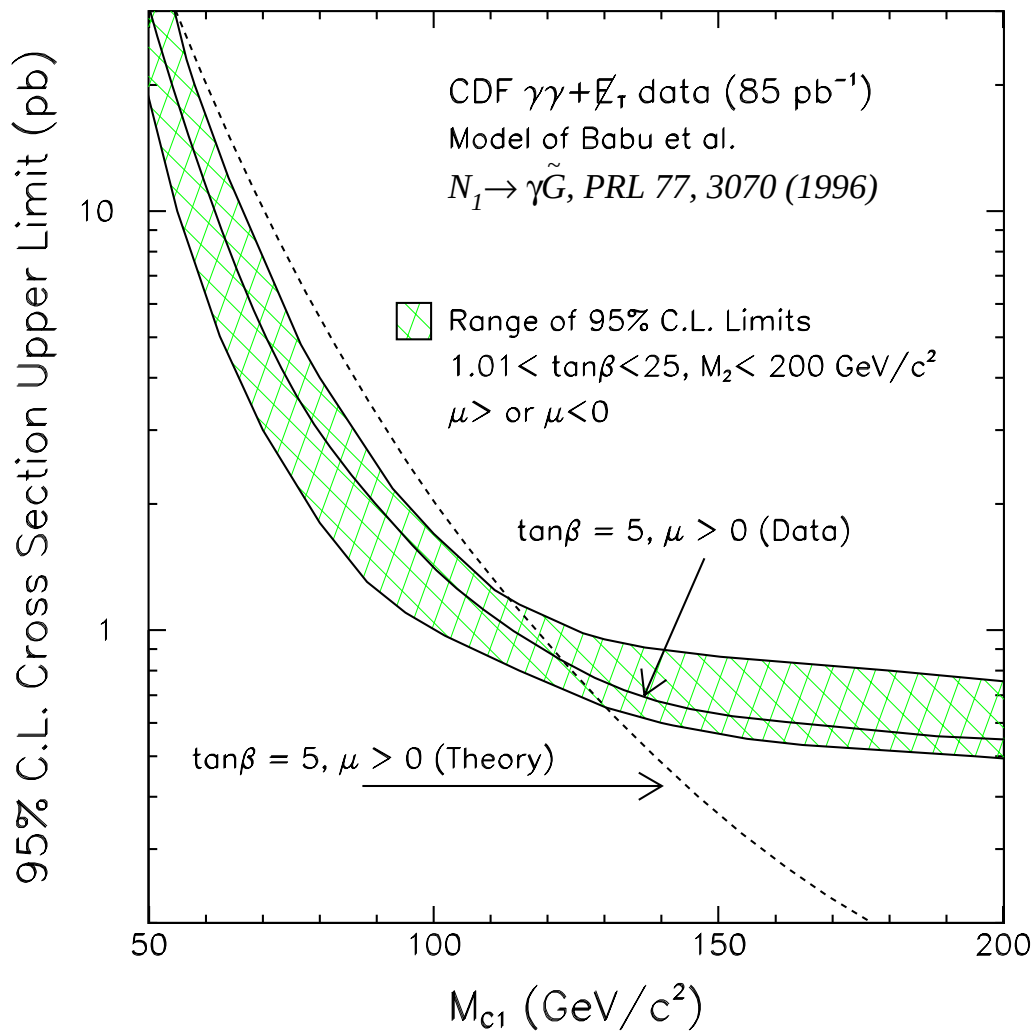

Figure 6.11: The 95% C.L. cross section upper limit from the data vs. the C_1 mass in the Minimal Gauge-Mediated Model. The shaded region shows the range of cross section limits as the parameters are varied within the ranges $1 < \tan\beta < 25, M_2 < 200$ GeV, and $\mu > 0$ or $\mu < 0$. The lines show the experimental limit (solid line) and the theoretically predicted cross section (dashed line) for the lowest value of M_{C_1} that is excluded ($M_{C_1} < 120$ GeV at 95% C.L., for $\tan\beta = 5$, $\mu < 0$).

Results for all sparticle production					
M_{N_1} GeV	M_{N_2} GeV	$\sigma^{95\% C.L.}$ (pb)	σ^{Theory} (pb)	Acceptance (%)	Events (85 pb^{-1})
36.6	64.6	31.58	11.50	0.24± 0.08	2.355± 0.810

Results for N_2N_2 production					
M_{N_1} GeV	M_{N_2} GeV	$\sigma^{95\% C.L.}$ (fb)	σ^{Theory} (fb)	Acceptance (%)	Events (85 pb^{-1})
36.6	64.6	1054.00	2.21	5.43± 0.44	0.010± 0.001

Table 6.6: The number of expected events, acceptances and 95% C.L. cross section upper limits for the $N_2 \rightarrow \gamma N_1$ model with M_{N_2} = 64.6 GeV, and M_{N_1} = 36.6 GeV. This model is not excluded. Results for N_2N_2 production are reported for reference, although the cross section is much to low to be detectable with this data set.

Chapter 7

Conclusion

If you come to a fork in the road, take it.

- Yogi Berra (New York Yankees)

How the hell should I know what it is?? I don't even know how a can opener works!

- Woody Allen

We have searched a sample of 85 pb^{-1} of $p\bar{p}$ collisions for events with two central photons and anomalous production of missing transverse energy, jets, charged leptons (e, μ, and τ), b-quarks and photons. We find good agreement with Standard Model expectations, with the possible exception of one event that sits on the tail of the $\not\!\!E_{\mathrm{T}}$ distribution as well as having a high-$\mathrm{E_T}$ central electron and a high-$\mathrm{E_T}$ electromagnetic cluster.

The $ee\gamma\gamma\not\!\!E_{\mathrm{T}}$ candidate event has sparked interest in the physics community. We have tried to address what we believe are the most important questions

1. What are the characteristics of the event?,

2. How many are expected from Standard Model sources?,

3. Are there any others like it? and

4. What is the origin of the event?

What are the characteristics of the event? Unfortunately, even after a detailed study, the answer is inconclusive. The most probable explanation is that this a single $\bar{p}p$ collision which produced a high-E_T, isolated electron, two high-E_T, isolated photons, a high-E_T isolated electromagnetic cluster which could be an electron, photon, tau or generic jet, and a significant amount of missing transverse energy.

How many are expected from Standard Model sources? A conservative estimate predicts that there should be a total of $(1 \pm 1) \times 10^{-6}$ events in the data with the $ee\gamma\gamma\not{E}_T$ signature. If sources which produce a second electron are excluded the rate drops to $(6 \pm 6) \times 10^{-8}$ events.

Are there any others like it? In this $\gamma\gamma + X$ search, with both photons in the central region, there are no others which would, by any reasonable or useful definition, be called *like* the $ee\gamma\gamma\not{E}_T$ candidate event. For completeness, we note that there is one event, a $\mu^+\mu^-\gamma\gamma jj$ candidate event [125] which is VERY similar to the $ee\gamma\gamma\not{E}_T$ candidate event. However, this event does not pass the *a priori* central photon selection criteria. A detailed description of the kinematics and properties of the event are given in Appendix A.

What is the origin of the event? The simplest interpretation of the event as anomalous $WW\gamma\gamma$ production is unlikely because there should be many more events with hadronic decays of the W in the data and none are observed. While a number of other scenarios are theoretically appealing, there is no experimental evidence for any of them.

The $ee\gamma\gamma\not{E}_{\mathrm{T}}$ candidate event is tantalizing. Perhaps it is a hint of physics beyond the Standard Model. Then again it may just be one of the rare Standard Model events that could show up in 10^{12} interactions. Only more data will tell.

Appendix A

The $\mu^+\mu^-\gamma\gamma jj$ Candidate Event

There is an event in the CDF Run 1 data which is very similar to the $ee\gamma\gamma\not{E}_{\mathrm{T}}$ candidate event, but is not a part of the central $\gamma\gamma$ dataset [126]. This event, a $\mu^+\mu^-\gamma\gamma jj$ candidate event, has one central photon and one photon candidate in the plug calorimeter and thus does not pass the *a priori* selection criteria. While a systematic study remains to be done, for completeness, this Appendix gives a detailed description of this unusual event and compares it to the $ee\gamma\gamma\not{E}_{\mathrm{T}}$ candidate event.

The event has been described as having two central muons with large invariant mass, a central photon, a photon in the plug calorimeter, two substantial central jets, and a large missing transverse energy. While the two muons in the event could be from a $Z^0 \to \mu^+\mu^-$ decay, the $\mu^+\mu^-$ mass is only consistent with being a Z^0 at the 6% level. A detailed study shows that the identification of the objects in the event (photons, muons and $\not{E}_{\mathrm{T}}$) is, as in the $ee\gamma\gamma\not{E}_{\mathrm{T}}$ candidate event, somewhat problematic. One of the muons does not pass one of the standard identification requirements; however, it looks golden in all other respects. In addition, one of the jets is rather diffuse. While each

of these problems causes the $\not\!\!E_T$, as calculated Section 3.1, to be incorrect, the vector sum of the P_T's of the muons, photons, and jets shows that the $\not\!\!E_T$ in the event is in fact very small.

A.1 Event Kinematics

The $\mu^+\mu^-\gamma\gamma jj$ candidate event (Run 65390, Event 16199) has two central muon candidates, one central photon candidate, one plug photon candidate, and two jets as shown in Figure A.1. Table A.1 gives the 4-vectors of the six objects in the event. The jets and $\not\!\!E_T$, for technical reasons, are treated in a manner which is slightly different from Chapter 3. These differences are discussed in Sections A.6 and A.7 respectively.

Run 65390, Event 16199					
	P_X	P_Y	P_Z	E	E_T
	(GeV)	(GeV)	(GeV)	(GeV)	(GeV)
μ^+	-20.20	53.00	-24.97	61.97	56.72
μ^-	-15.52	-52.46	-16.66	57.19	54.71
γ_1	8.91	47.52	30.21	57.00	48.35
γ_2	13.47	1.59	-20.76	24.80	13.57
J_1	28.88	-23.18	41.12	58.59	39.21
J_2	-8.26	-28.18	-26.35	40.29	29.98
$\not\!\!E_T$	-7.3	1.7	–	–	7.5

Table A.1: The 4-vectors of the $\mu^+\mu^-\gamma\gamma jj$ candidate event. All energies and momenta are corrected. The jets are clustered in a cone of $\Delta R = 0.7$ and the $\not\!\!E_T$ is the vector imbalance of the $\mu^+\mu^-\gamma\gamma jj$ system. The jet and $\not\!\!E_T$ selection and corrections are discussed in Sections A.6 and A.7 respectively.

The masses of various combinations of objects are given in Table A.2. The invariant mass of the muon pair is 105.8 GeV, close to the Z^0 mass. This is compared to a sample of muon pairs in Figure A.2 where both muons are

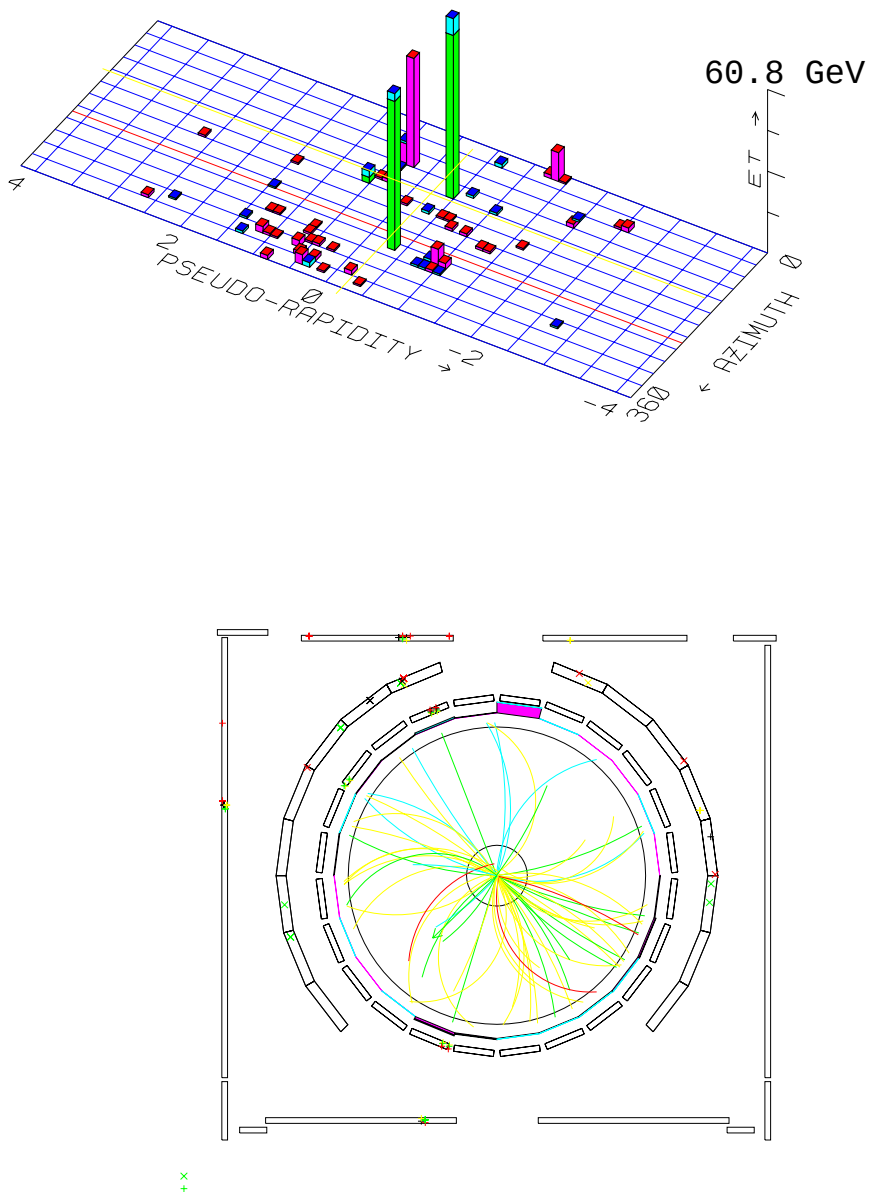

Figure A.1: The event display for the $\mu^+\mu^-\gamma\gamma jj$ candidate event.

required to pass the identification and isolation selection criteria used in the top-quark analysis (see Table 3.2) and have $P_T^{\mu} > 30$ GeV. A total of 97 of the 1,698 events in the sample (5.7%) have a dimuon mass greater than 105 GeV. One cannot rule out this being a Z^0, although it is unlikely at almost the 95% C.L. The $\mu^+\mu^-\gamma\gamma$ system has a mass of 192 GeV; highly unlikely to be from a radiative or double-radiative Z^0 decay. The invariant mass of the photon pair is 60.8 GeV. The invariant mass of the jet pair is 75.5 GeV, close to the W mass (the typical resolution on the $W \to jj$ mass is 10%). The second jet contains calorimeter energy in the tower traversed by the μ^-; correcting for this extra energy, the dijet mass is lowered to 68.6 GeV.

As shown in Table A.2, each sub-system has large P_T. The P_T of the dimuon pair is 36 GeV, the diphoton pair has a P_T of 54 GeV, and the P_T of the dijet system is 55.3 GeV, 49.5 GeV after corrections. Similarly, the $\mu^+\mu^-\gamma\gamma$ system has $P_T = 51.4$ GeV. However, since the total P_T of the $\mu^+\mu^-\gamma\gamma jj$ system is close to zero, any subset of the 6 objects in the event will balance the remaining subset. For example, the $\mu^+\mu^-\gamma\gamma$ system is back-to-back with the dijet system with transverse momenta that balance and are $\sim$50 GeV [127]. The pairings of three objects that give the closest match in mass are $\mu^+\gamma_1 J_2$ and $\mu^-\gamma_2 J_1$. The P_T is about 37 GeV for each system and three-body masses are 138 and 112 GeV, respectively. Alternatively, the $\mu^+\gamma_2 J_1$ and $\mu^-\gamma_1 J_2$ systems have a P_T of 75 GeV, and the masses are 137 GeV and 149 GeV, respectively.

A.2 The Interaction Vertex

The primary vertex [73] associated with the $\mu^+\mu^-\gamma\gamma jj$ candidate event is situated at $z = -45.6$ cm and has $\Sigma P_T = 149$ GeV of tracks (in-

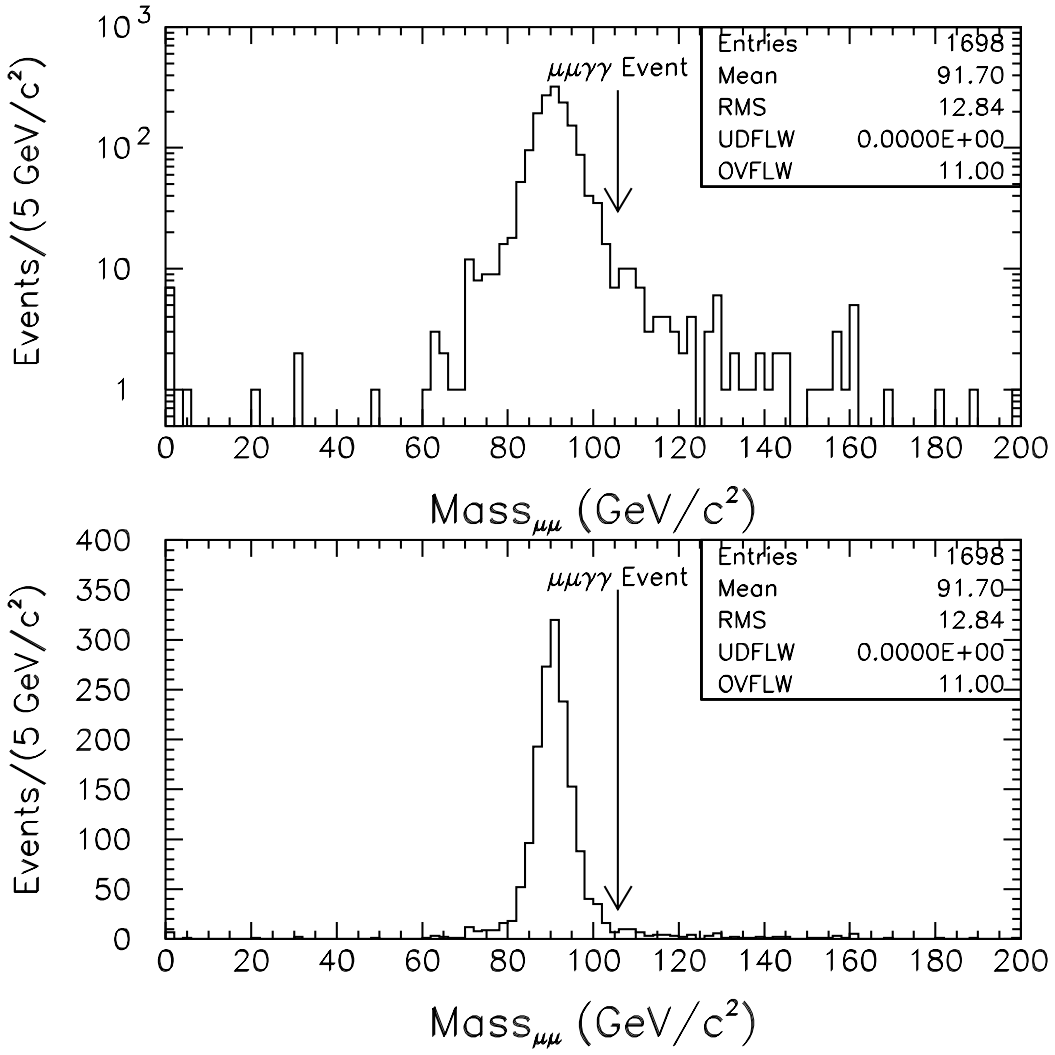

Figure A.2: The invariant mass of pairs of muons passing the tight identification and isolation selection criteria, each with $P_T^{\mu} > 30$ GeV.

System	Mass (GeV)	P_T^{System} (GeV)	ϕ (degrees)
$\mu^+\mu^-$	105.8	35.7	179°
$\gamma_1\gamma_2$	60.8	54.0	66°
J_1J_2	75.5	55.3	292°
$J_1J_2^{no\ \mu}$	68.6	49.5	297°
$\mu^+\gamma_1$	62.4	101.2	96°
$\mu^-\gamma_2$	52.2	50.9	268°
$\mu^+\gamma_2$	49.1	55.0	97°
$\mu^-\gamma_1$	113.1	8.3	217°
$\mu^+\mu^-\gamma_1$	167.0	55.0	119°
$J_1J_2\gamma_2$	103.1	60.3	304°
$\mu^+\mu^-\gamma_2$	127.8	22.3	175°
$J_1J_2\gamma_1$	141.9	29.8	253°
$\mu^+\gamma_1J_1$	148.1	79.3	72°
$\mu^-\gamma_2J_2$	65.8	79.7	262°
$\mu^+\gamma_1J_2$	138.0	74.9	105°
$\mu^-\gamma_2J_1$	112.4	78.6	289°
$\mu^+\gamma_2J_1$	136.7	38.4	55°
$\mu^-\gamma_1J_2$	148.8	36.0	246°
$\mu^+\gamma_2J_2$	99.1	30.4	120°
$\mu^-\gamma_1J_1$	156.4	35.9	308°
$\mu^+\mu^-\gamma_1\gamma_2$	191.6	51.4	105°
$\mu^+\mu^-\gamma_1\gamma_2J_1J_2$	295.0	7.5	347°

Table A.2: The mass and P_T for sub-systems of the $\mu^+\mu^-\gamma\gamma jj$ candidate event.

cluding 111 GeV from the central muons) associated with it. The instantaneous luminosity, $\mathcal{L}$, during this particular part of the run was measured to be $\mathcal{L} = 4.95 \times 10^{30}/(\mathrm{cm}^2 \cdot \mathrm{sec})$ which predicts that there should be, on average, 0.88 primary vertices. A total of 2 are observed. The other primary vertex in the event is situated at z = -28.1 cm and has 17 GeV of tracks associated with it. Both vertices are evident in Figures A.3 and Figure A.4, which show the number of tracks and the number of tracks weighted by P_T in the event

as a function of z and ϕ respectively. Both jets are clearly associated with the primary vertex.

The sum P_T of tracks associated with the second vertex is 17 GeV and is compared to the $Z^0 \rightarrow \mu^+\mu^-$ sample to see if this is unusual. A total of 49% of the events have at least two vertices. Figure A.5 shows the sum P_T of tracks associated with these other vertices if they are separated by at least 10 cm from the dimuon (first) vertex. A total of 7% of events with a second vertex have $>$ 17 GeV of associated ΣP_T. There is no indication that the second vertex in the $\mu^+\mu^-\gamma\gamma jj$ candidate event particularly energetic, or that any of the objects in the event are not from the first primary vertex. However, there is no information from either photon that can discriminate between the vertices.

A.3 The Muon Candidates

Both muons are fully reconstructed in the muon chambers [128] and their momenta are shown in Table A.1. The vertex is at z= -45.6 cm so the muons do not traverse the SVX. The μ^+ passes all the tight selection requirements except for the 6.0 GeV threshold on the hadronic energy of the muon tower (Had=6.8 GeV). The hadronic tower energy requirement has been measured to be 98% efficient [40]. The μ^- passes all selection criteria. The results for each criterion for the μ^+ and μ^- are shown in Table A.3.

As a check, the muon momenta are evaluated using the additional corrections used in measuring the mass of the W boson[129]. Using this method the P_T values change to 53.9 GeV and 55.1 GeV respectively. The invariant mass becomes 103.5 GeV.

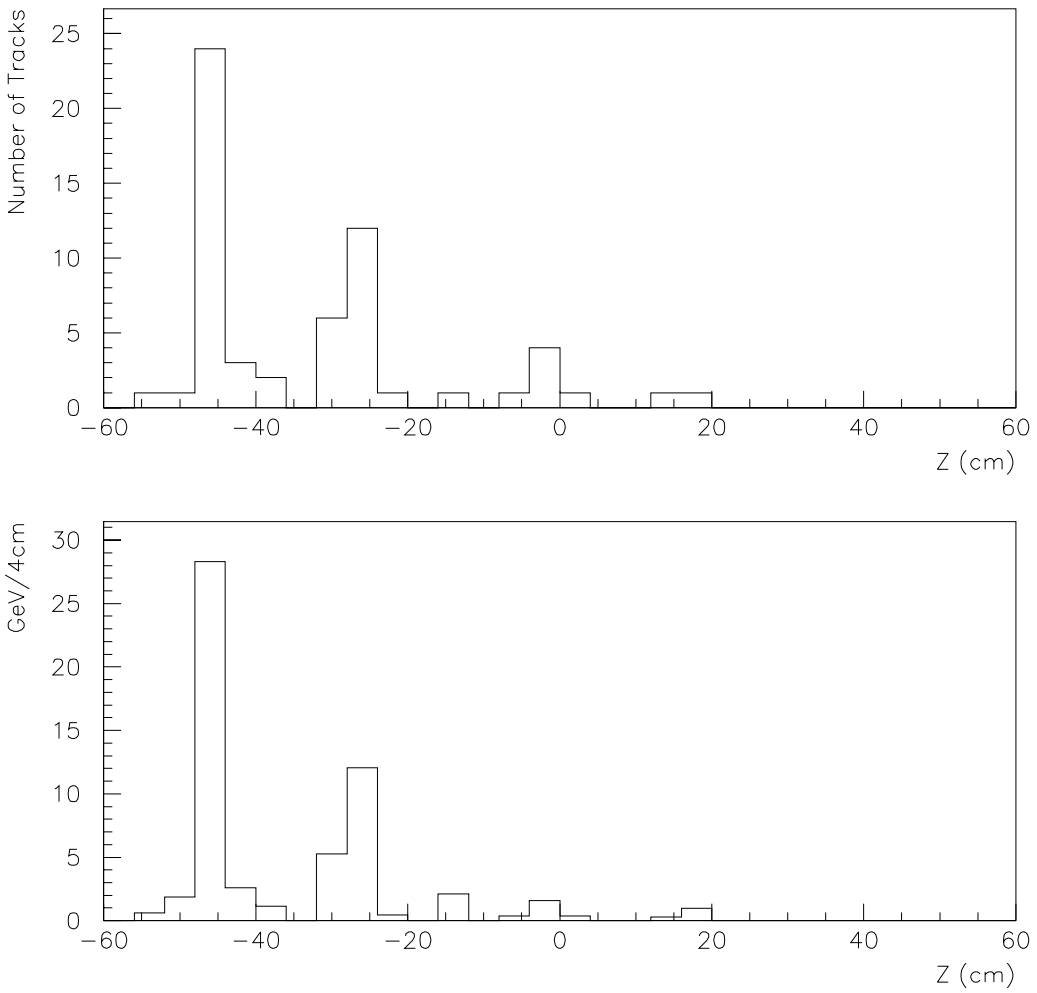

Figure A.3: The number of tracks in the central tracking chamber as a function of track z position in the $\mu^+\mu^-\gamma\gamma jj$ candidate event. The upper plots shows the number of tracks, the lower plot shows the number of CTC tracks weighted by track momentum (excluding the two muon tracks). The primary vertex is at $z = -46$ cm, the other vertex is at $z =$-28 cm.

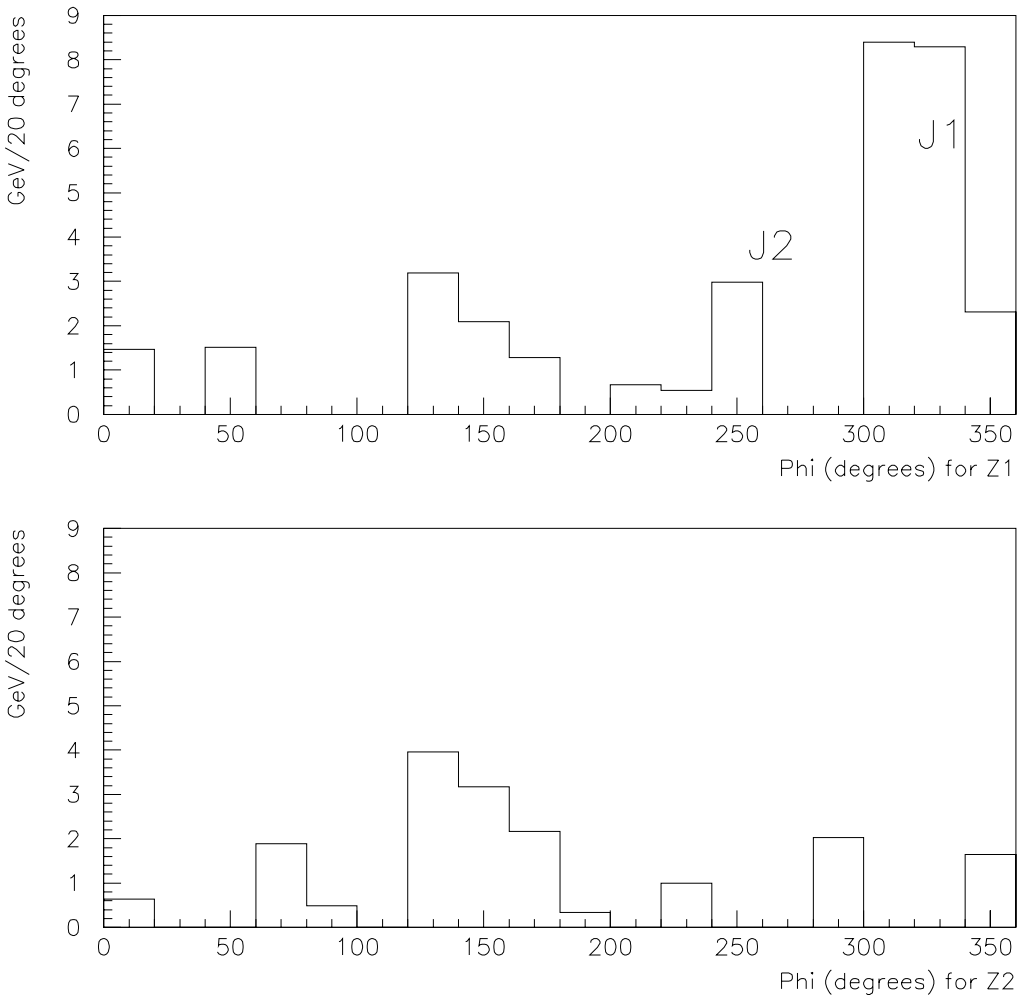

Figure A.4: The P_T weighted ϕ distribution of tracks associated with the two vertices in the $\mu^+\mu^-\gamma\gamma jj$ candidate event. The top plot shows the tracks associated with the primary vertex (Z_1), while the bottom plot shows the tracks associated with the other vertex (Z_2). Note that the jets, J_1 (at $\phi = 321°$) and J_2 (at $\phi = 254°$), are associated with the primary vertex.

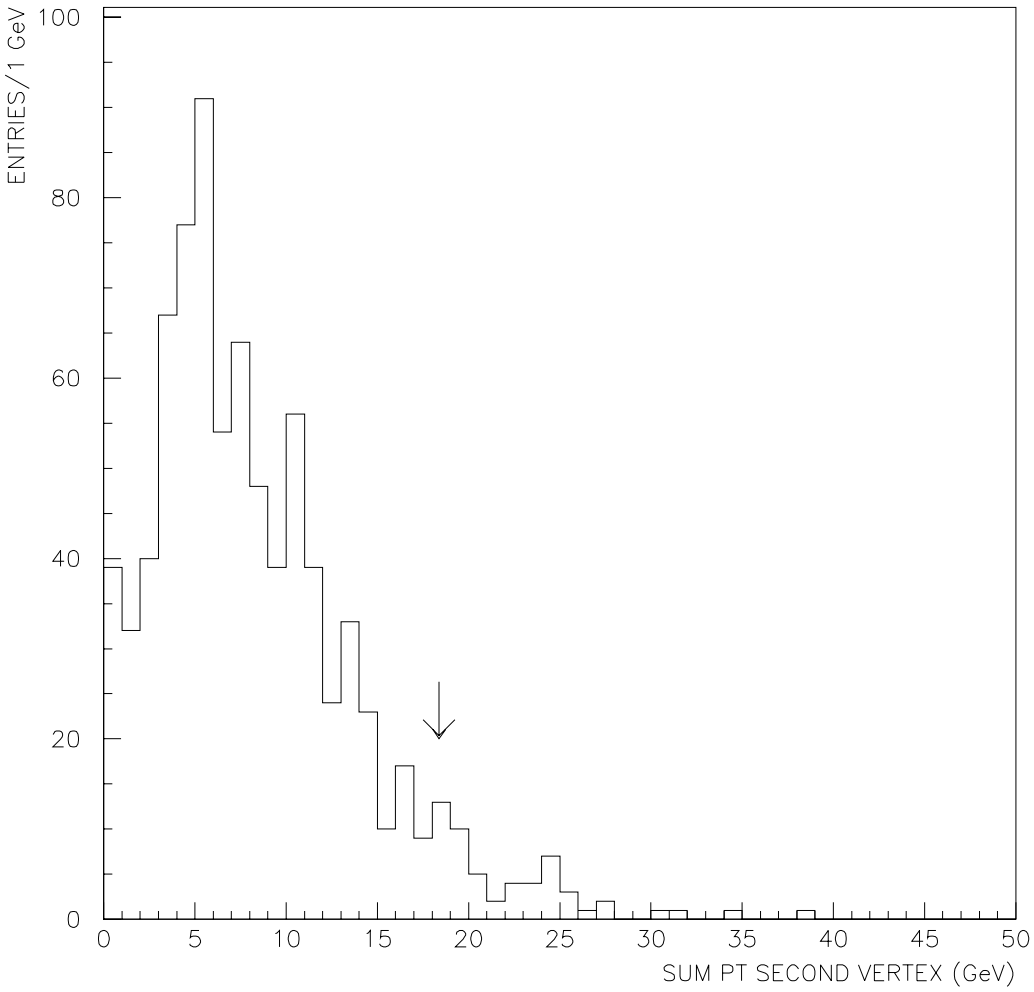

Figure A.5: The Sum P_T of tracks associated with other vertices in $\mu^+\mu^-$ events. The arrow represents the value for the $\mu^+\mu^-\gamma\gamma jj$ candidate event.

μ^+	
Requirements	Value
$P_T > 25$	P_T= 56.72 GeV
$E_{EM} < 2.0$ GeV	E_{EM} = 0.27 GeV
$E_{Had} < 6.0$ GeV	E_{Had} = 6.83 GeV
$E_{EM}+E_{Had} > 0.1$ GeV	$E_{EM}+E_{Had}$ = 7.10 GeV
$\lvert\Delta x_{CMU}\rvert < 2$ cm	Δx_{CMU} = 0.49 cm
$\lvert\Delta x_{CMP}\rvert < 5$ cm	Δx_{CMP} = 0.43 cm
$\lvert d_0\rvert < 0.3$ cm	$\lvert d_0\rvert$ = -0.02 cm
$N_{ASL} \geq 3$	N_{ASL} = 5
$N_{SSL} \geq 2$	N_{SSL} = 5
$N_{ASL}+N_{SSL} \geq 6$	$N_{ASL}+N_{SSL}$ = 10
$\lvert\Delta z(\text{vertex-track})\rvert < 5.0$ cm	$\Delta z(\text{vertex-track})$ = 0.76 cm
$\lvert z_{vertex}\rvert < 60.0$ cm	z_{vertex} = -45.59 cm
$E_T^{Iso}/\ P_T < 0.10$	$E_T^{Iso}/\ P_T$ = 0.03
$\Sigma P_T^{Iso}/\ P_T < 0.10$	$\Sigma P_T^{Iso}/\ P_T$ = 0.00

μ^-	
Requirements	Value
$P_T > 20$ GeV	P_T= 54.71 GeV
$E_{EM} < 2.0$ GeV	E_{EM}= 0.26 GeV
$E_{Had} < 6.0$ GeV	E_{Had}= 2.95 GeV
$E_{Had}+E_{EM} > 0.1$ GeV	$E_{Had}+E_{EM}$ = 3.21 GeV
$\lvert\Delta x_{CMU}\rvert < 2$ cm	Δx_{CMU} = -0.10 cm
$\lvert\Delta x_{CMP}\rvert < 5$ cm	Δx_{CMP} = 0.44 cm
$\lvert d_0\rvert < 0.3$ cm	$\lvert d_0\rvert$ = -0.02 cm
$N_{ASL} \geq 3$	N_{ASL} = 5
$N_{SSL} \geq 2$	N_{SSL} = 5
$N_{ASL}+N_{SSL} \geq 6$	$N_{ASL}+N_{SSL}$ = 10
$\lvert\Delta z(\text{vertex-track})\rvert < 5.0$ cm	$\Delta z(\text{vertex-track})$ = 0.31 cm
$\lvert z_{vertex}\rvert < 60.0$ cm	z_{vertex} = -45.59 cm
$E_T^{Iso}/\ P_T < 0.10$	$E_T^{Iso}/\ P_T$ = 0.01
$\Sigma P_T^{Iso}/\ P_T < 0.10$	$\Sigma P_T^{Iso}/\ P_T$ = 0.00

Table A.3: Summary of the muon identification and isolation variables in the $\mu^+\mu^-\gamma\gamma jj$ candidate event. The μ^- passes all the selection criteria. The μ^+ passes all the selection criteria except the $E_{Had} < 6.0$ GeV requirement. For a description of the variables used to identify muons see Ref. [39].

A.4 The Central Photon Candidate

The photon candidate in the central calorimeter passes all the standard identification and isolation selection criteria as shown in Table A.4.

Requirements	Value
$\leq$1 3D tracks, $P_T < 1$ GeV	# 3D Tracks = 0
$\chi^2_{CES} < 10$	$\chi^2_{CES} = 4.74$
$14 < \lvert Z_{strip} \rvert < 230$ cm	Z_{strip}= 69.65 cm
$\lvert X_{wire} \rvert$ <21.0	X_{wire} = 10.03 cm
$\lvert \sigma_{CES} \rvert < 2.0$	σ_{CES} = 1.36
$E^{cluster}_{2nd\ strip\ or\ wire} \leq 2.39 + 0.01 \times E^{\gamma}_T = 2.95$ GeV	$E_{2nd\ Strip}$ = 0.0 GeV
	$E_{2nd\ Wire}$ = 0.0 GeV
Had/EM < 0.055 + 0.00045E = 0.080	Had/EM = 0.02
$E^{Iso}_T/E_T < 0.10$	E^{Iso}_T/E_T= 0.02
$\Sigma P_T(\Delta R = 0.4) < 5.0$	$\Sigma P_T(\Delta R = 0.4)$= 0.0

Table A.4: Summary of the central photon variables in the $\mu^+\mu^-\gamma\gamma jj$ candidate event. The photon passes all the selection criteria.

A.5 The Plug Photon Candidate

The photon candidate in the plug calorimeter passes all standard photon identification and isolation selection criteria used in the $W\gamma$ analysis [130]. The selection criteria, along with values from the candidate, are given in Table A.5. A detailed inspection of the cluster shows that a small purely electromagnetic deposition of a few GeV in a nearby tower in the same quadrant causes the cluster to almost fail the isolation requirement. A layer profile of the quadrant shows an excess deposition in layer 5 that is consistent in magnitude with the electromagnetic tower mentioned above and suggests that it is noise. The cluster energy algorithm does not use this information and therefore the photon energy measurement is not affected by the spike in

layer 5 [131]. Thus, there is no indication that this cluster is not due to a photon.

Requirements	Value
$E_T > 7$ GeV	$E_T = 13.6$ GeV
Fiducial	Yes
Had/EM $< 0.028 + 0.00019E = 0.032$	Had/EM $= 0.0$
$\chi^2_{3x3} < 5.0$	$\chi^2_{3x3} = 3.681$
$\chi^2_{\eta} < 20.0$	$\chi^2_{\eta} = 3.463$
$\chi^2_{\phi} < 20.0$	$\chi^2_{\phi} = 3.942$
VTX occ $< 40\%$	VTX occ$= 0.12$
$E_T^{Iso}/E_T < 0.15$	$E_T^{Iso}/E_T = 0.12$

Table A.5: Summary of the plug photon variables in the $\mu^+\mu^-\gamma\gamma jj$ candidate event. The photon passes all the selection criteria described in Ref. [130].

A.6 The Jets

Two jets pass the requirements of Section 3.2 and are listed in Table A.6. However, a closer inspection reveals that this is problematic as shown in the top part of Figure A.1. The first jet, j_1, appears to be only one of three jets which are part of a single larger jet (J_1 in Table A.6).

Instead of using the standard cone size of $\Delta R = 0.4$ for jet clusters, a cone of $\Delta R = 0.7$ appears to be more appropriate for this event. While the results are not highly dependent on the cone size used, the larger cone size more accurately reflects the size and direction of the jet activity and is used for all kinematic calculations. While the diffuse jet, J_1, is fully contained in the larger cone, the algorithm picks up a third jet which is due mostly to the energy deposited by the μ^+ ($E_T^{Uncorr} = 10.1$ GeV, $E_{\mu}^{Had\ +\ EM} = 7.1$ GeV). This jet is ignored. The second jet, J_2, also picks up a second smaller jet due calorimeter energy deposited by the μ^-. This jet, in a cone of $\Delta R = 0.4$, has

$E_T^{Corr} = 7.2$ GeV. The energy is removed from J_2 and gives $E_T^{J_2 Corr} = 23$ GeV. Using the new values changes the dijet mass from $M_{J_1 J_2}$ =75.5 GeV to $M_{J_1 J_2}$ =68.6 GeV. The uncertainty on the dijet mass is taken to be 10% from jet energy resolution. In either case the dijet mass is consistent with the W mass. Figure A.6 shows the dijet invariant mass for the two most energetic jets in $\mu^+\mu^-$ events with two or more jets ($\Delta R = 0.7$).

$\Delta R = 0.7$					
	η	ϕ (degrees)	E_T (GeV)	Mass (GeV)	Corr
J_1	0.957	321.3	39.21	19.28	1.336
J_2	-0.807	253.6	29.98	8.14	1.455
$\Delta R = 0.4$					
	η	ϕ (degrees)	E_T (GeV)	Mass (GeV)	Corr
j_1	0.763	337.4	17.79	3.91	1.653
j_1'	0.864	309.9	13.91	3.12	1.751
j_1''	1.504	308.8	13.79	2.92	1.871
j_2	-0.899	252.7	29.28	3.39	1.829

Table A.6: The jets in the $\mu^+\mu^-\gamma\gamma jj$ candidate event. The values of E_T are already corrected using JTC96S('EY', 'DD'). Corr is the value of the correction.

A.7 The Missing E_T

Using the methods of Chapter 3.1, the $\not{E}_T$ is estimated to be $\not{E}_T = 31$ GeV. However, a closer investigation of the algorithm reveals three subtle problems with the method: 1) The μ^+ does not pass the standard muon cuts, so it is not corrected for, 2) photons in the plug calorimeter are treated like jets and given a large correction, 3) the other jets are identified using a

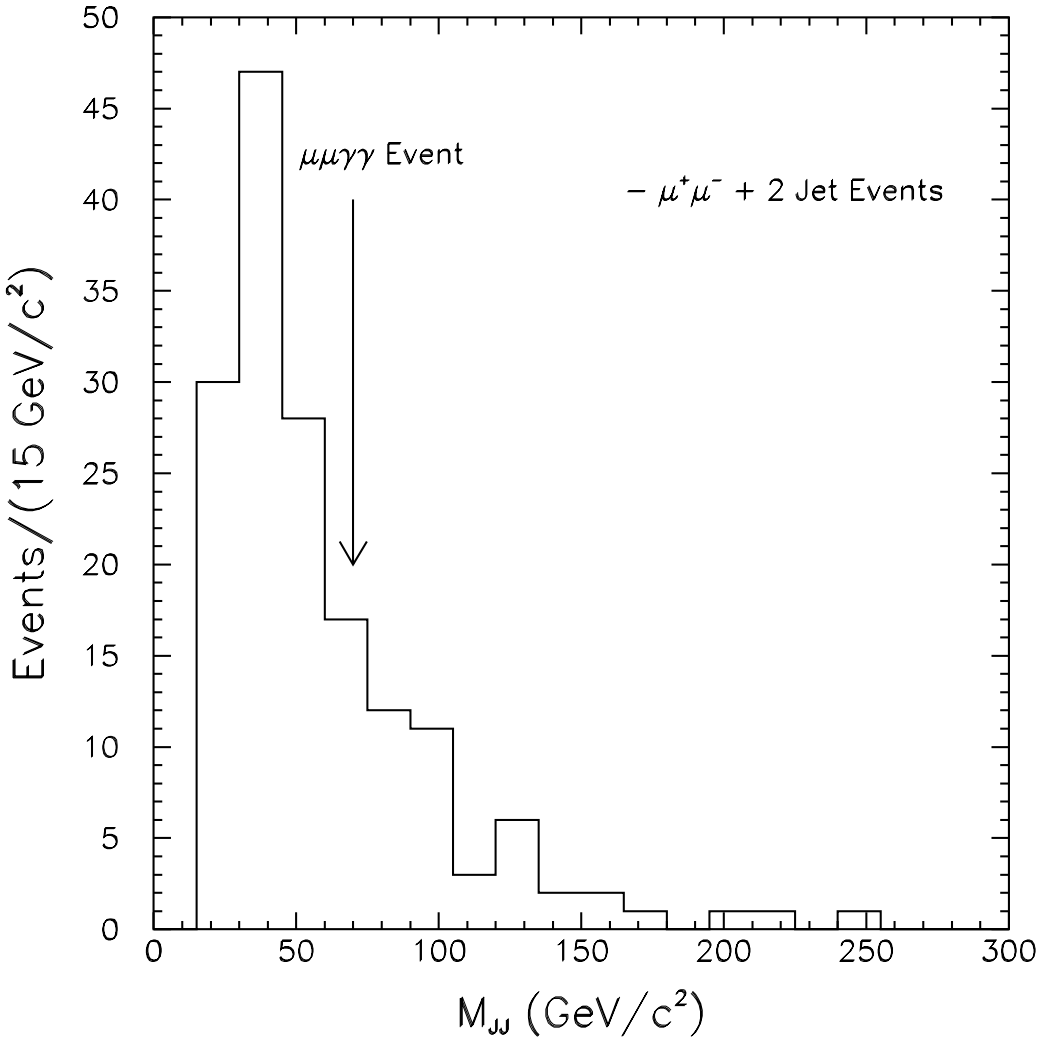

Figure A.6: The dijet invariant mass for jets produced in association with pairs of muons passing the tight identification and isolation selection criteria.

cone size of $\Delta R = 0.4$, not the $\Delta R = 0.7$ which is preferred for this event (see the previous section).

To deal with these problems and calculate a $\not{E}_T$ for this particular event, the $\not{E}_T$ is calculated in two ways. In Method 1, the raw value of the $\not{E}_T$ is corrected for both muons (and muon towers) and for J_1 and J_2. In Method 2, the 6 objects, $\mu^+\mu^-\gamma\gamma J_1 J_2$, in the event are vectorially added as they appear in Table A.1. The results are summarized in Table A.7. The $\not{E}_T$ significance, Sig$=\not{E}_T/\sqrt{\Sigma E_T(\gamma\gamma J_1 J_2)}$, is also shown.

$\not{E}_T$			
	ϕ (degrees)	E_T (GeV)	Sig
Method 1	234.3	15.6	1.4
Method 2	166.8	7.5	0.7

Table A.7: The missing transverse energy in the $\mu^+\mu^-\gamma\gamma jj$ candidate event. Method 1 corrects the RAW $\not{E}_T$ for all muons, jets and photons. Method 2 is the vector imbalance of the six objects.

Note that the $\not{E}_T$ in both cases is small and that the transverse momentum of the 6 objects is consistent with zero. The Method 1 $\not{E}_T$ is also close to the direction of the μ^-, which has $\phi = 254°$.

A.8 Estimating the Number of $\mu^+\mu^-\gamma\gamma jj$ Events from Standard Model Sources

The rate at which Standard Model sources produce this type of event is estimated for the following four sources:

- $Z^0/\gamma^* \rightarrow \mu^+\mu^- + \gamma\gamma jj$.

- $Z^0/\gamma^* \rightarrow \mu^+\mu^- + \gamma^{\text{central}}$ + jets where one of the jets fakes a loose photon.
- $Z^0/\gamma^* \rightarrow \mu^+\mu^- + \gamma^{\text{loose}}$ + jets where one of the jets fakes a central photon.
- $Z^0/\gamma^* \rightarrow \mu^+\mu^-$ + jets where both photons are fakes.

To estimate these contributions (as in Chapter 5) one of the photons is required to be in the central region and have $\mathrm{E_T} > 25$ GeV, the other photon, dubbed the loose photon, only needs $\mathrm{E_T} > 10$ and can be in the central or plug calorimeters.

To estimate the rates, the $\mu^+\mu^-$ sample is used [132]. The sample contains, 1,698 events, 1 event [133] has an additional central photon (no additional jets) and 2 events have an additional plug photon (no additional jets). A total of 162 events have two or more jets ($\Delta\mathrm{R} = 0.7$) with $\mathrm{E_T^{Uncorrected}} > 10$ GeV and $|\eta| < 2.2$; 68 have $\mathrm{M_{jj}} > 50$ GeV. The probability of finding an additional two jets in the event with $\mathrm{M_{jj}} > 50$ GeV is estimated to be:

$$\begin{aligned} R^{\text{Two Extra Jets}} &= \frac{\text{Events with } \mu^+\mu^-\text{jj}}{\text{Events with } \mu^+\mu^-} \\ &= \frac{68}{1,698} = 4.0 \times 10^{-2}. \end{aligned} \tag{A.1}$$

The rate at which real $\mu^+\mu^-\gamma\gamma jj$ events are produced by Standard Model sources is estimated using the 3 $\mu\mu\gamma^{\text{Loose}}$ events in the data. Multiplying by a factor of 5.8×10^{-4} for real additional central photons (from Section 5.4.2), and a factor of 4.0×10^{-2} for the two additional jets gives a total of 7×10^{-5} events expected with the $\mu^+\mu^-\gamma\gamma jj$ signature.

The rate at which fake events contribute is also calculated in a manner similar to that used in Chapter 5. The probability that an event will have an extra jet from physics processes is estimated to be equal to the fraction $\frac{\text{Additional Jets in } \mathrm{Z}^0/\gamma^* \text{ events}}{\text{Total number of } \mathrm{Z}^0/\gamma^* \text{ events}}$. Two types of jets which could fake a photon are

considered: Central ($E_T > 25$ GeV) and Loose (central or plug, $E_T > 10$ GeV). Jets which could fake a central photon are required to have $E_T > 25$ GeV and have $|\eta| < 1.0$; there are 79 such jets in the sample. Any jet which could fake a loose photon is required to have $E_T^{Corr} > 10$ GeV, and have $|\eta| < 1.0$ or $1.2 < |\eta| < 2.2$. There are 226 and 137 jets in the central and plug regions respectively. Putting this together with the photon fake rates [71] gives:

$$\begin{aligned} R_\gamma^{\text{fake central}} &\approx P_{\text{Extra Jet}}^{\text{Central}} \times P_\gamma^{\text{fake Central}} \\ &= \frac{79}{1,698} \times (1.3 \times 10^{-3}) \\ &= 6.0 \times 10^{-5} \end{aligned} \tag{A.2}$$

and for additional loose photons

$$\begin{aligned} R_\gamma^{\text{fake loose}} &\approx P_{\text{Extra Jet}}^{\text{Central}} \times P_\gamma^{\text{fake Central}} + P_{\text{Extra Jet}}^{\text{Plug}} \times P_\gamma^{\text{fake Plug}} \\ &= \frac{226}{1,698} \times (1.3 \times 10^{-3}) + \frac{137}{1,698} \times (4.0 \times 10^{-3}) \\ &= (1.7 \times 10^{-4}) + (3.2 \times 10^{-4}) \\ &= 5.0 \times 10^{-4}. \end{aligned} \tag{A.3}$$

As a check, Equation A.2 predicts:

$$\begin{aligned} N_{\mu^+\mu^-\gamma} &= N_{\mu^+\mu^-} \times R_\gamma^{\text{fake central}} \\ &= 1,698 \times (6.0 \times 10^{-5}) = 0.1 \text{ events} \end{aligned} \tag{A.4}$$

where one event is observed in the data.

The final results are summarized in Table A.8. A total of 2.9×10^{-5} Standard Model events are estimated to have the $\mu^+\mu^-\gamma\gamma jj$ signature in the data from fake sources. Note that no factor has been taken into account for the muon pair mass being above the Z^0 mass. Summing the real and fake sources gives a total of 1×10^{-4} events.

Real Process	Fake Process 1	Fake Process 2	Fake Process 3	Events in 85 pb^{-1}
$\mu^+\mu^-$ 1,698	$+\ \gamma^{\text{Fake Central}}$ $\times\ 6.0 \times 10^{-5}$	$+\ \gamma^{\text{Fake Loose}}$ $\times\ 5.0 \times 10^{-4}$	$R^{\text{Two Extra Jets}}$ $\times\ 4.0 \times 10^{-2}$	$= 2.0 \times 10^{-6}$
$\mu^+\mu^-\gamma^{\text{Central}}$ 1	$+\ \gamma^{\text{Fake Loose}}$ $\times\ 5.0 \times 10^{-4}$	$R^{\text{Two Extra Jets}}$ $\times\ 4.0 \times 10^{-2}$		$= 2.0 \times 10^{-5}$
$\mu^+\mu^-\gamma^{\text{Loose}}$ 3	$+\ \gamma^{\text{Fake Central}}$ $\times\ 6.0 \times 10^{-5}$	$R^{\text{Two Extra Jets}}$ $\times\ 4.0 \times 10^{-2}$		$= 7.2 \times 10^{-6}$
Sum				$\approx 2.9 \times 10^{-5}$

Table A.8: The number of fake $\mu^+\mu^-\gamma\gamma jj$ events expected from Standard Model sources.

A.9 Comparing the Event to the $ee\gamma\gamma\not{E}_T$ Candidate Event

The kinematics of the $\mu^+\mu^-\gamma\gamma jj$ event are quite similar to that of the $ee\gamma\gamma\not{E}_T$ candidate event. In particular the pair masses of one of the combinations of the leptons (assuming the cluster in the plug calorimeter in the $ee\gamma\gamma\not{E}_T$ event is indeed a lepton) are essentially identical with one of the combinations in the $ee\gamma\gamma\not{E}_T$ candidate event. One of the pairing gives masses of 62 GeV and 52 GeV in the $\mu^+\mu^-\gamma\gamma jj$ candidate event, to be compared with masses of 64 GeV and 57 GeV in the $ee\gamma\gamma\not{E}_T$ candidate event. The invariant masses for the lepton-photon combinations are shown in Table A.9. Another interesting similarity is that the $ll\gamma\gamma$ systems have $P_T = 48$ GeV ($ee\gamma\gamma\not{E}_T$) and 51 GeV ($\mu^+\mu^-\gamma\gamma jj$) respectively.

A.10 Physics Interpretation

While this could just be a very unusual $Z^0\gamma\gamma + 2$ jet event, it it instructive to speculate on possible Supersymmetric interpretations [134]. For

$ee\gamma\gamma\not{E}_T$ Candidate				$\mu^+\mu^-\gamma\gamma jj$ Candidate			
Run 68739, Event 257646				Run 65390, Event 16199			
	γ_1	γ_2	e_1		γ_1	γ_2	μ^-
e^{Central}	64.1	91.7	163.3	μ^+	113.1	52.2	105.8
e^{Plug}	97.0	56.5		μ^-	62.4	49.1	
γ_2	47.3			γ_2	60.8		

Table A.9: The invariant masses of combinations of the leptons and photons in the $ee\gamma\gamma\not{E}_T$ and $\mu^+\mu^-\gamma\gamma jj$ candidate events. All numbers are in GeV/c^2.

example in the models discussed in Chapters 1 and 6, $\tilde{W}\tilde{Z}$ pair production can produce the signature via:

$$\begin{aligned}\tilde{W}\tilde{Z} &\rightarrow (WN_1)(Z^0N_1)\\ &\rightarrow (jj)(\gamma\tilde{G})(\mu^+\mu^-)(\gamma\tilde{G})\end{aligned}$$

or

$$\begin{aligned}\tilde{W}\tilde{Z} &\rightarrow (WN_2)(Z^0N_2)\\ &\rightarrow (jj)(\gamma N_1)(\mu^+\mu^-)(\gamma N_1)\end{aligned}$$

Alternatively, each muon could come from a separate parent: looking at Table A.2 one sees there are several pairings that have similar masses on each leg (not necessary, however). The dimuon mass being close to that of the Z^0 would then be fortuitous. The two jets then would also be unrelated, and the dijet mass being close to that of the W would also be due to kinematics rather than to a W decay. For example, one could have:

$$\begin{aligned}\tilde{q}\tilde{q} &\rightarrow (q\tilde{W})(q\tilde{W})\\ &\rightarrow q(WN_1)q(WN_1)\\ &\rightarrow q(\mu\nu)(\gamma\tilde{G})q(\mu\nu)(\gamma\tilde{G})\end{aligned}$$

where the dimuon mass and dijet masses being close to the Z^0 and W masses is due to the kinematics and is not forced by the decay.

One of the flaws with these interpretation is that these decay chains in general have $\not\!\!E_T$. However, the $\not\!\!E_T$ in an individual event can be low due to the cancellation of the momentum carried off by the 2 LSP's, which in general tend to be back-to-back; the net $\not\!\!E_T$ thus is a broad distribution. For example $(12\pm1)\%$ of $ll\gamma\gamma$ events in the light gravitino model [29] have $\not\!\!E_T$ less than 25 GeV. The lack of $\not\!\!E_T$ may favor some non-SUSY interpretation[25, 26]. For example both the $ee\gamma\gamma\not\!\!E_T$ and $\mu^+\mu^-\gamma\gamma jj$ candidate events could be the same type of event with the $\not\!\!E_T$ in the $ee\gamma\gamma\not\!\!E_T$ event due to a high-P_T $Z^0 \rightarrow \nu\bar{\nu}$ decay, and the two jets in the $\mu^+\mu^-\gamma\gamma jj$ candidate event due to $Z^0 \rightarrow q\bar{q}$ and a mass which fluctuated low. Both events would then be $ll\gamma\gamma + Z^0$. Then again this may be just one of the rare Standard Model events that should show up in the data out of the many possible types in 10^{12} interactions.

A.11 Conclusions

The $\mu^+\mu^-\gamma\gamma jj$ candidate is similar to the $ee\gamma\gamma\not\!\!E_T$ event both kinematically, and in that both events are highly unusual. The Standard Model rate for this signature is estimated to be $\approx 1 \times 10^{-4}$ events. Its existence is relevant as it gives further evidence that either both it and the $ee\gamma\gamma\not\!\!E_T$ candidate event are due to sources of background which are not understood, or there is possibly a signal. Unfortunately, the $\mu^+\mu^-\gamma\gamma jj$ candidate event is not part of the central $\gamma\gamma + X$ searches because one of the photons is in the plug calorimeter. Another problem is that the event is flawed. While one the central muons fails the canonical muon requirement on hadron energy, it is a golden muon in all other respects. The primary differences between this event and the $ee\gamma\gamma\not\!\!E_T$ candidate event is that instead of $\not\!\!E_T$, (the missing E_T of the event is less than 10 GeV) the $\mu^+\mu^-\gamma\gamma jj$ candidate has two jets with an

invariant mass close to the W mass. Similarly, while the 'dilepton' mass in the $ee\gamma\gamma\not{E}_{\mathrm{T}}$ is well above the Z^0, only 6% of dimuon events in the data have a $\mu\mu$ mass larger than in the $\mu^+\mu^-\gamma\gamma jj$ event. Only more data will tell us the origin of these events.

Appendix B

Comments on the Diphoton Purity Estimate

This Appendix describes the purity estimate of Chapter 2. The techniques used to estimate the purity of the diphoton sample were developed to measure the single photon production cross section [36]. For each photon candidate an algorithm determines the fractional probabilities of the candidate being due to a single, prompt photon (ϵ_γ) or to a neutral meson (ϵ_b). In addition each photon is compared to a CES or CPR requirement if it has E_T greater than or less than 35 GeV respectively [135]. With these fractions the following vector equation is used to extract the true photon signal for the sample:

$$\begin{pmatrix} N_{fail} \\ N_{pass} \end{pmatrix} = \begin{pmatrix} \overline{\epsilon_b} & \overline{\epsilon_\gamma} \\ \epsilon_b & \epsilon_\gamma \end{pmatrix} \begin{pmatrix} N_b \\ N_\gamma \end{pmatrix} \tag{B.1}$$

where $\overline{\epsilon} \equiv 1 - \epsilon$, and N_{fail} and N_{pass} are the number of photons which fail or pass the CES/CPR requirements respectively.

In the diphoton case, there are 4 possible combinations: fail-fail, fail-pass, pass-fail and pass-pass. The number of possible cases for the com-

binations of signal and background become 4, which are $bb, b\gamma, \gamma b$ and $\gamma\gamma$. The vector equation becomes a 4×4 matrix instead of 2×2, as was used in Equation B.1:

$$\begin{pmatrix} N_{ff} \\ N_{fp} \\ N_{pf} \\ N_{pp} \end{pmatrix} = \begin{pmatrix} \overline{\epsilon_{b1}} \cdot \overline{\epsilon_{b2}} & \overline{\epsilon_{b1}} \cdot \overline{\epsilon_{\gamma 2}} & \overline{\epsilon_{\gamma 1}} \cdot \overline{\epsilon_{b2}} & \overline{\epsilon_{\gamma 1}} \cdot \overline{\epsilon_{\gamma 2}} \\ \overline{\epsilon_{b1}} \cdot \epsilon_{b2} & \overline{\epsilon_{b1}} \cdot \epsilon_{\gamma 2} & \overline{\epsilon_{\gamma 1}} \cdot \epsilon_{b2} & \overline{\epsilon_{\gamma 1}} \cdot \epsilon_{\gamma 2} \\ \epsilon_{b1} \cdot \overline{\epsilon_{b2}} & \epsilon_{b1} \cdot \overline{\epsilon_{\gamma 2}} & \epsilon_{\gamma 1} \cdot \overline{\epsilon_{b2}} & \epsilon_{\gamma 1} \cdot \overline{\epsilon_{\gamma 2}} \\ \epsilon_{b1} \cdot \epsilon_{b2} & \epsilon_{b1} \cdot \epsilon_{\gamma 2} & \epsilon_{\gamma 1} \cdot \epsilon_{b2} & \epsilon_{\gamma 1} \cdot \epsilon_{\gamma 2} \end{pmatrix} \begin{pmatrix} N_{bb} \\ N_{b\gamma} \\ N_{\gamma b} \\ N_{\gamma\gamma} \end{pmatrix} \tag{B.2}$$

The real number of signal ($N_{\gamma\gamma}$) and backgrounds ($N_{b\gamma}, N_{\gamma b}$ and N_{bb}) are estimated by inverting the matrix. One technical point is appropriate here. The CES/CPR methods require the use of data samples with $\chi^2_{\rm CES} < 20$ and are only applicable for photons in the tight fiducial region ($|X_{\rm wire}| < 17.5$ cm). In order to correct for the fact that the sample requires $\chi^2_{\rm CES} < 10$, events which pass all the selection criteria in Table 2.1 but with the $\chi^2_{\rm CES}$ requirement raised from 10 to 20 are added to create a sample to measure the purity. There are 3697 events in the sample, 3615 of which have $|X_{\rm wire}| < 17.5$ cm. The purity is assumed to be the same in the region 17.5 cm $< |X_{\rm wire}| <$ 21.0 cm and in $|X_{\rm wire}| <$ 17.5 cm. Inverting the matrix, Equation B.2 estimates there are 2447 ± 136 bb events, 782 ± 207 $b\gamma + \gamma b$ events and 386 ± 103 $\gamma\gamma$ events in the sample for a raw purity of $(11 \pm 3)\%$. Using the efficiency of the $\chi^2_{\rm CES} < 20$ requirement, which is measured to be 92.2% efficient per photon (see Table 2.3), and the 2164 events in the tight fiducial region with $\chi^2_{\rm CES} < 10$, the average purity is estimated to be $(15 \pm 4)\%$.

Appendix C

Detailed Event Displays

This Appendix shows the detailed event displays, in CDF jargon, the DF LEGO and CTC displays, for the events which pass the selection criteria of the $\gamma\gamma + X$ searches of Chapter 3. The $ee\gamma\gamma\not{E}_{\mathrm{T}}$ candidate event is displayed in Figures C.1 and C.2. Figure C.3 shows the $\gamma\gamma + \not{E}_{\mathrm{T}}$ which has both photons above 25 GeV and $\not{E}_{\mathrm{T}} = 34$ GeV. The other three $\gamma\gamma + \ell$ events are shown in Figures C.4, C.5 and C.6. The two $\gamma\gamma + b$-tag events are shown in Figures C.7 and C.8.

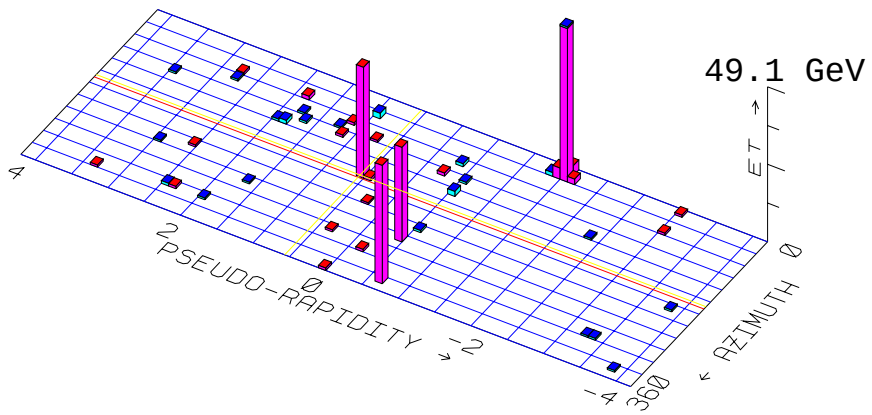

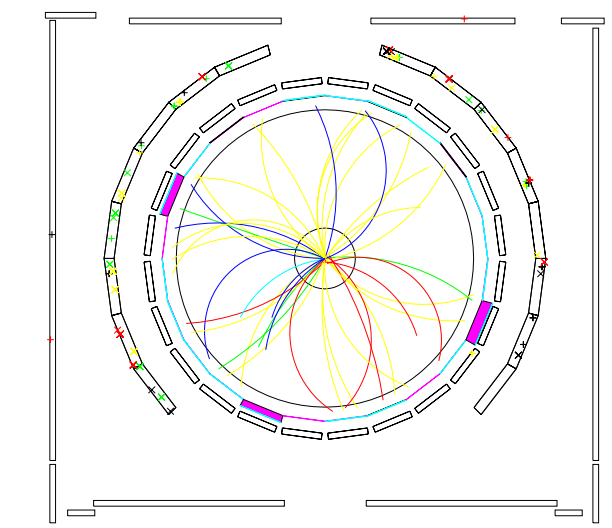

Figure C.1: The LEGO and CTC displays for the $ee\gamma\gamma\not{E}_T$ candidate event. Note that only towers with $E_T > 0.5$ GeV are shown.

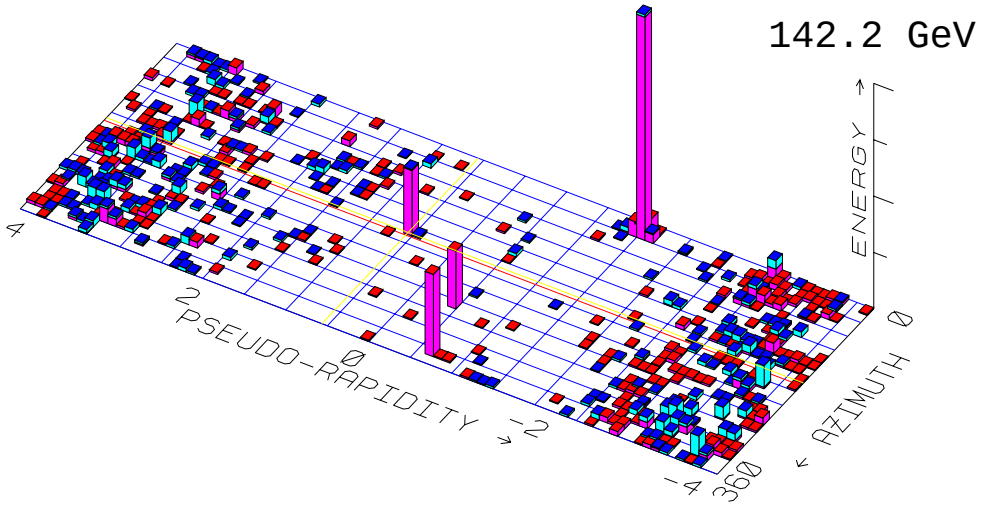

Figure C.2: The LEGO plot in energy for the $ee\gamma\gamma\not{E}_{\mathrm{T}}$ candidate event. Note that only towers with E> 0.5 GeV are shown.

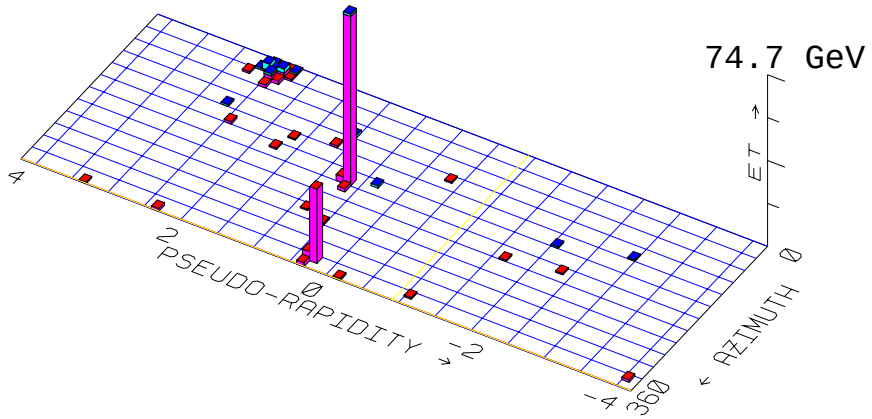

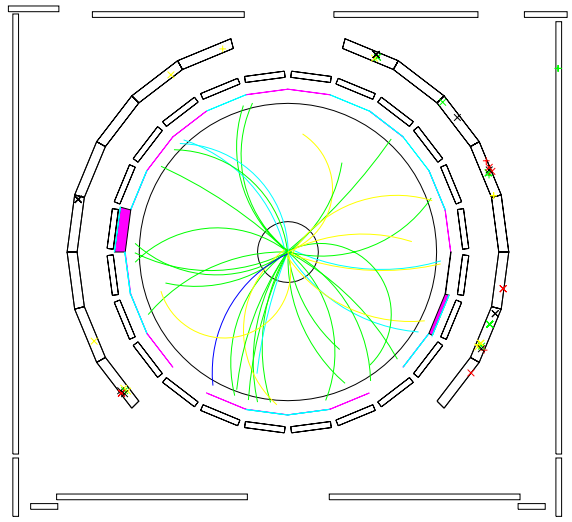

Figure C.3: The event display for the $\gamma\gamma + \not{E}_{\mathrm{T}}$ candidate event

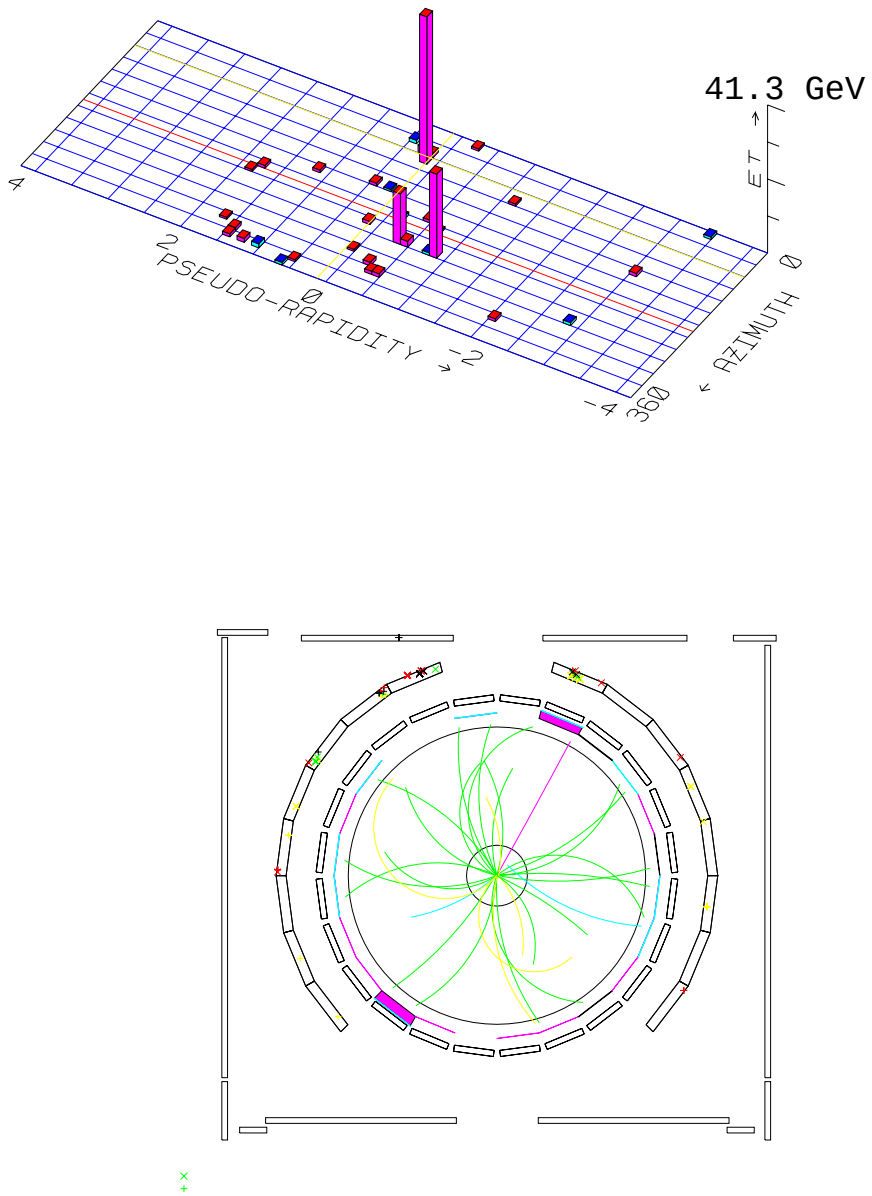

Figure C.4: The event display for the $\gamma\gamma + e^{\text{central}}$ candidate event

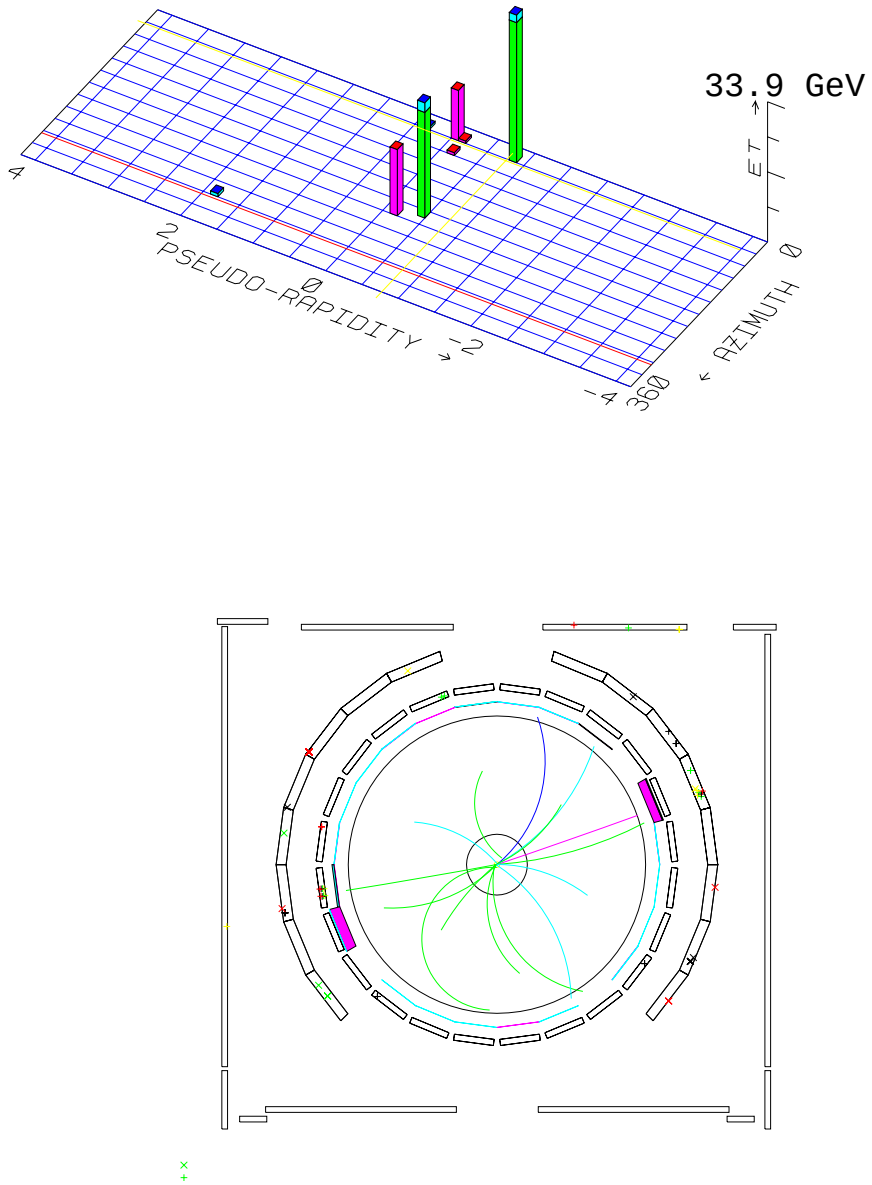

Figure C.5: The event display for the $\gamma\gamma + \mu\mu$ candidate event

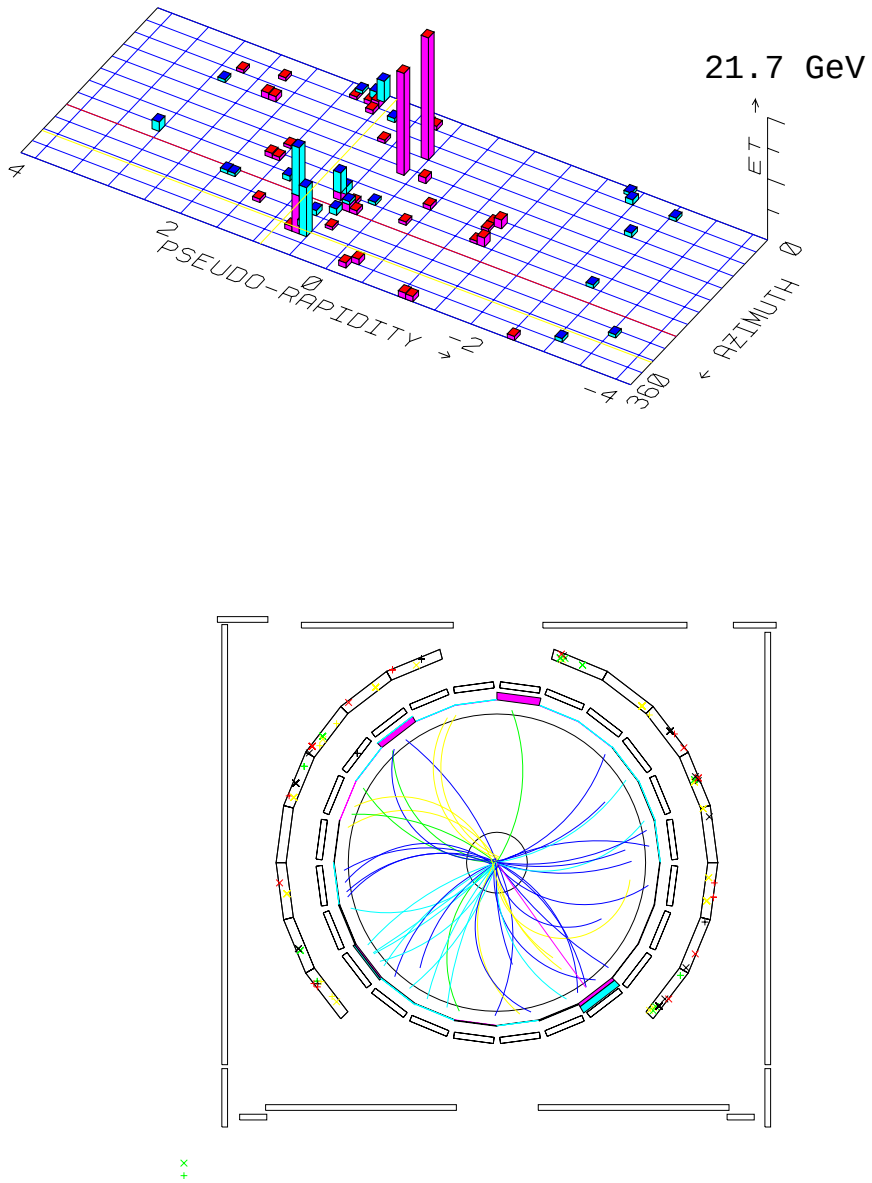

Figure C.6: The event display for the $\gamma\gamma + \tau$ candidate event

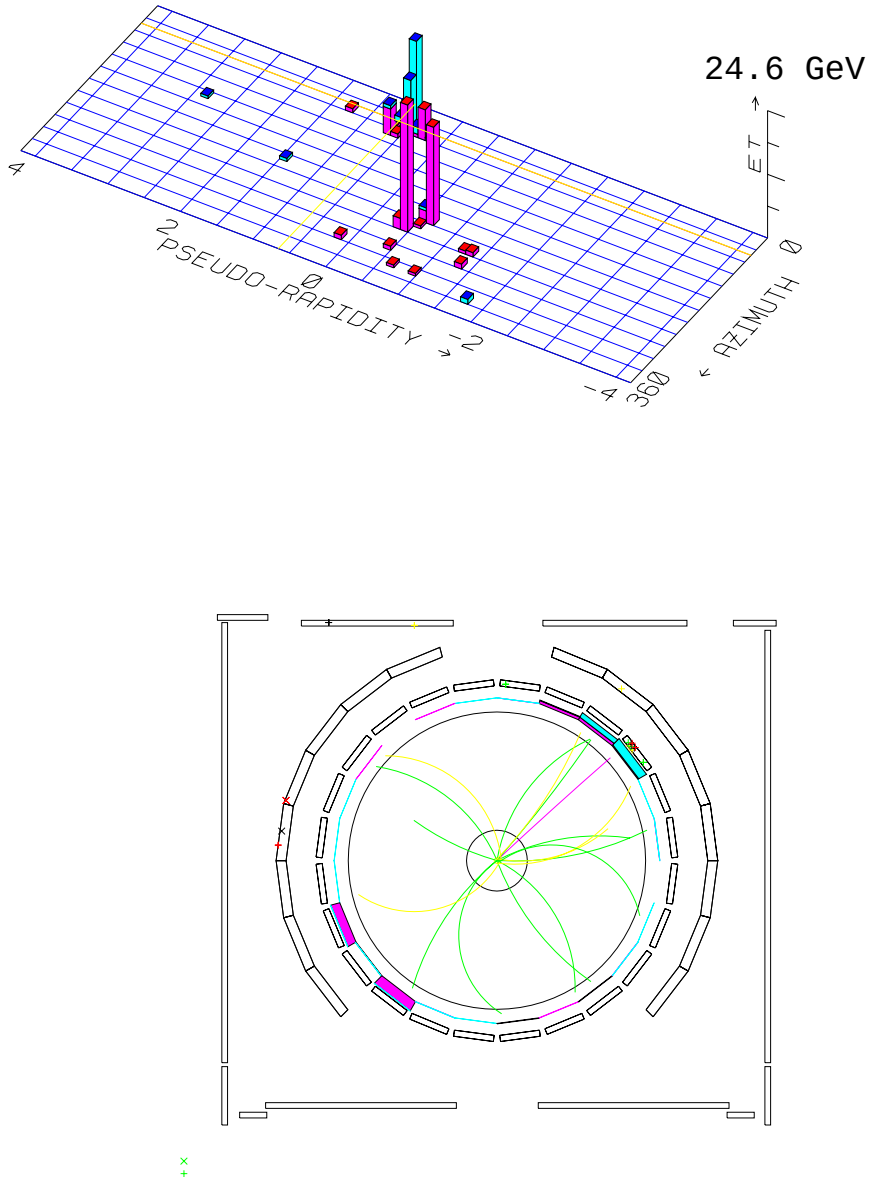

Figure C.7: The event display for the first $\gamma\gamma + b$-jet candidate event

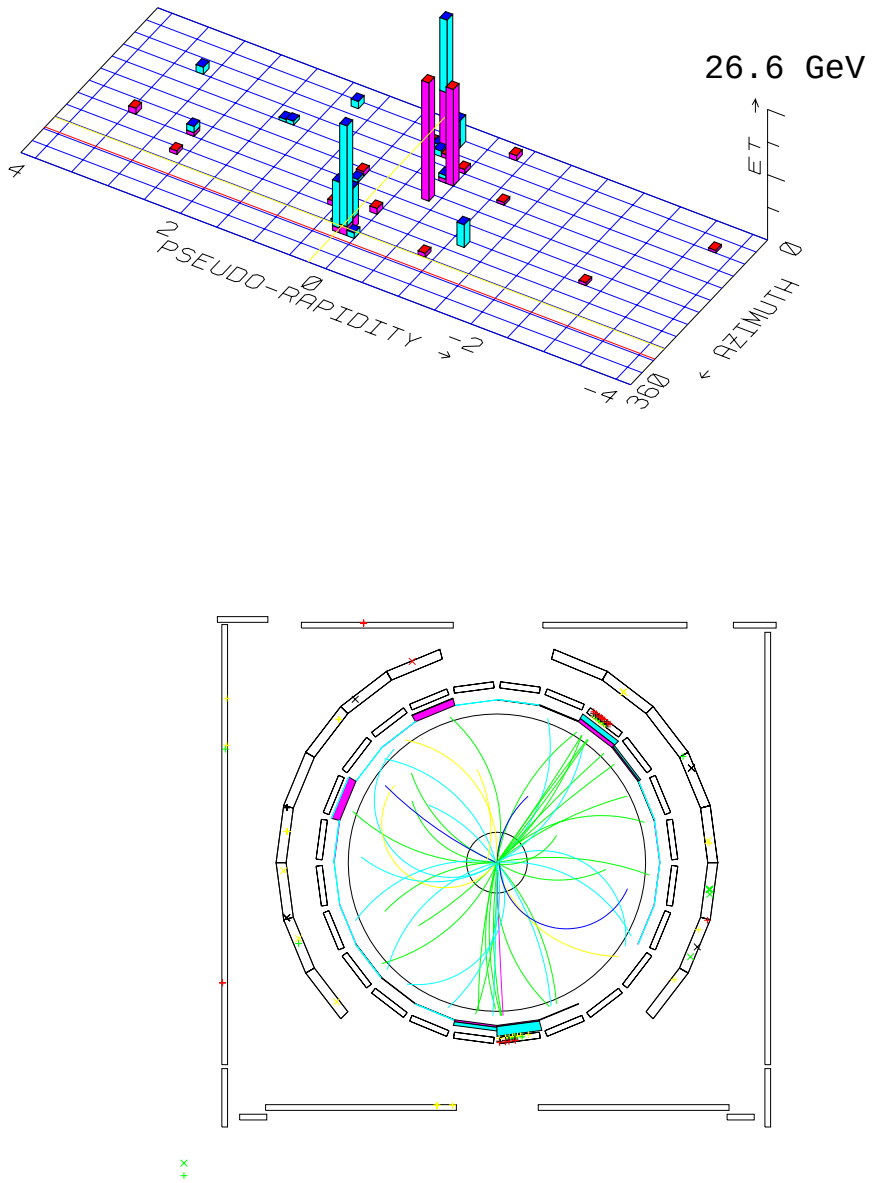

Figure C.8: The event display for the second $\gamma\gamma + b$-jet candidate event

Appendix D

Comments on the Calculation of the Jet Fake Rates

This Appendix discusses the rates at which generic jets fake the photon and electron selection criteria. The procedure uses a method and sample similar to that in Ref. [40]. The sample [136] consists of dijet events which are selected using the following requirements.

1. 2 jets with $E_T^{uncorr} > 10$ GeV, $|\eta| < 2.2$
2. $|\Delta\phi_{jj}| > 160^0$ (back-to-back cut)

Jets which could fake photons or electrons in the central calorimeter are selected as having $|\eta| < 1.0$; jets which could fake a photon or electron in the plug calorimeter are selected as having $1.2 < |\eta| < 2.2$. The Level 2 and Level 3 triggers measure cluster energies using slightly different methods. To remove a small bias, the following algorithm is used:

1. Select one of the two jets at random (even/odd event numbers are used to do this)

2. Try to match the selected jet to a L2 cluster within a cone of $\Delta R = 0.4$. If there is no match, skip the event.

3. If the E_T of the matched L2 cluster is below the trigger threshold, skip the event.

4. Put the other jet into the sample.

5. If both jets have matched L2 clusters which pass the trigger threshold, put both jets into the sample.

The E_T spectra of the jets are shown in Figures D.1, D.2, D.3 and D.4 along with the E_T spectra for clusters passing the electron/photon selection criteria. Dividing bin-by-bin yields the fake rate. The average rates are flat, within error, as a function of E_T for $E_T > 25$ GeV. The fake rate is taken to be the average fake rate per jet using jets with $E_T > 25$ GeV. The results are summarized in Table D.1.

Fake Rate	Generic Jets	Fakes	Rate (Per Jet)
Central Photons	40342	52	1.3×10^{-3}
Central Electrons	40342	0	$<7.4 \times 10^{-5}$ (95% C.L.)
Plug Electrons	18469	40	2.2×10^{-3}
Plug Photons	18469	74	4.0×10^{-3}

Table D.1: The rates at which jets pass the electron and photon selection criteria. Note that no attempt has been made to remove contributions from real physics objects.

D.1 The $\Delta\phi$ Distribution for Fake Electrons

To study the $\Delta\phi$ distribution of fake electrons a large sample of fake electrons is selected (using JET_50 and JET_70 as well). The distribution is

shown in Figure D.5. A total of 67 clusters that are SVX fiducial are found, 9 of which have a good stub with $|\Delta\phi| > 0.03$ rad.

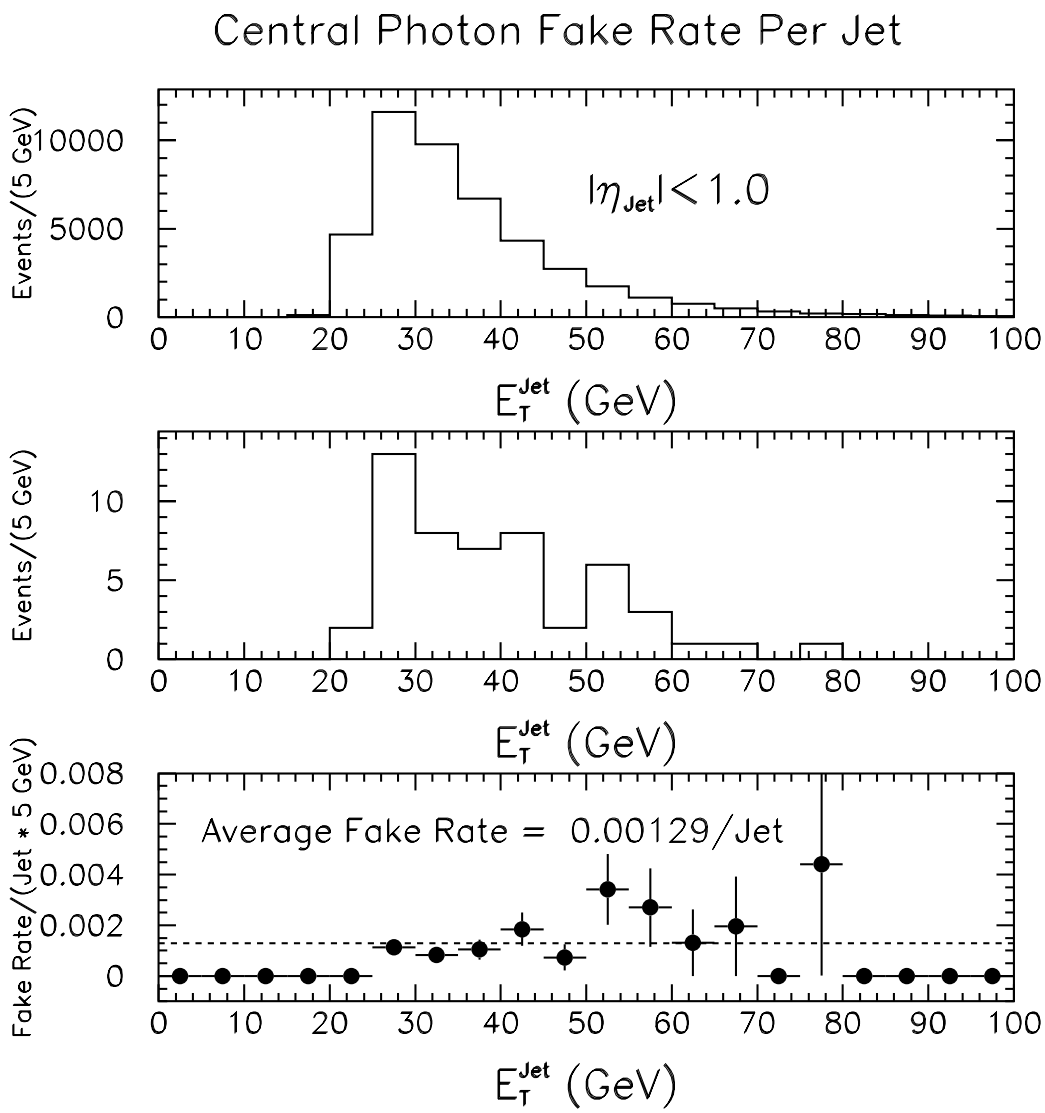

Figure D.1: The central photon fake rate as a function of E_T. The average fake rate is 1.3×10^{-3} per jet and is flat as a function of E_T for $E_T > 25$ GeV.

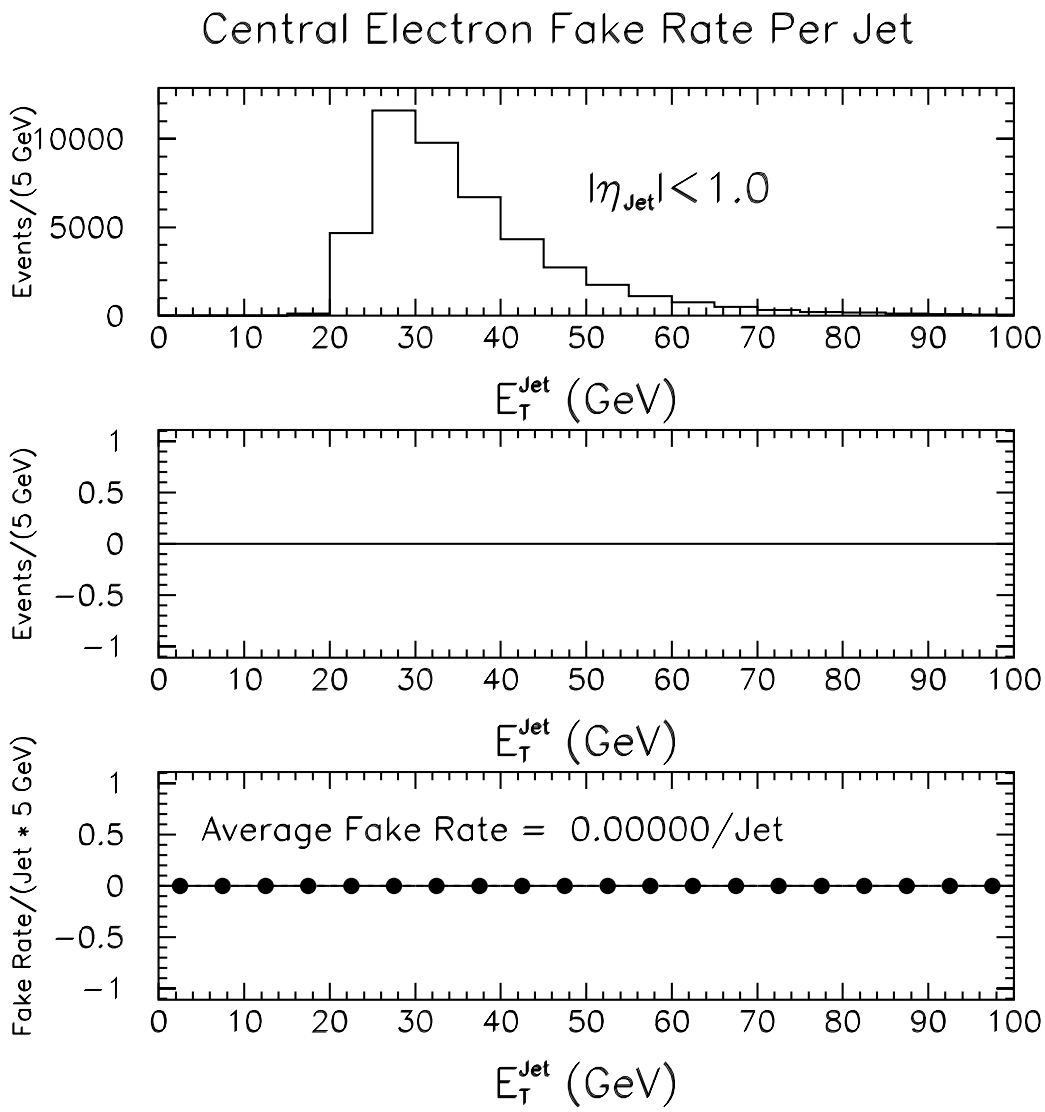

Figure D.2: The central electron fake rates as a function of E_T. No events pass the isolated central electron selection criteria for an upper limit of 7.4×10^{-5}/jet at 95% C.L.

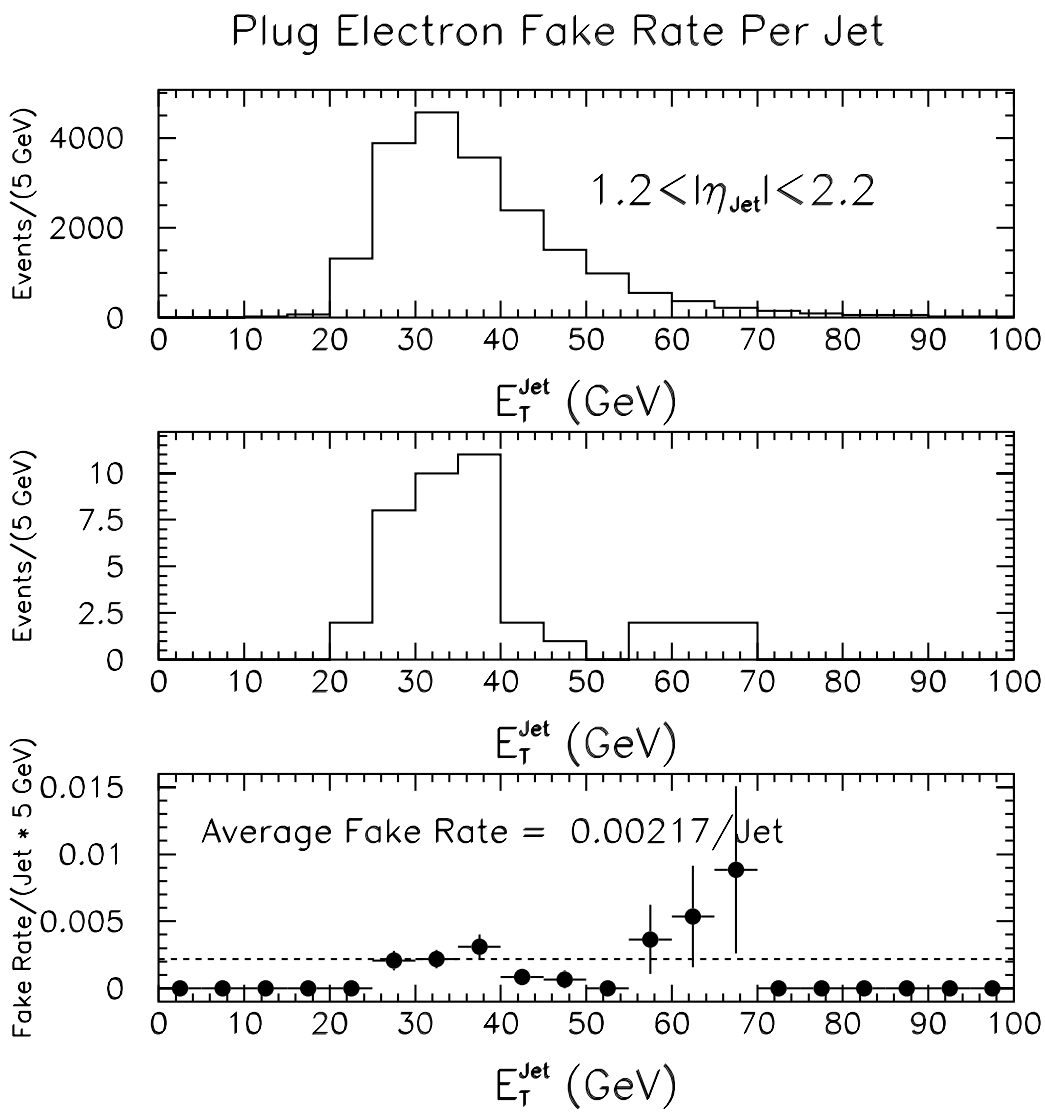

Figure D.3: The plug electron candidate fake rates as a function of E_T. The average rate is 2.2×10^{-3}/jet and is essentially flat as a function of E_T for $E_T > 25$ GeV.

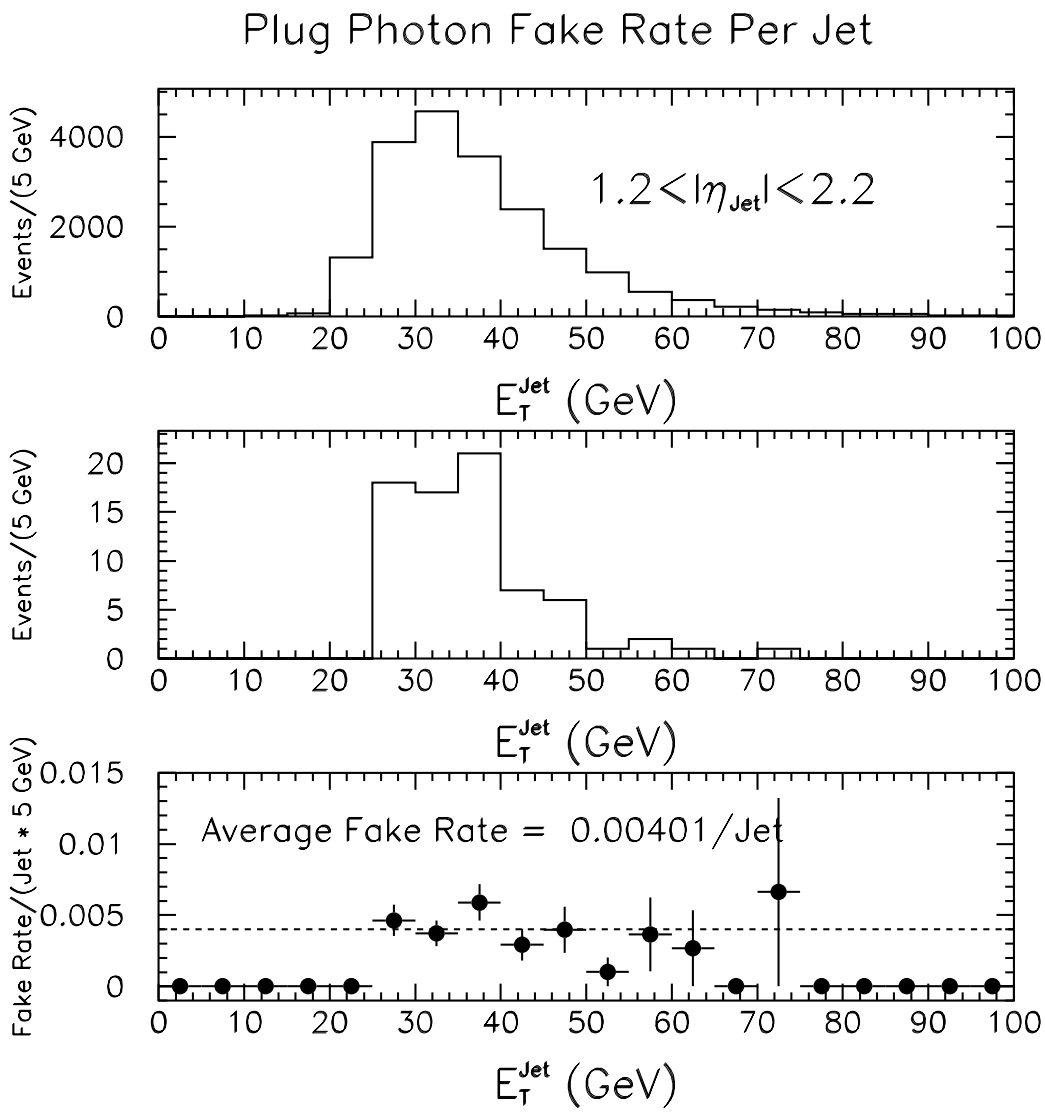

Figure D.4: The plug photon fake rates as a function of E_T. The average rate is 4.0×10^{-3}/jet and is essentially flat as a function of E_T.

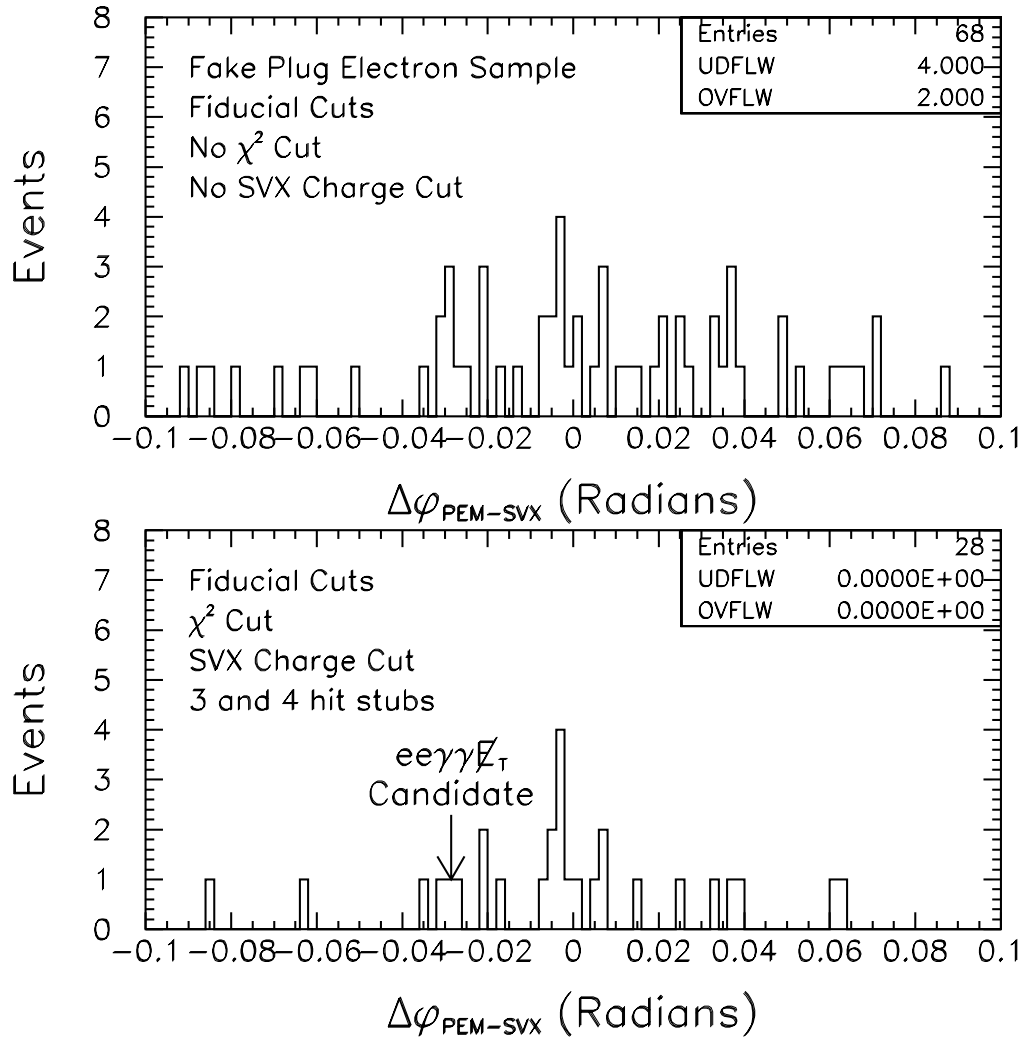

Figure D.5: The $\Delta\phi$ distribution between the cluster centroid and an associated SVX stub for fake plug electron candidates.

Appendix E

Comments on the Plug Electromagnetic Shower

This Appendix discusses an indication that the cluster in the plug calorimeter of the $ee\gamma\gamma\not{E}_{\mathrm{T}}$ candidate event has a shower which would be unusual for an electron. A coarse measurement of the full shower profile using proportional chambers, shown in Figure E.1, is consistent with the electron hypothesis. However, a detailed measurement of the profile using strip chambers at approximately shower maximum give results which would be unusual for an electron. A comparison shows that the results from the strip chamber are not consistent with the full profile measurement and may be due to noise in the detector. The cluster appears to be consistent with the shower expected from an electron or photon.

The plug electromagnetic calorimeter (PEM) consists of two modules (one forward, one backward) each of which consists of four quadrants of $\Delta\phi = 90^0$. Each quadrant consists of 34 layers of proportional tube arrays interleaved with 2.7 mm-thick lead absorber panels. Strip chambers (PES)

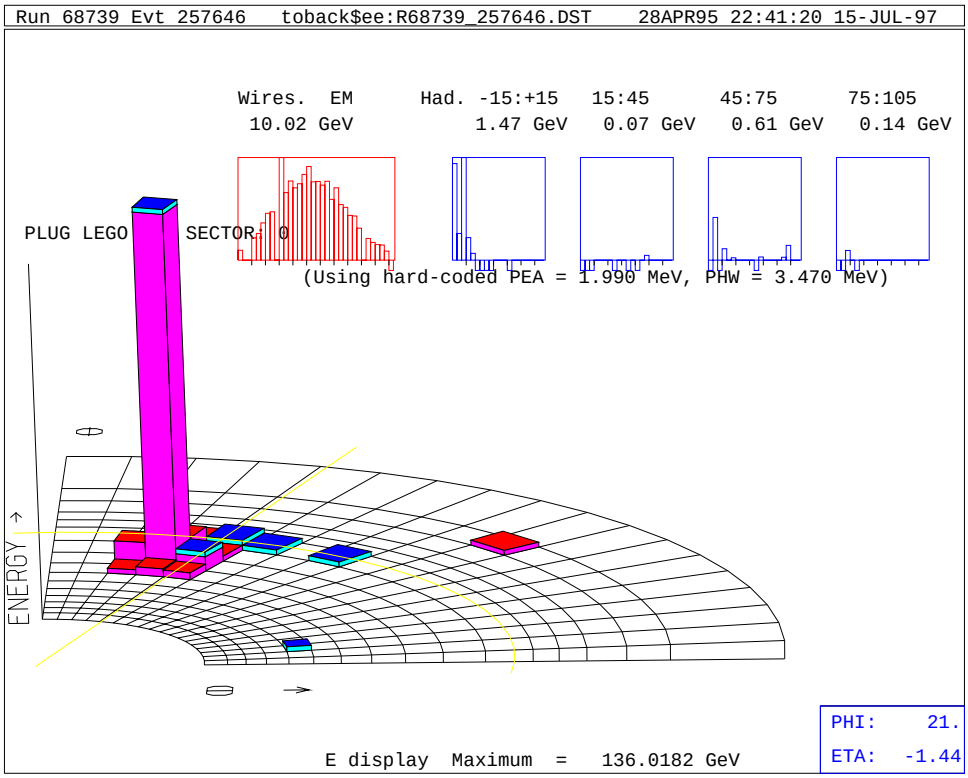

Figure E.1: The event display for the cluster in the PEM in the $ee\gamma\gamma\not{E}_T$ candidate event. Note that this is energy, not E_T. All towers with less than 0.5 GeV have been suppressed

are embedded near shower maximum, in layers 6-15. The five odd-numbered layers have 32 arc-shaped strips of $\Delta\eta$=0.02 which span 30° in ϕ (η strips). The remaining five even-numbered layers have thirty radial strips of $\Delta\phi = 1.0°$ (ϕ strips). The coverage of these strips in polar angle is limited to the region $1.2 < |\eta| < 1.84$. For more details on the plug electromagnetic calorimeter see Ref. [32].

Figure E.2 shows the energy deposited in the electromagnetic calorimeter as a function of the individual layers. Note that layers 2, 3, 9 and 27 were disconnected, and that there appears to be some type of noise in layer 10 (an η-strip layer). A quantitative comparison of the shower with expectations from test beam data [44] (see the χ^2_{3x3} and $\chi^2_{\rm Depth}$ values in Table 4.5 and Figure 4.5) shows that the shower is consistent with the electron hypothesis.

The shower shape, as measured in the strip chambers, can be compared to expectations from electrons using a χ^2 test [138]. An electron typically deposits energy in 11 strips in both the η and ϕ directions in the strip chamber. Separate comparisons are made in each direction and are denoted by χ^2_ϕ and χ^2_η respectively. The distributions for electrons from the $Z^0 \rightarrow e^+e^-$ control sample of Chapter 4 are shown in Figure E.3 along with the results for the cluster in the $ee\gamma\gamma\not{E}_{\rm T}$ candidate event. While the χ^2_ϕ measurement is in the middle of the distribution ($\chi^2_\phi = 2.2$), the χ^2_η measurement is on the tail of the distribution ($\chi^2_\eta = 11.7$) indicating that it would be unusual for an electron. A detailed, strip-by-strip, comparison of the pulse heights in the strip chamber with the expected shower shape is shown in Figures E.4 and E.5. There is some indication of an excess in the second and third bins in ϕ, and in the ninth bin in η. The ϕ deviations are not statistically significant. Given that χ^2_ϕ= 2.2, the results are consistent with the single electron hypothesis.

In the η direction, the one strip at $\eta = -1.69$ measures an energy

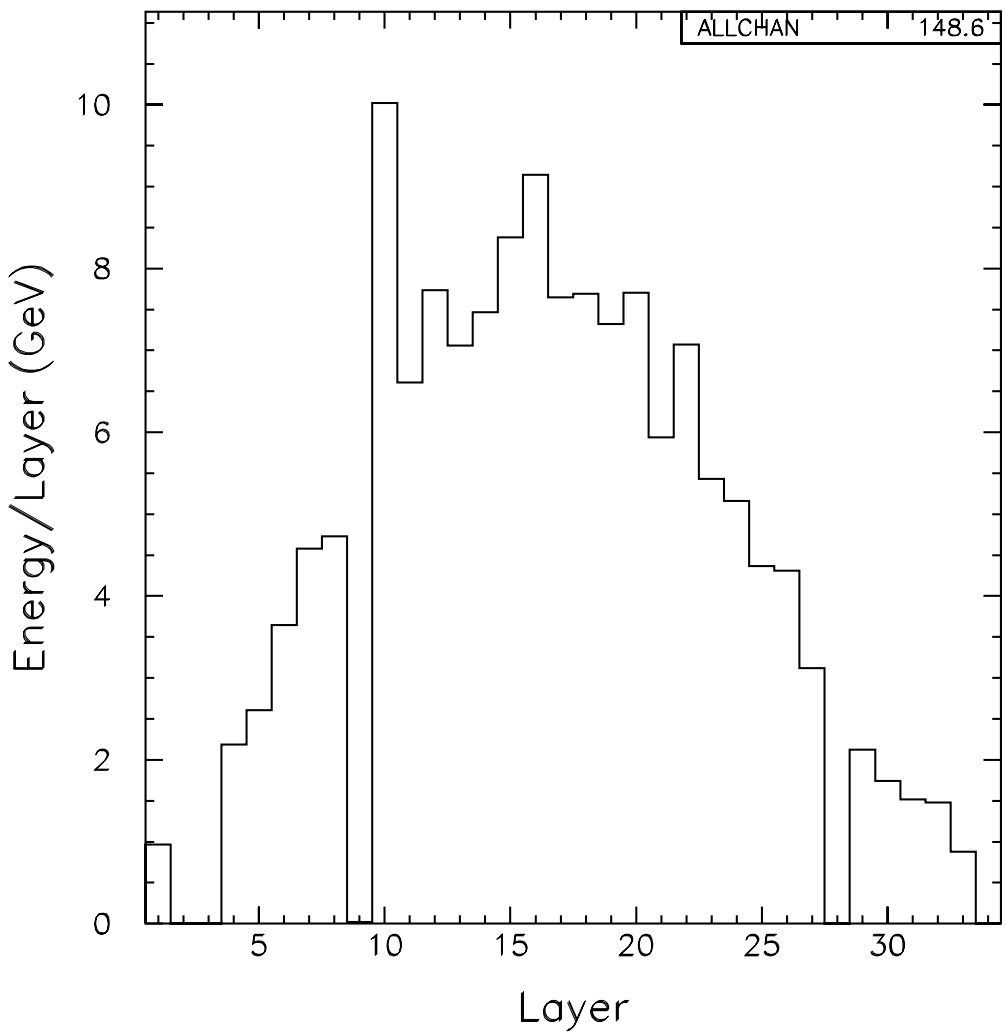

Figure E.2: The energy deposited in each layer of the calorimeter for the electromagnetic cluster in the $ee\gamma\gamma\not{E}_{\mathrm{T}}$ candidate event. Note that layers 2, 3, 9 and 27 were disconnected and that there appears to be some type of noise in layer 10 (an η-strip layer).

that significantly pulls the fit and gives most of the contribution to the χ^2. Note that in Figure E.2, layer 10 (which is an η-strip layer) is about 4 GeV higher than expected with the excess possibly due to noise or a low energy particle interacting in the gas of that one layer [137]. Since sampling calorimeters integrate the pulse height measured in each layer to make an energy measurement, each shower has three estimates of the total shower energy: one from the full 34 layers (the best estimate), one from the strip chambers in the ϕ direction, and one from the strip chambers in the η direction. In the η direction, the measurement is made using the integrated pulse height from layers 6, 8, 10, 12 and 14; the total shower energy is estimated to be 154.5 GeV. The full calorimeter, which uses all 34 layers for a more accurate energy measurement, uses the same integrated pulse height measurement to estimate that 33.6 GeV was deposited in those 5 layers. Normalizing the 4 GeV excess seen in Figure E.2 to the scale in the η strips corresponds to about 18 GeV of extra energy in the strips, which is about equal to the excess in bin 9 in Figure E.5. Removing that one strip from consideration yields χ^2_η=3.1 which is very much in the middle of the distribution in Figure E.3.

Another indication that the excesses seen in the strip chambers are due to noise is seen in Figure E.6 which shows the full shower energy measurement in the η and ϕ directions. After normalizing the energies measured in the strips to be equal to the energy as measured using the full calorimeter, it is evident that the excesses are only seen in the strip chambers. The conclusion appears to be that the measurement of the shower profile of the cluster is unusual, but is consistent with being from an electron or photon.

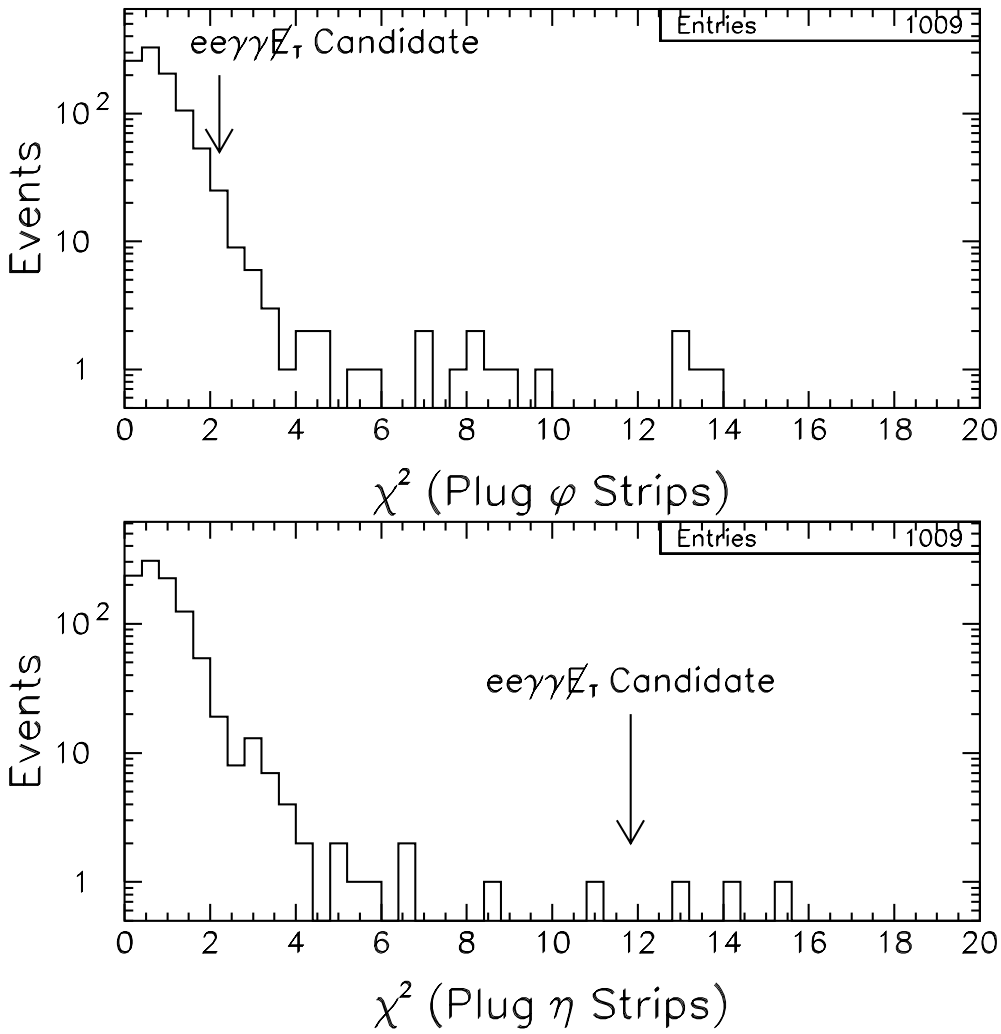

Figure E.3: The distribution of a χ^2 test between measured and expected pulse heights in the strip chambers in the plug calorimeter for electrons in the $Z^0 \rightarrow e^+e^-$ control sample. The results for the cluster in the $ee\gamma\gamma\not{E}_{\rm T}$ candidate event are illustrated on the plot by arrows.

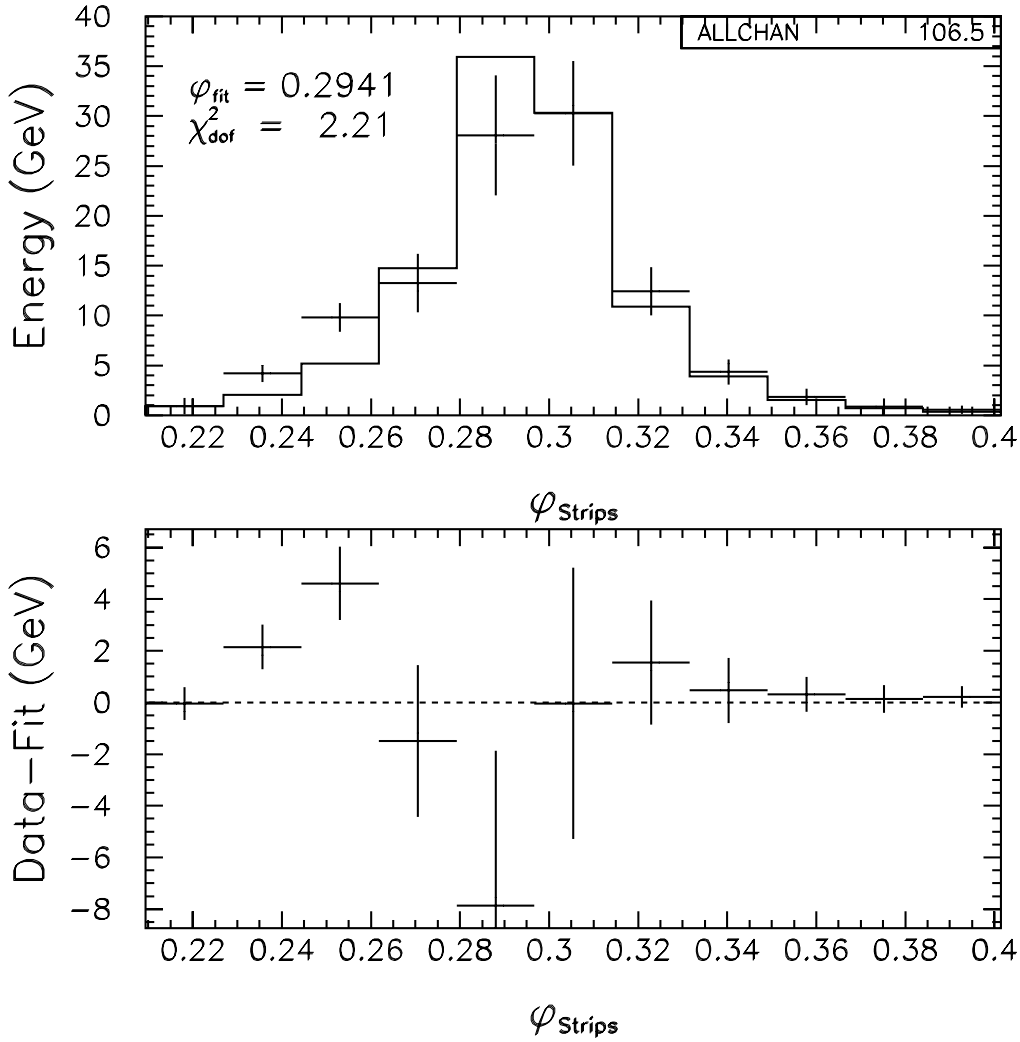

Figure E.4: The energies, as measured by individual strips in the strip chambers, in the ϕ direction for the cluster in the plug calorimeter in the $ee\gamma\gamma\not{E}_{\mathrm{T}}$ candidate event.

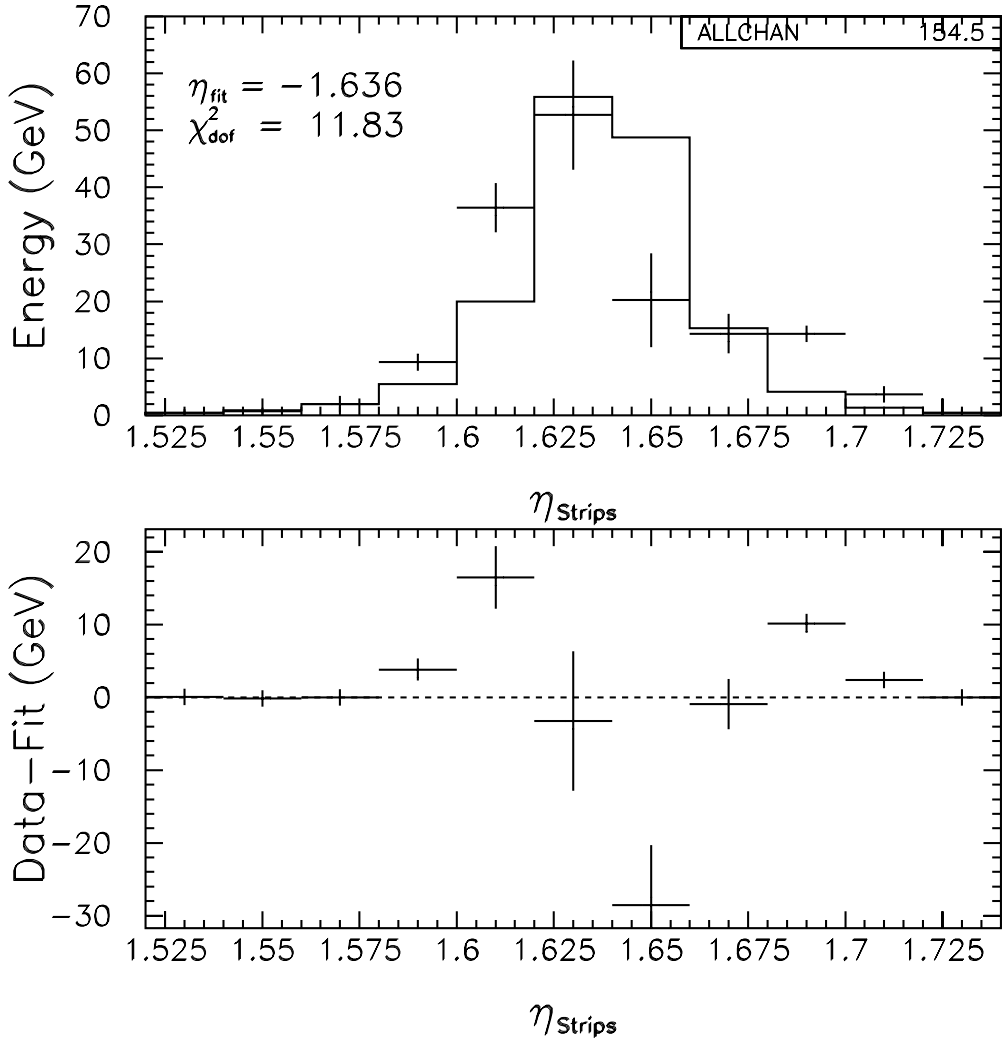

Figure E.5: The energies, as measured by individual strips in the strip chambers, in the η direction for the cluster in the plug calorimeter in the $ee\gamma\gamma\not{E}_{\mathrm{T}}$ candidate event.

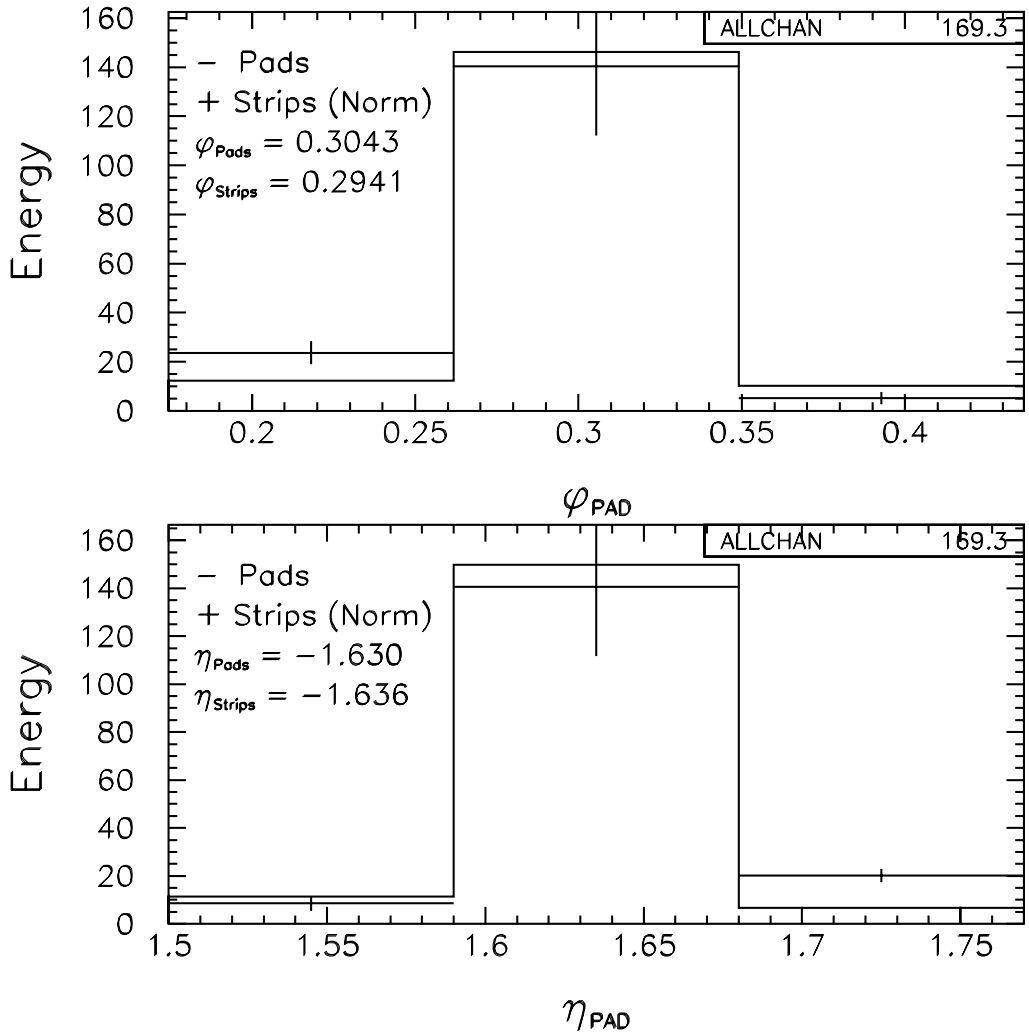

Figure E.6: A comparison of the energy deposition of the cluster in the plug using all 34 layers in the calorimeter and using just the strip chambers. The apparent excesses in the strips in the ϕ and η directions are only seen using the strip chambers. Note that the energies measured by the strip chambers have been summed in a given direction and normalized to be equal to the energy measured in all 34 layers.

Appendix F

Comments on the Calculation of the χ^2 variables in the Plug Strip Chambers

This Appendix describes the shower shape comparison for electron candidates in the plug strip chamber. The strip chambers are described in Appendix E and in more detail in Ref. [32], and a typical electron deposits energy in 11 strips in the η and ϕ directions in the strip chamber. In order to do a quantitative comparison to electron shower shapes we set up a 'frozen' shower which is parameterized by its energy and η.

The shower widths (in ϕ and η) for a sample of electrons, from the $Z^0 \rightarrow e^+e^-$ control of Chapter 4, are shown in Figure F.1, and as a function of the shower energy in Figure F.2. A parameterization is given by $\sigma_\phi = 0.02 + 0.0000275 \times E_\phi$ and $\sigma_\eta = 0.02 + 0.0000219 \times E_\eta$. After subtracting off these variations the width is still η dependent. This is shown in Fig-

ure F.3. The full parameterization is given by

$$\sigma_\phi = (0.02 + 0.0000275 \times E_\phi) + (-0.018 + 0.0122 \times |\eta|) \qquad \text{(F.1)}$$

$$\sigma_\eta = (0.02 + 0.0000219 \times E_\eta) + (-0.023 + 0.0151 \times |\eta|) \qquad \text{(F.2)}$$

The residual width, $\sigma_{\text{Measured}} - \sigma_{\text{Parameterization}}$, is shown in Figure F.4.

Using the width parameterization, the normalized shower shape is estimated using the following algorithm:

1. Take a plug electron from the $Z^0 \rightarrow e^+e^-$ sample.
2. Normalize the energy of the strips (ϕ and η separately) by dividing each strip energy by the total energy measured in the 11 strips.
3. Calculate the distance ($\Delta\phi$ or $\Delta\eta$) from the energy weighted mean for each of the 11 strips.
4. Normalize the distance by dividing it by the expected width from Equations F.1 or F.2.
5. Fill a histogram with the normalized energy in the strip at the normalized distance from the mean.
6. Repeat for all strips and events.
7. Determine the mean energy and variation (σ) as a function of distance from the mean. The result is shown in Figure F.5.

Using the shape and uncertainties from Figure F.5, the mean position in the strips, using a χ^2 test, can be found for each electron in the plug. To do this, the generic shower is converted to a specific shower by scaling to the measured energy of the strips. The width is set to be equal to the

expectation as calculated from the Equations F.1 and F.2. The mean is found by minimizing the χ^2.

The χ^2 distributions in the ϕ and η directions, labeled χ^2_ϕ and χ^2_η, for the $Z^0 \rightarrow e^+e^-$ control sample are shown in Figure E.3. A detailed study of the individual events with large χ^2 show that most have a few strips at the ends of the cluster which are indicative of a small second cluster. Each could be due to a number of effects. 1) the cluster is due to a fake electron, 2) the electron emitted a photon via Bremstrahlung while traversing the detector, 3) the shower simply fluctuated and 4) there could be additional, unrelated energy from the underlying event or a second collision in the event.

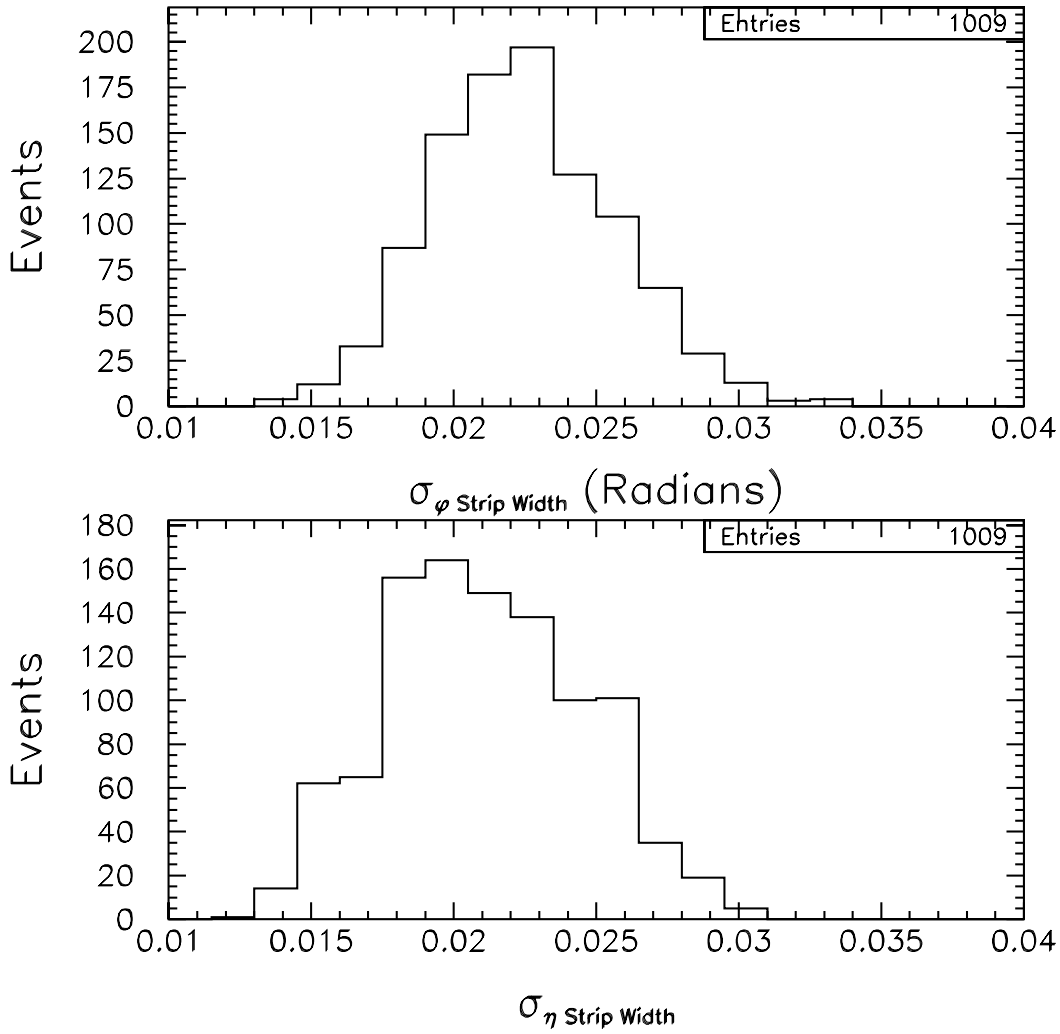

Figure F.1: Electron shower widths as measured in the plug strip chamber from the $Z^0 \rightarrow e^+e^-$ sample.

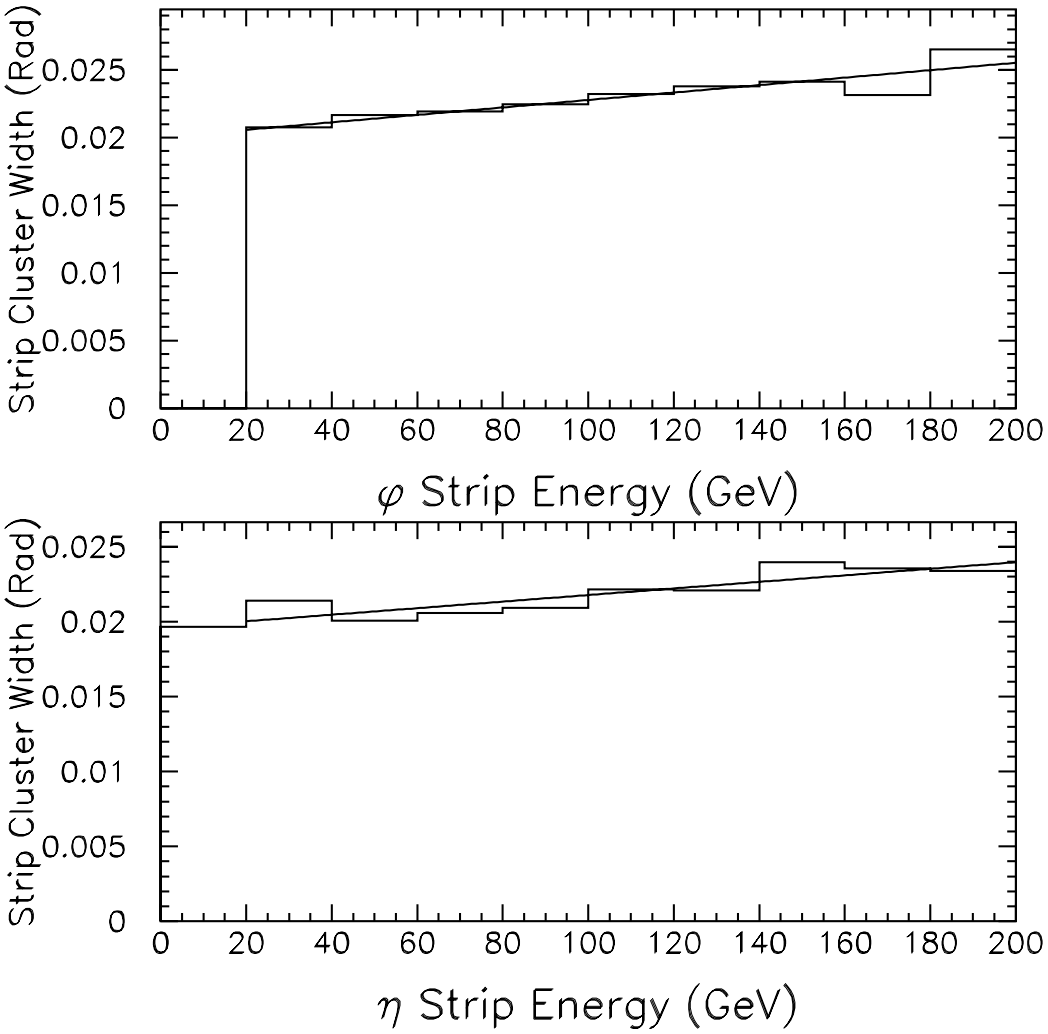

Figure F.2: The width of electron showers, as measured in the strip chambers, as a function of energy of the electron.

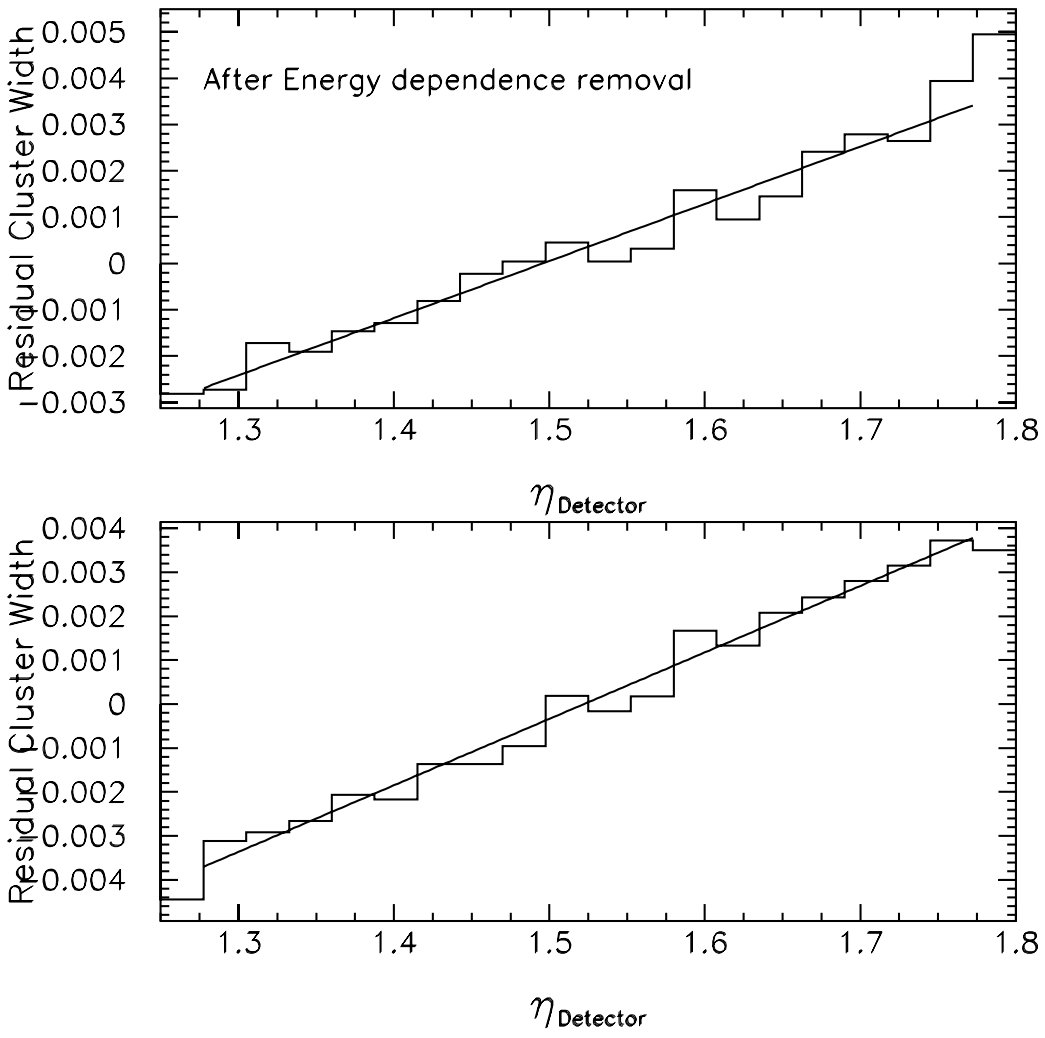

Figure F.3: The width of electron showers, as measured in the strip chambers, as a function of η of the electron. Note that energy dependence of the width has already been subtracted off.

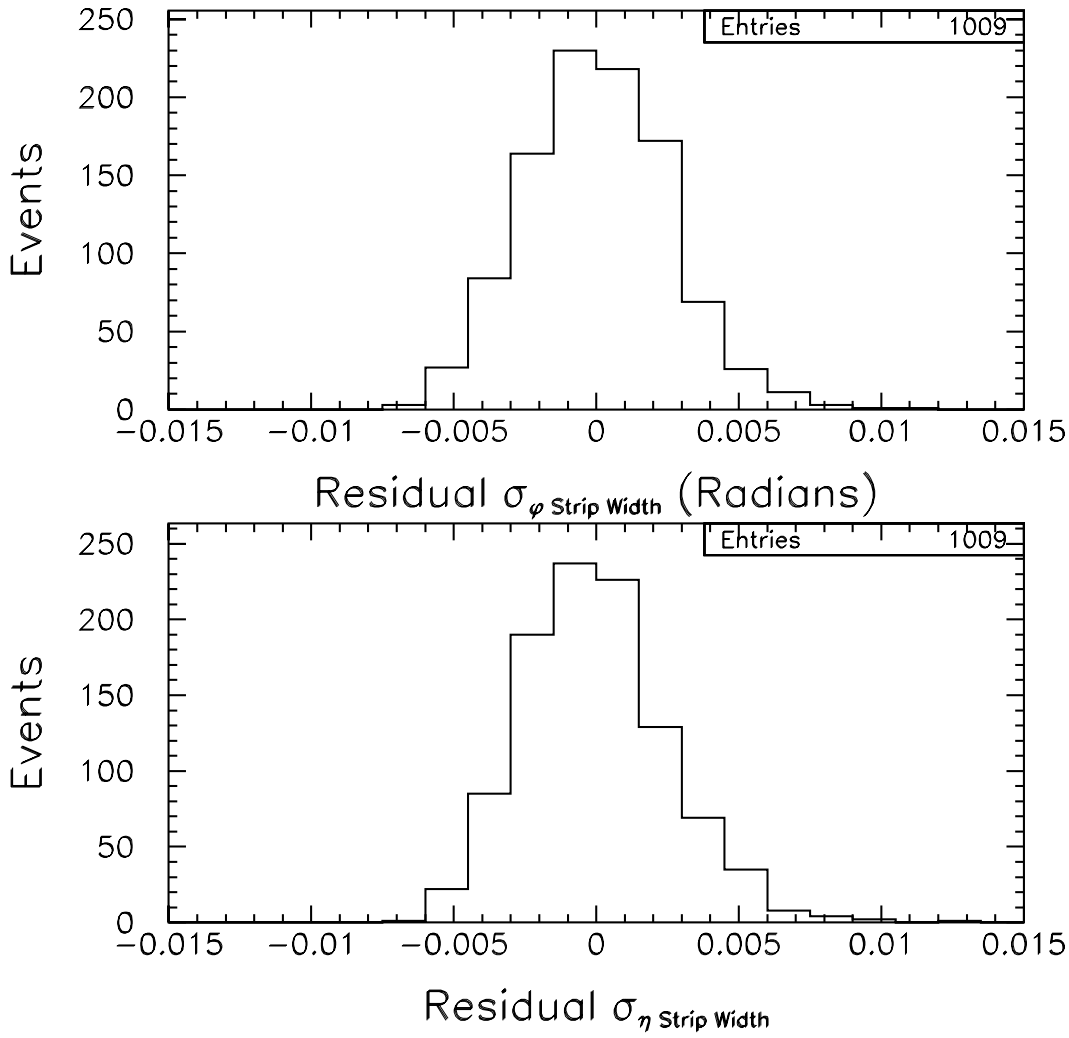

Figure F.4: The residual width of electron showers after energy and η dependences have been subtracted off

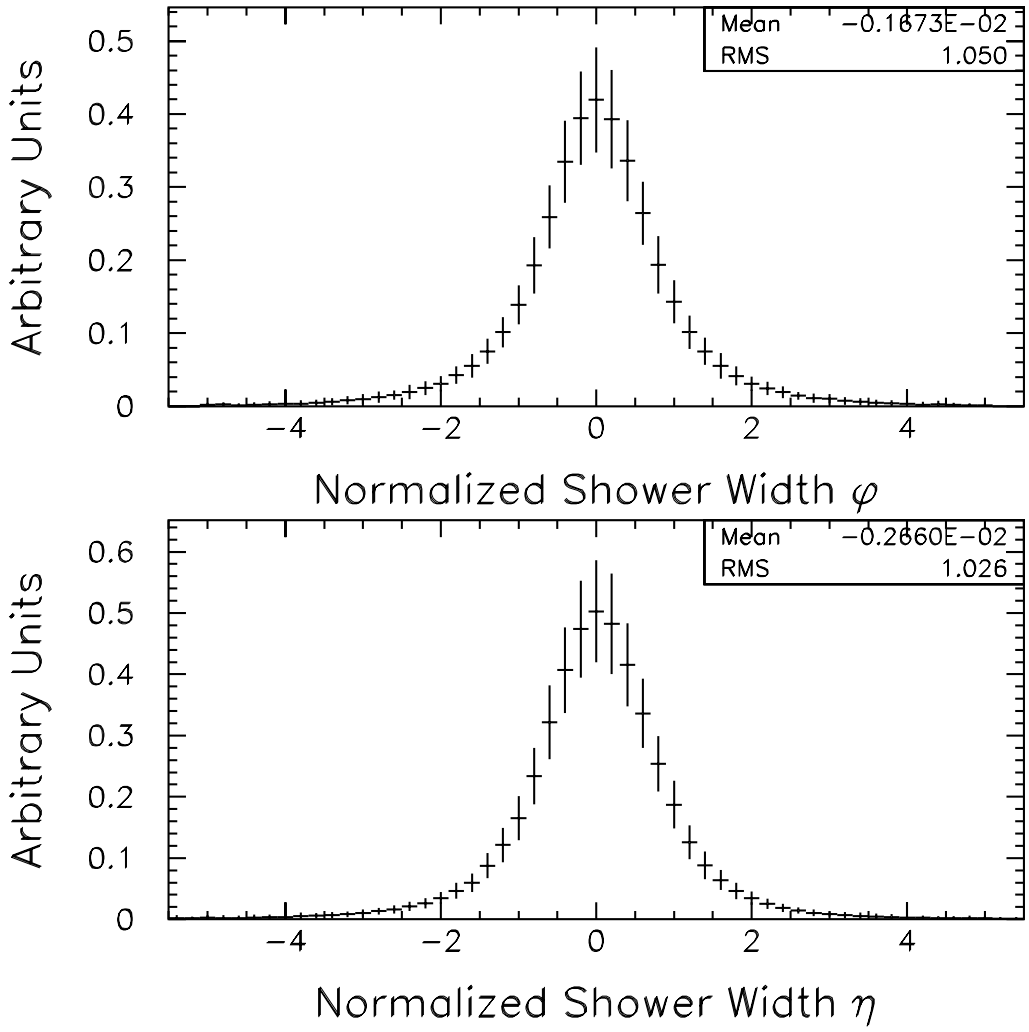

Figure F.5: The normalized electron shower shape in the ϕ and η directions as measured in the plug strip chambers

Appendix G

Comments on the SVX Stub Finding Algorithms

This Appendix describes the SVX tracking algorithm used to find the stubs in the SVX that are associated with electrons. The standard SVX algorithms search for SVX clusters along the trajectory defined by tracks in the central tracking chamber. While the efficiency for finding stubs is high, the efficiency for finding tracks in the central tracking chamber for electrons in the plug calorimeter can go to zero for large η. To deal with this problem a technique was developed to use the standard stub-finding algorithms but using fake track information ($\phi, \theta, D_0, \mathrm{P_T}$ and Z_0) based only on the calorimeter cluster and beam spot position information [86, 139].

The $\Delta\phi$ between the measured ϕ position in the strip chambers (CES and PES respectively) and from the SVX stub for electrons from the $Z^0 \rightarrow e^+e^-$ control sample of Chapter 4 is shown in Figure G.1. Two peaks, corresponding to the bending of positively and negatively charged electrons in the magnetic field, are clearly visible. The events with large $\Delta\phi$ are from

mismeasured or fake stubs. To remove obviously fake stubs, the hypothetical trajectory from the z position of the vertex to the measured position in the calorimeter is required to have passed through the fiducial part of at least 3 layers of the SVX [87]. A further requirement is that any stub found must have at least 3 or more clusters in the SVX. Figure G.2 shows the resulting $\Delta\phi$ distribution.

Two additional requirements are made to select only good SVX stubs and ensure they are consistent with central or plug electrons respectively. Well-measured SVX stubs are selected by requiring $\chi^2_{\rm SVX} < 2.0$ (see Figure G.3). Using $\frac{dE}{dX}$ techniques, the η for the stub can be inferred; the amount of charge (which is proportional to the energy deposited in the silicon) collected by the SVX strips, Q, helps determine the path length of the particle through the strip. For a given stub, the cluster with the smallest amount of charge deposited, normalized by the trajectory angle $Q^{\rm Uncorr}_{\rm Min} \times Sin(\theta) = Q_{\rm Min}$, is a good measure of the direction of the charged particle. Figure G.4 shows $Q_{\rm Min}$ for central and plug electrons respectively. Each stub is required to have $80 < Q^{\rm Central}_{\rm Min} < 200$ or $100 < Q^{\rm Plug}_{\rm Min} < 200$ for central or plug electrons respectively. The final $\Delta\phi$ distribution, after all requirements, is shown in Figure G.5.

G.1 SVX Only Information for the $ee\gamma\gamma\not{E}_{\rm T}$ Candidate Event

The SVX tracker finds a best-fit trajectory using the SVX clusters as well as the calorimeter cluster and beam position information. However three SVX clusters and the beam position uniquely determine a set of fit

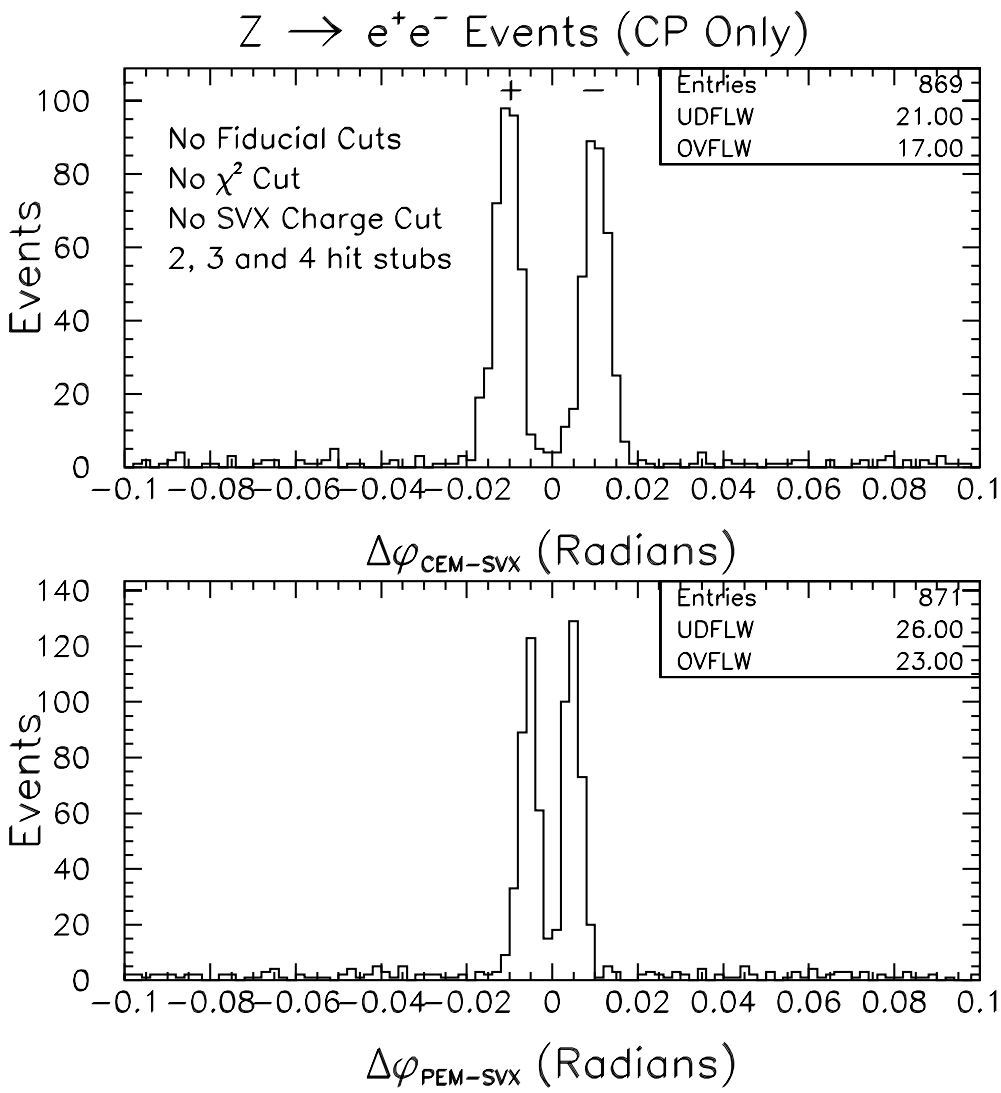

Figure G.1: The $\Delta\phi$ between the measured electron position from the strip chambers (CES and PES respectively) and the ϕ from the SVX tracker. The two peaks corresponding to the bending of positive and negatively charged electrons in the magnetic field are clearly visible. The events on the tails are from mismeasured or fake tracks.

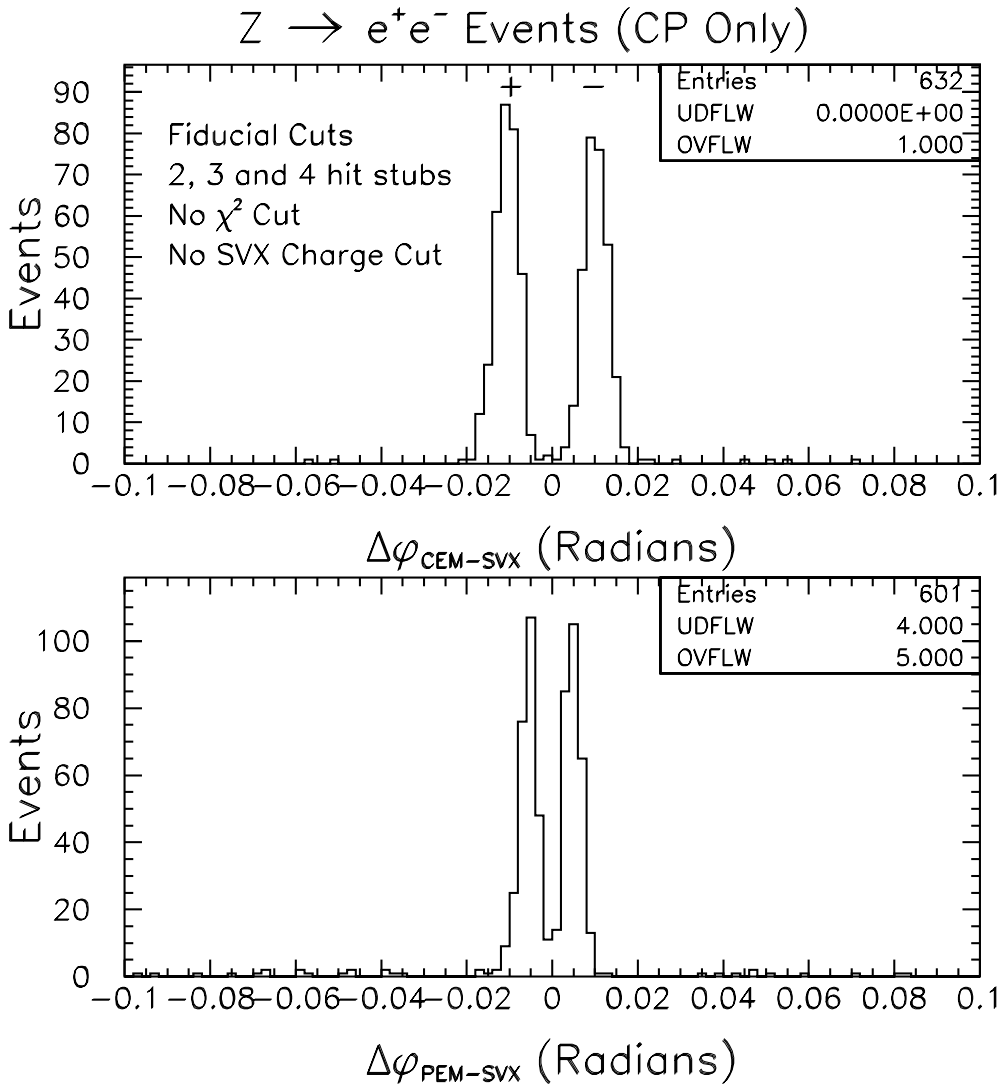

Figure G.2: The $\Delta\phi$ between the measured electron position from the strips and the ϕ from the SVX tracker. Here it is required that the electron trajectory traverse 3 or more layers of the SVX and that 3 or more clusters are observed [87].

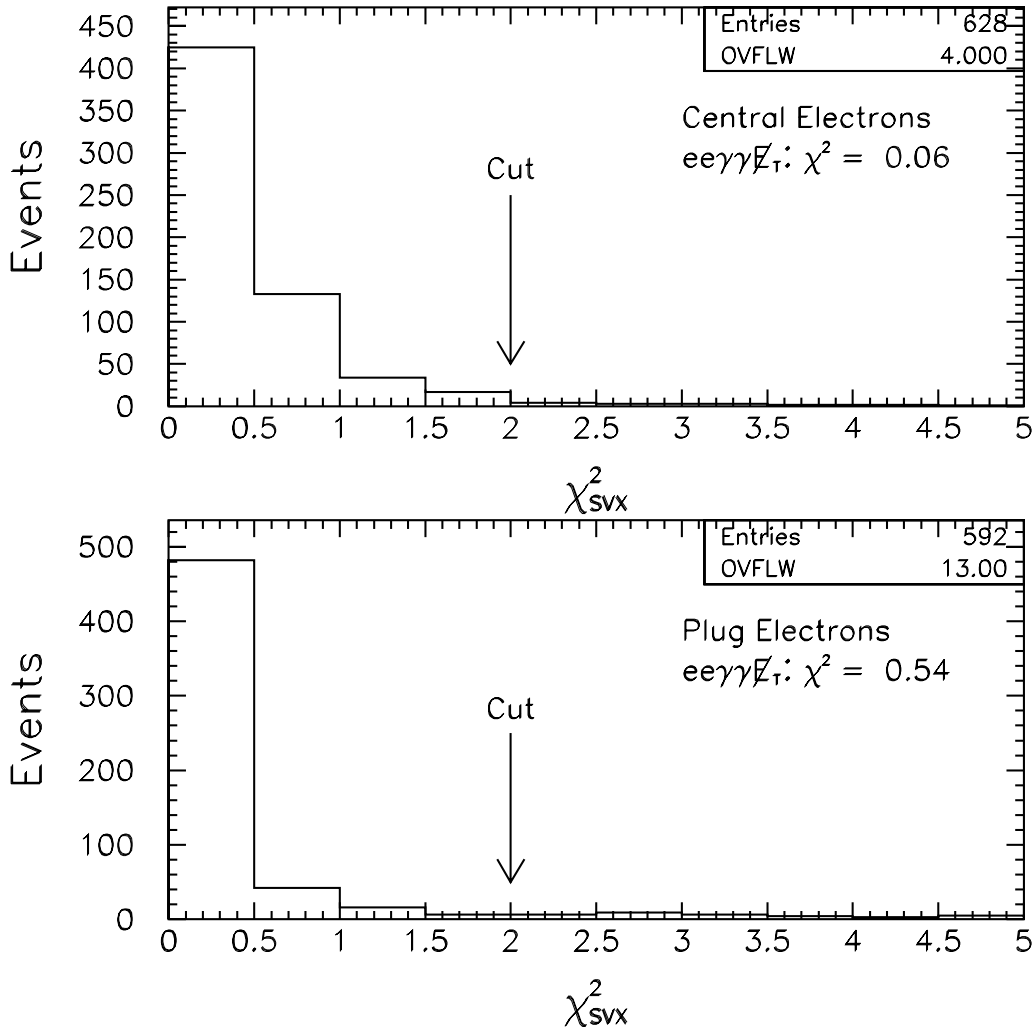

Figure G.3: The χ^2 distribution of SVX stubs found by the SVX tracker for electrons. All stubs are required to have $\chi^2 < 2.0$.

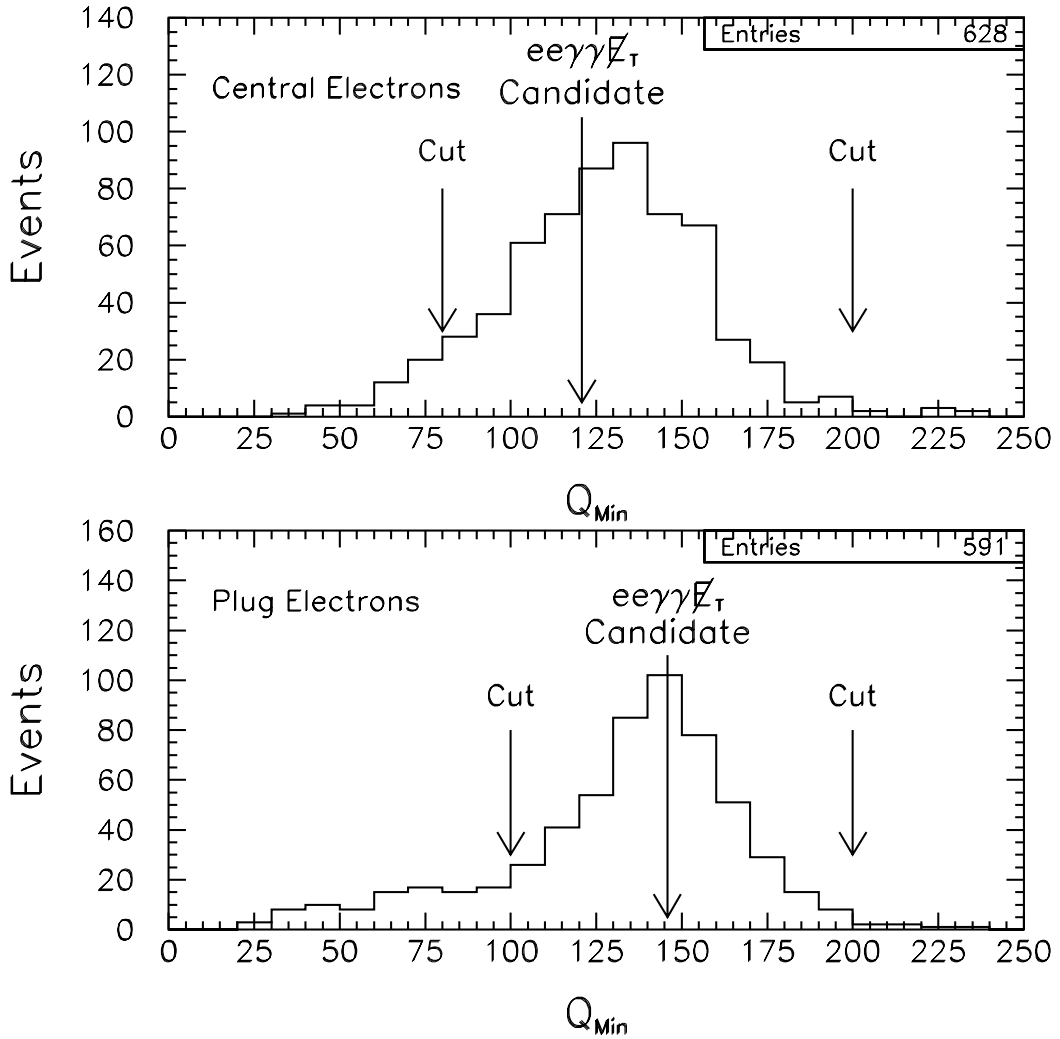

Figure G.4: The minimum charge deposited by electrons in any of the four SVX silicon layers. Note that the value has been corrected for the path length through the silicon. Each stub is required to have $80 < Q_{\rm Min}^{\rm Central} < 200$ and $100 < Q_{\rm Min}^{\rm Plug} < 200$.

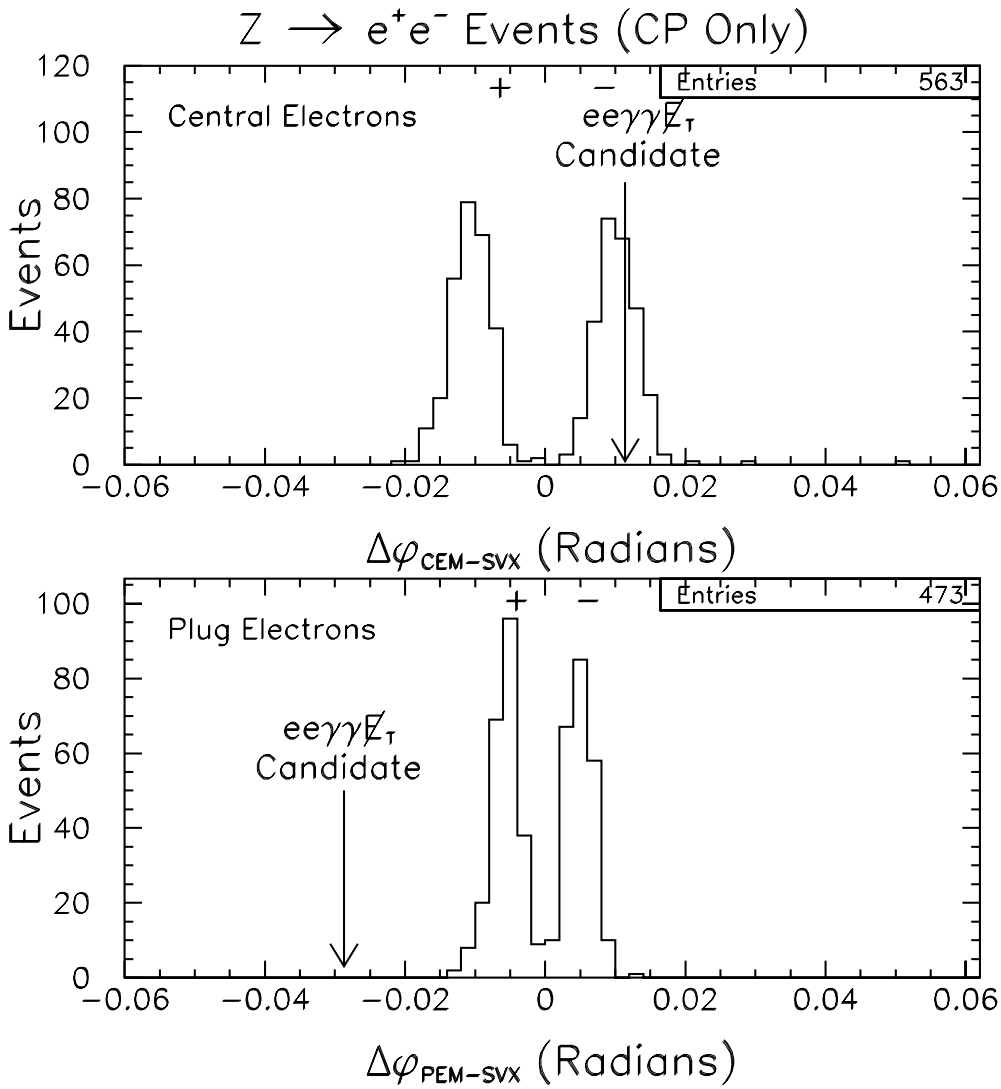

Figure G.5: The $\Delta\phi$ between the measured electron position and the ϕ from the SVX tracker after all requirements. Here it is required that the electron trajectory traverse 3 or more layers of the SVX and that 3 or more clusters are observed [87]. In addition the SVX stub is required to pass the $\chi^2_{\rm SVX}$ and $Q_{\rm Min}$ requirements discussed in the text.

parameters (ϕ_0, D_0 and curvature ($\mathrm{P_T}$)). This is not usually done because the SVX stand-alone momentum measurement is not very precise (due to such a small lever arm). To illustrate this point, and show why the D_0 measurement in the $ee\gamma\gamma\not{E}_{\mathrm{T}}$ event is sensitive to the cluster energy and ϕ information, we determine the parameters and the resolutions on them for the stub in the $ee\gamma\gamma\not{E}_{\mathrm{T}}$ candidate event, using the stand-alone SVX information. To do this the track parameters are found for a set of 10,000 pseudo-experiments in which the the position of the beam and the SVX clusters are independently varied according to their uncertainties. The results are shown in Figures G.6 and G.7. The best-fit curvature indicates that the stub is due to a positively charged particle with curvature $C = 9 \pm 11\mu\mathrm{m}^{-1}$ ($\mathrm{P_T}$ = 2.44 GeV/c and consistent, within errors, with infinite momentum), $\phi_0 = 0.258 \pm 0.009$ rad and $D_0 = 233 \pm 180$ μm. Figure G.7 shows that the three parameters are highly correlated and why the large $\mathrm{E_T}$ used to seed the tracking algorithm pulls the fit to larger ϕ and smaller impact parameter. These results clearly show that if the cluster and the stub are not from the same particle then the impact measurement is not constrained and is completely consistent with being zero.

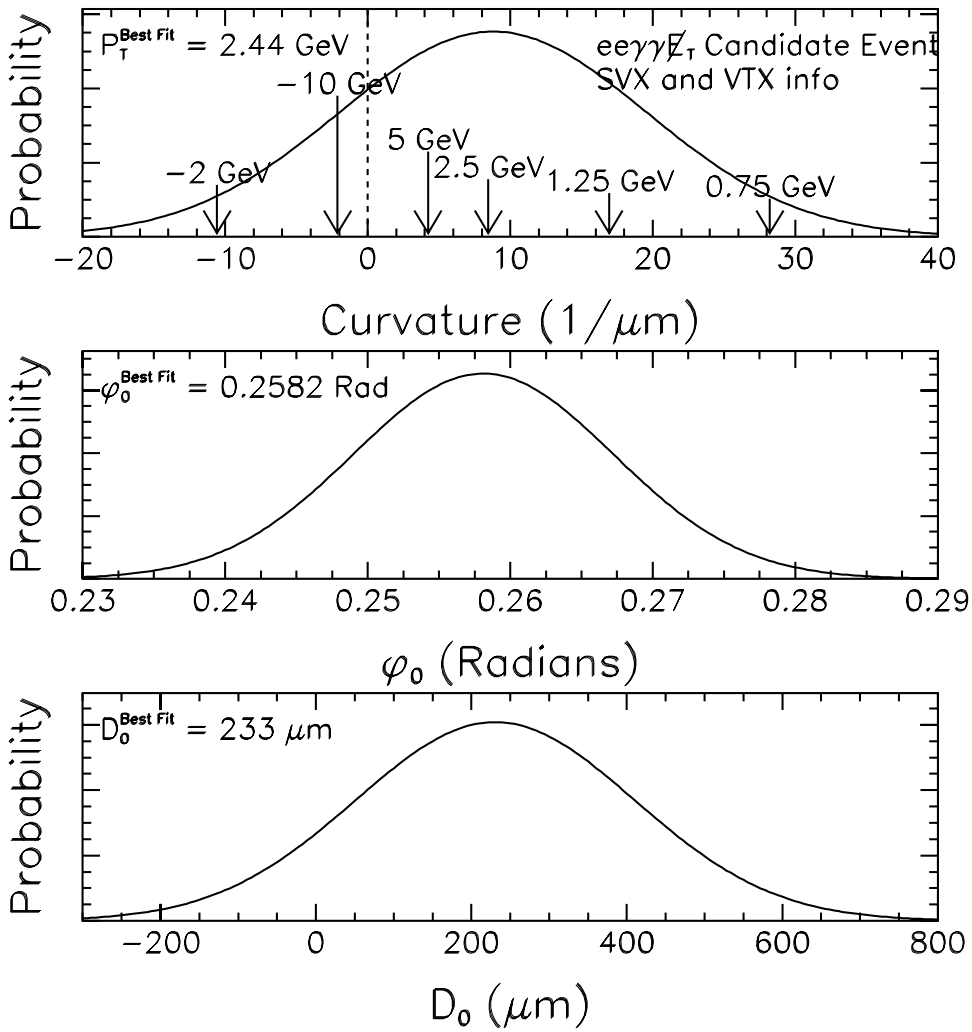

Figure G.6: The resolution of the SVX track parameters for the $ee\gamma\gamma\not{E}_T$ candidate event when no calorimeter information is used. Note that while the best-fit indicates that the track is due to a positively charged particle with $P_T = 2.44$ GeV, the P_T is consistent, within errors, with infinite momentum.

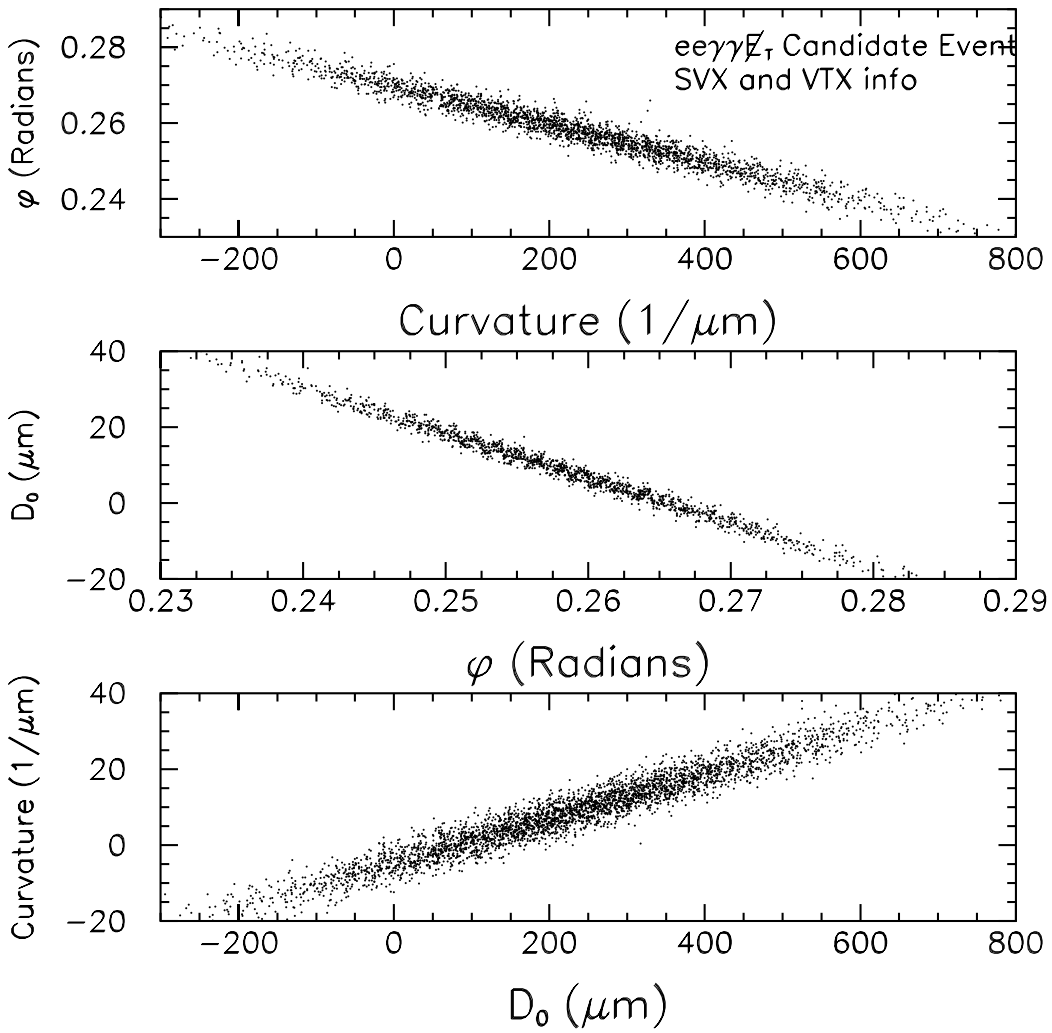

Figure G.7: The correlation between SVX track parameters in the $ee\gamma\gamma\not{E}_T$ candidate event when no calorimeter information is used. The three parameters are highly correlated.

Appendix H

Comments on the Electron Interpretation of the Cluster

This Appendix considers the possibility that the plug cluster in the $ee\gamma\gamma\not{E}_{\mathrm{T}}$ might be due to an electron in spite of the measurement of the probability for an electron to have $|\Delta\phi| > 0.03$ rad to be less than 0.3% at 95% C.L. For example, the electron could have emitted an energetic photon via Bremstrahlung while traversing the detector. Similarly, the electron could have had a high angle elastic scattering with a nucleus. Three cases are considered in detail:

- Case 1) The photon emission or collision occurs after the electron leaves the SVX. In this case there should be at least two final state particles and the SVX stub should, by conservation of momentum, point to the energy-weighted mean of the energy deposition in the calorimeter (within the expected resolution and bending due to the magnetic field). A back-of-the-envelope calculation shows that a high energy electron scattering off a stationary proton could (kinematically) be deflected by $\Delta\phi = 29$ mrad.

The recoil proton could have a transverse energy as small as E_T=2.7 GeV, and as large a scattering angle as $\Delta\phi_{ep} = 1.2$ rad.

Figures E.4 and E.5 show that while there is an excess within the shower which could be the second cluster, it is not statistically significant (see Appendix E). There are no extra clusters in a cone $\Delta R = 1.0$. The closest possible candidate is a low E_T cluster ($E_T = 4.9$ GeV, E=54 GeV) at large η ($\eta = -3.1$, $\phi = 0.17$ rad). This is unlikely to be related to the cluster in the plug: the signal-to-noise ratio for the energy measurement of this is cluster is so low that it may simply due to noise. Furthermore, the two particle kinematics require the 'target' particle to have at least 6 GeV of mass.

While there is no evidence for a photon emission or scattering scenario, this type of scenario cannot be ruled out as being anything other than highly improbable.

- Case 2) Before the electron reaches the SVX, it emits a photon via Bremstrahlung that carries off most of the energy. Since the initial direction of the electron is directly toward the center of the electromagnetic cluster (again by conservation of momentum), the SVX stub is due to the electron going off with low momentum and the electromagnetic cluster is due to the photon. In this case, there should be a measurable impact parameter. The smallest possible impact parameter is estimated by assuming that the earliest point the electron could emit the photon is at the beam pipe (radius = 1.95 cm), and that the smallest opening angle between the electron and the photon is 29 mrad (a fairer estimate is closer to 50 mrad since the beam pipe is almost half way to the SVX). This implies an impact parameter of $D_0 > R \times \Delta\phi_{min} = 1.95$ cm $\times$ 29 mrad = 565μm. The

impact parameter is measured to be 90 ± 45 μm which is inconsistent with this hypothesis.

- Case 3) The photon emission or collision occurs in the SVX. If this were the case, there should be a deviation, or kink, along the trajectory defined by the SVX hits and the primary vertex. No such occurance is seen. If it occurs early enough in the SVX then the same arguments as in Case 2 hold.

There is no indication that this cluster-stub combination is a particularly unusual example of an electron interacting with the detector.

Appendix I

The Datasets Used in Chapter 5

This Appendix describes the four datasets used for the rate estimates in Chapter 5. The datasets are: W-type events (central electron + $\not\!\!E_{\rm T}$, and plug electromagnetic cluster + $\not\!\!E_{\rm T}$), photon-type events, cosmic ray-type events (central photon + $\not\!\!E_{\rm T}$, and plug electromagnetic cluster + $\not\!\!E_{\rm T}$), and Z^0/γ^*-type events (central electron + central or plug electromagnetic cluster).

I.1 Z^0/γ^* and W-Type Processes

Samples of $Z^0/\gamma^* \rightarrow e^+e^-$ and $W \rightarrow e\nu$ events are preselected from the inclusive central electron sample [52] by requiring a high-$\rm E_T$, isolated electron in the central calorimeter that passes the selection requirements in Table 2.2. The $Z^0/\gamma^* \rightarrow e^+e^-$ events are selected by having a second electron (central or plug) with $\rm E_T > 25$ GeV; $Z^0 \rightarrow e^+e^-$ events additionally require 81 GeV $< M_{\rm e^+e^-} <$ 101 GeV. Note that the number of $Z^0 \rightarrow e^+e^- + \not\!\!E_{\rm T}$ events is a slight overestimate because there are other small backgrounds, such as $WW, WZ^0, t\bar{t}$ and $Z^0 \rightarrow \tau\tau$, which produce e^+e^- events which have *intrinsic* missing $\rm E_T$. In addition, there is significant jet activity in some of these

events which tends to smear out the $\not\!\!E_T$. The W-type events are selected by requiring a central electron and $\not\!\!E_T > 25$ GeV. Note that this includes Z^0/γ^* events in which the second electron is lost or grossly mismeasured.

I.2 Plug Electron Dataset

The plug electron dataset is created from events passing two separate triggers. In CDF Jargon, the triggers are from Stream A and are called ELEA_PEM_ALL_CUT, which requires an electromagnetic cluster which passes tight plug electron selection criteria, and ELEA_PEM_20_MET_20, which has only loose plug electron selection criteria but requires $\not\!\!E_T > 20$ GeV. In a sample of 32 pb^{-1} data, there are 77,633 events, 19,114 of which have a plug electron candidate which passes all the requirements; 8975 pass the additional $\not\!\!E_T > 25$ GeV selection criteria.

A technical point is that dataset covers only the region $1.2 < |\eta| < 1.8$, although the electrons described in Chapter 5 are accepted in the region with $1.2 < |\eta| < 2.2$. For simplicity [140] the event count is scaled by the total luminosity (85 pb^{-1}) as well as by the ratio of the coverages ($\frac{2.2-1.2}{1.8-1.2} = \frac{5}{3}$). Plugging in yields a prediction of

$$8975 \times \frac{5}{3} \times \frac{85}{32} = 39,733 \approx 40000 \text{ Events.} \tag{I.1}$$

There are 5 $e\gamma$ events and 1 $e\gamma\not\!\!E_T$ event in the sample of 32 pb^{-1}. Thus, a total of approximately 22 $e\gamma$ and 4 $e\gamma\not\!\!E_T$ events, respectively, are estimated to be in the full sample.

I.3 Diphoton Dataset

This is the original diphoton dataset which has two central isolated photons passing the high-threshold selection criteria in Table 2.1. There are 218 events in the sample with $E_T > 25$ GeV.

I.4 Photon + $\not\!\!E_T$ Dataset

The number of photons from cosmic ray sources is estimated to be equal to the number of photon + $\not\!\!E_T$ events in the data. The rate is determined by using, in CDF jargon, the Stream B 'W-No track' trigger dataset (a central electromagnetic cluster with loose identification selection criteria and $E_T > 22$ GeV, and $\not\!\!E_T > 22$ GeV). Events are selected by requiring a tight central photon with $E_T > 25$ GeV and $\not\!\!E_T > 25$ GeV. To remove sources other than cosmic rays, events which have a jet within $\Delta\phi < 0.4$ of the $\not\!\!E_T$ are removed. The results are shown in Table I.1.

Selection	Events	Events after $\Delta\phi$ removal
$\gamma + \not\!\!E_T$ + Good Run	20,971	10,477
ETOUT = 0	11,035	3181

Table I.1: The number of events in the $\gamma + \not\!\!E_T$ sample as additional selection criteria are added. The final column gives the number of events after events which have a jet within $\Delta\phi < 0.4$ of the $\not\!\!E_T$ are removed.

Appendix J

Theory Results of the Minimal Gauge-Mediated Model

In Chapter 6, a total of 50 points in parameter space for the Minimal Gauge-Mediated Model are modeled using the SPYTHIA Monte Carlo [115, 116]: M_2 = 75, 100, 125, 150 and 200 GeV, $\tan\beta$ = 1.1, 2, 5, 10 and 25 and Sgn(μ)= ± 1. Tables J.1, J.2, J.3 and J.4 list the masses and dominant production cross sections for combinations of the various parameters. The values in the Tables are shown in Chapter 6, in Figures 6.1 and Figure 6.2.

M_2 (GeV)	$\tan\beta$	Sgn(μ)	M_{N_1} (GeV)	M_{N_2} (GeV)	M_{C_1} (GeV)	M_{C_2} (GeV)
75	1.1	1	40.685	85.923	85.313	546.169
75	1.1	-1	32.721	63.403	61.478	549.363
75	2	1	42.087	90.380	90.074	211.453
75	2	-1	17.652	52.868	38.584	226.577
75	5	1	39.464	67.355	70.278	175.867
75	5	-1	21.473	52.216	40.006	185.115
75	10	1	36.407	60.001	60.993	174.063
75	10	-1	26.230	53.159	45.102	178.841
75	25	1	33.692	56.863	55.565	174.229
75	25	-1	29.443	54.256	49.117	176.155
100	1.1	1	53.124	108.201	107.929	707.917
100	1.1	-1	47.354	90.338	89.493	710.483
100	2	1	54.599	111.970	111.738	265.514
100	2	-1	37.989	76.689	69.250	279.620
100	5	1	52.076	93.235	94.895	212.568
100	5	-1	39.724	75.292	68.390	222.515
100	10	1	49.728	85.828	86.515	208.684
100	10	-1	42.845	76.908	72.457	213.971
100	25	1	47.850	82.159	81.597	208.300
100	25	-1	44.994	78.618	75.875	210.452
125	1.1	1	65.728	131.580	131.447	868.651
125	1.1	-1	61.137	116.861	116.399	870.795
125	2	1	67.160	134.723	134.590	319.842
125	2	-1	54.731	102.640	98.399	332.762
125	5	1	64.830	118.817	119.854	249.910
125	5	-1	55.641	100.407	96.170	259.945
125	10	1	62.901	111.738	112.202	243.858
125	10	-1	57.806	102.262	99.521	249.302
125	25	1	61.452	107.976	107.664	242.736
125	25	-1	59.340	104.164	102.483	244.968

Table J.1: The gaugino masses for various points in parameter space in the Minimal Gauge-Mediated Model with $M_2 < 150$ GeV

M_2 (GeV)	$\tan\beta$	Sgn(μ)	M_{N_1} (GeV)	M_{N_2} (GeV)	M_{C_1} (GeV)	M_{C_2} (GeV)
150	1.1	1	78.442	155.507	155.439	1027.856
150	1.1	-1	74.605	142.997	142.708	1029.700
150	2	1	79.793	158.171	158.101	373.931
150	2	-1	69.792	129.213	126.543	385.755
150	5	1	77.682	144.247	144.941	287.340
150	5	-1	70.352	126.302	123.463	297.202
150	10	1	76.025	137.549	137.866	279.012
150	10	-1	71.966	128.125	126.264	284.450
150	25	1	74.835	133.850	133.640	277.126
150	25	-1	73.154	130.031	128.884	279.369
200	1.1	1	104.336	204.170	204.153	1342.528
200	1.1	-1	101.427	194.539	194.393	1343.976
200	2	1	105.546	206.190	206.178	480.873
200	2	-1	98.220	182.284	180.970	490.915
200	5	1	103.796	194.868	195.223	361.718
200	5	-1	98.491	178.539	176.996	370.977
200	10	1	102.504	188.884	189.037	348.912
200	10	-1	99.571	180.086	179.042	354.145
200	25	1	101.614	185.423	185.285	345.407
200	25	-1	100.399	181.821	181.163	347.587

Table J.2: The gaugino masses for various points in parameter space in the Minimal Gauge-Mediated Model for $M_2 > 150$ GeV.

M_2 (GeV)	$\tan\beta$	Sgn(μ)	$\sigma_{\rm Tot}$ (pb)	$\sigma_{N_1C_1}$ (pb)	$\sigma_{N_2C_1}$ (pb)	$\sigma_{C_1C_1}$ (pb)
75	1.1	1	5.843	0.143	1.897	2.178
75	1.1	-1	25.640	2.976	9.436	8.781
75	2	1	4.442	0.194	1.403	1.572
75	2	-1	2466.000	1585.000	38.690	838.700
75	5	1	9.839	0.043	4.498	3.432
75	5	-1	2046.000	1333.000	30.640	665.700
75	10	1	19.120	1.478	8.061	6.232
75	10	-1	1033.000	776.900	20.350	220.500
75	25	1	38.020	7.279	10.830	9.985
75	25	-1	327.800	269.900	15.820	26.500
100	1.1	1	1.941	0.020	0.737	0.867
100	1.1	-1	4.155	0.098	1.836	1.785
100	2	1	1.566	0.032	0.581	0.694
100	2	-1	11.470	3.276	3.549	4.209
100	5	1	2.663	0.006	1.228	1.089
100	5	-1	11.280	2.937	3.511	3.862
100	10	1	3.729	0.095	1.763	1.483
100	10	-1	8.079	1.426	3.009	2.994
100	25	1	4.675	0.283	2.073	1.836
100	25	-1	6.401	0.806	2.592	2.438
125	1.1	1	0.772	0.005	0.299	0.366
125	1.1	-1	1.305	0.013	0.566	0.609
125	2	1	0.673	0.007	0.254	0.321
125	2	-1	2.397	0.265	0.987	1.046
125	5	1	0.992	0.001	0.429	0.451
125	5	-1	2.417	0.281	0.986	1.021
125	10	1	1.269	0.016	0.573	0.557
125	10	-1	2.040	0.176	0.881	0.842
125	25	1	1.509	0.042	0.678	0.633
125	25	-1	1.829	0.107	0.805	0.760

Table J.3: The dominant production cross sections for various points in parameter space in the Minimal Gauge-Mediated Model for $M_2 < 150$ GeV.

M_2 (GeV)	$\tan\beta$	Sgn(μ)	$\sigma_{\rm Tot}$ (pb)	$\sigma_{N_1C_1}$ (pb)	$\sigma_{N_2C_1}$ (pb)	$\sigma_{C_1C_1}$ (pb)
150	1.1	1	0.345	0.001	0.129	0.172
150	1.1	-1	0.513	0.003	0.215	0.250
150	2	1	0.309	0.002	0.115	0.154
150	2	-1	0.796	0.045	0.341	0.371
150	5	1	0.422	0.000	0.179	0.200
150	5	-1	0.822	0.053	0.345	0.379
150	10	1	0.509	0.004	0.219	0.236
150	10	-1	0.740	0.034	0.315	0.339
150	25	1	0.588	0.010	0.253	0.264
150	25	-1	0.681	0.021	0.291	0.306
200	1.1	1	0.079	0.000	0.028	0.040
200	1.1	-1	0.104	0.000	0.040	0.053
200	2	1	0.074	0.000	0.026	0.038
200	2	-1	0.141	0.002	0.058	0.072
200	5	1	0.093	0.000	0.036	0.048
200	5	-1	0.148	0.003	0.061	0.073
200	10	1	0.106	0.000	0.043	0.052
200	10	-1	0.138	0.003	0.057	0.068
200	25	1	0.119	0.001	0.048	0.058
200	25	-1	0.132	0.002	0.052	0.064

Table J.4: The dominant production cross sections for various points in parameter space in the Minimal Gauge-Mediated Model for $M_2 > 150$ GeV.

Appendix K

Optimization of the Selection Thresholds for E_T^γ and $\not{E}_T$

This Appendix discusses the selection of the $\not{E}_T$ and photon E_T thresholds used to set limits in Chapter 6. The optimal thresholds exclude the maximal amount of parameter space without being too sensitive to fluctuations in the data. For each point in parameter space the acceptance and background are estimated for E_T^γ thresholds of 12, 18 and 25 GeV, and $\not{E}_T$ thresholds of 25, 30, 35 and 40 GeV. The acceptances are estimated using the methods of Subsection 6.3 and are typically between 1% and 10%. Backgrounds are estimated using the measured $\not{E}_T$ resolution from Chapter 3.1 and shown in Figure K.1 for thresholds of $E_T^\gamma > 12$ GeV, $E_T^\gamma > 18$ GeV and $E_T^\gamma > 25$ GeV respectively. The number of events expected above each threshold combination is summarized in Table K.1.

For each set of thresholds the expected 95% C.L. cross section upper limit is calculated using the Monte Carlo acceptance and the background estimate for the number of 'observed events' [141]. A comparison to the theoretical

cross section determines whether, on average, a given point in parameter space is excluded.

	E_T^γ Threshold		
$\not{E}_T$ Threshold	E_T^γ >12 GeV	E_T^γ >18 GeV	E_T^γ >25 GeV
$\not{E}_T > 25$ GeV	7.144	1.144	0.499
$\not{E}_T > 30$ GeV	1.826	0.290	0.144
$\not{E}_T > 35$ GeV	0.474	0.075	0.041
$\not{E}_T > 40$ GeV	0.123	0.019	0.012

Table K.1: The number of events expected from backgrounds for various combinations of the E_T^γ and $\not{E}_T$ thresholds.

The optimization results are shown in Tables K.2 and K.3 with a 1 representing the expectation of excluding the model at the 95% C.L. From the Table a single set of requirements, $E_T^\gamma > 12$ GeV and $\not{E}_T > 35$ GeV, appears to exclude the maximal amount of parameter space. This appears consistent with Figure 6.3 and Table K.1; in the signal the second photon is often soft and the $\not{E}_T$ is fairly large, and pushing up the $\not{E}_T$ requirement quickly removes most of the background.

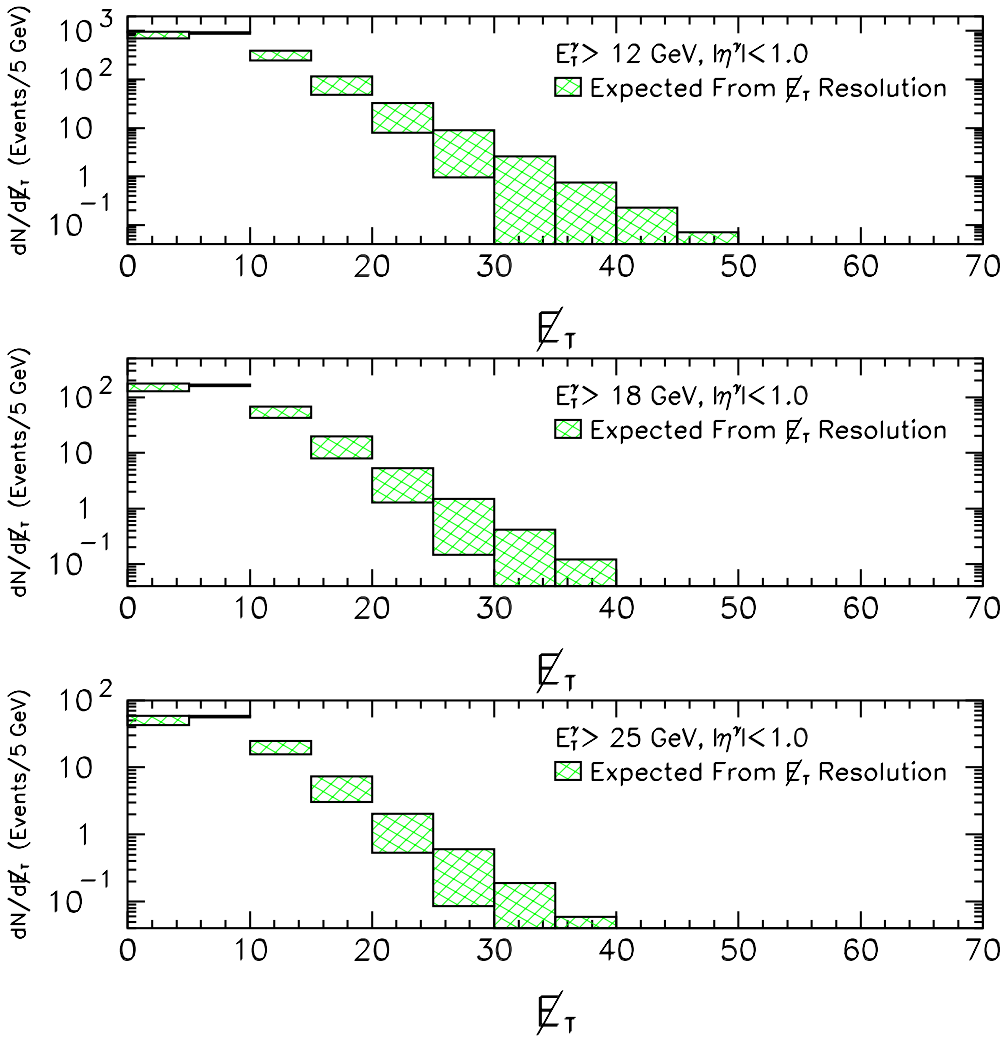

Figure K.1: The expected $\not\!\!E_T$ distribution for Standard Model diphoton events with $E_T^\gamma > 12$ GeV, $E_T^\gamma > 18$ GeV and $E_T^\gamma > 25$ GeV. The boxes represent the 1σ uncertainty in the expectation. The estimate is made using the measured $\not\!\!E_T$ resolution from $Z \to e^+e^-$ events.

		E_T^γ Cut:	12	12	12	12	18	18	18	18	25	25	25	25
		$\not{E}_T$ Cut:	25	30	35	40	25	30	35	40	25	30	35	40
M_2	$\tan\beta$	$\frac{\lvert\mu\rvert}{\mu}$												
75	1.1	1	1	1	1	1	1	1	1	1	1	1	1	1
75	1.1	-1	1	1	1	1	1	1	1	1	1	1	1	1
75	2	1	1	1	1	1	1	1	1	1	1	1	1	1
75	2	-1	1	1	1	0	1	1	0	0	0	0	0	0
75	5	1	1	1	1	1	1	1	1	1	1	0	0	0
75	5	-1	1	1	1	1	1	1	0	0	0	0	0	0
75	10	1	1	1	1	0	1	1	1	0	1	0	0	0
75	10	-1	1	1	1	0	1	1	0	0	0	0	0	0
75	25	1	1	1	1	1	1	1	1	0	1	1	0	0
75	25	-1	1	1	1	1	1	1	1	0	1	1	0	0
100	1.1	1	0	1	1	1	1	1	1	1	1	1	1	0
100	1.1	-1	1	1	1	1	1	1	1	1	1	1	1	1
100	2	1	0	1	1	1	1	1	1	0	1	0	0	0
100	2	-1	1	1	1	1	1	1	1	0	1	1	0	0
100	5	1	1	1	1	1	1	1	1	1	1	1	1	0
100	5	-1	1	1	1	1	1	1	1	0	1	1	0	0
100	10	1	1	1	1	1	1	1	1	1	1	1	1	0
100	10	-1	1	1	1	1	1	1	1	0	1	1	0	0
100	25	1	1	1	1	1	1	1	1	1	1	1	1	0
100	25	-1	1	1	1	1	1	1	1	1	1	1	1	1
125	1.1	1	0	0	1	0	0	1	0	0	0	0	0	0
125	1.1	-1	0	1	1	1	1	1	1	1	1	1	0	0
125	2	1	0	0	0	0	0	0	0	0	0	0	0	0
125	2	-1	0	1	1	1	1	1	1	1	1	1	0	0
125	5	1	0	0	1	0	0	1	0	0	0	0	0	0
125	5	-1	0	1	1	1	1	1	1	1	1	1	0	0
125	10	1	0	1	1	1	1	1	1	1	1	1	0	0
125	10	-1	0	1	1	1	1	1	1	1	1	1	1	0
125	25	1	0	1	1	1	1	1	1	1	1	1	1	0
125	25	-1	0	1	1	1	1	1	1	1	1	1	1	1

Table K.2: Results from the procedure used to select the optimal E_T^γ and $\not{E}_T$ selection criteria for the Minimal Gauge-Mediated Model with $M_2 < 150$ GeV. Every entry is either a 1 or 0; a 1 represents the expectation of excluding the model. A single set of requirements, $E_T^\gamma > 12$ GeV and $\not{E}_T > 35$ GeV, appears to exclude the maximal amount of parameter space on average.

		E_T^γ Cut:	12	12	12	12	18	18	18	18	25	25	25	25
		$\not{E}_T$ Cut:	25	30	35	40	25	30	35	40	25	30	35	40
M_2	$\tan\beta$	$\frac{\lvert\mu\rvert}{\mu}$												
150	1.1	1	0	0	0	0	0	0	0	0	0	0	0	0
150	1.1	-1	0	0	0	0	0	0	0	0	0	0	0	0
150	2	1	0	0	0	0	0	0	0	0	0	0	0	0
150	2	-1	0	0	0	0	0	0	0	0	0	0	0	0
150	5	1	0	0	0	0	0	0	0	0	0	0	0	0
150	5	-1	0	0	0	0	0	0	0	0	0	0	0	0
150	10	1	0	0	0	0	0	0	0	0	0	0	0	0
150	10	-1	0	0	0	0	0	0	0	0	0	0	0	0
150	25	1	0	0	0	0	0	0	0	0	0	0	0	0
150	25	-1	0	0	0	0	0	0	0	0	0	0	0	0
200	1.1	1	0	0	0	0	0	0	0	0	0	0	0	0
200	1.1	-1	0	0	0	0	0	0	0	0	0	0	0	0
200	2	1	0	0	0	0	0	0	0	0	0	0	0	0
200	2	-1	0	0	0	0	0	0	0	0	0	0	0	0
200	5	1	0	0	0	0	0	0	0	0	0	0	0	0
200	5	-1	0	0	0	0	0	0	0	0	0	0	0	0
200	10	1	0	0	0	0	0	0	0	0	0	0	0	0
200	10	-1	0	0	0	0	0	0	0	0	0	0	0	0
200	25	1	0	0	0	0	0	0	0	0	0	0	0	0
200	25	-1	0	0	0	0	0	0	0	0	0	0	0	0

Table K.3: Results from the procedure used to select the optimal E_T^γ and $\not{E}_T$ selection criteria for the Minimal Gauge-Mediated Model with $M_2 > 150$ GeV. Every entry is either a 1 or 0; a 1 represents the expectation of excluding the model. There is no expectation of being able to exclude any of this part of parameter space.

Appendix L

A Check on the Limits Using Different E_T Thresholds

This Appendix presents a check on the limits when the analysis is redone for the case where the E_T^γ requirement is raised to 25 GeV and the $\not{E}_T$ requirement is lowered to 25 GeV. In the data two events pass the selection criteria (the $ee\gamma\gamma\not{E}_T$ candidate event and another event which is described in Table 3.1 and Figure C.3). Figures L.1, L.2, and L.3 show the acceptance and number of events expected for the new requirements. From the optimization section (see Tables K.2 and K.3) while there is the expectation of being able to exclude some of the parameter space, the exclusion region shrinks for both large and small values of M_2, especially for $\tan\beta \approx 2$. These results are confirmed and are illustrated in Tables L.1 and L.2 and Figure L.4.

The results using these thresholds for the $N_2 \to \gamma N_1$ model are given in Table L.3. A total of 1.1 events are expected to pass the selection criteria with $E_T^\gamma > 25$ GeV and $\not{E}_T > 25$ GeV. For N_2N_2 production the acceptance

M_2 GeV	$\tan\beta$	$\frac{\lvert\mu\rvert}{\mu}$	M_{N_1} GeV	M_{C_1} GeV	$\sigma^{95\%C.L.}$ (pb)	σ^{Theory} (pb)	Acc (%)	Events (85 pb^{-1})
75	1.1	1	40.7	85.3	3.96	5.84	2.0(2)	10(1)
75	1.1	-1	32.7	61.5	9.10	25.64	0.9(2)	19(3)
75	2	1	42.1	90.1	3.50	4.44	2.2(3)	8(1)
75	2	-1	17.7	38.6	4583	2466	0.002(1)	4(1)
75	5	1	39.5	70.3	11.05	9.84	0.7(1)	6(1)
75	5	-1	21.5	40.0	3358	2046	0.003(1)	6(2)
75	10	1	36.4	61.0	18.49	19.12	0.5(1)	8(2)
75	10	-1	26.2	45.1	2356	1033	0.005(2)	4(2)
75	25	1	33.7	55.6	20.01	38.02	0.4(1)	14(3)
75	25	-1	29.4	49.1	246.9	327.8	0.034(7)	9(2)
100	1.1	1	53.1	107.9	1.94	1.94	3.9(4)	6.5(6)
100	1.1	-1	47.4	89.5	3.38	4.16	2.3(3)	8.1(9)
100	2	1	54.6	111.7	1.89	1.57	4.0(4)	5.4(5)
100	2	-1	38.0	69.3	10.36	11.47	0.8(1)	8(1)
100	5	1	52.1	94.9	2.13	2.66	3.6(3)	8.2(8)
100	5	-1	39.7	68.4	9.95	11.28	0.8(1)	8(1)
100	10	1	49.7	86.5	3.11	3.73	2.5(3)	7.8(9)
100	10	-1	42.8	72.5	7.30	8.08	1.1(2)	8(1)
100	25	1	47.8	81.6	3.15	4.68	2.4(3)	10(1)
100	25	-1	45.0	75.9	3.57	6.40	2.2(3)	12(1)
125	1.1	1	65.7	131.4	1.17	0.77	6.5(5)	4.3(3)
125	1.1	-1	61.1	116.4	1.46	1.30	5.3(4)	5.8(5)
125	2	1	67.2	134.6	1.22	0.67	6.2(5)	3.6(3)
125	2	-1	54.7	98.4	2.45	2.40	3.1(3)	6.4(7)
125	5	1	64.8	119.9	1.42	0.99	5.4(5)	4.5(4)
125	5	-1	55.6	96.2	2.72	2.42	2.8(3)	5.8(6)
125	10	1	62.9	112.2	1.38	1.27	5.5(5)	5.9(5)
125	10	-1	57.8	99.5	1.78	2.04	4.3(4)	7.5(7)
125	25	1	61.5	107.7	1.50	1.51	5.1(4)	6.5(6)
125	25	-1	59.3	102.5	1.60	1.83	4.8(4)	7.4(6)

Table L.1: The number of expected events, acceptances and the 95% C.L. cross section upper limits from the Minimal Gauge-Mediated Model for $M_2 < 150$ GeV, but using $E_T^\gamma > 25$ GeV and $\not{E}_T > 35$ GeV. The parenthesis represent the uncertainty in the last digit. The uncertainty on the number of expected events includes only the uncertainty in the acceptance.

M_2 GeV	$\tan\beta$	$\frac{\lvert\mu\rvert}{\mu}$	M_{N_1} GeV	M_{C_1} GeV	$\sigma^{95\%C.L.}$ (pb)	σ^{Theory} (pb)	Acc (%)	Events (85 pb^{-1})
150	1.1	1	78.4	155.4	0.86	0.34	8.8(6)	2.6(2)
150	1.1	-1	74.6	142.7	1.01	0.51	7.6(6)	3.3(2)
150	2	1	79.8	158.1	0.96	0.31	7.9(6)	2.1(2)
150	2	-1	69.8	126.5	1.23	0.80	6.2(5)	4.2(3)
150	5	1	77.7	144.9	1.01	0.42	7.6(6)	2.7(2)
150	5	-1	70.4	123.5	1.18	0.82	6.5(5)	4.5(4)
150	10	1	76.0	137.9	0.96	0.51	7.9(6)	3.4(3)
150	10	-1	72.0	126.3	1.07	0.74	7.1(5)	4.5(3)
150	25	1	74.8	133.6	1.01	0.59	7.6(6)	3.8(3)
150	25	-1	73.2	128.9	1.06	0.68	7.2(5)	4.2(3)
200	1.1	1	104.3	204.2	0.95	0.08	8.0(6)	0.54(4)
200	1.1	-1	101.4	194.4	0.92	0.10	8.3(6)	0.73(5)
200	2	1	105.5	206.2	0.91	0.07	8.4(6)	0.53(4)
200	2	-1	98.2	181.0	1.06	0.14	7.2(5)	0.87(7)
200	5	1	103.8	195.2	0.81	0.09	9.4(7)	0.74(5)
200	5	-1	98.5	177.0	0.76	0.15	10.1(7)	1.27(9)
200	10	1	102.5	189.0	0.73	0.11	10.4(7)	0.93(6)
200	10	-1	99.6	179.0	0.76	0.14	10.0(7)	1.17(8)
200	25	1	101.6	185.3	0.71	0.12	10.8(7)	1.09(7)
200	25	-1	100.4	181.2	0.75	0.13	10.1(7)	1.13(8)

Table L.2: The number of expected events, acceptances and the 95% C.L. cross section upper limits from the Minimal Gauge-Mediated Model for $M_2 > 150$ GeV, but using $E_T^\gamma > 25$ GeV and $\not{E}_T > 35$ GeV. The parenthesis represent the uncertainty in the last digit. The uncertainty on the number of expected events includes only the uncertainty in the acceptance.

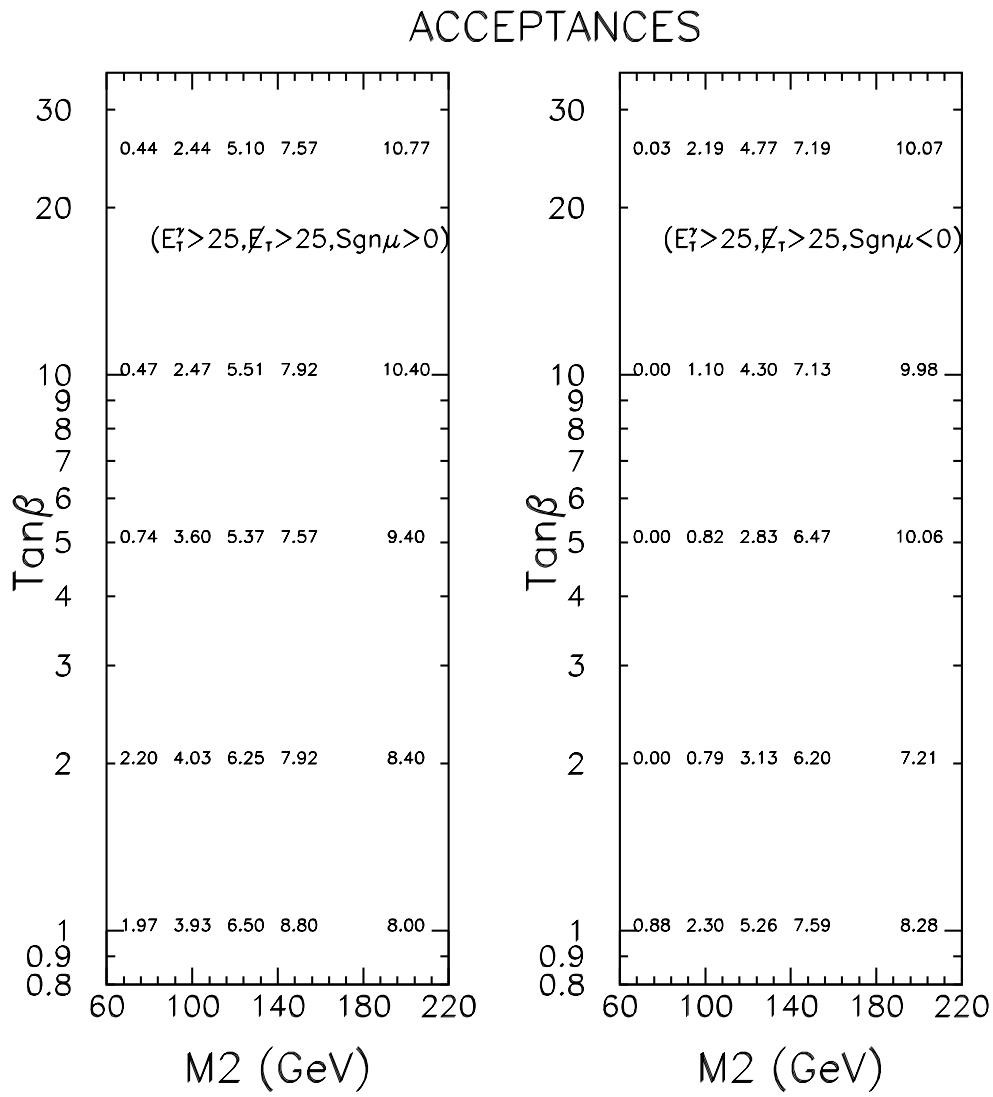

Figure L.1: The acceptances for various points in the $\tan\beta$ vs. M_2 plane using the $E_T^\gamma > 25$ GeV and $\not{E}_T > 25$ GeV thresholds for the Minimal Gauge-Mediated Model. The left hand plot shows the acceptance for Sgn(μ)> 0, the right hand for Sgn(μ)< 0.

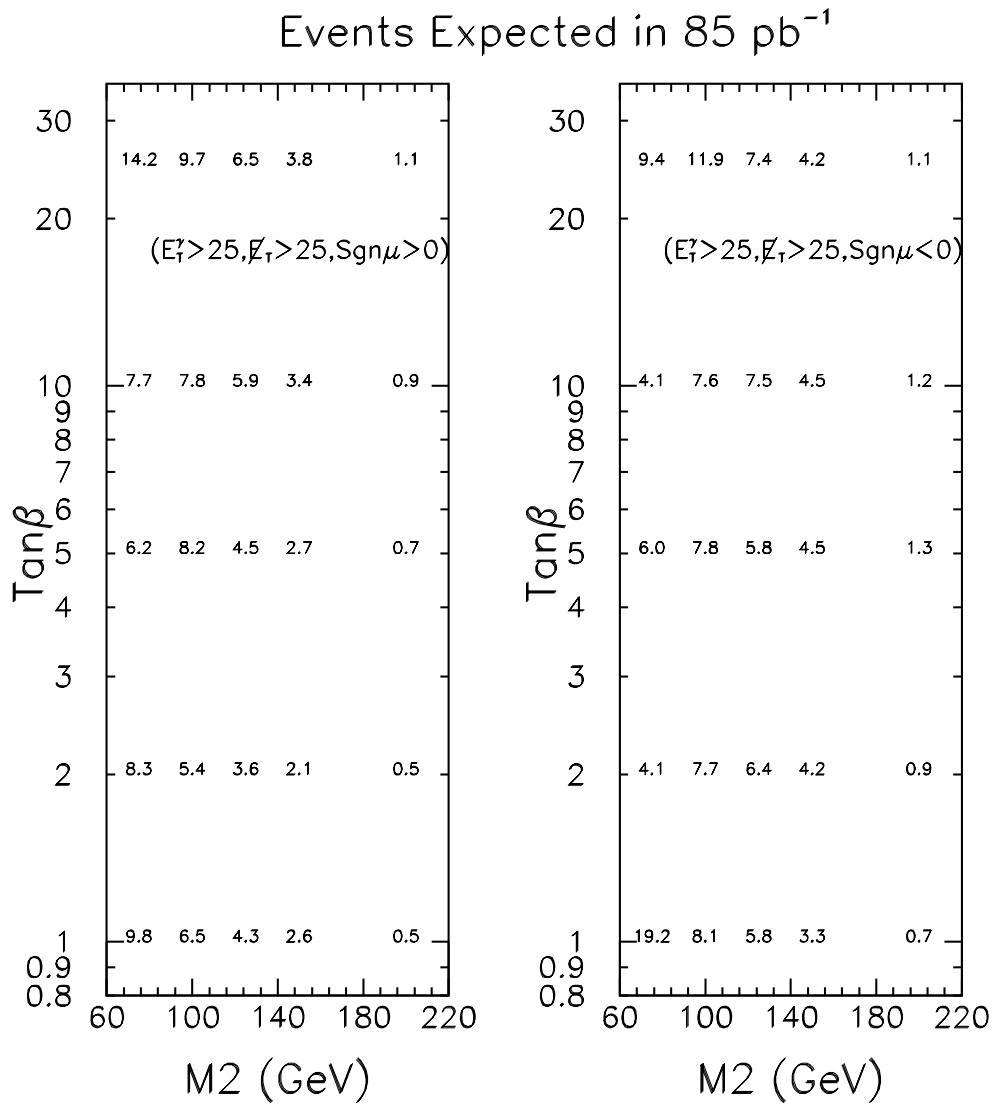

Figure L.2: The number of expected events for various points in the $\tan\beta$ vs. M_2 plane using the $E_T^\gamma > 25$ GeV and $\not{E}_T > 25$ GeV thresholds for the Minimal Gauge-Mediated Model. The left hand plot shows the acceptance for Sgn(μ)> 0, the right hand for Sgn(μ)< 0.

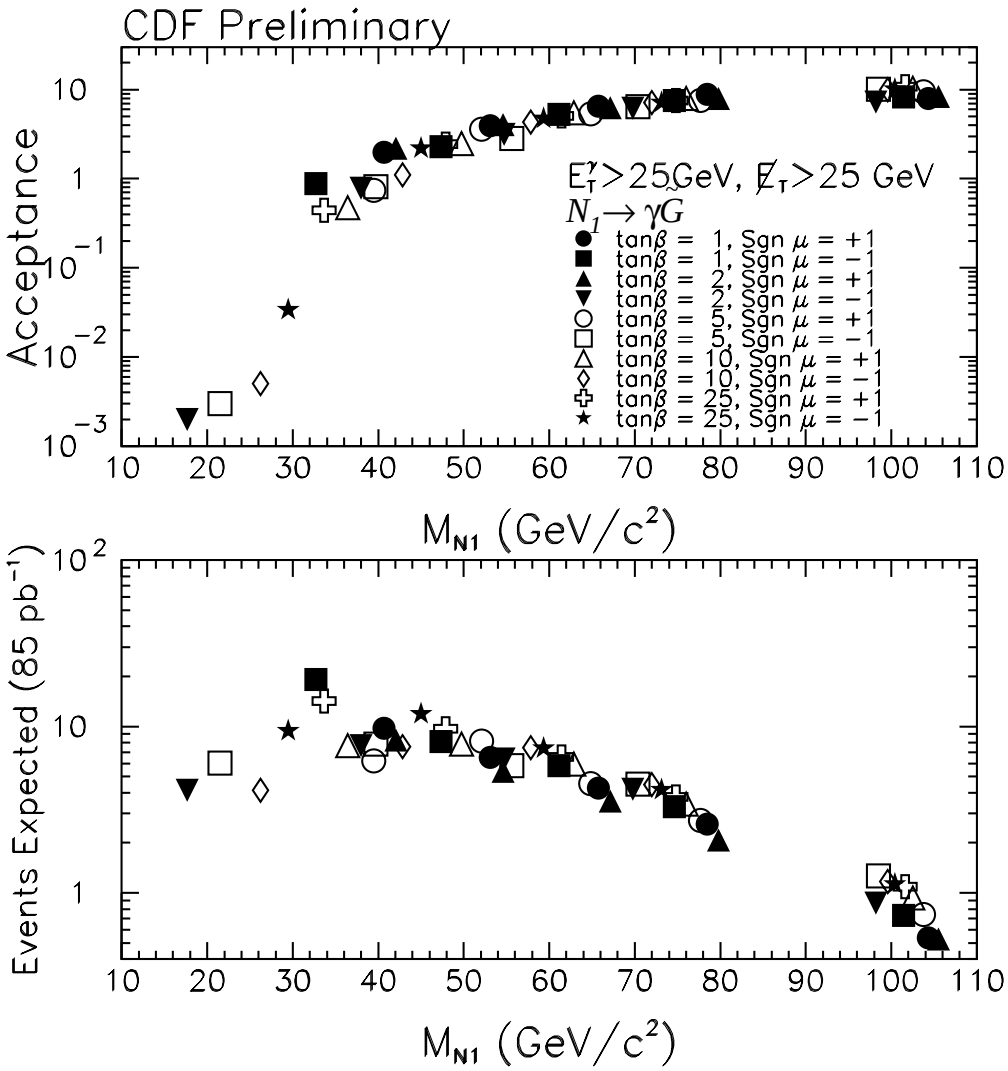

Figure L.3: The number of expected events and acceptances for various points plotted vs. the N_1 mass using the $E_T^\gamma > 25$ GeV and $\not{E}_T > 25$ GeV thresholds in the Minimal Gauge-Mediated Model.

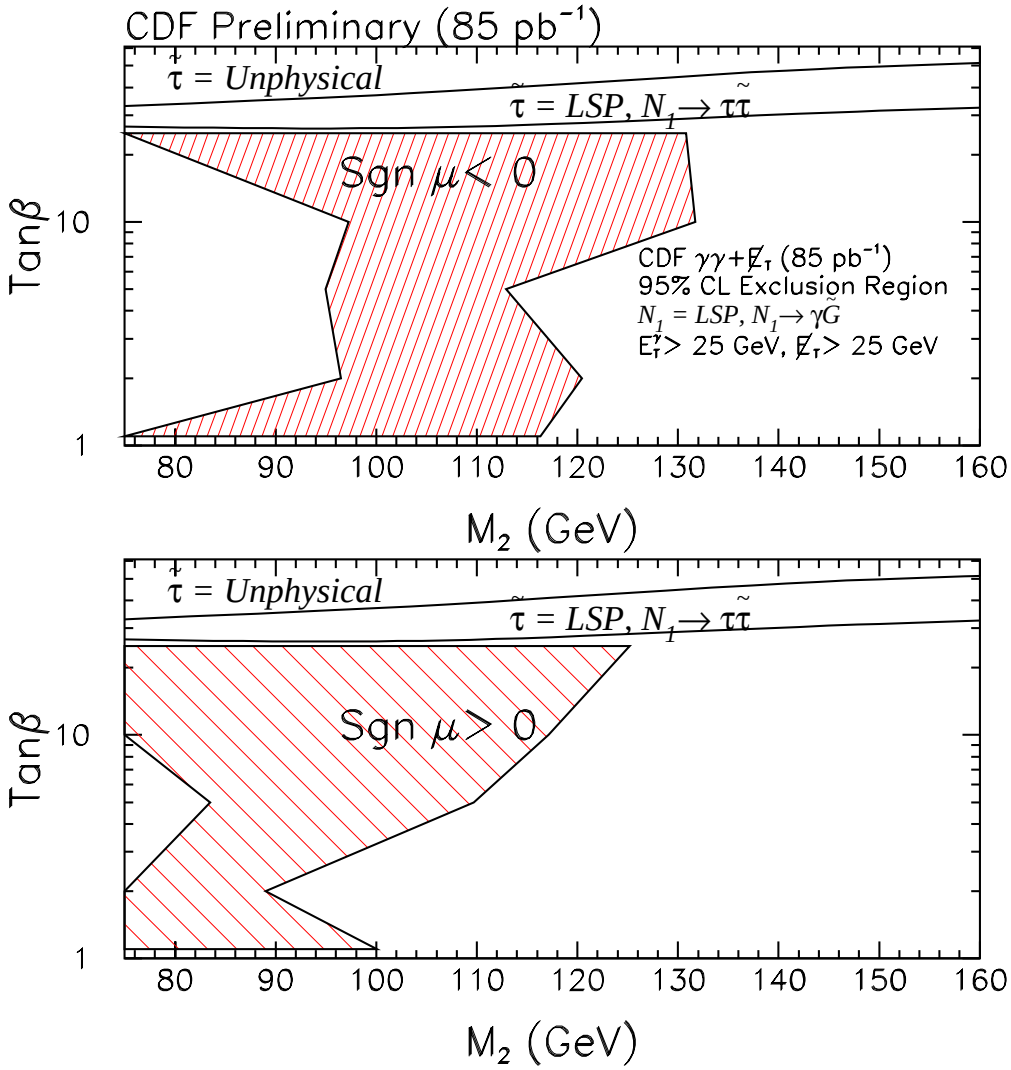

Figure L.4: A contour plot of the excluded region of the Minimal Gauge-Mediated Model in the $\tan\beta$ vs. M_2 plane using the $E_T^\gamma > 25$ GeV and $\not{E}_T > 25$ GeV thresholds.

is 6.2% with a 95% C.L. cross section upper limit of 1.2 pb. These results are tabulated and compared to the standard thresholds in Tables L.3 and L.4.

Results for $E_T^\gamma > 12$ GeV, $\not{E}_T > 35$ GeV					
M_{N_1} (GeV)	M_{N_2} (GeV)	$\sigma^{95\% C.L.}$ (pb)	σ^{Theory} (pb)	Acc (%)	Events (85 pb^{-1})
36.6	64.6	31.58	11.50	0.24± 0.08	2.355± 0.810
Results for $E_T^\gamma > 25$ GeV, $\not{E}_T > 25$ GeV					
M_{N_1} (GeV)	M_{N_2} (GeV)	$\sigma^{95\% C.L.}$ (pb)	σ^{Theory} (pb)	Acc (%)	Events (85 pb^{-1})
36.6	64.6	131.25	11.50	0.11± 0.05	1.077± 0.520

Table L.3: Results from the $N_2 \to \gamma N_1$ model for the two different thresholds $E_T^\gamma > 12$ GeV, $\not{E}_T > 35$ GeV and $E_T^\gamma > 25$ GeV, $\not{E}_T > 25$ GeV. All SUSY processes have been turned on and are allowed to contribute.

Results for $E_T^\gamma > 12$ GeV, $\not{E}_T > 35$ GeV					
M_{N_1} (GeV)	M_{N_2} (GeV)	$\sigma^{95\% C.L.}$ (fb)	σ^{Theory} (fb)	Acc (%)	Events (85 pb^{-1})
36.6	64.6	1054.00	2.21	5.43± 0.44	0.010± 0.001
Results for $E_T^\gamma > 25$ GeV, $\not{E}_T > 25$ GeV					
M_{N_1} (GeV)	M_{N_2} (GeV)	$\sigma^{95\% C.L.}$ (fb)	σ^{Theory} (fb)	Acc (%)	Events (85 pb^{-1})
36.6	64.6	1230.00	2.21	6.20± 0.50	0.012± 0.001

Table L.4: The results from the $N_2 \to \gamma N_1$ model for the two different thresholds: $E_T^\gamma > 12$ GeV, $\not{E}_T > 35$ GeV and $E_T^\gamma > 25$ GeV, $\not{E}_T > 25$ GeV. Note only $N_2 N_2$ production has been simulated and that cross section results are in fb.

Appendix M

Comments on Other Models and Limits from Other Experiments

In this Appendix we discuss some other Supersymmetric models and compare our results to LEP and DØ

M.1 Other Models

As pointed out in Ref. [143], in most light gravitino scenarios the total cross section for high-E_T diphoton events is dominated by gaugino-gaugino production. Thus, to a good approximation the models can be described in a fairly parameter-independent manner by just specifying the gaugino-higgsino sector, i.e, M_1, M_2, μ and $\tan\beta$. In many models, such as supergravity or models which are gauge-mediated, one finds the relation in Equation 6.5. This allows the model to be described by three parameters: M_2, μ and $\tan\beta$. In

gauge-mediated models the gaugino and scalar masses are determined using the relations in Equations 6.5, 6.6 and 6.8. In models such as no-scale supergravity [112] where there are additional constraints from string theory, the models can be completely specified by one parameter: $m_{1/2}$.

To help determine some of the parameters in these models some theorists use the kinematics of the $ee\gamma\gamma\not{E}_{\mathrm{T}}$ candidate event as well as production cross sections to reduce the possibilities. For example in [112], the authors use the kinematics of the event and two production hypotheses: $\tilde{e^+}\tilde{e^-}$ and $\chi^{\pm}\chi^{\mp}$. In the selectron pair-production scenario they find a 'preferred' region in the $\tilde{e} - N_1$ mass plane which spans 75 GeV $< M_{\tilde{e}} <$ 150 GeV and 40 GeV $< M_{N_1} <$ 100 GeV. Note that the upper bound on the $\tilde{e}$ mass is completely determined by requiring that the total number of $ee\gamma\gamma\not{E}_{\mathrm{T}}$ produced in the data be above about 1/2 an event. In addition, because the theory predicts the mass relation between the $\tilde{e}_R$ ($\tilde{e}_L$) and the N_1, the model appears to be inconsistent with an $\tilde{e}_L$, but completely consistent with an $\tilde{e}_R$. Similarly, they prefer the region 100 GeV $< m_{\chi^{\pm}} <$ 150 GeV.

M.2 DØ and LEP Results

The LEP and DØ collaborations work in both the $N_2 \rightarrow \gamma N_1$ and the light gravitino scenarios [123, 124]. While each tests a slightly different model, the results are fairly comparable to those presented in Chapter 6. To compare limits from the Tevatron, we note that the DØ collaboration works sets in the $N_2 \rightarrow \gamma N_1$ scenario for selectron, sneutrino and N_2 pair production. Limits on light gravitino scenarios are set using a gauge-mediated model where the gravitino is light, the decay $N_1 \rightarrow \gamma\tilde{G}$ dominates, and the relation in Equation 6.5 allows the model to be completely described by the parameters

μ, M_2 and $\tan\beta$. However, the relation in Equation 6.8 is ignored, so limits are set in a scenario closer to that of described in [143]. Since the μ dependence on these models is small, except around the $\mu = 0$, the limits are very similar to those presented in Chapter 6. For reference Table M.1 gives the magnitude of μ, as a function of $\tan\beta$ and M_2 for the model of Babu *et al.* [29].

		$\tan\beta$				
		1.01	2	5	10	25
	75 GeV	536	185	132	125	122
	100 GeV	700	245	177	168	165
M_2	125 GeV	862	303	220	209	205
	150 GeV	1022	360	248	261	243
	200 GeV	1338	470	341	323	317

Table M.1: The magnitude of μ for various points in M_2 vs. $\tan\beta$ parameter space for the Minimal Gauge-Mediated Model.

Note that DØ has slightly better cross section upper limits (a chargino mass limit of 150 GeV and a neutralino mass limit of 75 GeV, vs. the 120 GeV and 65 GeV limits presented here) because of three reasons:

- They use 106.3 pb^{-1} of data vs. 85 pb^{-1} used here.
- They use $|\eta_\gamma| < 1.2$ or $1.5 < |\eta_\gamma| < 2.0$ vs. the $|\eta_\gamma| < 1.0$ requirement used here
- They do a background subtraction while none is performed here.

REFERENCES

[1] S.L. Glashow, *Nucl. Phys* **22**, 579 (1961); S. Weinberg, *Phys. Rev. Lett.* **19**, 1264 (1967); A. Salam, Elementary Particle Theory: Relativistic Groups and Analyticity (Nobel Symposium No. 8), edited by N. Svartholm (Almqvist and Wiksell, Stockholm, 1968), p. 367.

[2] E. Witten, *Nucl. Phys.* B **188**, 513 (1981); N. Sakai, *Zeit. f. Physik* C **11**, 153 (1981); S. Dimopoulos and H. Georgi, *Nucl Phys.* B **193**, 150 (1981); R. K. Kaul and P. Manumdar, *Nucl. Phys.* B **199**, 36 (1982).

[3] L. Susskind, *Phys. Rev.* D **20**, 2619 (1980); G. 't Hooft, Recent Developments in Gauge Theories, Proceedings of the Cargèse Summer Institute, Cargèse, France, ed. G. t' Hooft *et al.*; M. Veltman, *Acta Phys. Pol.* B **12**, 437 (1981).

[4] Particle Data Group, *Phys. Rev.* D **54**, 1 (1996).

[5] At CDF, and other collider experiments, the collision occurs with no momentum in the plane transverse to the collision. By conservation of momentum the vector sum of the momentum of the final state particles must be zero in the transverse plane. Since the energies of most final state particles are measured by the detector, any 'imbalance' of energy could indicate the presence of a particle, such as a neutrino, which does not

interact with the detector. This imbalance is known as missing transverse energy or $\not\!\!E_T$.

[6] PHYSMON, Private communication April 28, 1995. The PHYSMON on-line monitoring program is designed to identify unusual events (defined somewhat arbitrarily) and alert the data-taking crew. For example, events with two electron candidates with a large invariant mass are identified. This event satisfied many such criteria.

[7] S. Park, 10th Topical Workshop on Proton-Antiproton Collider Physics, R. Raja and J. Yoh, eds., AIP press, May 1995, p. 62.

[8] This electromagnetic cluster passes all the standard electron selection criteria. While there is some indication that this cluster is not from an electron (discussed in Chapter 4) for the purposes of our current discussion we will treat it as being due to an electron.

[9] A detailed study of the event does not indicate any reason to believe the event is due to a detector mismeasurement or malfunction. Furthermore, the large energy and large angular separation of the photons from the leptons make it unlikely that they originated via Bremstrahlung from the electrons. In addition, the large invariant mass of the ee pair ($M_{ee} = 163$ GeV) is well above the Z mass. These issues are discussed in detail in Chapters 4 and 5.

[10] R. Vidal, A Model for the $ee\gamma\gamma + \not\!\!E_T$ Event, CDF Note 2904, November 1995.

[11] At CDF there is a concerted, but not yet completely systematic, effort to search in a wide range of signatures which do not fall under the auspices

of the standard *a priori* searches for hypothetical new particles. Event way out on the tails of the distributions are known as a 'Zoo' events; unfortunately, it is not obvious what to do with such events when they are found.

[12] R. Culbertson, H. Frisch and D. Toback, Search for Cousins of the $ee\gamma\gamma\not{E}_{\mathrm{T}}$ Event in the diphoton Channel, CDF Note 3456, December 1995. G. Kane suggested the specific decay $N_2 \to \gamma N_1$ mentioned in Ref. [20].

[13] Standard Model $WW\gamma\gamma$ production should produce roughly 10^{-6} such events in the data. This estimate is discussed in more detail in Chapter 5.

[14] While the event is probably a statistical fluctuation of some rare process, it is probably not too bad an assumption. On statistical grounds, one event was observed and is thus the best estimator of the parent population of the rate at which this type of event should be observed.

[15] M. Contreras, H. Frisch, C. Grosso-Pilcher, G. Sullivan and D. Toback, The 970 GeV $Z \to$ ee + 2 jets Event: Does It Have $Z \to q\bar{q}$ + 2 jet Cousins?, CDF Note 2483, February 1994.

[16] It is true that Standard Model neutrinos can be produced via the decay of $Z^0 \to \nu\bar{\nu}$. This idea has interesting consequences which are discussed in Appendix A.

[17] For an excellent introduction to Supersymmetry see S. Dawson, hep-ph/9612229.

[18] H. Baer *et al.*, Contributed chapter to DPF study group on Electroweak Symmetry Breaking and Beyond the Standard Model, hep-ph/9503479. There is no mention of any final state photon signatures.

[19] G. Kane, Private communication. This was pointed out after being shown the event, an early draft of Ref. [12] and asked for possible Supersymmetric interpretations.

[20] H. Haber, G. Kane and M. Quiror, *Phys Letters* B **160**, 297 (1985).

[21] As discussed in Ref. [17] selectrons are the Supersymmetric partner to the Standard Model electron. Similarly, Supersymmetric partners of the neutral bosons (*e.g.* γ, Z^0) are known as neutralinos and are labeled N. The lightest neutralino is labeled N_1, the next to lightest neutralino is labeled N_2.

[22] Dimopoulos *et al.*, *Phys. Rev. Lett.* **76**, 3494 (1996).

[23] S. Ambrosanio *et al.*, *Phys. Rev. Lett.* **76**, 3498 (1996).

[24] G. Kane and J. Wells, *Phys. Rev. Lett.* **76**, 4458 (1996).

[25] G. Bhattacharyya and R.N. Mohaptra, *Phys. Rev.* D **54**, 4204 (1996).

[26] J. L. Rosner, *Phys. Rev.* D **55**, 3143 (1997).

[27] For an excellent review of general of SUSY models with $N_2 \to \gamma N_1$ see S. Ambrosanio *et al.*, *Phys. Rev.* D **55**, 1372 (1997).

[28] S. Ambrosanio *et al.*, *Phys. Rev.* D **54**, 5395 (1996).

[29] K.S. Babu, C. Kolda and F. Wilczek *Phys. Rev. Lett.* **77**, 3070 (1996).

[30] P. Fayet, *Phys. Lett.* B **70**, 461 (1977); *Phys. Lett.* B **175**, 471 (1986).

[31] Report of the Snowmass Supersymmetry Theory Working Group, hep-ph/9609374.

[32] The Collider Detector at Fermilab, A compilation of articles reprinted from *Nuclear Instruments and Methods in Physics Research – A*, North-Holland (1988).

[33] D. Amidei *et al.*, *Nucl. Instrum. Methods*, **A350**, 73 (1994).

[34] P. Azzi *et al.*, SVX′: The New CDF silicon vertex detector, *Nucl. Instrum. Methods* A **360**, 137 (1995).

[35] The z (longitudinal) axis is along the proton beam axis; r is the transverse coordinate. Pseudorapidity (η) is $\eta \equiv -\ln(\tan(\theta/2))$, where θ is the polar angle. Transverse energy is defined as $\mathrm{E_T} = \mathrm{E}\sin(\theta)$.

[36] For a description of photon identification and determination of backgrounds (which are expected to be mostly from π^0's) in CDF see F. Abe *et al.*, *Phys. Rev. Lett.* **73**, 2662 (1994). The purity is measured to increase with the $\mathrm{P_T}$ of the photons, up to where the measurement is limited by statistics.

[37] F. Abe *et al.*, *Phys. Rev.* D **52**, 4784 (1995).

[38] F. Abe *et al.*, *Phys. Rev.* D **52**, 2624 (1995). Note that a much larger portion of the plug calorimeter is used to identify electrons than in the top-quark measurements of Ref. [39].

[39] F. Abe *et al.*, *Phys. Rev.* D **50**, 2966 (1994) and F. Abe *et al.*, *Phys. Rev. Lett.* **74**, 2627 (1995). The b-jet identification used here is the SECVTX algorithm only.

[40] F. Abe *et al.*, *Phys. Rev. Lett.* **79**, 3585 (1997). For more detail see M. Hohlmann, Observation of Top Quark Pairs in the Dilepton Decay

Channel using Electrons, Muons, and Taus dileptons with hadronically decaying tau leptons, Ph.D. thesis, University of Chicago (1997).

[41] D. A. Glenzinski, Observation of the Top Quark in Proton-Antiproton Collisions at a Center of Mass Energy of 1.8 TeV, Ph.D. thesis, The Johns Hopkins University, (1995).

[42] In CDF jargon, we are using the first vertex from the VTVZ bank and require it to have a Class $\geq$ 11. See CDF Note 2084 (May 1993) and references therein for a description of the vertex finding and classification algorithms.

[43] For a detailed description of the definition of an electromagnetic cluster see Ref. [37].

[44] L. Balka *et al.*, The CDF Electromagnetic Calorimeter, *Nucl. Instrum. Methods* A **267**, 272 (1988). Also see ref. [32].

[45] R. Blair, Private communication.

[46] Trigger towers subtend 0.2 $\times 15^\circ$ in $\eta - \phi$ space.

[47] D. Benjamin, 10th Topical Workshop on Proton-Antiproton Collider Physics, R. Raja and J. Yoh, eds., AIP press, May 1995, p. 370.

[48] D. Amidei *et al.*, *Nucl. Instrum. Methods*, **A269**, 51 (1988); T. Carroll *et al.*, *Nucl. Instrum. Methods*, **A263**, 199 (1988); G. W. Foster *et al.*, *Nucl. Instrum. Methods*, **A269**, 93 (1988).

[49] In CDF jargon, the L2 low-threshold diphoton is known as TWO_CEM_10_ISO, the L2 high-threshold trigger is known as

TWO_CEM_16. The corresponding L3 triggers are PHOB_DIPHO_10_ISO and PHOB_DIPHO_16 respectively.

[50] The L2 dielectron trigger is known as TWO_CEM_6_CFT_4_7.

[51] CEM_50 and JET_100 respectively.

[52] The inclusive electron and $Z^0 \rightarrow e^+e^-$ datasets were created by Marcus Hohlmann and myself. Thanks to Marcus for all his invaluable help with this large task. The original reference for this sample is D. Saltzberg, High-E_T Central Electron Datasets, CDF Note 2213, September 1993.

[53] H. Bengtsson and T. Sjöstrand, *Comput. Phys. Commun.* **46**, 43 (1987).

[54] In CDF jargon, the QFL detector simulation is used.

[55] Note that (as shown in Table 2.3) the biggest difference between the data and the Monte Carlo is the E^{Iso}_{3x3} selection; the detector simulation does not correctly simulate how the shower develops between towers. Also note that the outcome of the search in Chapter 3 is not affected by the size of this systematic uncertainty. However, the 95% C.L. cross section upper limits on new physics processes, as calculated in Chapter 6, are affected by this uncertainty and rise by $\approx 10\%$

[56] For more details on the purity estimate see Appendix B.

[57] See F. Abe *et al.*, *Phys. Rev. Lett.* **45**, 1488 (1992) for a description of the jet-finding algorithm and the jet energy corrections. Jets are reconstructed here with a cone in $\eta - \phi$ space of radius 0.4 and are required to have uncorrected $E_T > 10$ GeV to be counted. Reconstructed electrons and photon are not considered jets.

[58] Jet corrections can take into account possible jet energy mismeasurement due to energy from the underlying event or additional interactions, as well as for energy from the jet which falls outside the cone. We use none of these corrections. In CDF jargon these are the JTC96S corrections using the 'NN' and 'DD' parameters.

[59] The best measurement of electron and photon energies are made using corrections based on electron studies. L. Nodulman and K. Byrum, CEM tower calibration and map trip, CDF Notes 2487 (February 1994) and 3477 (January 1996). In the CDF jargon these are the routines CEMFIX, MAPFIX and CEMTWK.

[60] Standard Model $Z^0 \to e^+e^-$ events are used since they have a similar topology to $\gamma\gamma$ events and are not produced with any intrinsic $\not{E}_{\mathrm{T}}$. While other processes, such as WW, WZ and $Z^0 \to \tau\tau \to ee\nu\nu\nu\nu$, can fake the $Z^0 \to e^+e^-$ signature their contamination rate is less than 1%.

[61] The strip chamber measures, in the z direction, a shower energy of 52 GeV, to be compared with a 37 GeV measurement from the full calorimeter.

[62] A technical point worth noting here is that electrons and photons create clusters. However, any cluster not identified as either an electron or photon is counted as a jet. The jet counting algorithm used here only counts jets which are not identified as a photon or electron.

[63] B. Bailey, J. Owens and J. Ohnemus, *Phys. Rev.* D **46**, 2018 (1992), J. Huston, and J. Owens, Event Structure in the Production of High Mass Photon Pairs, hep-ph/9508341, and M. Drees and T Han, *Phys. Rev. Lett.* **77**, 4142 (1996).

[64] S.D. Ellis, R. Kleiss, and W.J. Stirling, *Phys. Lett.* B **154**, 435 (1985).

[65] S. A. Hauger, Measurement of the $Z^0 \to e^+e^-$ + N Jet Cross Sections in $\bar{p}p$ collisions at $\sqrt{S}$ = 1.8 TeV, Ph.D. thesis, Duke University, 1995.

[66] This method should be useful because, as shown in Chapter 2, approximately 85% of the diphoton candidates are due to events which contain jets which fake the photon signature.

[67] The photon at ϕ = 4.11 rad has a good SVX stub pointing directly at it. The SVX stub finding routines are discussed in Chapter 4 and in Appendix G.

[68] For completeness, we note that (in CDF jargon) the CMU-CMUP tight central muon criteria only require one $|\Delta x|$ cut to be satisfied. The isolation energy, $\mathrm{E_T^{Iso}}$, is the energy in a cone of $\Delta R = 0.4$ centered on the muon. The scalar sum of the $\mathrm{P_T}$ of the tracks, $\Sigma\mathrm{P_T^{Iso}}$, is performed in a cone of $\Delta R = 0.4$ centered on the muon but not including the $\mathrm{P_T}$ of the muon.

[69] In the CDF jargon, we are using the Method 1 b-tag estimate. See Ref. [39].

[70] This is done to be consistent with the background estimate which looks at jets produced in association with diphoton candidates. Note that this has some subtle consequences. For example, if the there are three photons in the event with 12, 12 and 26 GeV respectively, the first two pass the low-threshold requirements and the third photon passes the high-threshold requirement then this would be considered a three photon event. However, if an event has three photon candidates with 12, 26 and 26 GeV

respectively, and the two 26 GeV candidates pass the high-threshold criteria, but not the low-threshold criteria, (which is unlikely however) then this event will not be considered an additional photon candidate.

[71] For more details on the method in which fake rates are calculated see Appendix D. The inclusive dijet production sample is dominated by generic QCD jets and not other potential sources of background. The assumption here is that the jets in the processes we are looking at are the same as generic jets. We ignore any contributions from real physics processes.

[72] For example, the event could be due to two $\bar{p}p$ collisions occurring at the same time, each producing part of the event. Similarly, the event could be the overlap of a $\bar{p}p$ collision and a cosmic ray interaction. Perhaps parts of the event are due to jets which faked the electron and/or photon identification criteria.

[73] In the CDF jargon this is a Class 12 vertex. See Ref. [42].

[74] The efficiency for finding a track in the CTC falls rapidly for $|\eta| > 1.4$. The η for the cluster is η = -1.63. In addition the inner layers of the CTC have high occupancy in the event making finding any evidence of a track impossible.

[75] The average $\bar{p}p$ collision, or min-bias collision in CDF jargon, typically produces between 5 GeV and 10 GeV of ΣP_T in association with a vertex. Figure A.5 shows the ΣP_T for a set of min-bias collisions which occur in $Z^0 \rightarrow \mu^+\mu^-$ events.

[76] Note that if the clusters in the event were to come from any of the other vertices in the event their E_T would significantly change. For example the

E_T of the cluster in the plug calorimeter is, using the vertex at 20.4 cm, 63 GeV. The E_T becomes 72, 83, and 85 GeV for the vertices at -8.9, -33.7 and -38.9 cm, respectively, making each far less likely.

[77] S. Kuhlmann, Timing Information For Central Photons and the $ee\gamma\gamma\not{E}_T$ Event, CDF Note 4256, July 1997. Since most electrons and photons do not deposit energy in the hadronic calorimeters this method is not very efficient for finding timing information. It is thus not unusual that one of the three central clusters in the event does not have timing information.

[78] The sample of photons from cosmic rays is the same as used in Ref. [77]. Events are selected from a sample of single photon events in which the ratio of $\not{E}_T/E_T^{\gamma} > 1.0$.

[79] In CDF jargon, γ_1 is located at $Z_{\rm strip}$= -158.3 cm and $X_{\rm wire}$ = 16.5 cm, and γ_2 is located at $Z_{\rm strip}$= -107.7 cm and $X_{\rm wire}$ = 3.1 cm.

[80] The energy resolution of the central and plug electromagnetic calorimeters are $(\frac{\delta E}{E})^2 = (\frac{(13.5\pm0.7)\%\ \mathrm{GeV}^{1/2}}{\sqrt{E_T}})^2 + ((1.0 \pm 1.0)\%)^2$ and $(\frac{\delta E}{E})^2 = (\frac{(28)\%\ \mathrm{GeV}^{1/2}}{\sqrt{E}})^2 + ((2.0 \pm 2.0)\%)^2$, respectively.

[81] This is not strictly true. The identification of electrons in the plug calorimeter in the top-quark dilepton analysis require the presence of a track in the CTC. However, since the cluster in the event is in a region of the detector where the track finding efficiency is approximately zero, this requirement is removed.

[82] We note that the measurement of the shower in the electromagnetic calorimeter would also be unusual for an electron. However, a detailed study

indicates that the problem is not significant and may be due to noise in the calorimeter. For more details see Appendix E.

[83] For technical completeness we note that the trajectory passes through the fiducial part of module 7 of the VTX (more than ≈ 0.06 radians from the module boundary); 7 hits are expected and 7 are observed. In addition, the trajectory passes through the non-fiducial region of module 0 (the boundary is at $\phi = 0.294$). In that region 8 hits are observed where 10 hits are expected.

[84] Q. Fan, A. Bodek and H. Budd, New Information About the Plug e Candidate in the "$ee\gamma\gamma\not{E}_{\mathrm{T}}$" Event, CDF Note 3935, October 1996.

[85] Q.Fan and A.Bodek, Page 553, Proceedings of VIth International Conference on Calorimetry in High Energy Physics, June 8-14, 1996, Frascati (Rome), Italy.

[86] Typically, the SVX is used to find stubs associated with CTC tracks. The method used here works by using fake CTC information based only on the calorimeter and the vertex position information ($\phi, \theta, D_0, \mathrm{P_T}$ and Z_0) as an input to the SVX stub finding algorithms. This method was developed with the help of David Stuart and is described in detail in Appendix G.

[87] The SVX is only instrumented in the region approximately 1 cm $< |Z| <$ 28 cm. The fiducial part of the SVX is defined to be 2 cm $< |Z| <$ 26 cm. Using the z position of the vertex, the measured η of a given electron candidate from the calorimeter, and the radii of the SVX layers, the number of layers the trajectory of the electron should traverse is determined. The trajectory is required to pass through 3 or more layers, and 3 or more clusters are required for any stub.

[88] Using $\frac{dE}{dX}$ techniques, the η for the stub can be inferred. The amount of charge (which is proportional to the energy deposited in the silicon) collected by the SVX strips, Q, helps determine the path length of the particle through the strip. For a given stub, the cluster with the smallest amount of charge deposited, normalized by the trajectory angle $Q_{\mathrm{Min}}^{\mathrm{Uncorr}} \times Sin(\theta) = Q_{\mathrm{Min}}$, is a good measure of the direction of the charged particle. For more details see Appendix G and Refs. [84, 85].

[89] For more details about mismeasured or fake stubs see Appendix G.

[90] The SVX stub-finding algorithm, as shown in Appendix G, is designed to be very efficient for finding stubs, so that they may be compared to the selection criteria in Table 4.6. The algorithm often finds stubs which are completely unrelated to the electron/photon candidate. Thus, the fact that each photon in the event has a stub which does not pass the requirements is not unusual and does not indicate that these are not photons.

[91] The hypothetical trajectory between the vertex at 20.4 cm and the location of the cluster, as measured in the strip chambers, passes through the inner three layers of the SVX, and passes between the two SVX barrels at radius of the fourth layer, as shown in Figure 4.6.

[92] Note that there is only one other electron in the sample which has $|\Delta\phi| > 0.03$, as shown in the central electron plot in Figure 4.8. The stub picked up by the algorithm is a good 4-cluster stub which is attached to a soft, nearby track. The stub associated with the high P_T electron CTC track is a perfectly good 3-cluster stub with the appropriate $\Delta\phi$. It is not

selected because the algorithm selects 4-cluster stubs over 3-cluster stubs. There are no other such stubs found for the plug electromagnetic cluster.

[93] D. Stuart, Private communication. The amount of energy deposited in each layer of the SVX is given by a Landau distribution. The probability of the amount of energy deposited to be below the requirement to create a cluster is less than 1

[94] As a check, the charge deposition in the SVX clusters can be studied (see Appendix G for more details on the variables used here). The stub for the plug cluster has $Q_{\mathrm{Min}}^{\mathrm{Uncorr}} = 422$. Using the vertex at 20.4 cm and $\eta = -1.72$ gives $Q_{\mathrm{Min}} = 145$ is as expected from a charged particle at this appropriate η. Turning the information around, a best guess η region for the stub can be inferred. From Figure G.4 a best guess is that the Q_{Min} should be 100 $< Q_{\mathrm{Min}} < 200$. Using $100 < Q_{\mathrm{Min}}^{\mathrm{Uncorr}} Sin\theta < 200$ and $Q_{\mathrm{Min}}^{\mathrm{Uncorr}} = 422$ yields the prediction that $1.42 < |\eta| < 2.11$. Similarly, assuming the vertex at 20.4 cm, the cluster pattern (i.e, only the inner three layers were hit in a single barrel) implies the range $-1.9 < \eta < -1.61$ or $0.7 < \eta < 0.8$.

[95] The SVX tracking region only extends in the region 2.8 cm $<$ Radius $<$ 7.8. Consequently, any measurement of the impact parameter, D_0, azimuthal angle ϕ and $\mathrm{P_T}$ are highly correlated. If the stub is not due to the cluster in the PEM, then the $\mathrm{P_T}$ is not constrained by the energy measurement. Removing all calorimeter information changes the impact parameter measurement to be $D_0 = 233 \pm 180\mu$m. For more details see Appendix G.

[96] For a more detailed description of the arguments see Appendix H.

[97] It is important to note that while the photon sample was selected as having no nearby tracks (see Table 2.1), the efficiency of these criteria is estimated in Section 2.6.3 as 95.3%. Assuming all of the photons rejected from the sample have a VTX occupancy of greater than 50% and $|\Delta\phi|$ >0.03 rad, the estimates could be as large as 15% and 7% respectively.

[98] S. Jadach *et al.*, TAUOLA version 2.5 (June 1994); Also see *Comput.Phys.Commun.* **76** 361, (1993) and references therein.

[99] Note that if the cluster were due to the hadronic decay of a τ, the measured energy of the cluster, as seen in Figure 4.13b, should be between 20% and 100% of the original τ energy. Thus, the true energy of the original τ is only loosely constrained. It is also important to point out that the $\not\!\!E_{\mathrm{T}}$ could significantly be affected. For example, a τ with 275 GeV of energy (95 GeV of transverse energy) could deposit 63 GeV of transverse energy in the electromagnetic calorimeter with the neutrino carrying away 32 GeV of $\mathrm{E_T}$ pointing at the cluster. Adding this to the $\not\!\!E_{\mathrm{T}}$ in the event indicates that the $\not\!\!E_{\mathrm{T}}$ of the true system would have to be increased to 87 GeV to accommodate the ν_τ cancellation.

[100] For a plot of the $\Delta\phi_{SVX-PES}$ distribution for a sample of fake electrons see Appendix D.

[101] If the cluster in the plug were due to an electron then the plug and central calorimeters should be treated similarly as it shouldn't matter in which area the electron landed. However, if the cluster is due to a fake, then the fake rates for the plug and central calorimeters are taken into account naturally using the methods of Appendix D.

[102] Note that the list of electron requirements does not include the SVX $\Delta\phi$ cut or the χ^2_η and χ^2_ϕ variables since they are not part of the standard selection criteria. One further complication is that the CTC track requirement is removed since it restricts the η range in which electrons can be found to be so small that the $ee\gamma\gamma\not{E}_{\rm T}$ candidate event would not pass the topology requirements. Removing these requirements is conservative as it only increases the rate at which Standard Model processes could produce the event.

[103] S. Mrenna, Private communication. This calculation was performed using MADGRAPH [104] and PYTHIA [53]. Also See Ref. [23]. Based on experience with Diboson production there is about a 30% uncertainty on the $WW\gamma\gamma$ cross section because of higher order corrections and structure function uncertainties.

[104] T. Stelzer and W.F. Long, *Comput.Phys.Commun.* **81**, 357, (1994).

[105] For completeness, we note that in the $WW\gamma\gamma$ Monte Carlo sample a total of 468 events in the sample have both electrons in the central calorimeter (CC) and 270 have one in the central calorimeter and one in the plug calorimeter (CP). Requiring one of the electrons to be in the plug calorimeter would reduce the prediction to 2.8×10^{-7} events.

[106] Both electrons are selected using the standard electron requirements and a pair invariant mass with $81 < \mathrm{M}_{\mathrm{e}^+\mathrm{e}^-} < 101$ GeV.

[107] Both methods used here for finding an additional central photon are probably an overestimate by a factor of two because they include contributions from real photons and fakes.

[108] Note that the number of events has been overestimated because all the numbers used include the $ee\gamma\gamma\not{E}_{\rm T}$ candidate event. A less conservative estimate of the number of $ee\not{E}_{\rm T}$ events would not include the event. Similarly, the calculation of the rate for additional photons should not include the event.

[109] F. Abe *et al.*, *Phys. Rev. Lett.* **78**, 4537 (1997).

[110] Note that this assumes a high triggering efficiency for each process. The trigger rate for every process listed here is very close to 100%.

[111] Note that SUSY scenarios could produce such a situation. For example $C^+C^- \to WN_1WN_1 \to W(\gamma\tilde{G})W(\gamma\tilde{G})$.

[112] J. Lopez and D. Nanopoulos, *Mod. Phys. Lett.* A**10**, 2473 (1996).

[113] This section was written with the help of C. Kolda.

[114] The 'observable sector' includes all known Standard Model particles as well as their SUSY partners.

[115] S. Mrenna, *Comput.Phys.Commun.* **101**, 232, (1997).

[116] C. Kolda, Private communication.

[117] For more details on the Minimal Gauge-Mediated Model see Ref. [29] and Appendix J.

[118] It should be pointed out that the amount of 'parameter' space in which the decay $N_2 \to \gamma N_1$ dominates is considered 'small' and therefore unattractive by some theorists. The $M_1 \approx M_2$ assumption is different from the SUGRA hypothesis where $M_1 \approx M_2/2$, and does not assume

common scalar or gaugino masses at the unification scale. While this effectively removes the SUGRA SU(5) relation between the $U(1)$ coupling and the other couplings the model remains consistent with Supergravity and the squarks (except possibly Stop) and sleptons are often found to be mass degenerate.

[119] We have used the model in Appendix B (Table 12) of Ref. [27] which assumes that the $ee\gamma\gamma\not{E}_{\mathrm{T}}$ candidate event is real and due to $\tilde{e}_L\tilde{e}_L$ production, and the $\tilde{t}$ is not light.

[120] The mean number of expected signal events for a given cross section is determined using the acceptances, efficiencies and luminosity. This number is smeared by the systematic uncertainties (ignoring cases where the number of 'smeared' events is less than zero) and then smeared again using Gaussian/Poisson statistics to determine the number of 'observed' signal events.

[121] For a description of the optimization procedure see Appendix K.

[122] For a more detailed comparison see Appendix M.

[123] ALEPH Collaboration, submitted to *Phys. Lett. B*, CERN-PPE-97-122, DELPHI Collaboration, submitted to *Zeit. f. Physik C*, CERN-PPE-97-107, L3 Collaboration, submitted to *Phys. Lett. B*, CERN-PPE-97-076, OPAL Collaboration, *Phys. Lett.* B **391**, 210 (1997).

[124] DØ Collaboration papers. S. Abachi *et al.*, *Phys. Rev. Lett.* **78**, 2070 (1997) and B. Abbott *et al.*, hep-ph/9708005

[125] Note that this is not the same event found in Chapter 3.

[126] The $\mu^+\mu^-\gamma\gamma jj$ candidate event was originally found in the diboson ($W\gamma$ and $Z^0\gamma$) by H. Sato.

[127] Note that the $\mathrm{P_T}$ of the $\mu^+\mu^-\gamma\gamma$ system is similar to that of the $ee\gamma\gamma$ system in the $ee\gamma\gamma\not{E}_{\mathrm{T}}$ candidate event.

[128] In CDF jargon, both muons pass through the CMU/CMP compartments.

[129] Muon 4-vectors are typically measured using, in CDF jargon, the beam-constrained track measurements. The W mass measurement uses CTC alignment corrections. These values were provided by A. Hardman via private communication.

[130] D. Benjamin *et al.*, Plug Photons in $W\gamma$ Production, CDF Note 3205, Measurement of QCD Backgrounds for Plug Photons in $W\gamma$ Events, CDF Note 3206.

[131] T. Kamon, Private communication. This is known as a 'Texas' tower.

[132] As a check, the real event rate is estimated using the PYTHIA Monte Carlo and a detector simulation [53, 54] to simulate $Z^0\gamma$ events and allow final state radiation to contribute the extra photon. In 4,545 pb^{-1} of simulated data no events are found. The 95% C.L. upper limit is thus 0.07 events. Note that this does not include requiring two extra jets. Adding in the probability of finding two jets yields an expectation of less than 2.8×10^{-3} events.

[133] Remember that the $\mu^+\mu^-\gamma\gamma jj$ event is not in this sample because the μ^+ does not pass the HAD requirement.

[134] Many of the aspects are still valid in a non-SUSY interpretation. The similarity between final state SUSY and E(6) or other models is often striking. For example see Ref. [25, 26, 27].

[135] For $E_T^\gamma <$ 35 GeV the CES $\chi^2_{\rm CES}$ is studied. For candidates with $E_T^\gamma >$35 GeV, the pulse height in the CPR to is compared to an equivalent pulse height of greater than 1 minimum ionizing particle. For more details see Ref. [36].

[136] Thanks go to Ping Yeh for collecting the relevant dataset. Events were selected from the inclusive jet triggers which were, in CDF Jargon, Stream B JET_20, JET_50 and JET_70 triggers.

[137] A look at events in the same run indicate that anode layer is not always systematically higher than expected.

[138] For a more detailed description of the method used to determine the shower shape see Appendix F.

[139] Note that this method is similar to, but not the same as, that used in Refs.[84, 85].

[140] The acceptance is not flat as a function of η, rather it is falling off rather steeply. This method is thus an overestimate.

[141] To avoid being too sensitive to fluctuations in the data the the number of 'observed' events is set to be the mean number of expected events from the background rounded up to the nearest integer.

[142] $N_{Expected} = \sigma_{theory} \cdot L \cdot Acc$

[143] J. Ellis, J. Lopez and D. Nanopoulos, *Phys. Lett.* B **394**, 354 (1997).